Search for dark matter with EDELWEISS-III excluding background from muon-induced neutrons

Co-supervised thesis prepared at

Université Claude Bernard Lyon 1, France
according to the decree from January 6th, 2005
Numéro d'ordre: 20-2016

Karlsruher Institut für Technologie, Germany
according to the *Promotionsordnung des Karlsruher Instituts für Technologie (KIT) für die Fakultät für Physik* from November 30th, 2012

Approved version

by

Cécile Kéfélian

Examination date:	05.02.2016
President:	Prof. Dr. Martin Wegener
Co-director:	Prof. Dr. Corinne Augier
Co-director:	Prof. Dr. Dr. h.c. Johannes Blümer
Korreferent (KIT):	Prof. Dr. Josef Jochum
External reviewers (UCBL):	Dr. Vitaly Kudryavtsev
	Dr. Fabrice Piquemal
Other examiners:	Prof. Dr. Milada Margarete Mühlleitner
	Prof. Dr. Dany Davesne

Search for dark matter with EDELWEISS-III excluding background from muon-induced neutrons

Zur Erlangung des akademischen Grades eines
DOKTORS DER NATURWISSENSCHAFTEN
von der Fakultät für Physik
des Karlsruher Instituts für Technologie
und der Universität Claude Bernard Lyon 1

genehmigte
DISSERTATION
von

Cécile Kéfélian

Contents

Abstract

Evidence for the existence of a non-baryonic dark matter can be found on all astrophysical and cosmological scales in the Universe. From observations of the Cosmic Microwave Background Radiation, the dark matter contribution to the total energy content of the Universe is estimated to be 27%. A generic class of particles to solve the dark matter puzzle is known as *Weakly Interacting Massive Particles* (WIMPs) with masses in the GeV-TeV range and expected interaction rates with ordinary matter of the order of the weak scale interaction. The aim of the EDELWEISS-III experiment is to detect the elastic scattering of WIMPs from the galactic dark matter halo on germanium bolometers. At cryogenic temperatures of $\approx 18\,\mathrm{mK}$, the expected energy deposit of $\mathcal{O}(\mathrm{keV})$ from a WIMP-induced nuclear recoil produces measurable heat and ionization signals. The main challenge of such a direct detection experiment is the low expected rate of WIMP-nucleon scattering, constrained by the latest results to be below a few events per year per 100 kg. Therefore, multiple layers of external shielding protect the experiment from ambient radioactivity. The remaining background coming from the radioactivity of elements inside the shields are rejected by using a particle identification based on the recoil type. The most problematic background arises from neutrons, which induce nuclear recoils indistinguishable from a WIMP signal in the detectors. In particular, neutrons are produced by cosmic ray muons and their shower. Therefore, the experiment is located in the underground laboratory of Modane, where 4800 m w.e. of rock attenuate the cosmic muon flux by a factor 10^6 down to $5\,\mu/\mathrm{m}^2/\mathrm{day}$. The remaining muons are tagged using an active μ-veto system surrounding the experiment, which is made of 46 plastic scintillator modules.

This thesis was performed in the context of the EDELWEISS-III experiment, whose goal is to probe WIMP-nucleon cross-sections at least one order of magnitude smaller compared to EDELWEISS-II, down to 10^{-9} pb. To reach this goal, many improvements were applied to the experimental setup in order to reduce the residual background level to less than 1 event for one year of data taking. Particular attention was paid to previously negligible backgrounds, such as μ-induced neutrons. A careful monitoring of the μ-veto system was performed in the context of this thesis, to ensure a maximum efficiency. For a precise estimation of the remaining μ-induced background, new GEANT4 Monte Carlo simulations had to be performed, which included the new bolometer configuration inside the cryostat as well as the newly implemented polyethylene shielding. In parallel, data taken during the 8 months of WIMP search of Run308, with 24 bolometers of FID800 type, was studied in the framework of this thesis.

With a selected subset of this data, a dedicated analysis was performed to study coincidences between the μ-veto system and the bolometers. Characteristics of the μ-induced events were studied and compared with simulations. In particular, the rates were found to be consistent within uncertainties. For an accumulated fiducial exposure of $1603\,\mathrm{kg}\cdot\mathrm{days}$, no WIMP-like event (single nuclear recoil) was seen in coincidence with the μ-veto. This result is consistent with the rate of WIMP-like events expected from simulations.
Knowing the signatures of μ-induced bolometer events, a lower limit on the μ-veto efficiency was derived by identifying a sample of μ-induced bolometer events and verifying

that they were seen in coincidence with the μ-veto. A sample of 32 bolometer events was selected, all seen by the μ-veto, leading to a lower limit on the tagging efficiency of:

$$\varepsilon_{\mu\text{-veto}} > 93\% \ (90\% \ \text{C.L.})$$

This efficiency can also be derived from simulation. In the previous EDELWEISS-II experiment, the determination of this efficiency was limited by the lack of knowledge of the module response at low energies. Therefore, a new method was set up to derive the position-dependent trigger threshold of individual μ-veto modules. The method is based on the comparison of the measured energy spectrum of an AmBe source with the simulated spectrum, which is folded with the parametrized module response function. The set of function parameters giving the best match between the two spectra is derived with a likelihood analysis, while the uncertainties on the parameters are estimated using a Monte Carlo Markov Chain. By repeating this procedure for several positions of the source along the module axis, the position-dependent trigger threshold is extracted. To finally derive the muon detection efficiency of a module, its position-dependent response is applied on the simulated energy spectrum of muon interactions. The method was successfully applied on a test module and gave an efficiency of $(95.0 \pm 0.5)\%$, where the error is dominated by the uncertainty on the source activity. From here on, it is possible to calculate the overall μ-veto efficiency, by applying the method to the remaining modules.

An estimation of the expected μ-induced neutron background was performed for the WIMP search analysis of EDELWEISS-III data. An analysis for WIMPs in the standard mass range [10,1000] GeV was performed for an accumulated exposure of $600 \, \text{kg} \cdot \text{days}$ and revealed an excess of neutrons. Two dedicated studies performed in the framework of this thesis showed that this background cannot be induced by untagged muons and must thus be of radiogenic origin. An additional low mass WIMP analysis with 8 selected bolometers and a similar fiducial exposure was performed for the mass range [3,30] GeV. For both analyses, the expected μ-induced neutron background was calculated to be $\ll 1$ events, even before vetoing and thus negligible. A coincidence analysis confirmed that there are no events in the signal region in coincidence with the μ-veto.

The initial design goal of EDELWEISS-III was to reach a background free exposure of first $3000 \, \text{kg} \cdot \text{days}$ and then $12000 \, \text{kg} \cdot \text{days}$, after which background is expected to appear. A projection of the μ-induced neutron background for these two exposures, extrapolated from Run308 results, was performed. A conservative estimation showed that the remaining background after vetoing is below 1 event, even in the extended exposure scenario. In conclusion, the μ-induced neutron background is not a limiting factor for WIMP search with EDELWEISS-III.

Résumé

L'existence de la matière noire, une matière qui n'asborbe, ni n'émet de lumière, se manifeste par ses effets gravitationnels à toutes les échelles de l'Univers, aussi bien astrophysique que cosmologique. À partir de l'observation du fond diffus cosmologique, il a été estimé que cette matière noire, dont la nature est inconnue, représente 26% du contenu total en énergie de l'Univers, tandis que la contribution de la matière baryonique n'est que de 5%. Les 69% restant constituent une forme d'énergie inconnue responsable de l'expansion de l'Univers, appelée énergie noire. La quasi-totalité de l'Univers nous étant inconnue, de nombreuses expériences ont été mises en place, notamment pour détecter et déterminer la nature de la matière noire. Une classe de particules particulièrement privilégiée pour constituer la matière noire est connue sous le nom de Weakly Interacting Massive Particle (WIMP) : ces particules sont massives, non-relativistes et interagissent faiblement avec la matière baryonique. Le but de l'expérience EDELWEISS (Expérience pour détecter les WIMPs en site souterrain) est la détection directe de WIMPs, par leur diffusion élastique sur les noyaux de germanium constituant les détecteurs bolométriques. À des températures cryogéniques avoisinant $18\,\mathrm{mK}$, le dépôt d'énergie attendu, de l'ordre du keV, induit des signaux chaleur et ionisation mesurables.

Le principal challenge d'une telle expérience de détection directe de matière noire est le taux de diffusion WIMP-nucléon attendu, contraint par les observations les plus récentes à moins de quelques événements par an par centaines de kilogrammes. Ce taux d'événement est bien plus faible que celui attendu de la radioactivité ambiante et dans la même gamme d'énergie. Des couches successives de blindage sont donc utilisées afin de réduire la quantité de bruit de fond atteignant les détecteurs. Grâce à la double mesure de l'énergie déposée, les reculs électroniques induits par les γ et β issus de la radioactivité peuvent être distingués des reculs nucléaires induits par les WIMPs. Le plus problématique des bruits de fond provient donc des neutrons qui interagissent dans un seul détecteur, indiscernables des reculs nucléaires induits par des WIMPs. Ces neutrons sont notamment induits par les muons cosmiques et les gerbes qu'ils produisent. C'est pourquoi EDELWEISS est située dans le Laboratoire Souterrain de Modane (LSM), dans le tunnel du Fréjus, sous une couverture rocheuse de $1800\,\mathrm{m}$. Le flux de muons atteignant le laboratoire est ainsi atténué d'un facteur 10^6, avec un flux résiduel de $5\,\mu/\mathrm{m}^2/\mathrm{jour}$. Ces muons résiduels sont détectés par un système veto muon (veto-μ) composé de 46 modules de scintillateur plastique entourant l'expérience, permettant de rejeter une grande partie du bruit de fond interagissant dans les bolomètres inhérent aux muons.

Cette thèse s'inscrit dans le cadre de la troisième phase de l'expérience (EDELWEISS-III), dont le but est de sonder une section efficace d'interaction WIMP-nucléon au moins 10 fois plus faible qu'avec EDELWEISS-II, atteignant $10^{-9}\,\mathrm{pb}$. Pour ce faire, de nombreuses modifications ont été apportées au dispositif expérimental de la seconde phase, afin de réduire le taux de bruit de fond résiduel total à moins d'un événement pour une année de prise de données. Ainsi, les bruits de fond autrefois négligeables, tels que celui induit par les muons, ont dû être contrôlés avec attention et précisément estimés.

Dans le cadre de cette thèse, un monitoring quotidien du veto-μ a été réalisé afin d'assurer

une efficacité maximale du système à rejeter les événements induits par les muons dans les détecteurs Ge. Dans ce but, les outils de monitoring ont été considérablement améliorés afin de contrôler le fonctionnement des 46 modules du veto-μ. Afin d'estimer précisément le bruit de fond résiduel induit par les muons, essentiel pour l'identification des WIMPs, l'efficacité de rejet du veto-μ ainsi que le taux d'événement indistinguable des WIMPs ont été déterminés. Ce taux de coïncidence dépend en particulier de la géométrie de l'expérience ainsi que des matériaux utilisés, qui ont subi d'importantes modifications dans le cadre de la 3$^{\text{ème}}$ phase de l'expérience. On peut notamment citer une plus grande granularité et densité du groupe de détecteurs Ge, augmentant la probabilité de diffusion multiple des particules induites par les muons, qui peuvent ainsi être rejetées. De plus, de nouveaux blindages de polyéthylène, installés pour atténuer les neutrons issus de la radioactivité ambiante, atténuent également les neutrons induits par les muons dans le blindage de plomb. Pour quantifier l'effet de ces changements sur le bruit de fond neutron induit par les muons, il est indispensable d'effectuer des simulations et d'analyser les coïncidences entre le veto-μ et les détecteurs Ge dans les données.

Les huit mois de données accumulés avec 24 détecteurs Ge de $800\,$g durant le run cryogénique Run308 ont été analysés en terme de coïncidence dans le cadre de cette thèse. Dans le but de comparer les résultats avec la simulation, des coupures strictes ont été appliquées sur les données veto-μ et bolomètre, aboutissant à une sélection de (133.6 ± 2.7) jours. Chaque événement veto-μ a été associé à l'événement bolomètre le plus proche. La différence en temps $\Delta t = t_{\text{bolo}} - t_{\text{veto}}$ attendue pour des coïncidences induites par des muons a été extraite et est incluse dans une fenêtre en temps $\Delta t = \pm 12\,\mu$s. Un total de 190 coïncidences a été mesuré dans cette fenêtre, comprenant (32.1 ± 0.4) coïncidences accidentelles. Le taux d'événement bolomètre en coïncidence avec la détection d'un muon par le veto-μ (au moins 1 module avec un dépôt d'énergie) est donc de :

$$\Gamma^{\mu}_{\text{M}_{\text{veto}}\geq 1} = 1.18 \pm 0.10 \text{ (stat) } {}^{+0.03}_{-0.02} \text{ (sys) événements/jour}$$

Parmi ces coïncidences, seuls les événements fiduciels dans la bande de recul nucléaire à 90%, ayant un seul bolomètre avec un dépôt d'énergie $E_{\text{rec}} = [10, 200]\,$keV limite la sensibilité de l'expérience. Aucun événement de ce type n'a été mesuré en coïncidence avec le veto-μ durant les (133.6 ± 2.7) jours sélectionnés, aboutissant à la détermination d'une limite inférieure sur le taux d'événement similaire à des WIMPs induit par les muons qui vaut :

$$\Gamma^{\text{WIMP-like}}_{\text{M}_{\text{veto}}\geq 1} < (1.7 \times 10^{-2}) \text{ événements/jour} \quad (90\% \text{ C.L.})$$

Ces résultats ont été comparés avec ceux obtenus à partir de simulations Monte Carlo GEANT4 du passage des muons dans le dispositif expérimental, réalisées avec le logiciel existant mis à jour avec la nouvelle géométrie. À partir de ces simulations, le taux de coïncidence entre les détecteurs Ge et le veto-μ ainsi que leur topologie ont été extraits. La simulation prédit un taux de coïncidence pour un veto-μ 100% efficace de :

$$\Gamma^{\mu}_{\text{simu}} = 1.09 \pm 0.01 \text{ (stat) } {}^{+0.24}_{-0.00} \text{ (sys) événements/jour}$$

Le taux d'événement indistinguable de WIMP a également été déterminé en sélectionnant les événements fiduciels dans la bande de recul nucléaire à 90%, ayant un seul bolomètre avec un dépôt d'énergie avec $E_{\text{rec}} = [10, 200]\,$keV. Ce taux, pour $\varepsilon_{\text{veto-}\mu} = 100\%$, est de :

$$\Gamma^{\text{WIMP−like}}_{\text{simu}} = (7.6 \pm 0.1 \text{ (stat) } {}^{+2.6}_{-1.7} \text{ (sys)}) \times 10^{-3} \text{ événements/jour}$$

Ainsi, les taux simulés et mesurés sont en accord dans la limite des incertitudes. La comparaison des deux taux ne permet pas de conclure sur l'efficacité du veto-μ à cause des incertitudes élevées.

L'analyse des coïncidences entre le veto-μ et les detecteurs Ge a également montré que les événements induits par les muons dans les bolomètres peuvent être distingués d'autres bruits de fond en appliquant des coupures sur le nombre de bolomètre ayant mesurés un dépôt d'énergie et sur l'énergie totale déposée. Une limite inférieure sur l'efficacité du veto-μ a pu être établie en sélectionnant un jeu d'événements explicitement induits par des muons, en vérifiant s'ils ont été détectés par le veto-μ. 32 événements ont ainsi été sélectionnés, tous mesurés en coïncidence avec le veto-μ dans une fenêtre de temps de $\pm 12\,\mu$. Considérant la statistique limitée, une limite inférieure sur l'efficacité de rejection du veto-μ est extraite :

$$\varepsilon_{\text{veto-}\mu} > 93\% \ (90\% \ \text{C.L.})$$

L'efficacité du système veto muon peut également être calculée à partir de simulations des muons dans le dispositif expérimental. Pour ce faire, la réponse de chacun des 46 modules de scintillateur, notamment leur seuil de déclenchement, doit être extraite et implémentée dans la simulation. La contrepartie de se protéger des muons par un épais blindage de roche est qu'ils ne sont plus assez nombreux pour être utilisés afin de déterminer la réponse des modules. C'est pourquoi une nouvelle méthode, basée sur l'utilisation d'une source radioactive d'AmBe, a été mise au point dans le cadre de cette thèse. Elle permet de déterminer la réponse des modules en fonction de la position de l'interaction qui varie fortement à cause de l'absorption des photons de scintillation dans ces modules de 2 à 4 m de longueur. Cela peut être réalisé en comparant le spectre AmBe mesuré avec le spectre simulé, auquel a été préalablement appliqué la réponse du module paramétrée par 4 inconnues. Une analyse de maximum de vraisemblance a été mise en place pour déterminer ces paramètres et répétée pour différentes positions de la source le long de l'axe du module. L'incertitude sur ces paramètres a été déterminée à l'aide d'une analyse par *Markov Chain Monte Carlo*. Le seuil de déclenchement en fonction de la position peut ainsi être extrapolé, permettant de déterminer l'efficacité individuelle de chaque module à détecter le passage d'un muon à partir de la simulation. Cette méthode a été appliquée avec succès sur un module test (module M42) et donne une efficacité de :

$$\varepsilon_{\text{M42}} = (95.0 \pm 0.5)\%$$

où l'erreur est dominée par l'incertitude sur l'activité de la source d'AmBe. En appliquant cette méthode sur les autres modules, il est donc possible de déterminer précisément l'efficacité du système veto muon à partir de la simulation.

À partir des études décrites ci-dessus, le bruit de fond neutron induit par les muons a été estimé pour les deux analyses du Run308 en terme de matière noire. Une analyse dédiée à la recherche de WIMPs de masse standard, comprise entre 10 et 100 GeV, a été effectuée pour une exposition totale de $600\,\text{kg} \cdot \text{j}$ basée sur une sélection de 17 bolomètres. Cinq reculs nucléaires simples ont été observés dans la région d'intérêt, ce qui révèle la présence d'une source de neutron inconnue. Deux analyses effectuées dans le cadre de cette thèse ont montré que ce bruit de fond n'est pas d'origine cosmogénique mais radiogénique. Tout d'abord, le bruit de fond neutron induit par les muons attendu pour cette configuration a été simulé en prenant en considération la réponse moyenne des bolomètres, et est estimé avant rejet par le veto-μ à :

$$N_{\text{simu}}^{\text{WIMP-like}} = 0.36 \pm 0.02 \ (\text{stat}) \ ^{+0.12}_{-0.08} \ (\text{sys}) \ \text{événements}$$

En considérant la limite inférieure sur l'efficacité de rejet du veto-μ et les 6% du temps accumulé pendant lequel un dysfonctionnement du veto-μ a été détecté, une limite supérieure sur le nombre d'événements similaires à des WIMPs attendus dans les données a été extraite :

$$N_{\text{WIMP-like}}^{\mu} < 0.06 \ \text{events} \quad (90\% \ \text{C.L.})$$

Ainsi, même en négligeant le veto-μ, le bruit de fond neutron induit par les muons attendu ne peut pas expliquer les reculs nucléaires observés. Une autre preuve de l'origine radiogénique de ce bruit de fond provient de la comparaison de la topologie des événements neutrons mesurés avec celle des événements neutrons induits par les muons.

Une estimation du bruit de fond induit par les muons a également été réalisée pour la recherche de WIMPs de basse masse entre 3 et 30 GeV, montrant que le bruit de fond attendu est négligeable.

Pour ces deux analyses, aucun événement similaire à un WIMP n'a été mesuré en coïncidence avec le veto-μ, conformément aux prédictions issues de la simulation. Ainsi, le bruit de fond neutron induit par les muons ne limite pas la sensibilité actuelle de l'expérience.

Le but initial d'EDELWEISS-III était d'atteindre dans un premier temps une exposition de 3000 kg · j sans bruit de fond, puis une exposition de 12000 kg · j pour laquelle le bruit de fond devrait apparaitre. Une projection du bruit de fond neutron induit par les muons attendu pour ces deux expositions a été réalisée en extrapolant les résultats du Run308. Bien qu'aucun événement similaire à un WIMP n'ait été mesuré en coïncidence avec le système veto lors du Run308, il est indispensable de garantir le bon fonctionnement du système veto pour une exposition plus large. En effet, pour 3000 kg · j et un seuil d'analyse de 10 keV, $2.07^{+0.71}_{-0.40}$ événements indistinguables d'un WIMP sont attendus. Considérant la limite inférieure sur l'efficacité du système veto muon de 93% et un dysfonctionnement du veto-μ pendant 6% du temps d'acquisition, la limite supérieure sur le bruit de fond neutron irréductible est de $0.24^{+0.08}_{-0.05}$ événement. Le bruit de fond irréductible reste inférieur à 1 événement, même pour une exposition prolongée de 12000 kg · j.

Ainsi, même si le bruit de fond neutron induit par les muons pourrait constituer un bruit de fond irréductible limitant la sensibilité de l'expérience à la recherche de matière noire, il peut être efficacement rejeté par l'utilisation d'un système veto-μ. Pour conclure, le bruit de fond neutron induit par les muons n'est pas un facteur limitant pour la recherche de matière noire, lorsqu'il est bien géré.

1. The case of dark matter

Nowadays, it is established knowledge that the well-known baryonic matter makes up only 5% of the total energy content of the Universe. According to the standard model of cosmology, 69% is made of the so-called *dark energy*, responsible for the expansion of the Universe, and 26% of an invisible cold non-baryonic so-called *dark matter*. This picture of the Universe is well supported by observations on all scales of the Universe. Cosmological observations provide notably a precise and full description of the Universe, as will be shown in section 1.1. The implications of these observations on the nature of dark matter will be described in section 1.2. The focus will be put on Weakly Interacting Massive Particles (WIMPs), as the EDELWEISS experiment was designed to search for this generic class of particles. Other strategies to detect dark matter will be lastly summarized in section 1.3.

1.1. Observational evidences at cosmological scales

The first hints of the existence of dark matter were found by the study of the local neighbourhood of the Milky Way in 1922 and of nearby galaxy clusters in 1933 [1]. F.Zwicky first introduced the concept of *cold dark matter* to explain the radial velocity dispersion of galaxies inside the Coma cluster. However, nearly 40 years were needed for his idea to be universally recognized by the scientific community [2].
Since then, numerous observations at all scales in the Universe strengthened this idea. A non-exhaustive selection of the most striking evidences at cosmological scales is presented in the following, after a review of the founding principles of modern cosmology.

1.1.1. Cosmological framework

The ΛCDM model is the simplest parametrization of the Big-Bang cosmological model and particularly successful to reproduce cosmological observations [2]. It is often referred to as the "standard model of cosmology". Some alternative models exist, the most well-known being the model of Modified Newtonian Dynamics (MOND) [3]. MOND was originally introduced to explain the abnormal rotation curves of stars in galaxies, but although it successfully explained galactic dynamics, it failed to explain observations at the scale of galaxy clusters and at cosmological scales.
Three elements are used to construct the ΛCDM model: Einstein's equations of general relativity, which relate the geometry of the Universe with its matter and energy content; a metric to describe the symmetries; and last an equation of state describing the physical

properties of the matter and energy content [4]. The ΛCDM model is based on the so-called *cosmological principle*, which states that the Universe is isotrope at any point and therefore homogeneous at large scale. No observation until now shows any disagreement with this postulate. Consequently, the Universe at large scales can be described by the Friedmann-Lemaître-Robertson-Walker (FLRW) metric, which describes an isotropic expanding Universe with uniform density and a curvature. The element of space-time ds is related to the element of time dt and the element of space as follows (here written in the Robertson-Walker form following [5]):

$$ds^2 = -dt^2 + a^2(t)R(t_0)^2 \left[\frac{dr^2}{1 - kr^2} + r^2 d\Omega^2 \right] \tag{1.1}$$

where $d\Omega^2$ is equal to $d\Omega^2 = d\theta^2 + \sin^2(\theta)d\phi^2$ with θ the zenith angle and ϕ the azimuth angle. The parameter k is the curvature parameter and takes on the values $+1$, 0 or -1 for a curved, flat or negatively curved Universe, respectively. $a(t)$ is the scale factor: it gives the relationship between the distance $R(t_0)$ between two objects at the present time t_0 and their distance $R(t)$ at a time t as:

$$R(t) = R(t_0) \times \frac{a(t)}{a(t_0)} \tag{1.2}$$

with $a(t_0) = 1$ by normalization. The scale factor can therefore be written here in a normalized form $a(t) = R(t)/R(t_0)$. Note that the redshift of electromagnetic radiation, which is explained by a stretching of the wavelength due to the expansion of the Universe, can be related to the scale factor at the time it was emitted.

Using the FLRW metric, the general relativity equations developed by Einstein for a static Universe ($\dot{a} = 0$) are reduced to the two following Friedmann equations, which give the dynamics of the Universe:

$$H^2 \equiv \left(\frac{\dot{a}}{a} \right)^2 = \frac{8\pi G}{3}\rho + \frac{\Lambda}{3} - \frac{k}{a^2 R(t_0)^2} \tag{1.3}$$

$$\frac{\ddot{a}}{a} = -\frac{4\pi G}{3}(\rho + 3p) + \frac{\Lambda}{3} \tag{1.4}$$

where $H \equiv \dot{a}/a$ is the so-called *Hubble parameter*, G the gravitational constant, ρ and p the sum of all contributions to density and pressure in the Universe and k the space curvature. Λ, the so-called *cosmological constant*, was added by Einstein to the formulation of general relativity to allow a stable static solution to the equations [6]. It quantifies the energy density of the vacuum. The effects of the cosmological constant can be taken into account by including the vacuum energy density ρ_Λ in the total density of the Universe ρ. Then, one can define from eq. 1.3 the critical energy density ρ_c as the total density for which the Universe if flat ($k = 0$):

$$\rho_c \equiv \frac{3H^2}{8\pi G} \tag{1.5}$$

The total density is often expressed in terms of the critical density by introducing:

$$\Omega_i = \frac{\rho}{\rho_c} = \left(\frac{8\pi G}{3H^2} \right) \rho_i \tag{1.6}$$

with $i = m, r, \Lambda$ the individual contribution to the Universe total density from non-relativistic matter, radiation and relativistic matter, and the cosmological constant, respectively. If the Universe is flat, then $\Omega_{tot} = \sum_i \Omega_i = 1$. With this parametrization, there is a direct link between the value of Ω_{tot} and the curvature k of the Universe.

As the individual components can be described as perfect fluid with a simple equation of state, the Friedmann equations have a simple solution. For a flat Universe, the dependence of Ω_i with the scale factor varies as follow [7]:
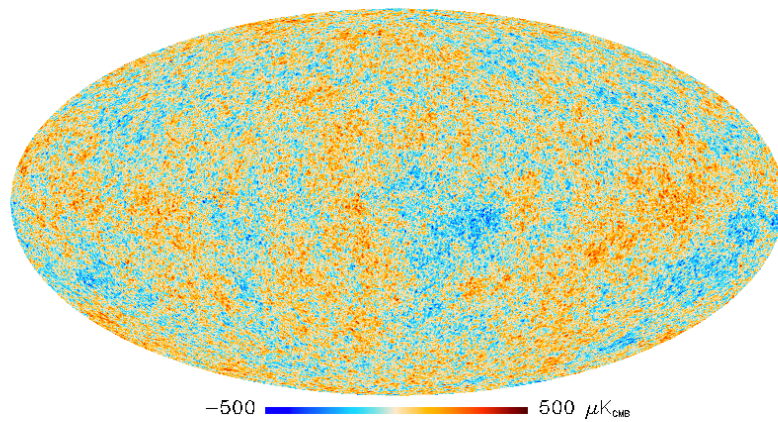
Figure 1.1. – CMB full sky map of the temperature anisotropies as observed by the Planck satellite. The color scale indicates the measured temperature fluctuations of the order of the μK. Extracted from [8].

— for massive particles with negligible relative velocities, the energy density is given by their number density times their rest mass. As the Universe expands, the number density decreases with the volume, leading to $\Omega_m \propto a^{-3}$.

— for relativistic particles and photons, referred to as radiation in cosmology, the energy density is given by their number density times their energy. As the Universe expand, radiation is redshifted, decreasing its energy proportionally to a^{-1}. Thus, $\Omega_r \propto a^{-4}$.

— only the vacuum energy density, referred to as dark energy, is independent from the scale factor.

Thus, for low redshift, i.e. in the early Universe, radiation was dominating the energy density and determined the expansion. At higher redshift, matter starts to dominate and determines the expansion rate.

The component Ω_m can be further divided in two sub-components $\Omega_m = \Omega_b + \Omega_{cdm}$, where Ω_b and Ω_{cdm} are the baryonic and non-baryonic components of the non-relativistic matter, respectively. From cosmological and astrophysical observations, the unknown parameters characterizing the ΛCDM model can be extracted, giving a full picture of the Universe. This can notably be achieved by studying the cosmic microwave background.

1.1.2. Cosmic microwave background

At the earliest age of the Universe, after quarks and gluons combined to form neutrons and protons, matter and radiation were in equilibrium in a hot plasma. Electrons and protons were prevented to combine by high energy photons, which were dominating the energy content of the Universe. These photons were scattering off free electrons, with a small mean free path between successive collisions due to the high density of the medium. Their energy spectrum was therefore continuous and described by a black body spectrum. With its expansion, the Universe cooled down, reaching a temperature of $\sim 3000\,\mathrm{K}$ around 380000 years after the Big-Bang. At this temperature, the mean energy of the photons became too low to prevent the formation of neutral hydrogen. Photons were then able to travel on large scales without being deflected and radiation decoupled from matter. The relic of this radiation contains information about the last scattering surface, notably on the matter density distribution. Due to the expansion of the Universe, these thermal photons are red-shifted and nowadays measured with a black body spectrum at $2.725\,\mathrm{K}$ in the microwave range. This Cosmic Microwave Background (CMB) was first accidentally discovered by A. Penzias and R. Wilson in 1963 as they were studying the microwave
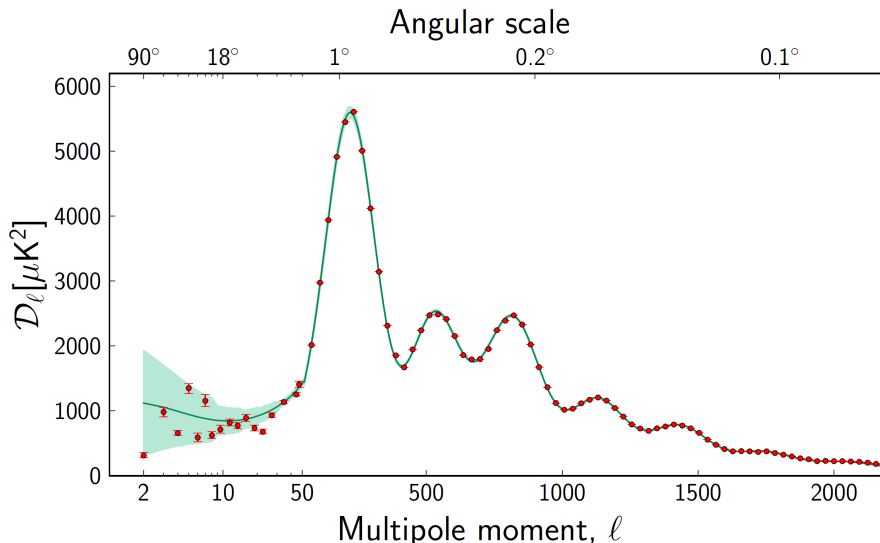
Figure 1.2. – Power spectrum of the temperature anisotropies in the CMB as measured by Planck (red markers). The green band shows the spectrum for the ΛCDM model adjusted to the data. Extracted from [8].

signal of the Milky Way. The COBE satellite mission later measured that the CMB is an almost perfect black body radiation spectrum, but with small anisotropies of temperature [9]. A better precision on the CMB was achieved with the WMAP satellite [10] and with Planck satellite [8], which is currently still taking data.

The latest full sky map provided by the Planck satellite after subtraction of the foreground is given in fig. 1.1. Temperature fluctuations of the order of the μK can be resolved and correlations between two points can be calculated and expanded in spherical harmonics. The power spectrum derived from these correlations is given in fig. 1.2. It shows the intensity of the temperature anisotropies versus the angular scale l of the fluctuations, knowing that small values of l indicate large structures and vice versa. The measured peaks can be associated to acoustic oscillations in the plasma before the decoupling of matter and radiation. The position of the first peak of highest amplitude gives information on the curvature of the Universe. The density of baryonic and non-baryonic matter can be extracted from the amplitude of the second and third peaks. Indeed, these acoustic waves were generated from overdensities and underdensities of baryons in the primordial plasma, similarly to sound waves. The origin of these fluctuations is postulated to arise from quantum fluctuations in the inflaton fields after the Big-Bang, smeared by the exponential expansion. The overdense regions gravitationally attracted the surrounding matter, whereas the radiation pressure from photons and heat had the opposite effect. As baryons interact with photons, they were sensitive to the radiation pressure and moved away from overdense regions. Dark matter mainly interacts gravitationally and remained in overdense regions. Thus, the density fluctuations of baryons did not grow but oscillated due to the balance between radiation pressure from photons and heat and the gravitational attraction from dark matter. At the time of the decoupling between baryons and photons, the acoustic waves were frozen in the baryon distribution. These acoustic waves are referred to as Baryonic Acoustic Oscillations (BAO).

By fitting the ΛCDM model to the CMB power spectrum extracted from the latest published measurements of the Planck satellite data [11], the density of cold dark matter

$\Omega_{\mathrm{cdm}}h^2$ and of baryonic matter $\Omega_{\mathrm{b}}h^2$ were estimated to be:

$$\Omega_{\mathrm{cdm}}h^2 = 0.1188 \pm 0.0010 \tag{1.7}$$

$$\Omega_{\mathrm{b}}h^2 = (0.02227 \pm 0.00014) \tag{1.8}$$

$$\Omega_{\mathrm{m}} = (0.309 \pm 0.006) \quad \text{with } H = (67.7 \pm 0.5)\,\mathrm{km/s/Mpc} \tag{1.9}$$

where h is the dimensionless Hubble parameter such that $H = h \times 100\,\mathrm{km}/(\mathrm{s} \cdot \mathrm{Mpc})$. Thus, the contribution of cold dark matter to the total energy content of the Universe is $\Omega_{\mathrm{cdm}} \approx 27\%$.

In addition from the CMB measurement, independent measurements of the cosmological parameters can be performed with other observations.

1.1.3. Type Ia supernovae

Supernovae are the brightest astrophysical objects in the Universe and can therefore be detected from large distances and allow to probe the early Universe. They are classified according to their optical properties, namely their light curve and the absorption lines observed in their energy spectrum. Among them, one type is of interest to determine the properties of the Universe: the type Ia supernovae (SNe) have the characteristic that their luminosity is approximatively the same from one supernova to the other. Thus, they can be used as a "standard candle". The special feature of such supernova is that they are mostly produced from a binary system made of one white dwarf and a star. A white dwarf is a highly dense star remnant, whose mass is not high enough for oxygen and carbon to be fused. As there is no undergoing fusion reactions, gravitational collapse is not balanced by radiation pressure but by electron degeneracy pressure, leading to a highly dense object. Due to its high density, the white dwarf in a binary system accretes matter from its companion star. The maximum mass for which equilibrium can be ensured is the so-called *Chandrasekhar mass*, which is approximatively equal to 1.4 solar masses. Before reaching this mass, the pressure and density in the white dwarf are high enough for the carbon to fuse. As the electron degeneracy pressure restricts contraction, a significant portion of carbon fuses at once, leading to an explosion, which releases matter into the interstellar medium. Thus, because of the specific mass and composition of the white dwarf before its explosion, the optical properties of SNe are similar.

Knowing the absolute magnitude M, constraints on the cosmological parameters can be set. Indeed, supernovae are so bright that they allow to measure their distances accurately even at large redshifts. The measured distance can then be related to the expansion rate of the Universe $H \equiv \dot{a}/a$. By measuring a large set of SNe distributed in a large region of redshift z, the cosmological parameters can be measured by studying the distance-redshift relation, as shown in fig. 1.3. This so-called Hubble diagram shows the size of the variation in the apparent magnitude (smaller magnitudes represent brighter objects) for two surveys of SNe at low and high redshifts [12]. As can be seen, SNe at high redshift deviate from the expected Hubble's law: the SNe appear further away than predicted. This observation can be explained by an acceleration of the expansion of the Universe [13], [12].
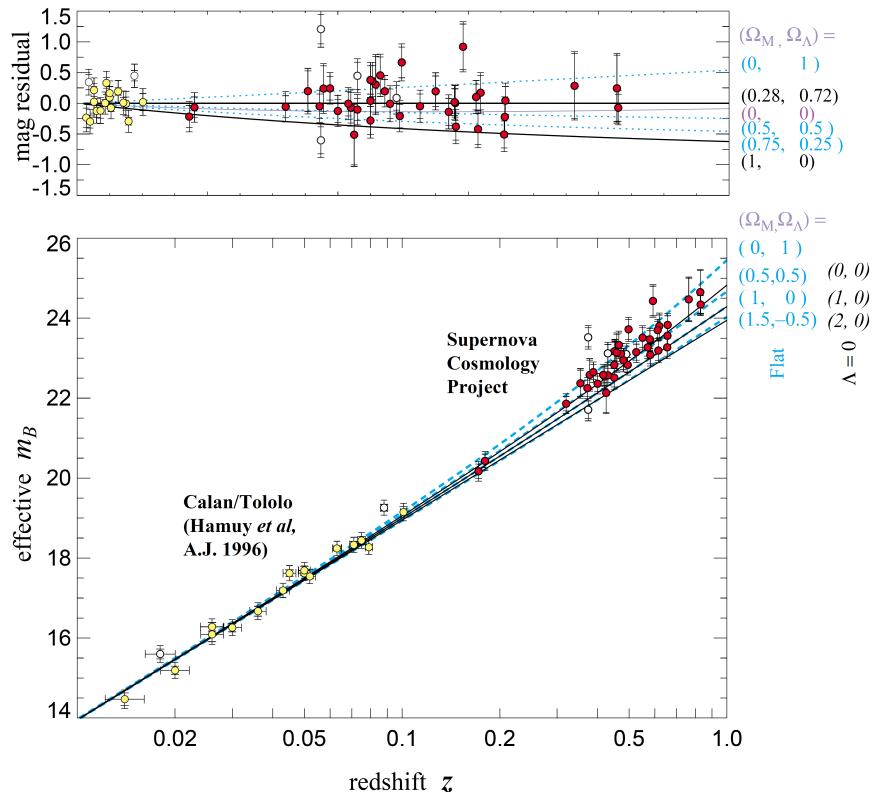
Figure 1.3. – Hubble diagram for 42 high-redshift type Ia supernovae from the Supernova Cosmology Project (red markers) and 18 low-redshift type Ia supernovae from the Calán/Tololo Supernova Survey (yellow markers). The dashed curves display the expected relation for a range of flat cosmological models. The middle solid curve shows the expected relation as given by the Hubble law. The upper panel shows the residual magnitude relative to an open universe. Extracted from [12].

1.1.4. Big-Bang nucleosynthesis

The Big-Bang nucleosynthesis (BBN) predicts the primordial abundance of light elements (D, ^{3}He, ^{4}He and ^{8}Li) in the Universe [14]. It allows to derive the density of baryonic matter Ω_b with precision. Together with the measurements of the total matter density Ω_m from other probes, it gives a proof of the existence of a non-baryonic matter of density $\Omega_{cdm} = \Omega_m - \Omega_b$. These abundances are essentially governed by the physics during the first few minutes after the Big-Bang [15]. They notably depend on the baryon density as well as on the neutron-to-proton ratio at the time when nuclear reactions took place. As the Universe expands and thus the baryon density decreases, the baryon-to-photon ratio η_B/η_γ is used.

For a temperature[1] $T \gtrsim 3\,\text{MeV}$, neutrinos interacted frequently enough so that neutrons and protons were in thermal equilibrium via the reaction:

$$p + e^- \leftrightarrow n + \nu_e \tag{1.10}$$

The neutron-to-proton ratio at equilibrium was then fixed by the temperature of the Universe $n/p = e^{-Q/T}$, with Q the mass difference between proton and neutron ($Q = 1.293\,\text{MeV}$). As the Universe expanded and cooled down, the rate of inter-conversion of protons to neutrons became smaller than the expansion rate: neutrinos decoupled from

---

1. With $1\,\text{eV}/k_B = 11605\,\text{K}$, where k_B is the Boltzmann constant

baryons and the n/p ratio was frozen to $\simeq 1/6$. Free neutrons were unstable until $\tau \simeq 15$ min and underwent β decay $n \rightarrow p + e + \bar{\nu}_e$, leading to a drop of the neutron fraction to $\sim 1/7$ at the time nuclear reactions started. A few minutes after the Big-Bang, at temperatures of $T \simeq 0.03\,\mathrm{MeV}$, the mean energy of the photons was low enough so that the deuterium formed by fusion of a proton and a neutron was not dissociated anymore. Heavier elements such as helium, tritium, lithium and beryllium were then formed until they were no more free neutrons in the plasma. As there was no stable nucleus made of 5 or 8 nucleons, the Big-Bang nucleosynthesis only produced nuclei up to beryllium because of the high Coulomb barrier that has to be overcome to fuse two heavier elements. The main reactions occurring were D(p,γ)^{3}He and ^{3}He(D,p)^{4}He, i.e. most neutrons were fused into ^{4}He. As the temperature dropped below $\sim 30\,\mathrm{keV}$, at a time of ~ 20 minutes after the Big-Bang, the nuclear reactions stopped because the Coulomb barrier was too high to overcome. The abundances of light elements froze-out at that point.

The photon density - and therefore the neutron-to-proton ratio - set the time and duration of the nucleosynthesis. For a given photon density, a higher baryon density leads to a faster rate of ^{4}He fusion and therefore less D and ^{3}He. As the photon density is determined with high precision from the CMB, the expected abundance of light elements can be calculated. The experimental determination of the light element abundances is not trivial, as there is another contribution from *stellar* nucleosynthesis. Contrary to primordial nucleosyntehsis, stellar nucleosynthesis also produces heavy elements such as carbon, nitrogen, oxygen and iron. Therefore directions in the sky where a low metal abundance is measured are used to determine the light element abundances with a minimum bias from stellar nucleosynthesis. The predictions from the BBN as well as the measured abundances are shown in fig. 1.4. The abundances are spanning over 9 orders of magnitude. An overall concordance between measurements and the model predictions is seen when taking into account the statistical and systematic uncertainties. The measured abundances of D and ^{4}He from BBN and CMB are in agreement but the measured abundance of ^{7}Li is at least a factor 2 away from the expected abundance. This disagreement might be a hint of new physics. From this measurement, limits on the baryon content were set to $0.017 \leqslant \Omega_\mathrm{b} h^2 \leqslant 0.024$ at 95% C.L.. Knowing the overall matter density of $\Omega_\mathrm{m} \approx 0.3$, this shows that the Universe is dominated by non-baryonic matter.
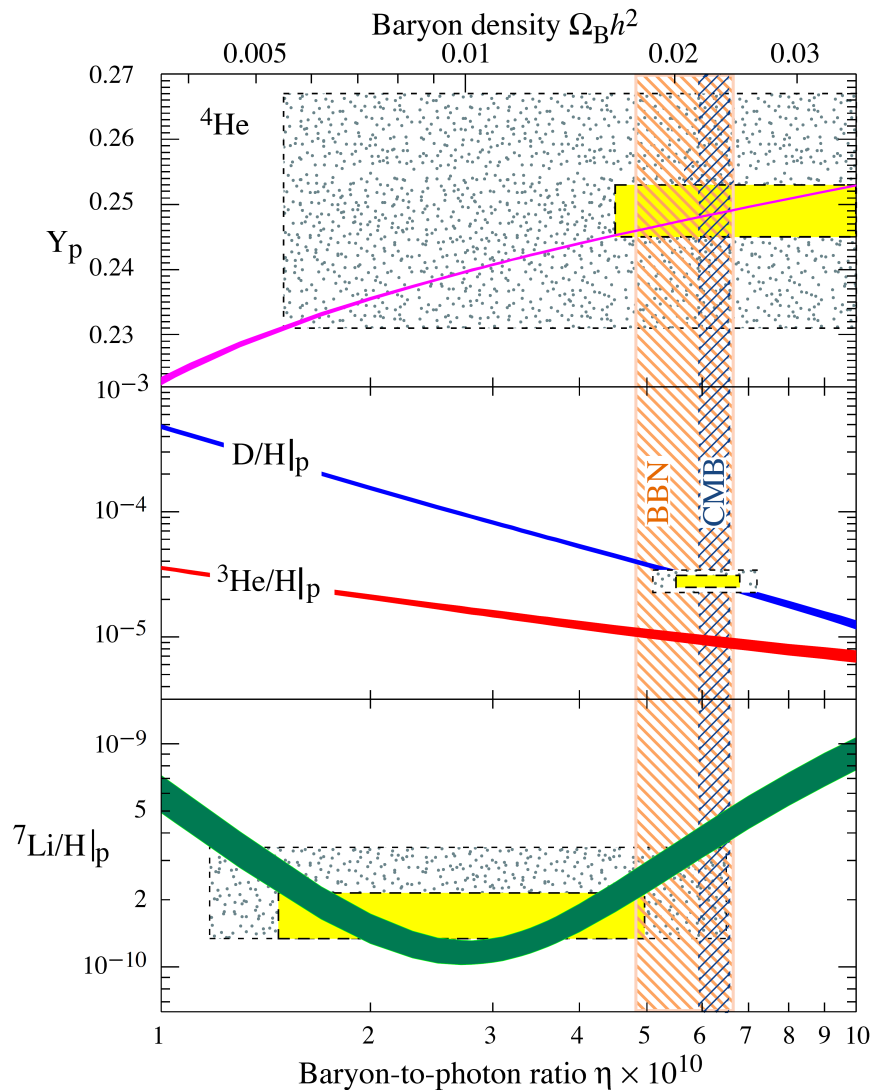
Figure 1.4. – Predicted abundances of ^{4}He, D, ^{3}He and ^{7}Li from the Big-Bang nucleosynthesis (coloured bands) at 95% C.L.. The boxes indicate the observed light element abundances, the smaller boxes showing the $\pm 2\sigma$ statistical errors and the larger boxes showing the $\pm 2\sigma$ statistical and systematic errors. The narrow vertical band indicates the CMB measurement of the cosmic baryon density $\Omega_b h^2$ and the wider band indicates the BBN concordance range for $\Omega_b h^2$ (both at 95% C.L.). Extracted from [15].

1.2. Dark matter candidates

The observational evidences for dark matter existence at various scales in the Universe lead to the following conclusions on its properties:

— it has to be electrically uncharged, i.e. neutral

— it is mostly collision-less, i.e. interacts only weakly with itself and with baryonic matter, as well as gravitationally

— it is dominantly non-baryonic

— it can be either cold or warm but not hot, i.e. it had to be non-relativistic at the time of structure formation, as required from the structure formation at large scales

— it must be stable or at least long-lived compared to the age of the Universe, as its gravitational effects are seen nowadays.

No particle of the standard model satisfies all of the above requirements, not even weakly-interacting neutrinos, as they would constitute hot dark matter which can be ruled out due to the observations regarding structure formation. Beyond the standard model, a zoo of potential candidates for dark matter exists and is depicted in fig. 1.5. Some of these particles were postulated to solve the dark matter problem itself, others emerged naturally as a by-product of theories to solve problems in particle physics such as strong CP violation. While each of them has interesting properties and would deserve a full description, the focus of this work is given on the particle candidate, for the EDELWEISS-III experiment was designed to search for.

Weakly Interacting Massive Particles (WIMPs) are a generic class of hypothetical particles and a prominent candidate for dark matter. A possible production mechanism out of a thermal equilibrium could explain both their number density, and their interaction rate with normal matter and is therefore a strong indication for their existence [17]. In this framework, WIMPs were in thermal equilibrium with the hot plasma of standard model particles in the early Universe after inflation. WIMPs were created from SM-particles and annihilated into SM-particles constantly, as long as the temperature was larger than their rest mass, i.e. $k_B T > m_{\mathrm{WIMP}} c^2$. The number density of all particles, including dark matter particles, was therefore roughly equal to the photon density. As the universe expanded and cooled, the number density of WIMPs n_{WIMP} decreased together with the photon density. As seen in section 1.1.1, the decrease of the matter number density is $\propto a^{-3}$, and consequently $\propto T^{-3}$. Therefore the notion of comoving number density $Y \equiv n_{DM}/T^3$ is commonly introduced to encounter for changes in n_{WIMP} which are not induced by a temperature change. Once the temperature of the Universe reached the mass of the WIMPs, only high energy photons on the tail of the thermal distribution would produce them. Therefore, the number density of WIMPs n_{WIMP} dropped exponentially due to the annihilation following $n_{\mathrm{WIMP}} \propto e^{-m_{\mathrm{WIMP}}/T}$. The WIMPs dropped out of thermal equilibrium once the reaction rate became smaller than the Hubble expansion rate of the Universe. After this so called *freeze-out*, the relic density is essentially constant, and can be approximated by

$$\Omega_{\mathrm{WIMP}} h^2 \simeq const \cdot \frac{T_0^3}{m_{\mathrm{planck}}^3 \cdot \langle \sigma_{\mathrm{A}} v \rangle} \simeq \frac{0.1\,\mathrm{pb} \cdot c}{\langle \sigma_{\mathrm{A}} v \rangle} \tag{1.11}$$

where T_0 is the current temperature of the CMB, m_{planck} the Planck mass and c the speed of light in vacuum. Thermal averaging is assumed for the product $\langle \sigma_{\mathrm{A}} v \rangle$ of total annihilation cross section σ_{A} for a pair of WIMPs into SM-particles and their relative velocity v to each other. Almost independently of the properties of WIMPs, this freeze-out would happen at a temperature of $T_{\mathrm{F}} \simeq m_{\mathrm{WIMP}}/20$ as shown in fig. 1.6. The resulting relic density that is produced by such a process, is in good agreement with observations
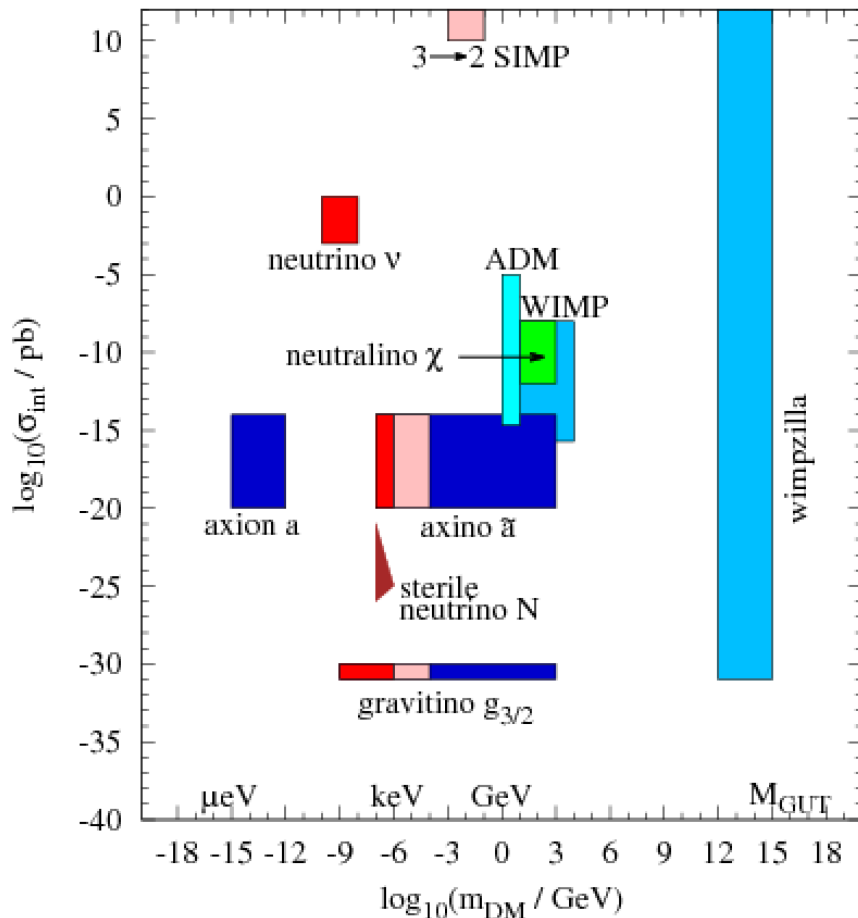
Figure 1.5. – Scattering cross-section of hypothetical dark matter particles with baryonic matter versus the mass of the particle (both in logarithmic scales) for several well-motivared candidates. The red, pink and blue colors represent hot dark matter, warm DM and cold DM, respectively. Extracted from [7]

for dark matter. The intriguing fact, that this is the case for weak scale interactions as expected for WIMPs, is referred to as the *WIMP miracle*.

A natural candidate for a WIMP would be a supersymetric (SUSY) particle. SUSY is a theoretical extension of the standard model predicting for each SM-particle a heavier SUSY superpartner with a spin differing by a half-integer. In the framework of the Minimal Supersymmetric Standard Model (MSSM), an additional symmetry, called the R-parity, is postulated such that $(-1)^R = (-1)^{3B-L+2S}$, with B the baryon number, L the lepton number and S the spin number [18]. If this symmetry is preserved, the lightest superparticle (LSP) of R-parity (-1) would be a prime candidate, as its decay into SM-particles of R-parity (+1) would be forbidden. The most promising candidate for the LSP on the other hand, is the so called *neutralino*, which would be a linear combination of the four SUSY particles bino, wino and higgsinos [4].

While the total dark matter density can be derived in the case of WIMPs with a simple thermal freeze-out process, what is interesting for dark matter search is the local density. That is the density in our solar "neighborhood" coming from the distribution of dark matter in our own galaxy. Observations of the rotation curves of stars around the galactic center suggest that dark matter is distributed in galaxies in the form of a spherical halo. This halo would be $\mathcal{O}(10)$ times more massive than the visible stars that it envelopes.
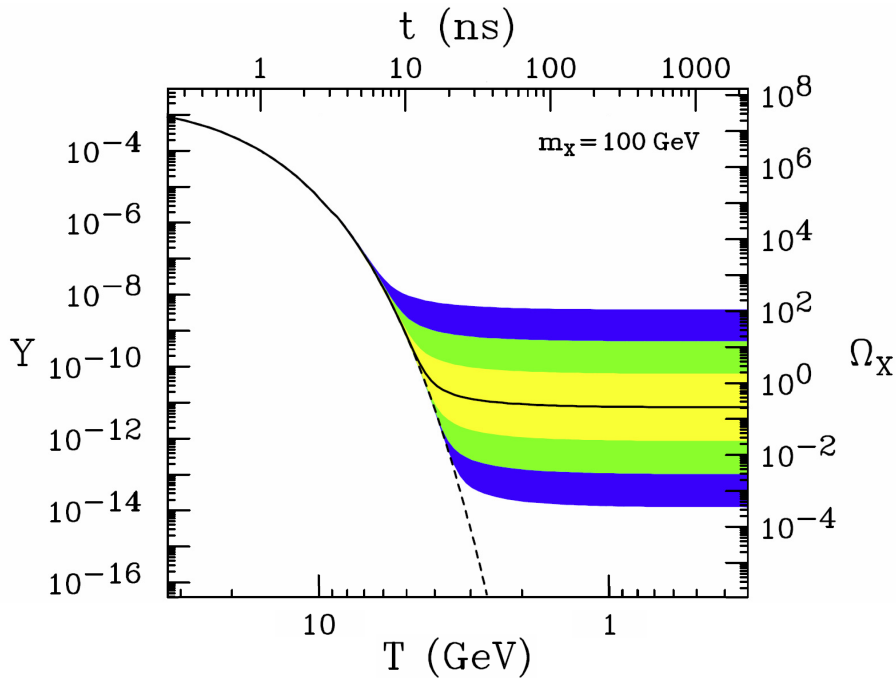
Figure 1.6. – Comoving number density Y (left) and resulting relic density (right) for a 100 GeV WIMP as a function of temperature T (bottom) and time t (top). The black line is for an annihilation cross section giving the measured relic density of dark matter, while coloured bands give the uncertainty for cross section differing by a factor of 10, 10^2 and 10^3. Extracted from [16].

The density of dark matter is expected to decrease with distance from the center. A commonly used model to describe the spacial mass distribution of dark matter halos is the Navarro-Frenk-White (NFW) profile[19], based on N-body simulations of cold dark matter particles:

$$\rho(r) = \frac{\rho_0}{\frac{r}{R_s}\left(1 + \frac{r}{R_s}\right)^2} \tag{1.12}$$

where the density ρ_0 and the scale radius R_s are parameters which vary from halo to halo. The local dark matter density at the distance of the sun to the galactic center was calculated to be

$$\rho_{\mathrm{DM}}^{\mathrm{local}} = 0.39 \pm 0.03 \, \mathrm{GeV \, cm^{-3}} \tag{1.13}$$

for two different parametrizations of the dark halo density profile[20].

1.3. Dark matter detection techniques and current status.

There are three main ways to detect dark matter, as pictured in fig. 1.7: dark matter can be produced at colliders by the collision of two standard model particles. It can be detected indirectly, by measuring the standard model particles produced in the annihilation of two dark matter particles. Lastly, it can be detected directly by measuring the recoil energy induced by a dark matter particle scattering on a detector. All three detection strategies will be reviewed briefly in the following.
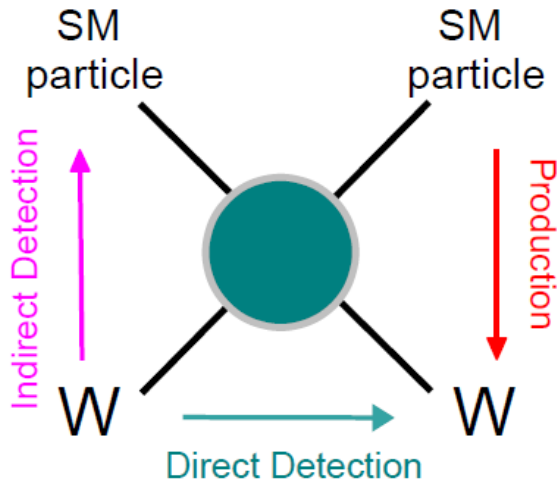
Figure 1.7. – Schematic summarizing the detection principles of dark matter. *SM parti-*
cle and *W* refers to as standard model particles and dark matter particles,
respectively.

1.3.1. Production at colliders

High energy colliders, such as the Large Hadron Collider at CERN, can produce heavier
particles beyond the standard model such as dark matter (DM) particles, and eventually
detect them. The advantage of collider experiments in comparison to other DM detection
techniques is that their sensitivity to low mass DM is not limited and the results are in-
dependent of unknown astrophysical parameters [21]. In addition, they provide a higher
sensitivity to spin-dependent interactions.

Many theoretical models developed to solve limitations of the standard model provide a
natural DM candidate which can be searched for at collider experiments. The most pop-
ular class of models is SuperSymmetry (SUSY), providing an extension of the standard
model by introducing a new symmetry between spin 1/2 fermions and integer spin bosons.
Several candidates for DM are provided by the minimal supersymmetric model (MSSSM).
The most motivated one is the lightest stable SUSY particle (LSP).

The main process generating DM is the direct production of a SUSY particle by the colli-
sion of two standard model particles, which then decays in the LSP. As DM is by definition
weakly interacting, it cannot be directly detected, in the same way as the neutrino which
thus becomes a background for DM search at colliders. The characteristic signature is
therefore missing energy. At LHC, only the missing transverse energy can be used, as the
longitudinal momentum fractions of the partons in the incoming hadrons are not known
[22]. What can be detected is radiation, e.g. a photon, a gluon or a weak gauge boson Z
and W, emitted either in the initial or in the final state, together with missing transverse
energy. Events with a single particle jet of high transverse energy and a large missing
transverse energy, referred to as *monojets*, are used to search for dark matter. DM candi-
dates such as the LSP can also be produced by the decay of heavier non-standard particles
into DM and jets.

In order to interpret the results independently from a specific model, the analysis of mono-
jets is performed in the general framework of the effective field theory. The interaction of
DM with standard model particles is then modelled with only two parameters, the mass
of the DM particle, and the so-called *suppression scale* related to the mass of the mediator
particle and therefore to the coupling between the two particles.

As of now, no excess of events has been measured in the monojet searches at LHC and
exclusion limits could be set on the coupling between DM and standard model particles.
In addition, no hints of SUSY were found at collider experiments.

1.3.2. Indirect detection

If dark matter particles are of Majorana type, i.e. their own anti-particle, they can annihilate into standard model particles. The principle of indirect DM detection is to measure the products of this self-annihilation or their interaction with matter [22, 23]. As the annihilation rate is proportional to the square of the DM density, the probability to detect the annihilation products is enhanced in region with large density. DM particles are notably trapped in high gravitational potential regions, and even slowed down in very dense objects. The potential targets range from large scale structures such as galactic haloes, substructures e.g. dwarf galaxies or massive objects such as the Sun or the Earth. Thus, indirect DM detection experiments are more sensitive to the astrophysical properties of DM such as its distribution. The limits on the DM mass and annihilation cross-section are therefore significantly depending on the considered model.

Indirect dark matter experiments are either ground-based or located in space and can be distinguished according to the type of annihilation products they can measure, i.e. neutrinos, gamma-rays, or anti-particles (positrons, anti-protons and anti-nuclei). Photons and neutrinos are particularly useful as they allow to probe over-dense regions with low luminosity and thus limit the contribution from background.

Gamma-rays are particularly adequate to probe the existence of DM as they do not loose their directionality while crossing extragalactic distances. They can be produced by secondary interactions of the annihilation products of two DM particles, which gives a continuous energy spectrum. They can also be produced directly in the annihilation, giving mono-energetic photons appearing as a clear line in the detectors, easily distinguishable from the continuum backgrounds. A limitation to the observation of such line comes from foregrounds and backgrounds which should be precisely estimated, before a potential signal can be extracted. Several times in the past, an excess of γ-rays, which could be interpreted as a signal for DM annihilation, has been measured.

As for charged particles, they are diffused in the galactic magnetic field and therefore require good modelling. Positrons annihilate with electrons of the interstellar medium, giving rise to an emission line at $511 \, \mathrm{keV}$. However, this detection channel is limited by large background due to the e^+ production by β-decay of unstable isotopes.

In the photon channel, two potential signals are often discussed. Data from the FERMI/LAT satellite shows an excess around $2 \, \mathrm{GeV}$ in a search region around the galactic center, after the contributions of all known point sources have been subtracted. This excess is compatible with various DM models and DM masses of the order of tens of GeV [24]. However, the statistical significance of this signal varies from one analysis to the other. The favoured hypothesis to explain this signal is the presence of unsolved sources at the very center of the galaxies, whose contribution is not fully subtracted.

Another excess in the photon channel was found by an independent analysis of the public FERMI data. A line from DM annihilation into 2 γ-rays was measured at $130 \, \mathrm{GeV}$. The subsequent analysis performed by the FERMI collaboration led to a statistical significance of the excess of only $1.5 \, \sigma$ [24]. In addition, the width of the line was found to be smaller than the expected resolution.

The highest statistics results in the antimatter channel have been extracted from the space experiment AMS-02 [25], which is on the international space station. It confirmed the excess in the positron-to-electron fraction $N_{e^+}/(N_{e^-} + N_{e^+})$ of cosmic rays previously reported by the PAMELA experiment [26], rising from 8 to $275 \, \mathrm{GeV}$. The origin of this excess can be constrained using the measured energy spectrum. If this excess would be induced by DM annihilation, a sharp cut-off would be expected at an energy corresponding to the mass of the DM particle. In addition, a similar rise would be seen in the anti-proton channel, which has not been measured. Therefore the dark matter hypothesis to explain this signal is unfavoured. However, a clear origin was not found yet but it could be explained by one or several local pulsars.
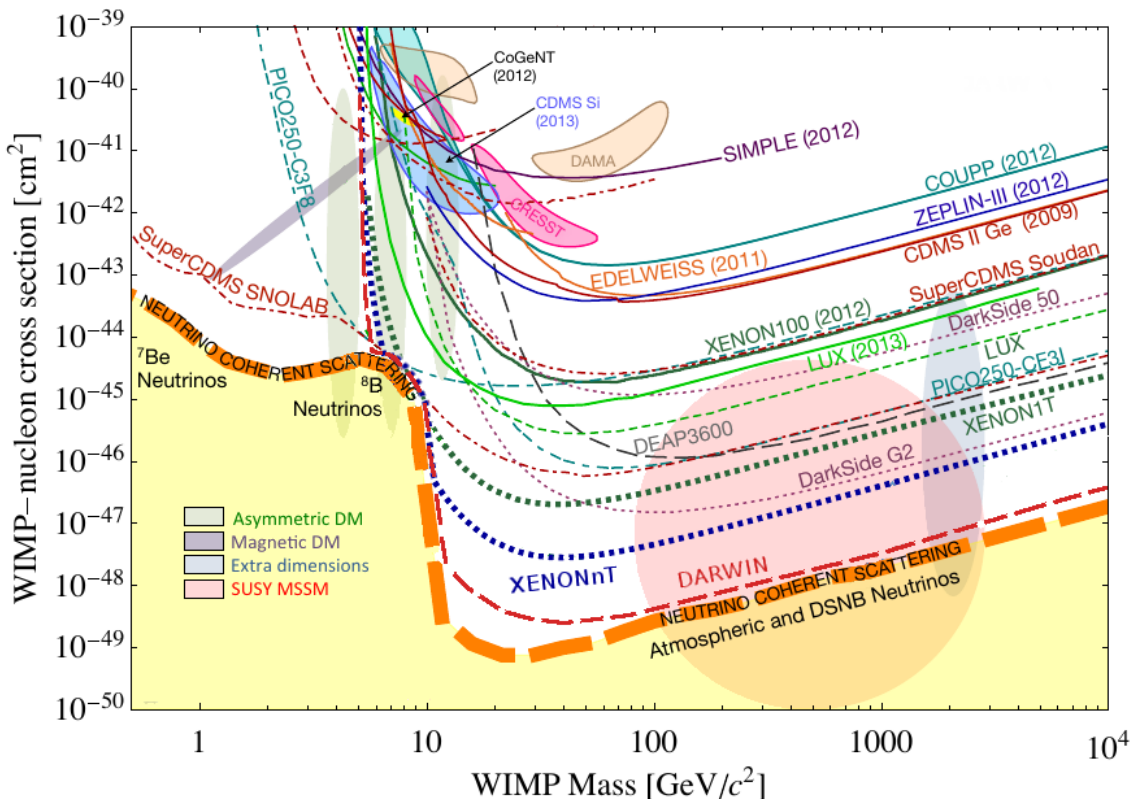
Figure 1.8. – Overview of different direct detection experiments in the parameter space of spin-independent WIMP-nucleon cross section versus WIMP mass. Solid curves give 90% C.L. exclusion limits of performed dark matter searches, while dashed lines are projections of future experiment. Signal regions of dark matter claims are in coloured contours. Delimiting the parameter space is the *neutrino-floor*, where signals from coherent scattering of solar and atmospheric neutrinos could not be distinguished from a dark matter signal without additional directional information. Possible regions predicted by theoretical models are shown as semi-transparent contours. Extracted from [22].

1.3.3. Direct detection

Direct detection of dark matter is attempted in laboratory-based experiments on Earth. The goal of such experiments is to detect the scattering of a dark matter particle in a detector. In the following, the discussion is focused on the direct detection of WIMPs.

As the solar system -and therefore the Earth- is moving through the dark matter halo in which the Milky Way is embedded, a WIMP flux is passing through every object constantly. Due to the extremely small scattering cross-section, the interaction rate is expected to be smaller than 1 event per 100 kg per year, much lower than the usual backgrounds from radioactivity. Therefore, direct dark matter detection experiments are generally located in deep underground laboratories to shield the detectors from cosmic-rays, and notably from cosmic muons. In addition, successive thick layers of shielding are used to reduce background from radioactivity originating from outside the detectors, and a careful selection of radio-pure materials making up the close vicinity of the detectors is performed. The control of the various backgrounds is the prime difficulty for direct dark matter search, as will be illustrated in the case of the EDELWEISS experiment in chapter 2.

The differential rate of nuclear recoils in a detector is proportional to the WIMP flux,

the interaction probability with a nucleus and the number of target nuclei exposed to the WIMP flux following [27]:

$$\frac{dR}{dE_{\text{rec}}} = N_T \frac{\rho_W}{m_W} \int dv f(v) \frac{d\sigma}{dE_{\text{rec}}}(v, E_{\text{rec}}) \tag{1.14}$$

with N_T the number of target nuclei per unit of mass; m_W and ρ_W the mass and mass density of the WIMP, respectively; E_{rec} the recoil energy and $f(v)$ the normalized WIMP velocity distribution. In the most simple models, the velocity distribution is described by a Maxwell-Boltzmann distribution cut off at the escape velocity for which WIMPs can leave the gravitational pull of the halo. From the unknown interaction cross section σ_0 of the WIMP, the differential scattering cross section for a dark matter particle on a nucleon of mass m_N can be calculated as follows:

$$\frac{d\sigma}{dE_{\text{rec}}} = \frac{\sigma_0}{E_{\text{rec}}^{max}} F^2(q) \tag{1.15}$$

where $F(q)$ is the nuclear form factor and q the momentum transfer $q = \sqrt{2m_N E_{\text{rec}}}$ and E_{rec}^{max} is the maximum energy transferred.

The scattering process can be of different types: elastic or inelastic, coherent or incoherent and, in the latter case, can dependent on the spin. Concerning the coherence, the contribution of each nucleon making up a target nucleus has to be considered to derive the WIMP-nucleus scattering. If the De Broglie wavelength of the WIMP is larger than the diameter of the nucleus, the amplitudes of all nucleons add up coherently. Consequently, the scattering amplitude is proportional to the number of nucleons A and the differential rate to A^2. On the contrary, if the wavelength is at the scale of the nucleus or below, wave functions interfere and partially cancel. The computations of the scattering cross section has to take into account constructive and destructive interferences from the individual WIMP-nucleon scattering amplitudes.

The elastic scattering of the dark matter particle on a nucleus leads to a recoil energy in the keV range, which can be discriminated from electronic recoils by a double measurement of the energy deposit. An inelastic scattering leads to a nuclear recoil but leaves the nucleus in an low-energy excited state and is therefore followed $\sim 1\,\text{ns}$ later by the emission of a decay photon in the range $(10 - 100)$ keV [28]. The neutron and the γ are both contributing to the total measured energy as both signatures cannot be distinguished, making the discrimination difficult or even impossible.

In addition, WIMPs can couple differently to standard matter: either via a scalar current leading to a spin-independent interaction, or via an axial-vector current leading to a spin-dependent interaction. In the latter case, the interaction cross-section results from the coupling to the total spin J of the target nucleus. As the interaction amplitudes of opposite spins interfere destructively and cancel out, only unpaired spin contribute at first order to the interaction cross section. There is no A^2 enhancement of the cross section as seen in the spin-independent case. Thus, heavy nuclei are not more suited to search for spin-dependent interacting dark matter. As neutrons and protons of the target might contribute differently to the total spin depending on the dark matter model, spin-dependent cross section are given considering only the coupling for one or the other [29]. Target nuclei with an odd number of neutrons or protons are needed in order to search for spin-dependent interactions. Light nuclei are favoured in order to maximize the nuclear spin per unit of mass, which is maximized in the case of ^{19}F and ^{7}Li.

Bolometric detectors

Bolometric detectors measure the energy deposited from a particle recoil via the rise of temperature in an absorber in the form of phonons. If kept at cryogenic conditions, the

increase of temperature is on the order of μK per keV of a particle recoil. Different technologies are used to measure this temperature increase, such as Neutron Transmutation Doped (NTD) Ge-sensors, but also Transition Edge Sensor (TES) thermometers. Experiments such as CDMS and EDELWEISS use Ge and Si-crystals as bolometers, materials which are semi-conductors. A particle recoil thus creates charge carriers as well, which are quenched depending on the recoil type and can thus be used for discrimination. The working principle of the EDELWEISS Ge-bolometers will be explained in more detail in section 2.

Crystal scintillators

Scintillation experiments, such as DAMA [30], rely on the measurement of the scintillation light produced by a recoiling WIMP in a detector, read out by a photomultiplier or, after transformation into phonons, a heat sensor (as is the case for the CRESST experiment [31]). A partial discrimination between electronic and nuclear recoils can be achieved by pulse shape analysis of the scintillation pulse. The DAMA experiment however does not use the capacity to discriminate between electron and nuclear recoils. It was thus designed to search for the expected annual modulation of the WIMP signal induced by the Earth's rotation around the Sun. Such a modulation has been observed for more than a decade and interpreted as dark matter, claiming a signal (see fig. 1.8). However, the parameter space for the possible signal(s) has been excluded for several years now by a multitude of other direct detection experiments and different theories have been brought forward to explain the modulation signal with a different origin.

Noble liquids

Detectors based on noble liquids are often designed as time projection chambers with both a liquid and a gaseous phase, allowing the discrimination between nuclear and electronic recoils. Such detectors have several advantages: first, the target material is itself a shield against external radioactivity and enables the selection of an inner volume where the contribution from external radioactivity is small or negligible. This is particularly true in the case of xenon, as its atomic number $Z = 54$ is high. In addition, noble liquids have a low intrinsic background and can be efficiently purified from radio-isotopes. In the case of xenon, its high mass number $A \sim 131$ makes it efficient to search for spin-independent scatterings, while isotopes with an unpaired nucleon allow to also search for spin-dependent scattering. The technology based on noble liquids is comparably easy to scale to larger detector mass. Experiments based on xenon are currently providing the most sensitive limit on the WIMP-nucleon cross section. Leading exclusion limits in direct dark matter detection come from the LUX experiment (see fig. 1.8). Other experiments with this technology are DarkSide (based on argon), XMASS (which uses only a single phase medium) and the XENON-1T experiment, which is currently in the final phase of construction.

The current limits of these experiments are given in fig. 1.8. Over the past years, several experiments have observed an excess of events, which could be interpreted as a signal. However, these signal claims are in strong disagreement with exclusion limits set by competing experiment or even the successor experiments themselves.
The following chapter focuses on the EDELWEISS-III experiment, and the working principle of the Ge-bolometers used to search for dark matter via heat and ionization signal measurements.

2. Dark matter detection with the EDELWEISS-III experiment

The goal of the EDELWEISS experiment is to detect the scattering of WIMPs from the galactic halo on a Germanium nucleus in the detectors. As all extremely rare event searches, the main challenge is to distinguish a potential WIMP signal from recoils induced by natural radioactivity and cosmic rays. Therefore both passive and active background rejection techniques are used and described in section 2.1. First, the background level reaching the detectors is reduced using successive layers of shielding. The remaining background interacting in the detectors can be mostly rejected by discriminating nuclear recoils from electronic recoils using a detector technology based on double measurements of the energy deposit.

In order to achieve the EDELWEISS-III original goal to probe WIMP-nucleon cross sections down to 10^{-9} pb with 12000 kg·days exposure (for which background should start to appear), many upgrades were made to reduce the backgrounds measured in the second phase of the experiment. In addition, the detector performance at low energy was improved in order to increase the sensitivity to low mass WIMPs, which are motivated by the absence of SUSY hints at LHC, cosmological observations and new theories as shown in chapter 1. These improvements and their outcome will be detailed in section 2.2.

2.1. The EDELWEISS-III experiment

2.1.1. Experimental setup

In order to reduce the cosmic muon flux reaching the experiment, EDELWEISS is operated in the Fréjus tunnel in the Alps. It is located in the deepest active underground laboratory in Europe called *Laboratoire Souterrain de Modane* (LSM). Muons are particularly dangerous for dark matter search as they induce high energy neutrons in the surrounding rock or the materials of the experiment, mostly in high density materials such as the lead shield. These neutrons can interact in the bolometers via nuclear recoils and mimic a WIMP interaction. The mean rock thickness of 1780 m (equivalent to a water overburden of 4800 m w.e.) allows to reduce the cosmic muon flux by more than a factor 10^6, down to 5 muons/m^2/day [32]. Remaining muons going through the experiment are tagged using an active muon veto system (μ-veto) surrounding the whole experimental setup (green panels in fig. 2.1, more details will be given in section 3.2.1). Muon-induced events in the
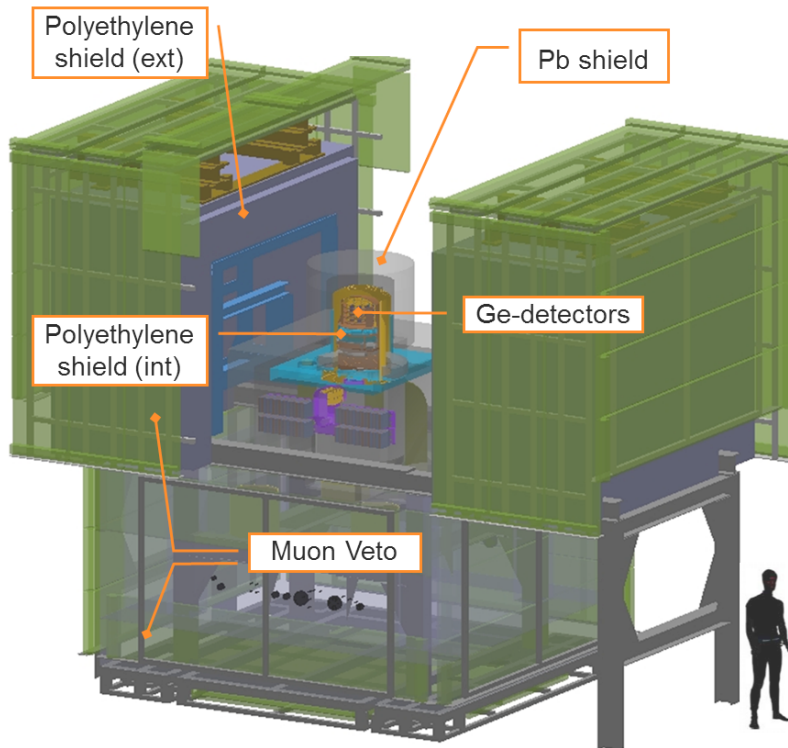
Figure 2.1. – Schematic view of the EDELWEISS-III setup showing in the center the cryostat hosting the germanium bolometers, surrounded by passive lead (Pb) and polyethylene (PE) shields and an active muon veto in order to protect the detectors from various backgrounds.

Ge detectors can therefore be rejected by a precise time analysis of coincidences with the μ-veto (see chapter 5). With the 46 modules of plastic scintillator covering a surface of 100 m^2, a geometric coverage of $\simeq 98\%$ for through-going muons is achieved [33]. The determination of the muon detection efficiency in EDELWEISS-III is a key point of this thesis and will be discussed in chapters 4 and 5.

A polyethylene (PE) shield of at least 50 cm thickness follows the μ-veto. It is used to capture or at least moderate radiogenic neutrons from natural radioactivity present in the cavern rock and materials of the experiment [34]. The neutron flux in the LSM cavern below 4 MeV is dominated by spontaneous fission and (α,n) reactions of ^{238}U, ^{232}Th and their daughters (U/Th natural decay chains can be found in appendix A) present in the rock and concrete. The activities in ^{238}U and ^{232}Th have been measured to be respectively of (1.9±0.2) ppm and (1.4±0.2) ppm in the rock and of (0.84±0.2) ppm and (2.45±0.2) ppm in the concrete [35]. However, a factor 2.3 higher concentrations are required to fit the neutron flux measurements performed in the vicinity of the EDELWEISS experiment and detailed in [35]. This could be explained by an inhomogeneous rock composition, later demonstrated in [36]. Using a proportional counter filled with ^{3}He, studies of the flux variation day by day and at various locations in the underground laboratory have been performed [36]. It has been shown that the point-to-point thermal neutron flux varies by more than a factor of two depending on the location inside the laboratory. The averaged 4π thermal neutron flux in the vicinity of the EDELWEISS experiment, outside the shields, has been measured to be $\Phi = (3.57\pm0.05\,\text{(stat)}\pm0.27\,\text{(sys)})\times10^{-6}$ neutrons/sec/cm^2. The PE castle reduces this neutron flux by 5 to 6 orders of magnitude [34]. The fast neutron flux above 1 MeV outside the shields was evaluated to be of $\Phi = (1.1 \pm 0.1\,\text{(stat)}) \times 10^{-6}$ neutrons/sec/cm^2 [37]. Only fast neutrons affect the sensitivity for dark matter search as they produce recoils of similar energy than expected from WIMPs.

Figure 2.2. – Picture of the experimental setup with on the left and right the opened external PE and Pb shields and at the center, the cryostat and the 300 K electronics (bolometer boxes).

The inner part of the shielding is a 20 cm thick lead shield of 40 tonnes used to suppress ambient γ background. Lead itself contains the long-lived radioactive isotopes ^{210}Pb, ^{238}U and ^{232}Th. Therefore the innermost 2 cm of the lead shield are made of Roman lead from a sunken galley [38]. As the half-life of ^{210}Pb is $T_{1/2} = 22.3$ years, its activity in ^{210}Pb is reduced by two order of magnitudes to less than 120 mBq/kg.

The upper part of the μ-veto as well as the PE and lead shields are located in a clean room (class 10000) to avoid contamination from dust. They are mounted on a mild steel structure with rails, which allows the opening of the shields in halves to access the cryostat (as illustrated in fig. 2.2).

Another significant source of background arises from the radon isotope ^{222}Rn. This radioactive gas with a half-life $T_{1/2} = 3.8$ days is a decay product of ^{238}U present in the rock and the contaminated materials. The radon level is controlled in the whole laboratory and in the EDELWEISS clean room. By renewing the whole air on a daily basis, the radon level is of $\sim$ 20 Bq/m^3 in the laboratory and of $\sim$ 10 Bq/m^3 in the EDELWEISS clean room. The empty space between the lead shield and the outermost thermal screen of the cryostat is flushed with radon depleted air with a residual activity less than 20 mBq/m^3. Thanks to these shields, the contribution from external background becomes negligible. Materials inside the shields have been carefully selected by systematic radiopurity measurements in order to minimize their contribution to the background.

The bolometers are installed in a home-designed reversed dilution cryostat with an effective volume of $\sim$ 50 l built with selected low-radioactivity materials. Its inverted geometry makes the access to the detectors easier and decouples them from mechanical vibrations induced by the cryogenic pumps (see fig. 2.2). This cryostat can be operated down to 10 mK with temperature fluctuations of $\pm$10 μK. It is enclosed by 5 consecutive thermal screens at 10 mK, 1 K, 4 K, 40 K and 300 K. The experimental volume on top of the cryostat is made of 4 copper plates to hold the bolometers, which are arranged in towers. Each bolometer is fully surrounded by a copper casing to protect it from infrared radiation and is held by Teflon clamps. Connection to the cold electronics at the bottom of the cryostat (100 K stage) is made with in-house developed Kapton cables [39]. The cold

electronics consists of Field Effect Transistors (FET) to pre-amplify the signals. The proximity of these highly contaminated materials with the bolometers is needed to minimize the electromagnetic noise. In addition, the cable length between the bolometers and the amplification is shorter, which minimizes the signal loss due to parasitic capacitance.

The signal post-amplification and digitization as well as the control of the cold electronics is done at room temperature by multi-channel electronics called *bolometer boxes* (see fig. 2.2). The digitized data stream is then sent to the network via optical fibres to the acquisition computers. A dedicated acquisition software controls the acquisition and incorporates the filtering and triggering algorithms to detect and store events.

2.1.2. Working principle of the Ge bolometers

The EDELWEISS detectors are bolometers made of high-purity germanium mono-crystals. They are covered by concentric aluminium ring electrodes and equipped with two Neutron Transmutation Doped (NTD) Ge sensors used as thermistors. First, it will be shown how the simultaneous measurement of heat and ionization signals makes it possible to distinguish on an event-by-event basis electronic recoils (induced by γ's or β's) from nuclear recoils (induced by WIMPs or neutrons). Afterwards follows a discussion on the electrode configuration. It allows to reject surface events which, due to incomplete charge collection, can be mistaken for nuclear recoils.

2.1.2.1. Discrimination of the recoil type

Ionization measurement

Germanium is a semi-conductor which exhibits one of the lowest band gap energy of 0.67 eV at 300 K. Only 2.96 eV are needed in average to create a pair of charge carriers [40], making the conversion of an energy deposit highly efficient. By applying a bias voltage to the surface electrodes, the created electron/hole pairs are drifted across the bolometer and collected. The density of charged impurities in the crystal is therefore kept to less than 10^{10} per cm^3 to minimize charge trapping, which is a leading factor for the worsening of the energy resolution and detector threshold.

The measured ionization signal following an energy deposit by a particle p is proportional to the number of charge carriers N_p induced by the particle:

$$E_{\text{ion}}^p = \varepsilon_c N_p \tag{2.1}$$

with ε_c being the calibration coefficient. The advantage of the ionization measurement is that the number of charge carriers induced by a recoil energy E_{rec} depends on the recoil type:

$$N_p = \frac{E_{\text{rec}}}{\varepsilon_p} \tag{2.2}$$

with ε_p the energy deposit required from a particle p to create an electron/hole pair [41]. While γ's and β's scatter off electrons, WIMPs and neutrons scatter off nuclei. Therefore an average energy of $\varepsilon_\gamma = 3$ eV is needed for an electronic recoil to produce a pair of charge carrier whereas an average of $\varepsilon_n = 9$ eV is required for a nuclear recoil. More generally, this ionization quenching Q depends on the contribution from the electronic and nuclear stopping powers with the energy. A semi-empirical parametrization of $Q(E_{\text{rec}})$ was deduced by Lindhard from the study of energy losses of low energy ionizing particles in matter, including screening effects from electrons [42, 43].

The ionization energy measured for an electron recoil (E_{ion}^γ) and a nuclear recoil (E_{ion}^n)

can then be written as:

$$E_{\text{ion}}^{\gamma} = \varepsilon_c N_{\gamma} = \varepsilon_c \frac{E_{\text{rec}}}{\varepsilon_{\gamma}} = Q^{\gamma} E_{\text{rec}} \tag{2.3}$$

$$E_{\text{ion}}^{n} = \varepsilon_c N_n = \varepsilon_c \frac{E_{\text{rec}}}{\varepsilon_n} = Q^{n} E_{\text{rec}} \tag{2.4}$$

The calibration coefficient ε_c is determined from γ calibration data obtained with a radioactive ^{133}Ba source. It produces γ's from $53\,\text{keV}$ up to $384\,\text{keV}$ energy, with a main contribution at $356\,\text{keV}$ (62%). At these energies, γ's mostly deposit energy via photoelectric effect, leading to recognizable photopeaks in the energy spectrum, which are used for the energy calibration. A usual practice is to rescale the calibration coefficient so that $\langle Q^{\gamma} \rangle = 1$. Consequently, the average ionization quenching of a nuclear recoil Q^n for E_{rec} in keV can be written:

$$\langle Q^n \rangle = \frac{\varepsilon_{\gamma}}{\varepsilon_n} \sim 0.3 \tag{2.5}$$

In EDELWEISS, the energy dependence of the neutron quenching factor was determined by a fit to the neutron calibration data [44] and gives good agreement with the Lindhard theory:

$$\langle Q^n \rangle = 0.16 \cdot E_{\text{rec}}{}^{0.18} \tag{2.6}$$

Heat measurement

The measurement of the energy deposit using the temperature rise allows to probe the full energy of an interaction regardless of the recoil type. The principle of the bolometer is used to measure heat: the Ge crystal is the absorbing element coupled with a resistive sensor and connected by a thermal link (gold wires between the detector and the casing) to a thermal reservoir (the cryostat). A particle interaction within the crystal induces vibrations of the lattice, described in quantum mechanics as quasiparticles called phonons. The phonon signal corresponding to the temperature rise is measured via the change of resistance in two NTD Ge sensors glued on the top and bottom surfaces of the crystal. The fastest thermal sensors, based on Transition Edge Sensors (TES) technology, are able to measure non-equilibrium phonons and therefore allow eventually to reconstruct the position of the energy deposits. This technology is notably used in the CDMS collaboration to reject surface events suffering from incomplete charge collection [45]. As for the EDELWEISS thermal sensors, they are made to measure thermalized phonons, for which the signal amplitude is proportional to the heat increase. The small temperature rise ΔT following an energy deposit E_{rec} can be written as [46]:

$$\Delta T = \frac{E_{\text{rec}}}{C(T)} \tag{2.7}$$

with $C(T)$ being the combined heat capacity of the germanium crystal and the NTD sensors. To optimize the detection efficiency of low energy deposits, the combined heat capacity of the Ge bolometer and thermometers should be as low as possible. At low temperatures, the heat capacity of the germanium crystal follows the Debye law i.e. $C(T) \propto (\frac{T}{T_D})^3$ with T_D being the Debye temperature ($T_D \sim 360\,\text{K}$ for germanium). As for the NTD sensors and the glue, they have an equivalent contribution to the heat capacity despite their small contribution to the total mass.
NTD sensors are produced by irradiation of a Ge wafer with a high neutron flux from a nuclear reactor in order to dope it p-type. This is done via capture of thermal neutrons by ^{70}Ge, ^{74}Ge and ^{76}Ge isotopes which decay with short life-times to both donors and acceptors (Ga, As and Se) [47]. Therefore the exposition to the neutron flux should be carefully controlled depending on the isotopic composition of the Ge wafer in order to obtain a thermal sensor with good conducting performance. Moreover, high energy neutrons

from the reactor can damage the lattice structure of the crystal, leading to a loss of the number of charge carriers available [48]. However, this method has the advantage of giving a uniform doping for large pieces as the neutron mean free path in Ge is $\mathcal{O}(\text{cm})$.

In EDELWEISS, the Ge wafer is then cut in rectangular pieces of $\sim 7\,\text{mm}^3$ which are glued on the crystal. They are designed to have a similar heat capacity as the detector. The electrons are able to hop between the valence and the conduction bands via intermediate energy levels due to impurities, allowing the conduction. However the conduction is highly dependent on the electron temperature: the NTDs are operated in the resistive transition where the dependence of the resistance R with temperature T is given by [46]:

$$R = R_0 \exp \sqrt{\frac{T_0}{T}} \tag{2.8}$$

with R_0 (few Ω) and T_0 (few Kelvins) being characteristic for the NTD type and production process. At an operating temperature of $20\,\text{mK}$, the resistance is a few MΩ. The NTDs are biased with a constant current and the change of resistance is obtained by measuring the change of voltage of $\sim 50\,\text{nV}$. The bolometer then slowly returns to its equilibrium state with a time constant of $(100\text{-}500)\,\text{ms}$ as it is weakly coupled to the cryostat thermal bath via thin gold wires.

It should be noted that the measured heat energy does not give directly access to the recoil energy. There is an additional contribution to the measured heat from scattering of the drifted charge carriers on the crystal electrons. This phenomenon is known as the Luke-Neganov signal amplification [49, 50]. Thus, the total heat energy E_{tot} measured by the NTD sensors is equal to:

$$E_{\text{tot}} = E_{\text{rec}} + E_{\text{Luke}} \quad \text{where} \quad E_{\text{Luke}} = N \cdot e \cdot V \tag{2.9}$$

with N the number of charge carriers, e the fundamental charge and V the voltage applied between the upper and lower collecting electrodes evaporated on the detector. It was shown (eq. 2.2) that N can be expressed as a function of the recoil energy and the average energy to create an electron/hole pair. Re-normalizing ε_p to contain the elementary charge e, the Luke-Neganov energy can be written as:

$$E_{\text{Luke}} = \frac{E_{\text{rec}} V}{\varepsilon_p} \tag{2.10}$$

Using the ionization quenching Q introduced in eq. 2.5, the energies measured via the heat channel for an electron recoil (E_{tot}^{γ}) and for a nuclear recoil (E_{tot}^{n}) are respectively:

$$E_{tot}^{\gamma} = E_{\text{rec}} \left(1 + \frac{V}{\epsilon_\gamma}\right) \tag{2.11}$$

$$E_{tot}^{n} = E_{\text{rec}} \left(1 + \frac{Q \times V}{\epsilon_\gamma}\right) \tag{2.12}$$

In practice, the total energy measured in heat is re-scaled by calibration so that, for a γ, the measured heat energy is equal to the recoil energy, leading to:

$$E_{\text{heat}}^{\gamma} = E_{\text{rec}} \tag{2.13}$$

$$E_{\text{heat}}^{n} = E_{\text{rec}} \left(\frac{1 + Q\frac{V}{\epsilon_\gamma}}{1 + \frac{V}{\epsilon_\gamma}}\right) \tag{2.14}$$

Conclusion on the double measurement

To summarize, by combining eq. 2.4 and eq. 2.14, the double measurement of the energy deposit via heat and ionization provides the recoil energy and the recoil type via the

estimation of the ionization yield Q:

$$E_{\text{rec}} = E_{\text{heat}} \left(1 + \frac{V}{\varepsilon_\gamma}\right) - E_{\text{ion}} \frac{V}{\varepsilon_\gamma} \qquad (2.15)$$

$$Q = \frac{E_{\text{ion}}}{E_{\text{rec}}} \qquad (2.16)$$

The electronic recoil discrimination power of the detectors is illustrated in fig. 2.3. It shows the ionization yield Q versus the recoil energy E_{rec} for neutron calibration data, obtained using an AmBe source. This source emits neutrons up to $11\,\text{MeV}$, inducing nuclear recoils which appear gaussian distributed around $\langle Q \rangle \sim 0.3$. It emits also high-energy γ's at $4.4\,\text{MeV}$ which loose energy via Compton scattering on the electrons, leading to the population of events gaussian distributed around $\langle Q \rangle = 1$. Events between the electronic and nuclear recoil bands arise from the inelastic scattering of a neutron on a ^{73}Ge isotope, which is brought in its first ($13.3\,\text{keV}$) or second ($66.8\,\text{keV}$) excited state. Both states are short-lived ($T_{1/2} = 2.95\,\mu\text{s}$ and $T_{1/2} = 0.49\,\text{s}$ respectively) and decay by emitting a γ, which can be measured in coincidence with a neutron from the AmBe source. The resulting measured quenching is the weighting of the neutron and γ contribution to the total energy deposit.
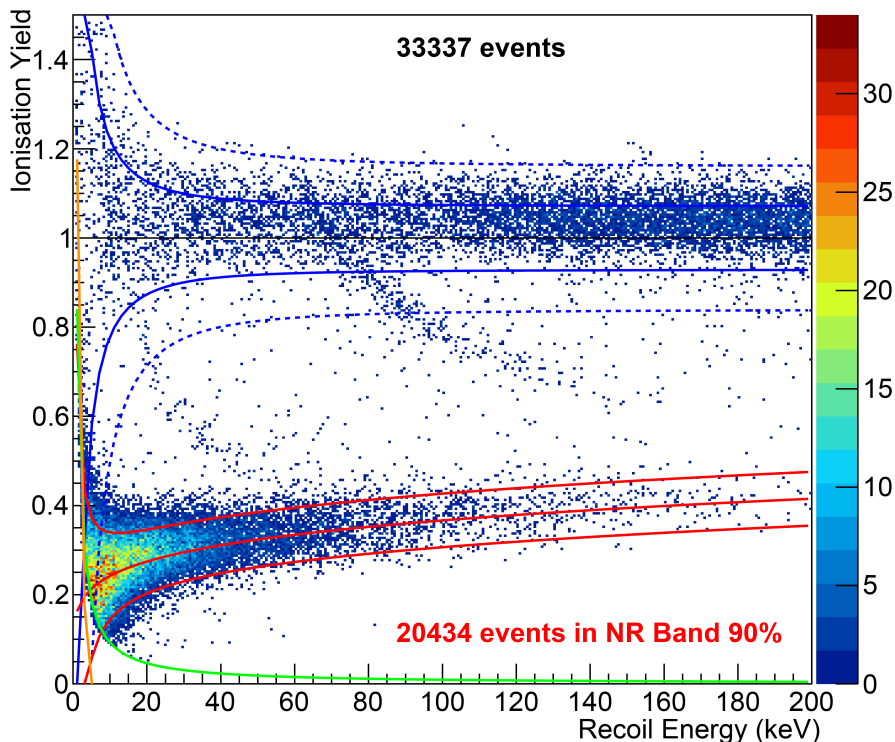
Figure 2.3. – Ionization yield versus recoil energy for a large statistics of events of a neutron calibration using an AmBe source. The red band represents the 90% C.L. nuclear recoil band. The solid and dashed blue lines delimit respectively the 90% and 99% electronic recoil bands. See text for more details.

2.1.2.2. Discrimination of surface events

Events occurring in the first 20-100 μm underneath the electrodes (mostly from β's or X-rays) suffer from a deficit in charge collection which degrades the discrimination efficiency [51]. Indeed, charges are trapped and recombined in the electrodes because of the electric field screening induced by mobile charge carriers. In conventional detectors, the surface is

passivated using a slightly doped amorphous layer of Ge or Si. In cryogenic detectors, the addition of a passive layer over a thickness of several hundreds of μm is not acceptable as it induces a large additional heat capacity [52]. Nevertheless, deposition of a thin layer of the order of $10\,\mu$m [53] just underneath the aluminium electrodes still leads to a strong passive rejection, even if surface events are not completely suppressed. The physics behind these structures is not yet known with certainty but one of the common hypotheses is that the amorphous layer of Ge/Si introduces a potential barrier as its effective band gap is nearly twice as large as the band gap of the Ge from the bulk [54]. Thus, the free charge carriers are not lost by diffusion to the electrodes, but are reflected by this blocking layer and driven across the detector by the electric field.

Different strategies have been developed to discriminate the remaining surface events. The CDMS collaboration is using non-equilibrium phonons to reconstruct the position of the interaction [45]. An alternative solution has been chosen within the EDELWEISS collaboration [55] based on the co-planar grid technique for event localization [56],[57]. The concentric electrodes, which can be seen in fig. 2.4 left, are alternatively biased and connected by ultra-sonic bonding. Electrodes A and B on the upper part of the detector (fig. 2.4, right) are biased with $-1.5\,$V and $+4\,$V respectively, whereas the electrodes C and D from the bottom part are biased with $+1.5\,$V and $-4\,$V. The calculation of field lines shows different volumes of the detector where the charge collection differs (fig. 2.4, right): a fiducial volume for which the charge collection is complete and a surface volume for which it may not. The electric field lines in the bulk are perpendicular to the detector surface and charges are drifted to the electrodes with the highest bias, namely B and D, at the top and bottom of the detector. These electrodes are therefore called *fiducial* or *collecting* electrodes. At the surface, the field lines are parallel to the detector surface and charges are drifted to both electrodes on one side, namely (A and B) or (C and D). As a surface event can suffer from incomplete charge collection, events with a signal on the veto electrodes (A and C) are rejected.
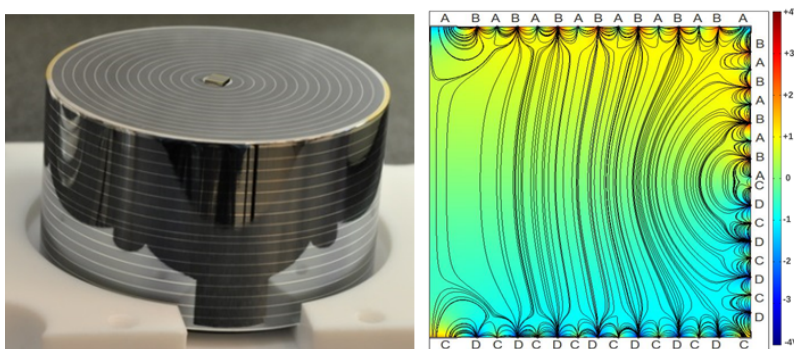
Figure 2.4. – **Left:** Photo of a FID800 detector with concentric ring electrodes and one of the two NTD sensors glued on the top surface. **Right:** Simulation of the electric field lines for a cross section of a FID800 detector from $r = 0$ to $r = r_{max}$. The color code indicates the electric potential, the electric field lines being drawn in black. Charges induced by fiducial events are collected by the B and D electrodes only, whereas charges induced by surface events are partly collected by at least one of the veto electrodes A and C.

2.1.3. Acquisition of WIMP search data with EDELWEISS-III

In the framework of this thesis, the WIMP search data taken during the cryogenic cooldown labelled Run308 is studied. The configuration of this run as well as the data processing will be introduced in the following.

2.1.3.1. Configuration of Run308

During the Run308, 36 FID detectors as well as 3 ZnMoO detectors from the LUMINEU collaboration [58] were installed in the EDELWEISS cryostat. Due to a technical defect of part of the cabling, 24 FIDs were actually cabled and readout. The arrangement of these 24 bolometers in the cryostat towers is shown in fig. 2.5. The detectors with read-out are installed in 6 towers, containing 4 bolometers each. Note that the number of bolometers as well as the geometry and the compactness of the array significantly influence the multiplicity of μ-induced events and thus the μ-induced background for dark matter search. Some detectors could not be used for dark matter search due to specific problems (see chapter 6) but all could be used to determine the multiplicity of an event and thus reject single events more efficiently. Three independent Mac computers of the DAQ system labelled *S1*, *S2* and *S3* are used to control and store the data of 8, 4 and 12 bolometers respectively (see color code in fig. 2.5).

The Run308 started the 22nd of July 2014 and ended the 3rd of April 2015. During that time, data taking was focused on WIMP search, with frequent calibrations and several tests in between as shown in fig. 2.6. Gamma calibration were regularly performed with a ^{133}Ba source to monitor the energy calibration and the γ rejection performance over time. One neutron calibration of 3.2 days was performed to cross-check the empirical parametrization of the nuclear recoil band (see eq. 2.6). In addition, some tests were performed to improve the bolometer performance or for R&D purposes. The WIMP search data was used to search for both standard mass and low mass WIMPs. The results of these analyses are summarized in chapter 6, when the expected μ-induced background is discussed. From the 5th of January 2015, once the performance of the detectors and the background level had been checked, the data was blinded for the standard WIMP analysis: single nuclear recoils in the region of interest (ROI), which could be induced by WIMPs, were excluded from the data set. The low mass analysis is a fully-blind analysis as side bands were used to estimate the background.

Figure 2.5. − Configuration of the 24 readout EDELWEISS FIDs and the 3 LUMINEU Zn-MoO detectors (orange) during the Run308. The color code indicates by which acquisition Mac each bolometer is readout.

Figure 2.6. – Accumulated live-time versus the number of days accumulated since the 22nd of July 2014.

2.1.3.2. Triggering and data processing

Both triggering and processing of the bolometer data are optimized for low energy nuclear recoils expected from WIMPs. The DAQ system is therefore not adapted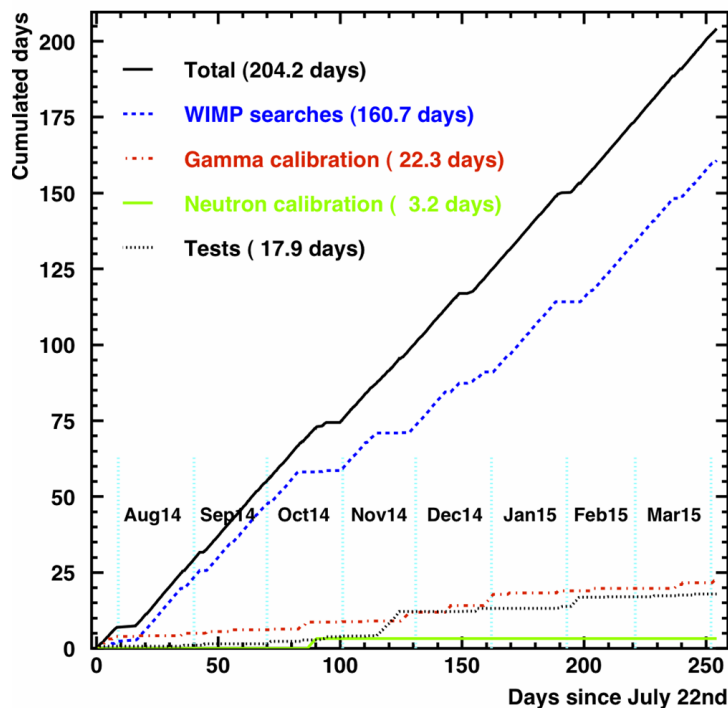 to high energy deposits as typically induced by muons, which can saturate the ADCs. To understand the associated limitations for the coincidence analysis between the μ-veto and the bolometers, the triggering procedure and the trigger time determination are described below.

Each detector is equipped with 4 ionization channels (2 veto and 2 collecting) and 2 heat channels, all sampled at a frequency of 100 kHz. The triggering is done simultaneously on all 48 heat channels (24 detectors). The choice of triggering on heat instead of ionization is mostly motivated by the ionization quenching, i.e. the fact that a larger heat signal than ionization is expected for nuclear recoils from WIMPs. This trigger is performed after a demodulation procedure to eliminate the square wave excitation due to the alternative polarisation of the NTDs. Consequently, the sampling frequency is reduced down to 500 Hz. A high-pass Butterworth filter is then continuously applied on the data to remove low frequency noise. High frequency noise is eliminated when the signal is convoluted with a template on which the same filter was previously applied. This template is constructed by selecting clear 356 keV events from ^{133}Ba calibration and fitting the heat pulse shape by a rise and two exponential decays. The pulse shape of the heat signal varies with the operation temperature of the NTDs. The template is therefore redone whenever the temperature of the bolometers changes. From the fit of the heat pulse, a first estimation of the timing t_{online} and of the energy deposit is done. The trigger decision is taken whenever the output of the cross-correlation is above a fixed threshold. The threshold value is adjusted depending on the noise level to keep a constant rate (adaptive trigger).

Once a bolometer has triggered, the signal traces for all its 6 channels (4 ionizations, 2 heats) as well as the ones from its two nearest neighbours are stored to disk. Among the
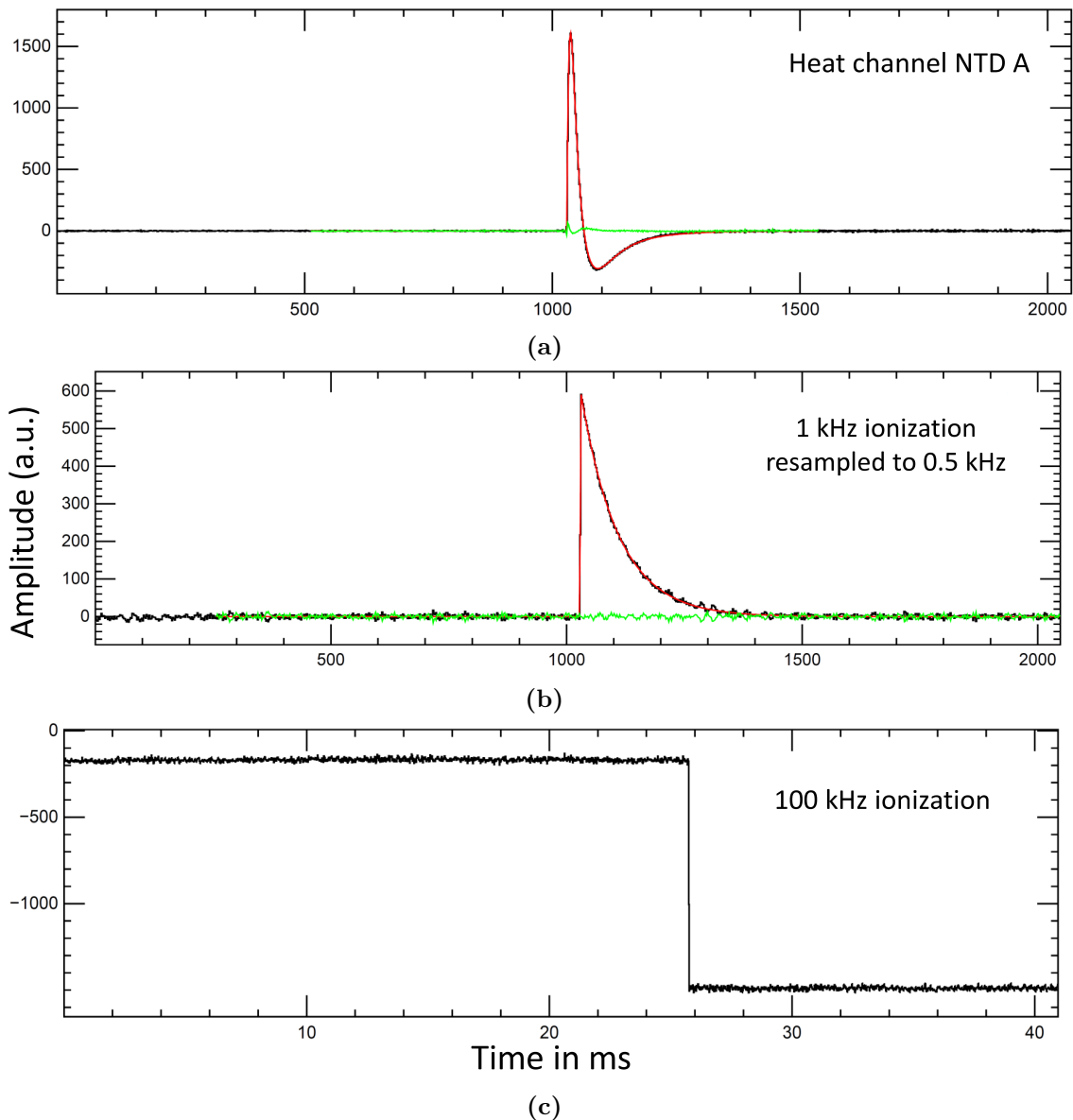
Figure 2.7. – Example of pulse traces recorded for a random high energy fiducial event (black traces). The green curves show the fit applied to determine the heat and ionization baseline resolutions, whereas the red curves show the fit applied to derive the pulse amplitude and timing (a) heat trace after filtering, fitted by the heat pulse template determine from ^{133}Ba calibration (red curve). (b) 1 kHz ionization trace of the veto channel C after filtering, fitted with a Heaviside function on which the same filter was applied (red curve). (c) 100 kHz ionization trace of the channel combination C-D (used to minimize the combined noise for a more precise determination of the hit timing) without filtering, which can be described as a Heaviside function.

6 heat channels fitted, the heat pulse with the highest amplitude is used to perform the first estimate of the trigger time t_{online}, which is then used as the center of the recorded traces. A trace of 1024 sample points of the demodulated heat signal (500 Hz) is recorded around t_{online}, corresponding to a width of 1.024 sec. An example of a heat trace is given in fig. 2.7a. Each ionization trace is recorded twice. One is registered with a sampling frequency of 100 kHz for a precise determination of the bolometer trigger time. This is needed to reconstruct the coincidences between the μ-veto and the bolometers or between the bolometers themselves. Due to the limited storage space available, only a small fraction

of the 100 kHz ionization traces is registered. Before the 4$^{\text{th}}$ of October 2014, the width of the recorded trace was of 20.48 ms but was increased afterwards to 40.96 ms (see fig. 2.7c for an example of unfiltered 100 kHz pulse). The same ionization trace is recorded a second time but down-sampled to 1 kHz over a larger window width of 1.024 sec (fig. 2.7b for an example of filtered 1 kHz pulse). This second trace is necessary in case the pulse is not included in the 100 kHz window. That happens when the estimation of the trigger time from the heat pulse fit is off tens of milliseconds because the pulse shape cannot be described by the template, e.g. in case of large energy deposit saturating the ADC or of pile-up. Finally, 2 heat and 8 ionization traces are recorded per bolometer in case of trigger, for 3 neighbouring bolometers. The raw traces are re-processed offline in order to derive a better estimation of the energy deposit and trigger time.

An accurate determination of the trigger time is crucial for the offline reconstruction of the coincidences between the μ-veto and the bolometers. If the bolometer time resolution is large, the time window used to veto bolometer events needs to be large. Consequently, the probability to reject a bolometer event only because of background in the μ-veto becomes higher. The first estimate of the trigger time is done online by the fit of the heat pulse. A more precise estimation is done in the offline analysis, after all traces have been pre-processed (the baseline is subtracted and the residual slope is corrected), filtered and fitted with the heat and ionization pulse templates. The final trigger timing t_{final} is then determined according to these following steps: first, the two heat pulses are searched ± 6 ms around the window center and fitted with the heat pulse template, giving an estimate of the energy E_{heat} and trigger time t_{heat}. If E_{heat} is inferior to 5 times the heat baseline, the final trigger time is fixed at $t_{\text{final}} = t_{\text{heat}}$, with a precision on the time of $\mathcal{O}(\text{ms})$. In the opposite case, t_{heat} is used to search for the pulse in the 1 kHz ionization traces. The traces were previously down-sampled to 0.5 kHz to improve the search speed and avoid pattern removal. The precision on the time estimate $t_{1\,\text{kHz}}$ is inversely proportional to the energy deposit. From $t_{1\,\text{kHz}}$, it is deduced whether or not there is a pulse in the 100 kHz ionization window. If not, the final trigger time is fixed to $t_{\text{final}} = t_{1\,\text{kHz}}$. In the opposite case, the fast ionization is used to determine the final timing of the hit $t_{\text{final}} = t_{100\,\text{kHz}}$. Despite a sampling point of 10 μs, a μs precision on the time determination can be achieved by fitting the filtered 100 kHz pulse. As the ionization rise time is short (a few μs) before the sampling time, the shape of ionization pulse before filtering is known and described by a Heaviside function, as shown in fig. 2.7c. By applying the same filter on the pulse template as on the data, the pulse rise of the filtered 100 kHz pulse can be fitted and the trigger time is extracted with a μs precision.

To conclude, the resolution on the trigger time depends on the energy deposit: it is of the order of 1 ms for low energy deposits below few keV, between the ms and the μs depending on the pulse amplitude for high energy deposits saturating the electronics (which happens around few MeV), and of 1 μs for energy deposits in between. The proportion of events with a μs precision is bolometer dependent, since some bolometers saturate more easily than others. For the most saturating detector, 99% of the hits have a timing determined from the 100 kHz window. Thus, this issue of energy-dependent time resolution concerns a negligible number of events. The question arising is how many of these events are μ-induced events. This smearing in time should be studied during the determination of the time window used to veto bolometer events in coincidence with the μ-veto, as discussed in chapter 5.

2.1.4. Updates of the electronics and cryogenics systems

With the goal of improving the detection efficiency for low mass WIMPs, the electronics and cryogenics systems have been upgraded to improve the energy resolutions and subsequently decrease the energy threshold.

In EDELWEISS-II, the energy threshold was limited by the ionization channel read-out
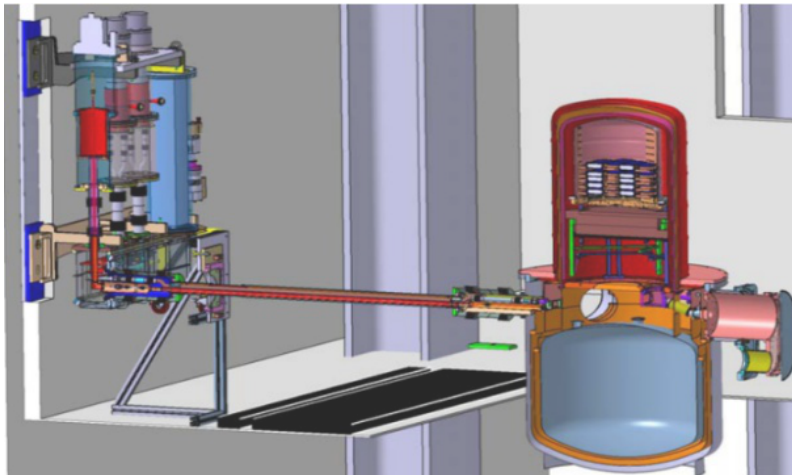
Figure 2.8. – Mechanical drawing of the cryogenic system designed for EDELWEISS-III with, on the left, the thermal machines connected to the cryostat via a cryoline.

scheme [59]. The active feedback system needed to reset the bolometers' ADC was therefore replaced by a DAC-controlled relay system. Resistors not needed any more were removed to avoid Johnson noise and thus improve the noise level at low energies. This new design enables long decay time constants for pulses and therefore improves the signal to noise ratio as most of the signal lies in the low frequency part of the power spectrum. It is also compatible with a full 100 K setup on the contrary to the EDELWEISS-II read-out scheme, where the passive RC components were placed at the 1 K stage. This has two advantages. Firstly, it prevents the numerous cables going up to the 1 K stage where the available space is limited. Secondly, it allows to further take away the cold electronics from the bolometers. Indeed, the printed circuit boards (PCBs) are particularly dangerous for rare event search. They are contaminated with radioactive isotopes and contain components with high (α,n) cross-sections. Another upgrade is the installation of an integrated DAQ system developed at the Institute of Data Processing and Electronics (IPE) of Karlsruhe [60] improving the reliability of the data taking and the event building: all the individual bolometer data are processed through a single crate which provides a common clock for the bolometer data acquisition and the muon veto. This DAQ system is also able to do a real time processing of the data stream (e.g. take a trigger decision) in parallel for all channels. Based on this fast trigger decision, it allows to extend the ionization read-out bandwidth to several MHz needed to develop a time-resolved acquisition of the ionization signal. The rising edge of the ionization signal contains information about the localization of the energy deposit inside the crystal and the charge transport [51, 55]. Data with MHz sampling is available in EDELWEISS-III for a test bolometer and is under analysis.

In addition, a new cryogenic system was set up to reduce microphonic noise and mechanical vibrations. They can couple to the read-out cables, which decrease the heat and ionization resolutions. Notably, the pulse tubes below the cryostat used to cool down the 40 K and 100 K thermal screens were replaced by Gifford-McMahon thermal machines outside the shields, connected to the cryostat using a $\sim$2 m long cryoline (see fig. 2.8).

Upgrades on both the electronic and cryogenic systems led to the improvement of the average FWHM of the heat baselines from 1.2 keV to 1.0 keV and of the ionization baselines from 900 eV to 600 eV. Thanks to these improvements, a lower analysis threshold can be achieved as well as a sensitivity down to 1 keV necessary for the detection of low mass WIMPs.

2.2. Backgrounds in EDELWEISS-III

Many improvements had to be made to the setup of the EDELWEISS experiment in order to reach the final goals of EDELWEISS-III. The first goal was to reach a background free exposure of $3000 \, \text{kg} \cdot \text{days}$ and then increase the exposure to $12000 \, \text{kg} \cdot \text{days}$, which might be background free depending on the actual contamination levels of materials for which only upper limits could be derived. These improvements were motivated by the outcome of the EDELWEISS-II phase, during which 5 events had been observed in the energy range $E_{\text{rec}} = [20, 200] \, \text{keV}$ for the accumulated fiducial exposure of $384 \, \text{kg} \cdot \text{days}$. These events were compatible with an upper fluctuation of the 3 expected background events and exclusion limits on the WIMP-nucleon were set [61]. A strong background reduction was therefore required for EDELWEISS-III by improving both active (see section 2.2.1) and passive (see section 2.2.2) background rejection. More detection mass was also required to reach a WIMP-nucleon cross section of $10^{-9} \, \text{pb}$ with EDELWEISS-III in a time scale of a couple of years. In addition, the EDELWEISS-II low mass WIMP [62] and axion [63] analyses showed the necessity to improve energy resolutions and lower the thresholds to increase the detection efficiency. The subsequent upgrades performed on the electronics and cryogenics systems have been described in section 2.1.4.

2.2.1. Active rejection of backgrounds

The detector technology was significantly improved between the two phases of the experiment. In EDELWEISS-II, the detectors used were so-called *Inter-digitized* (ID) detectors, covered with ring electrodes on the top and bottom surfaces and with a planar electrode on the side. Their total mass was of $\sim 400 \, \text{g}$ and their fiducial volume approximately 40% of the total detector volume [61]. The bolometers used in EDELWEISS-III are so called *Fully Inter-Digitized* (FID) detectors of $\sim 800 \, \text{g}$ each [55]. The total detector mass was doubled by increasing the height of the detector from 2 to $4 \, \text{cm}$, with the diameter remaining at $7 \, \text{cm}$. All the faces of the detectors are now covered with interleaved electrodes, leading to the electric field line configuration shown in fig. 2.4 right. Consequently, the fiducial volume of the detector is larger, up to $\sim$75% of the detector volume, and the rejection capabilities of γ's and surface events have been improved.

Misidentified γ's

It was observed in EDELWEISS-II during extensive γ calibration of the ID detectors with a ^{133}Ba source, that 6 γ's above $20 \, \text{keV}$ had a reduced charge signal which could mimic a nuclear recoil. The probability of misidentification was therefore calculated to be $(3\pm1)\times10^{-5}$ [61]. These events were understood later using simulations of charge migration to be due to the large low field guard region of the EDELWEISS-II detector design. The misidentified γ's could be reproduced by unrejected multiple scatterings of γ's in the bulk (full charge collection) and near the planar electrode on the side of the detector (incomplete charge collection). It could happen that the signal on the veto electrode is compatible with the noise because of bad charge collection. Thus, the event could not be rejected by applying a cut on the veto signal and the ionization quenching Q was underestimated. The expected background from γ-ray leakage for the accumulated exposure in EDELWEISS-II was estimated to be $0.9 \, \text{events}$ [61].

The active rejection of misidentified γ's was shown to also be considerably improved with the FID detector design. By replacing the planar electrode on the side by interleaved electrodes, the multiple scattering events described can now be efficiently rejected. The rejection power of γ's was measured using a ^{133}Ba source and determined to be more than 5 times better than in EDELWEISS-II. As shown in fig. 2.9, none of the 4.11×10^5 measured gammas leaked into the 90% nuclear recoil band above $20 \, \text{keV}$, leading to a rejection factor $< 6 \times 10^{-6}$ nuclear recoil/γ [65].
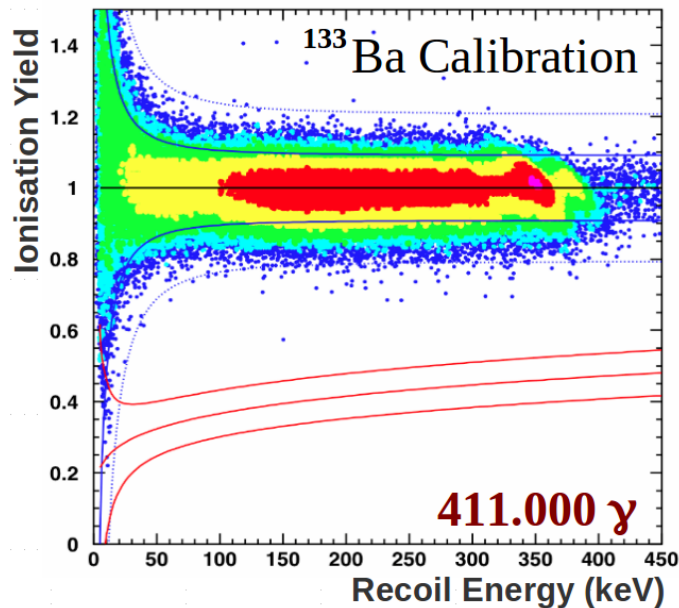
Figure 2.9. – Ionization yield as a function of the recoil energy for events from γ calibration in FID detectors using a ^{133}Ba source. The dashed and continuous blue lines are respectively the 90% C.L. and the 99.98% C.L. electronic recoil bands whereas the continuous red lines corresponds to the 90% C.L. nuclear recoil band. There is no single event leaking in the nuclear recoil band over the 411 000 measured. Extracted from [64].

Surface events

As discussed in section 2.1.2.2, events occurring at the detector surfaces are dangerous for dark matter search. They suffer from incomplete charge collection, which leads to an underestimation of the ionization yield Q. The main source of surface events is ^{222}Ra, which is deposited on the detector surface and the copper housing. ^{222}Ra quickly decays into ^{210}Pb, which itself decays with a half-life $T_{1/2} = 22$ years into the stable ^{206}Pb isotope by emitting both low and high energy β's, as well as an α of 5.3 MeV and a 100 keV recoiling ^{206}Pb nucleus (see scheme in fig. 2.10 left and appendix A). To measure the rejection capabilities of surface events, some ID and FID detectors were equipped with ^{210}Pb sources fabricated by exposing copper adhesive tape to a radon source. These sources were placed on the copper housing of the detector facing one of the detector surfaces. Depending on the particle type and its energy, the ^{210}Pb daughter penetrates more or less deep into the detector volume as illustrated in fig. 2.10. The charge collection is therefore more or less complete. Most of these events should be rejected by requiring no signal on the veto electrodes. By counting the number of remaining events after applying a cut on the veto electrodes, the number of misidentified surface event can be determined. For the ID design, one event was measured above 20 keV in the 90% C.L. nuclear recoil band after applying a cut on the veto electrodes for an exposure of 6×10^4 α's [55]. A corresponding surface rejection factor of 6×10^{-5} events/alpha at 90% C.L. was obtained for an energy threshold of 20 keV. Consequently, the number of expected misidentified surface events in the EDELWEISS-II WIMP search data was estimated to be 0.3 events [61]. As for the FID design, one event is remaining at 15 keV in the 90% nuclear recoil band after applying a cut on the veto electrodes for an exposure of 10^5 α's (see fig. 2.10 right). Thus, a surface rejection factor of 4×10^{-5} events/alpha at 90% C.L. is derived for an energy threshold of 15 keV [61]. To conclude, despite the extension of the interleaved design at the non-flat surfaces, the rejection is not degraded and even improved by a factor 1.5 despite a lower threshold of 15 keV compared to the ID technology used in EDELWEISS-II [65].
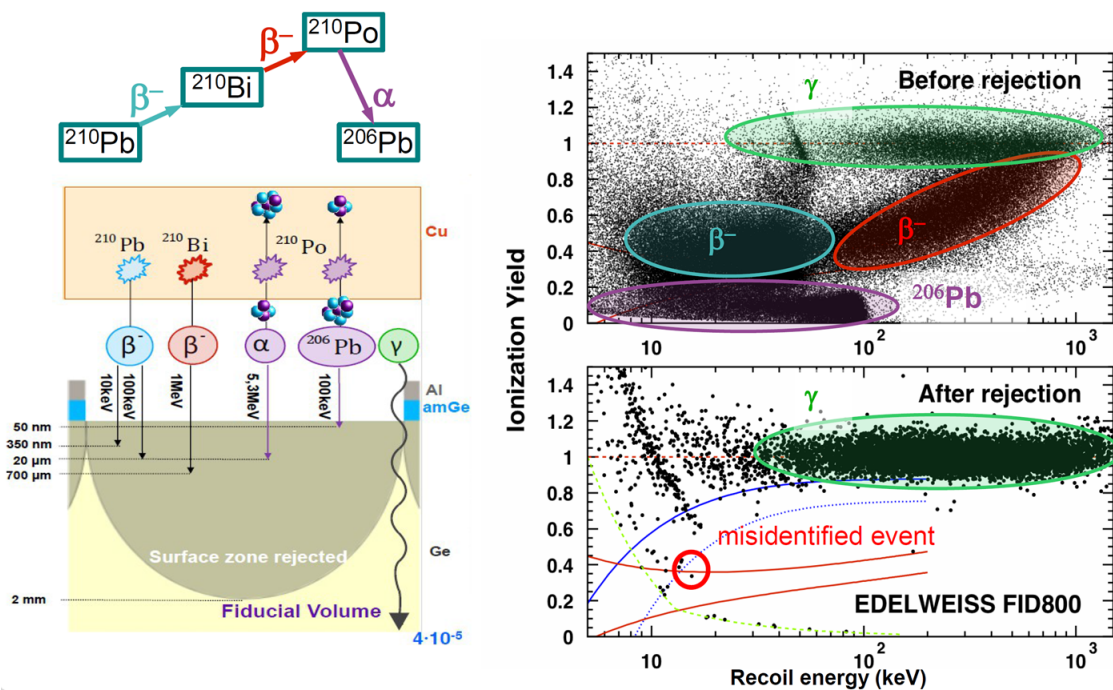
Figure 2.10. – **Left:** Schematic of the surface calibration with a ^{210}Pb source, which decays in β and α emitters of various energies. **Right:** Ionization yield as a function of the recoil energy in two FID detectors for events from surface calibration using a ^{210}Pb source (top). The same data is shown after rejection of all events with significant signals on the surface veto electrodes and differences between both fiducial electrodes (bottom). The red dot-dashed lines represent the 90% C.L. nuclear recoil band. The solid and dashed blue lines show the 90% and 99% C.L. electronic recoil bands. The green dashed hyperbola indicates the 2 keV ionization threshold cut. The coloured contours delimit the various populations accordingly to the color code use in the schematic on the left. One event is remaining at 15 keV for an exposure of 10^5 decays from ^{210}Pb decays. Extracted from [65].

2.2.2. Passive rejection of backgrounds

2.2.2.1. Gamma background

Due to incomplete charge collection in the detectors, there is a small but non-negligible probability that an electronic recoil induced by a γ is misidentified as a nuclear recoil. Therefore the γ background in the experiment has to be reduced, controlled and well understood. Extensive GEANT4 Monte Carlo simulations [66] based on radiopurity measurements have been performed to determine the γ background induced by radioactive decays in the setup materials.

Firstly, the EDELWEISS-II γ background estimation as published in [34] is reviewed in the view of understanding the upgrades made for EDELWEISS-III. Decays from ^{226}Ra, ^{228}Ra, ^{60}Co, ^{40}K, ^{54}Mn and ^{210}Pb isotopes present in the cryostats copper structures and screens, connectors and cables, detector casings and holders as well as in the lead shields have been simulated. Intrinsic γ background from cosmic activation of the germanium isotopes was also simulated and normalized to the data using the associated measured cosmogenic lines. These so-called 10 keV lines arise mainly from ^{65}Zn (8.98 keV), ^{68}Ga (9.66 keV) and ^{68}Ge (10.37 keV). The γ rate in the energy range $E_{\rm rec} = [20, 200]$ keV in the fiducial volume was then compared between simulation and data. A good agreement was found in both the shape of the energy spectra and the count rate: 82 events/(kg · days) were measured

whereas from 79 to 82 events/(kg · days) were expected from simulation, depending on the retrieved contamination for the oxygen free copper Cu-OF (containing less than 1 ppm of oxygen and a purity of 99.95%, also referred as CuC1 copper). The biggest contribution to the γ background (from 39% to 52%) was found to come from the U/Th contamination of the thermal screens and the 100 mK vacuum chamber. The second most important source (between 27% and 37%) arose from radium isotopes in some parts at the 300 K stage. This pollution has to be assumed in order to fit the measured energy spectrum but its exact origin is unknown. It could be explained by radioactive impurities in the cryogenic pipes, uncontrolled contamination of the 300 K thermal screen or the warm electronics, or by a higher radon concentration than expected in the air between the lead shield and the cryostat. The third most intense γ source arose from the ^{210}Pb decay coming from the radon decay on the detector surface and on the surface of the casing.

Thus the EDELWEISS-II simulations showed that few materials or components inside the shields were mostly responsible for the γ background. For this reason, parts of the copper structures of the cryostat were replaced by new ones made of more radiopure copper in EDELWEISS-III. The thermal screens as well as the experimental chamber of the cryostat (bolometer plates and holders) were replaced with pieces made of low activity copper (NOSV from Norddeutsche Affinerie, Germany). The associated radiopurity measurements performed at the Gran Sasso Underground Laboratory [67] showed that the contaminations were reduced by at least a factor 2 compared to CUC2 (with a concentration of oxygen limited to 5 ppm and a high purity of 99.99%, also referred as Cu-OFE copper) and at least a factor 100 compared to CuC1 copper [34]. The 10 mK stage of the cryostat above the 1K internal lead shield is now made of NOSV copper. In addition, the gasket between the two movable parts of the shields was redesigned to guarantee no leak of the laboratory air in the space between the lead shield and the cryostat, which is continuously flushed with de-radonized air.

The contribution of the various components and materials of the EDELWEISS-II setup after these improvements have been simulated using the GEANT4 v9.6.3 software, with the `Shielding` physics list [68], which was optimized for shielding simulations for high energy or underground detectors. The relevant materials and components as well as their activity in mBq/kg are listed in table 2.1. The preliminary results presented hereafter have been published in [69].

The interaction of γ's from ambient radioactivity dominates the event rate in the detectors. Due to the external lead shield, most of the observed γ's arise from contaminated materials inside the shields. Efforts have been done to describe and simulate small mass of materials particularly contaminated inside the cryostat, such as connectors or screws. The comparison of the measured energy spectrum with the simulated one was first performed outside the ROI for dark matter search, in the range $E_{\rm rec} = [0.1, 4]$ MeV. The contribution of each simulated decay chain was fitted to match the measured fiducial energy spectrum. The best fit gives an additional scaling for the following radioactive chains: 0.45 for ^{60}Co, 0.405 for ^{40}K, 0.54 for ^{238}U and 0.9 for ^{232}Th. These additional scaling factors are needed as upper limits on the contamination have been used as input of the simulation when not measured long enough. The simulated energy spectrum normalized to the experimental livetime is compared to the measured one in fig. 2.11a. The comparison is shown for the total detector volume on the left plot and for the fiducial volume on the right one, for an accumulated exposure of 544 kg · days and 380 kg · days respectively. Due to the excellent energy resolution of the bolometers, the following features are recognizable in the energy spectra: the backscattering peak at ∼200 keV and the photo-peaks from ^{60}Co, ^{40}K, and from the ^{238}U and ^{232}Th chains. Looking at the fiducial energy spectrum (fig. 2.11a right), a good agreement in shape between simulation and data is found, with a slight overestimation of the simulated spectrum. A comparably good agreement remains for the total detector volume although the scaling factors were fixed using the fiducial spectrum (see

Table 2.1. – The sources of background radiation and their mass used in the simulations. Individual contaminations for each radioactive isotope considered are given in the other columns. All values are in mBq/kg. Limits are given at 90% C.L.. All measurements were performed with HPGe detector in 2011, if not denoted otherwise. ($^{(1)}$ ICP-MS 2015 @ENS-Lyon; $^{(2)}$ M.Laubenstein (GEMPI)). Extracted from [69].

Element	Mass (kg)	^{238}U series		^{232}Th series	^{40}K	^{60}Co	^{137}Cs
		^{210}Pb	^{238}U				
10 mK connectors							
Delrin PTFE	0.04	<26	<16	1.5±1	± <43	<2.3	<2
Pins Brass	0.007	$(1.1 \pm 0.1)\cdot10^4$	<62$^{(1)}$	<20$^{(1)}$	675± 221	<36	<47
Sockets Brass	0.009	$(2.6\pm 0.4)\cdot10^4$	<62$^{(1)}$	<20$^{(1)}$	<2645	<129	<132
Press-Fit Contacts	0.002		$(1.2\pm 0.2)\cdot10^{4(1)}$	980 ±196$^{(1)}$			
Kapton Connectors	0.09	187	14± 7	67± 31	150±98		
PTFE Contacts	0.06		10±5	20±7			
Brass FID Casings	0.4	524± 102	<16	<15	<75	5±3	3 ± 2
Cu Kapton Cabling 10 mK	0.505	549±111	8±6	15±10	66±26	3 ±2	<4
Brass Screws 10 mK area	2	620±254		3.5± 0.9	<19	<3	2.6±1.5
NOSV Copper$^{(2)}$	294.7		<0.016	<0.012	<0.11		
EDWII Copper	328.0		<3	<2	<25	<2	
Internal PE	151.4	<3	0.65±0.08	0.3±0.07	<1	<0.06	<0.06
1K Axon Cabling	3.5	138±53	4 ± <3	5±2	177±22	<5	<2
Connectors 1K-100K axon	0.428	$(6.0\pm0.5)\cdot10^3$	$(2.6\pm 0.4)\cdot10^3$	450±44	<571	<36	<39
Stainless Steel cryostat	1236		<1	<1			
Cold/warm electronics + cabling							
PCB FET Boxes 100 K	0.55	$(1.4\pm0.3)\cdot10^4$	$(7.5\pm0.2)\cdot10^3$	$(10.1\pm0.1)\cdot10^3$	$(11.5\pm0.6)\cdot10^3$		
PCB FID Boxes 300 K	10.4		<1660	<1215			
Al FID Boxes 300 K	27.8	88± 36	4±3	<2	65±34	5±3	2.0±1.3
Axon Cabling 100 K-300 K	6.3		182±70	13.0±2.5			
External shields							
Mild Steel Structure	8.6 (t)		1.0	1.0			
Polyethylene	40 (t)		12	0.4	16±2	<3	
Lead	39 (t)		1.0	1.0			
Rock			1.0	1.0			

agreement between measured and simulated spectra in fig. 2.11b left).

The γ background in the ROI for WIMP search can be derived by integrating the simulated and measured fiducial spectra in the energy range $E_{\text{rec}} = [20, 200]\,\text{keV}$. The comparison of the γ rate in events/$(\text{kg} \cdot \text{days})$ are shown for the fiducial and total volume in table 2.2. The contribution of each decay chain and material after scaling is shown fig. 2.11a and summarized in table 2.2 for materials with a contribution $> 3\%$. Thus, the total γ background was measured to be of 70 events/$(\text{kg} \cdot \text{days})$ that is a reduction of 12% compared to the EDELWEISS-II background. The γ background is dominated by the close environment of the detector, notably by the connectors used to read-out the detectors and the brass screws maintaining the Teflon holders. Taking into account the improved gamma rejection capabilities of the FID design (see 2.2.1) of $< 6 \times 10^{-6}$ at 90% C.L., an upper limit of 1.26 events above a 20 keV threshold is expected for a $3000\,\text{kg} \cdot \text{days}$ exposure.
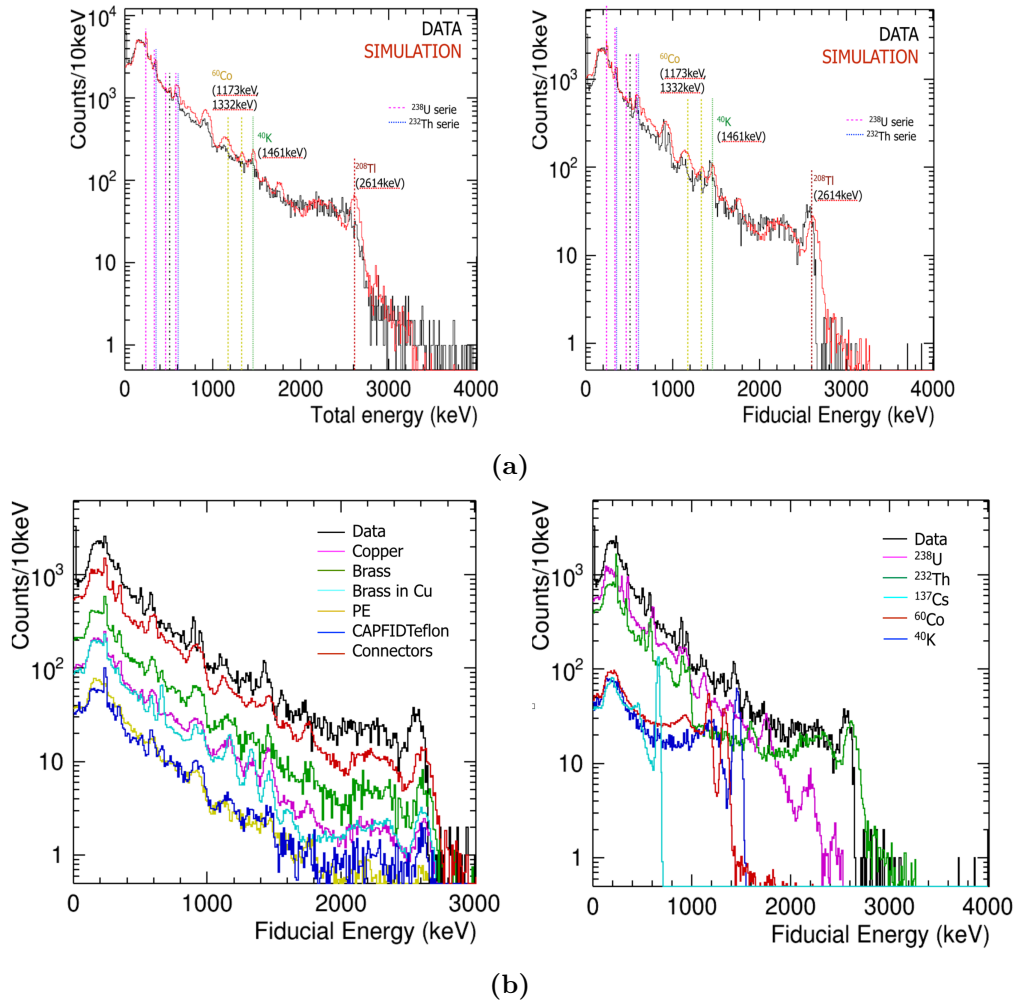
(a)

(b)

Figure 2.11. – **(a)** Comparison of the simulated and measured γ backgrounds. **Left:** comparison for the total detector volume for an accumulated exposure of $554\,\mathrm{kg \cdot d}$. **Right:** comparison for the fiducial volume for an accumulated exposure of $380\,\mathrm{kg \cdot d}$. **(b)** Simulated γ background energy spectra in the fiducial volume for a total exposure of $380\,\mathrm{kg \cdot days}$ (in black). **Left:** energy spectra for different materials as quoted in the legend. **Right:** energy spectra for different contaminants as quoted in the legend. Extracted from [69].

Table 2.2. – Gamma event rate in events/(kg · days) in the total and fiducial volume, in the ROI 20-200 keV. Only materials with a contribution larger than 3% have been listed. Extracted from [69].

Volume	Rate evts/(kg · days)		Copper	Brass	Brass in Cu	PE	Teflon	Connectors
	Data	MC						
Fiducial	70	78	7.3(10%)	14.7(20%)	6.9(9.4%)	2.6(3.5%)	2.2(3%)	39.7(54%)
Total	125	128	12.8(10%)	22.9(18%)	10.3(8%)	4.6(3.6%)	4.0(3%)	63.1(50%)

2.2.2.2. Radiogenic neutron background

The radiogenic neutron background arises from spontaneous fissions of ^{238}U and ^{232}Th decay chains (see appendix A) and (α,n) reactions in light materials. As a nuclear recoil in a single detector induced by a radiogenic neutron cannot be distinguished from a nuclear recoil induced by a WIMP, radiogenic neutrons are an irreducible background for dark matter search. This background is reduced by using PE shields and by a careful selection of materials based on radiopurity measurements. The residual background is estimated by simulations of spontaneous fissions and (α,n) reactions. The energy spectrum and neutron yield for each material were generated using the software SOURCES4A [70, 71, 72, 73, 74]. The propagation of the neutrons in the experimental setup was simulated using the GEANT4 software.

Firstly, the neutron background sources in EDELWEISS-II [34] are briefly reviewed to understand the motivation behind the shielding improvements in EDELWEISS-III. The GEANT4 v4.9.2 version with the `low energy electromagnetic interactions` physics list [75] was used to propagate the neutrons. The contribution of the following parts or materials have been simulated: the cavern walls (rock and concrete), the lead and PE shieldings, the stainless and mild steel support structures, the copper of the cryostat and detector housing, the electronic components at 300 K, the cables and the connectors. The contribution from small components close to the detectors, such as the crystal holders or the aluminium electrodes, has also been simulated: they can significantly contribute to the neutron background because of high (α,n) cross sections. The U/Th concentrations of the corresponding materials have been measured using HPGe γ-spectroscopy or mass-spectroscopy, assuming secular equilibrium of the U/Th chains. As the measured contaminations were mostly 90% C.L. upper limits, the neutron rate was also quoted as an upper limit: the radiogenic neutron rate estimate gave 1.0-3.1 events at 90% C.L. in the recoil energy range $E_{\rm rec} = [20, 200]$ keV in the EDELWEISS-II data. The contribution from the cavern, the external shields and the mounting structures were efficiently reduced by the external PE, leading to less than 0.25 events expected. The neutron background was highly dominated by (α,n) reactions in materials inside the shields. The main contributions came from the cable connectors at 1K (with an expected contribution of 0.5±0.2 neutrons) and from the PCB of the warm electronics below the detectors (with a contribution of 1.0±0.5 neutron).

The outcome of the EDELWEISS-II simulations led to the following improvements: first, materials showing a high contribution to the neutron background were replaced. The coaxial cables from Axon going from a bolometer to the bottom of the cryostat were replaced by in-house designed radiopure copper-Kapton cables [39]. Indeed, Axon cables contain Teflon (PTFE) as insulator, which can be highly contaminated in U/Th. The aluminium connectors at the 10 mK stage were replaced by Delrin body (Teflon) and Millmax pins. From the bottom of the cryostat at 10 mK to the 300 K stage, the same Axon cables and connectors as in EDELWEISS-II are used. In addition, new PE shields were installed inside and around the cryostat to further attenuate the neutron background (see fig. 2.12). A new PE shield of ~10 cm thickness was installed above the internal lead plate to attenuate neutrons from the 1 K and 100 K electronics. The new PE around the cryostat is made of several pieces: one is placed above the rack containing the warm electronics and the other around the cryostat, lying on the helium can, both pieces being of ~13 cm thickness. And last, a ring of 2 cm thickness surrounds the 300 K screen.

All the upgrades of the experimental setup (including other upgrades described in section 2.2.2.1) have been implemented in the simulation software. Most changes concern the 10 mK and 1 K stage. Due to the higher number of detectors and of electronic channels per detector, a larger number of electronic components were installed (FET boxes at 1 K, bolometer boxes at 300 K, cabling and connectors as described in section 2.1.1). They significantly contribute to the neutron background as they are made of PCB, copper and
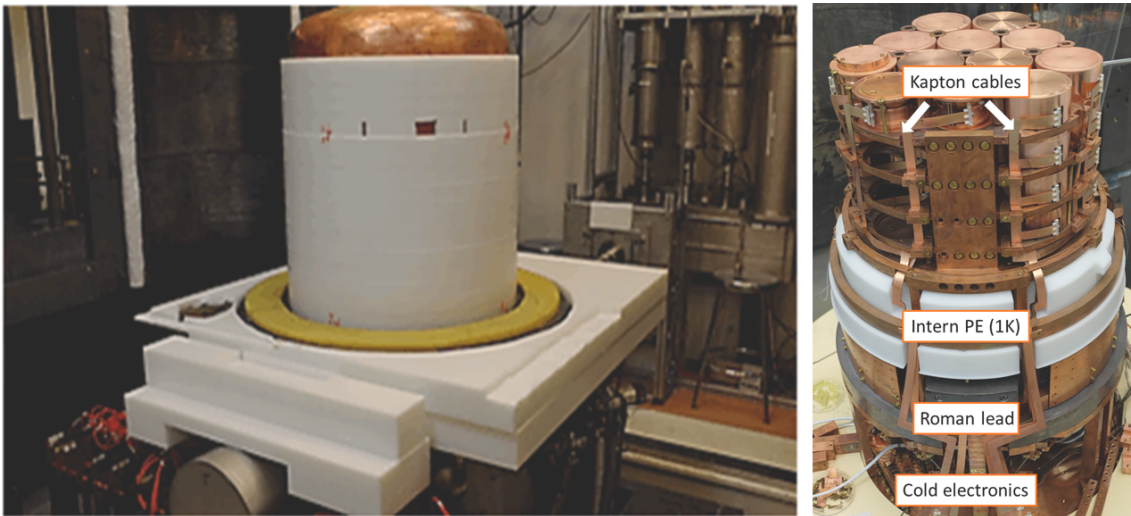
Figure 2.12. – Picture of the external (left) and internal (right) PE shields added in EDELWEISS-III.

aluminium particularly contaminated in uranium and thorium. A more realistic and updated description of these components was included in the EDELWEISS-III simulation. The geometry and contaminated materials of the warm electronics (300 K) were newly implemented (its contribution was only roughly estimated in EDELWEISS-II). Consequently, a more reliable and complete description of the contaminated materials was performed in the EDELWEISS-III simulation software.

The relevant materials and components of the EDELWEISS-III setup listed in table 2.1 were simulated. The attenuation of the neutron background from the new internal and external PE shields was extracted from simulations, by comparing the rate of neutrons interacting in the bolometers with and without the new shields [76]. This estimation is given for two values of the analysis threshold (10 and 20 keV) and for two threshold values used to distinguish a single hit from a multiple one (3 keV and 10 keV). Depending on the energy range and threshold considered, the following attenuation factors were obtained: from 16 to 17 for the 1 K connectors below the internal PE plate; from 34 to 35 for the 100 K FET boxes, the connectors and the cabling from the 100 K to 300 K stages; from 28 to 29 for the bolometer boxes and connectors at 300 K.

The total and single event rates in the 90% C.L. nuclear recoil band and in the fiducial volume (approximated to be 620 g) are summarized in table 2.3, for the Run308 configuration (24 FIDs), for one year of data taking. The estimated radiogenic neutron background is reduced by at least a factor 10 compared to the EDELWEISS-II estimation.

A large contribution to the neutron background (35%) arises from the sockets of the Delrin connectors, which contain CuBe spring contacts [77]. These so-called *press-fit* are made of 98.1% Cu and 1.9% Be to ensure the elasticity necessary for the contact between the pin and the socket. However, ^{9}Be has a high (α,n) cross section and is often contaminated by U/Th chains involving α emitters. Together with the bolometer holders in Teflon, the contribution of these components in contact with the bolometers amounts to 51% of the radiogenic neutron background; 22% are due to the warm electronics at 100 and 300 K stages; 16% to the external shields and the rock and 11% to the 10 mK stage. Thus, the neutron background in EDELWEISS-III is mostly dominated by components close to the bolometers and by the electronics.

Table 2.3. – Total and single simulated neutron event rate, in the 90% C.L. nuclear recoil band, in the ROI (< 200 keV), in the fiducial volume (ionization energy on veto electrodes <1 keV) considering a fiducial detector mass of 620 g and for one year of data acquisition. The estimation was performed for two values of the recoil energy threshold at 10 (1st and 2nd columns) and 20 keV (3rd and 4th columns). In the 1st and 2nd columns, an event is considered in coincidence if there is more than 3 keV recoil energy in any other detector of the 24 detector array. In the last two columns, this threshold is raised to 10 keV. Extracted from [69].

Number Ge detectors	kg · days	$E_{th} > 10$ keV: 2nd hit > 3 keV		$E_{th} > 20$ keV: 2nd > 10 keV	
		Total	Single	Total	Single
24	5431	4.8	1.4	3.2	1.1

2.2.2.3. Muon-induced neutron background

The μ-veto was designed such that it can detect most muons crossing the experimental setup. However, some of them travelling through the veto volume remain undetected because of gaps in the structure or because the amount of energy they deposit in a module is below the module trigger threshold. In these rare cases, the eventual neutrons induced by the muon or its showers which interact in a bolometer cannot be rejected. Therefore a precise estimation of the μ-veto efficiency is required, as well as the rate of μ-induced events which can be confused with WIMPs i.e. single nuclear recoils in the ROI.

The μ-induced neutron background in EDELWEISS-II was estimated in [78, 32]. The μ-veto detection efficiency was derived using two independent methods giving consistent results: either using data from high energy bolometer events induced by muons; or using a detailed MC simulation of the experimental setup including the modular trigger efficiencies. Both methods will be explained in more details in section 3.2.4.1, after introduction of the μ-veto. The efficiency of detecting muons that may produce secondaries near or inside the cryostat was extracted from both methods. The first one gave a lower limit of 93.5%, entirely limited by statistical uncertainties, whereas the second method provided an efficiency of 97.7% $\pm$ 1.5%. The rate of WIMP-like events depends on the configuration of the detector array and was measured for the EDELWEISS-II dark matter Run12 to be:

$$\Gamma_{\text{EDW-II}}^{\mu-n} = (0.008_{-0.004}^{+0.005}) \text{ events}/(\text{kg} \cdot \text{days}) \quad (2.17)$$

By multiplying it with the accumulated exposure of 384 kg · days and a conservative μ-veto inefficiency $(1 - \varepsilon_{tot})$, the associated μ-induced background was extracted. During a total exposure of (38 ± 11) kg · d, the μ-veto was not taking data or the synchronization between the bolometers and the μ-veto was faulty. Considering this time period during which μ-induced bolometer events could not be rejected, the number of expected unvetoed μ-induced events was calculated to be 0.40 events. Taking into account all uncertainties on the $\Gamma^{\mu-n}$, ε_{tot} and the exposure, an upper limit of 0.72 (at 90% C.L.) muon-induced WIMP-like events in bolometers was derived, corresponding to less than 20% of the total background contribution [32].

In 2010, as part of the upgrades towards EDELWEISS-III, four modules of plastic scintillator were added to cover the gap between the two parts of the shielding (see fig. 2.1). This upgrade was motivated by the exchange of the pulse tube with a cryoline of bigger diameter, linked to the thermal machines outside of the shields. Since then, the two parts of the shielding cannot be closed as tight as before. This gap is particularly dangerous as it is located just above the cryostat and could induce a significant loss of μ detection efficiency.

An estimation of the μ-induced background in EDELWEISS-III was performed by extrap-

olating the results obtained for the EDELWEISS-II phase in [32]. It was performed for the initial goal of EDELWEISS-III to reach an exposure of $3000 \, \text{kg} \cdot \text{days}$ in 6 months with 40 FID detectors, scaling the measured rate of μ-induced WIMP-like events in EDELWEISS-II $\Gamma^{\mu-n}_{\text{EDW-II}} = (0.008^{+0.005}_{-0.004})$ events/$(\text{kg} \cdot \text{days})$, with the expected exposure, considering the derived μ-veto efficiency of 97.7% [78]. The expected background in EDELWEISS-III is then:

$$N^{\mu-n} = \Gamma^{\mu-n}_{\text{EDW-II}} \cdot 3000 \, \text{kg} \cdot \text{days} \cdot (1 - \varepsilon_{\mu-\text{veto}}) = (0.6^{+0.7}_{-0.6}) \, \text{events} \qquad (2.18)$$

However, only a full modelling of the EDELWEISS-III specific geometry can give a precise estimation of the μ-induced neutron background. Indeed, the granularity and the density of the bolometer array increased, leading to a higher probability of multiple scatterings. Additionally, the installation of internal PE shields to moderate radiogenic neutrons also attenuates μ-induced neutrons produced in the lead. As 24 FID were actually read-out in Run308, the time required to reach the $3000 \, \text{kg} \cdot \text{days}$ is longer, leading to a higher μ-induced background. Thus, the extrapolation from EDELWEISS-II results represents only a first estimate which calls for a complete re-analysis of the expected μ-induced background.

The simulation and measurement of the μ-induced neutron background in EDELWEISS-III are the goals of this thesis and will be described in the following chapters.

3. Simulation and detection of muons in EDELWEISS-III

With increasing sensitivity of dark matter search experiments such as EDELWEISS, attention should be payed that negligible backgrounds do not become the limiting factor. One of the most dangerous background are neutrons induced by cosmic ray muons. The origin of cosmic rays muons and their interaction in matter, in particular the production of neutrons, are discussed in section 3.1. To shield against muons, the experiment is located in the deep underground laboratory of Modane, where the rock overburden attenuates the muon flux by a factor of 10^6. The neutrons produced by the remaining high energy muons, have a hard spectrum up to GeV-energies, which cannot be moderated with the PE shield. Therefore, remaining muons are tagged with an active μ-veto surrounding the experiment, allowing to reject μ-induced bolometer events. The working principle of this system is detailed in section 3.2. To understand and model the μ-induced neutron background, a full Monte Carlo (MC) simulation of muons in the experiment based on the GEANT4 package is used and presented in section 3.4.

3.1. Muon interactions and propagation

3.1.1. Parametrization of the muon flux at sea level

Muons are second generation leptons with a mass of 105.7 MeV and a mean life-time of $2.2\,\mu$s [17]. There were discovered in 1936 by C. Anderson and S. Neddermeyer who compared cosmic radiation at sea level and at 4300 m altitude using a cloud chamber [79]. At this altitude, they observed cosmic ray showers and bursts occurring more frequently and generally made of more tracks than the ones observed at sea level. In addition, the number of bursts and showers increased more rapidly with altitude than the total radiation. From this, they concluded of the presence of a strongly ionizing particle deposing so much energy, that its source had to be in cosmic rays.

It was later on discovered that muons are produced in the atmosphere at $\sim$15 km height, mostly by the decay of charged pions $\pi^{\pm}$ ($m_{\pi} = 139.6$ MeV) and kaons $K^{\pm}$ ($m_{\mathrm{K}} = 493.7$ MeV) [17]. Muons produced by heavier flavoured mesons containing charmed quarks are negligible due to the energy threshold of the process. $\pi^{\pm}$ and $K^{\pm}$ are themselves produced by fragmentation of nuclei in the atmosphere induced by high energy cosmic protons of energy up to $\sim$1 PeV. These protons make up about 79% of the primary cosmic rays, the rest being mostly helium nuclei ($\sim$ 10%), electrons and heavier nuclei such as carbon

or oxygen [17]. Below $\sim 1\,\mathrm{PeV}$, they mostly originate from our galaxy and are therefore isotropic because of the diffuse propagation in the galactic magnetic field. Above this energy, they are postulated to come from extragalactic regions but their sources are still unknown. The cosmic ray flux below $15\,\mathrm{GeV}$ is modulated by the solar wind with a cycle of 11 years, inducing a modulation of the muon production.

The differential energy spectrum of primary nucleons including protons can be parametrized by a steeply falling power law in the energy range from a few GeV up to $\sim 100\,\mathrm{TeV}$, as shown in fig. 3.1:

$$\frac{dN}{dE} \propto E^{-\gamma} \tag{3.1}$$

with $\gamma \simeq 2.8$ for energies below the so-called *knee* at $10^{15}\,\mathrm{eV}$, and $\gamma \simeq 3.2$ up to the so-called *ankle* at $\sim 10^{18}\,\mathrm{eV}$, measured by several experiments in the light nuclei component [80].
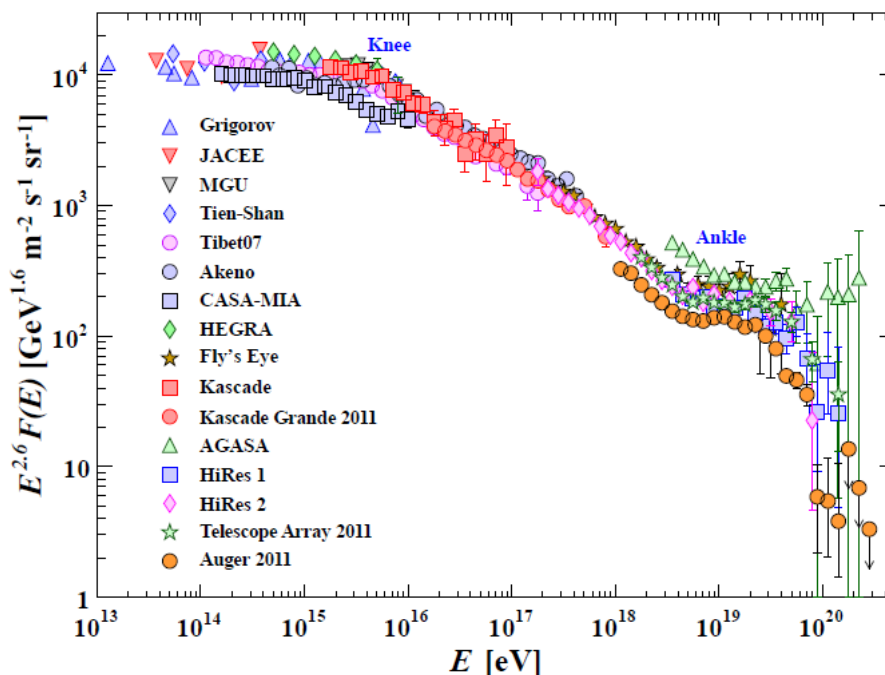

Figure 3.1. – Cosmic ray differential energy spectrum from air shower measurement, multiplied by $E^{2.6}$ in order to show the features of the spectrum. Extracted from [17].

Each cosmic-ray particle entering the atmosphere induces a cascade of ionized particles. The electromagnetic component is made of electrons, positrons and photons produced either by the decay of neutral mesons produced from the interaction of primary cosmic rays with the atmosphere, or by the muon decay and interaction in the atmosphere. The shower has a hadronic core due to spallation interaction with nuclei in the atmosphere, producing knock-on and evaporation neutrons and protons. The hadronic shower breeds itself an electromagnetic sub-shower, mostly by the decay of neutral pions. The muon component is called the penetrating component of the cosmic ray shower: despite their short life-time, muons can reach the Earth's surface and even underground laboratories as they mostly travel at relativistic speeds, leading to time-dilation effects. Additionally, they have relatively small interaction cross section with matter and loose less energy than electrons via emission of Bremsstrahlung photons due to their greater mass.

The energy and angular distributions of muons at the Earth's surface are the convolution
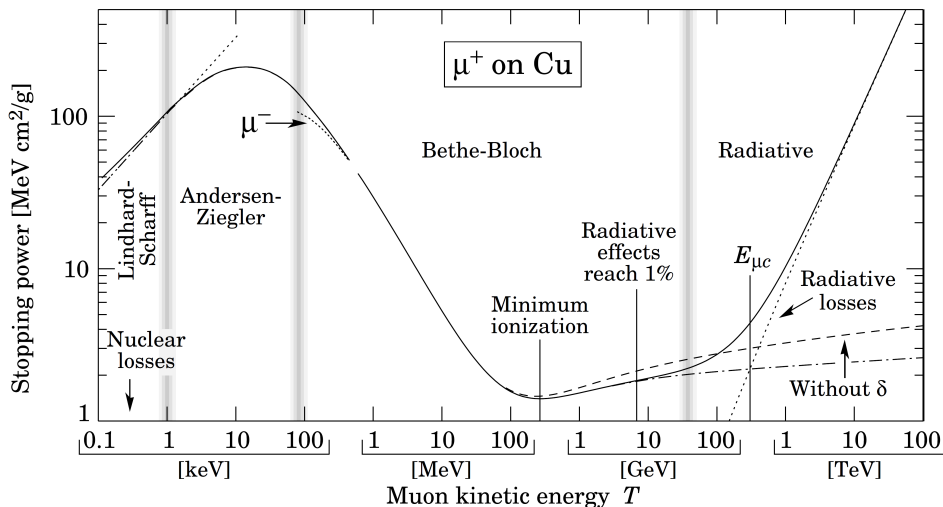
Figure 3.2. – Stopping power $\langle -dE/dX \rangle$ for positive muons in copper as a function of the muon kinetic energy T. Vertical bands indicate boundaries between different theoretical approximations or dominant physical processes. For more details, see [85].

of the production spectrum in the high atmosphere, the energy loss in the atmosphere ($\sim$ 2 GeV [17]) and the muon decay. The energy spectrum of light mesons decaying into muons has approximatively the same spectral index as the primary cosmic ray spectrum. Their angular distribution is also similar to the one from primary cosmic rays and is therefore isotropic. When the muon decay is negligible (for $E_\mu > (100/\cos\theta)$ GeV and $\theta < 70°$) as well as the Earth's curvature, the differential energy distribution is well described by the Gaisser parametrization [81], given here in its numerical form:

$$\frac{dN_\mu}{dE_\mu d\Omega} \approx \frac{0.14 E_\mu^{-2.7}}{\text{cm}^2 \text{ s sr GeV}} \times \left\{ \frac{1}{1 + \frac{1.1 E_\mu \cos\theta}{115 \text{ GeV}}} + \frac{0.054}{1 + \frac{1.1 E_\mu \cos\theta}{850 \text{ GeV}}} \right\} \qquad (3.2)$$

where the left term in the brackets is the contribution of pions and the right term the contribution from kaons. The contribution from the muon flux of charm and heavier flavour particles is neglected here.

The energy spectrum of muons at sea level is given by a power law following the primary spectrum except at low energies when muon decay is non negligible. It is approximatively flat below 1 GeV, increases at $10 - 100$ GeV following the primary spectrum, with a further steep increase above due to the interaction of π in the atmosphere before they decay [17]. Their mean energy at ground level is ≈ 4 GeV, with an average muon flux of about 1 muon/cm^2/min through an horizontal surface. As for the angular dependence, the distribution of muons at sea level follows a $\cos^2\theta$ for muons with energy ~ 3 GeV [17]. At large zenith angles, muons have a longer path to the surface and therefore a higher probability to decay before reaching the surface. In addition, high energy pions interact before they decay, which leads to a flatter angular distribution.

Note, that the muon charge ratio μ^+/μ^- is larger than 1 and increases with energy due to the excess of π^+ (K^+) over π^- (K^-) [82]. To reach the LSM underground laboratory, the minimal energy required for a muon is 2.5 TeV [83, 81]. For this energy, this ratio between muons and antimuons is [84]:

$$\frac{N_{\mu^+}}{N_{\mu^-}} \simeq 1.37 \qquad (3.3)$$

3.1.2. Energy loss of muons in matter

Muons loose energy according to four basic processes, either continuously via electronic losses (ionization, excitation and knock-on electrons), or via discrete radiative processes (namely e^+/e^- pair production, bremsstrahlung γ and muon nuclear interaction) [86]. The total stopping power in copper over kinetic energies in a large range from the keV to the TeV is shown in fig. 3.2 [85]. Several phenomenological models and theories are used to describe the muon stopping power depending on the muon kinetic energy. As only high energy muons with $E_\mu > 2.5\,\text{TeV}$ at sea level are reaching LSM, with an average energy $\langle E_\mu \rangle = 260\,\text{GeV}$, the description of the muon stopping below the GeV-range will not be reviewed here. A detailed description can be found in [85] and references therein. Nevertheless, it can be noted that in the keV range, the stopping power of muons is described by the Lindhard theory [42, 43], as for nuclear recoils in the germanium bolometers described in section 2.1.2.1.

The stopping power of energetic muons depends on the individual contributions of continuous and discrete processes with the muon kinetic energy, noted $a(E)$ and $b(E)$. The energy loss via radiative processes increases linearly with the muon kinetic energy up to $\mathcal{O}(\text{TeV})$. The mean muon energy loss in a path length in matter X is therefore usually parametrized as [87] :

$$\langle -dE/dX \rangle = a(E) + b(E)E \tag{3.4}$$

where $b(E)$ is the sum of energy loss via radiative processes $b \equiv b_{brems} + b_{pair} + b_{nucl}$. $a(E)$ and $b(E)$ both slowly vary with the muon energy, mostly when the energy loss is dominated by discrete processes: the contribution from radiative processes $b(E)E$ is less than 1% of $a(E)$ for $E \leq 100\,\text{GeV}$ for most materials [85]. The energy at which the continuous and radiative stopping powers are equal is called the critical energy $\varepsilon = a(E)/b(E)$. Both $a(E)$ and $b(E)$ are depending on the material which is crossed. For muon energy loss in standard rock [1], ε is equal to $500\,\text{GeV}$.

If the mild energy dependence of $a(E)$ and $b(E)$ is neglected, the average path length a muon can cross, also called the continuous-slowing-down-approximation (CSDA) range, can be calculated by integrating eq. 3.4:

$$R(E) = \int_{E_0}^{E} \left[a(E') + b(E')E' \right]^{-1} dE' \tag{3.5}$$

Thus, the relation between the energy of a muon at the Earth's surface $E_{\mu,0}$ and the average energy $E_{\mu,X}$ after traversing a rock of thickness X can be written:

$$\langle E_{\mu,X} \rangle = (E_{\mu,0} + \varepsilon)e^{-bX} - \varepsilon \tag{3.6}$$

The minimum energy needed in average for a muon to pass through the rock is given for $E_{\mu,0}$:

$$\langle E_{0,min}(X) \rangle = \varepsilon(e^{Xb} - 1) \tag{3.7}$$

Fluctuations from this parametrization are especially significant at high energies, when energy loss via radiative processes dominates. Monte Carlo (MC) simulations are then used for an accurate calculation of the total energy loss. A precise parametrization of the cross section of each of the four processes described above is needed as input for these simulations.

Energy loss via ionization

The stopping power of moderately relativistic heavy charged particles such as muons for intermediate Z materials is well described, with few percent accuracy, by the Bethe equation

---

1. defined by a density of $\rho = 2.65\,\text{g/cm}^3$, an atomic mass $A = 22$ and a charge $Z = 11$

[88]:

$$-\left\langle \frac{dE}{dX} \right\rangle = 4\pi N_{AV} r_e^2 m_e c^2 \frac{Z}{A} \frac{z^2}{\beta^2} \left[\frac{1}{2} \ln \left(\frac{2m_e c^2 \beta^2 \gamma^2 E_{max}}{I^2} \right) - \beta^2 - \text{corrections} \right] \quad (3.8)$$

with the Avogadro number N_A, r_e the classical electron radius, m_e the electron rest mass, Z and A the atomic and mass numbers of the absorber, z the charge of the incoming particle ($z = z_\mu = 1$ here), and I the excitation energy of the medium. The maximum kinetic energy transfer in one collision is given by:

$$E_{max} = \frac{2m_e c^2 \beta^2 \gamma^2}{1 + \frac{2\gamma m_e}{m_\mu} + \left(\frac{m_e}{m_\mu} \right)^2} \quad (3.9)$$

A number of corrections are added at both low and high energies, e.g. to take into account the polarization of the medium δ at high energies. These corrections are described in details in [85]. For standard rock, the muon stopping power for muon energies above $10\,\text{GeV}$ can be approximated with an accuracy of $\sim 5\%$ by [81]:

$$-\left\langle \frac{dE_\mu}{dX} \right\rangle \approx 1.9 + 0.08 \cdot ln \left(\frac{E_\mu}{GeV} \right) \frac{\text{MeV}}{\text{g/cm}^2} \quad (3.10)$$

For a minimum ionizing particle, i.e. a particle whose mean energy loss through matter is close to the minimum (see fig. 3.2), it can be approximated to:

$$-\left\langle \frac{dE_\mu}{dX} \right\rangle \approx 2 \frac{\text{MeV}}{\text{g/cm}^2} \quad (3.11)$$

Energy loss via Bremsstrahlung

The emission of a so-called bremsstrahlung photon occurs when the muon is deflected in the Coulomb field of a nucleus or an electron. A significant part of the muon energy can be emitted as one or two photons. Thus, the energy loss via bremsstrahlung cannot be described continuously as the fluctuations in energy loss are large. It is the dominant process of energy loss for electrons and positrons in most material at $\mathcal{O}(\text{MeV})$. For muons, it becomes significant at an energy of $\mathcal{O}(\text{GeV})$, as they are harder to deflect due to their higher mass.

At first approximation, the interaction cross section of muons via bremsstrahlung can be obtained from the Bethe-Heitler formula for the electron bremsstrahlung [89]. It was corrected for muons by Petrukhin-Shestakov [90], taking into account the finite size of the nucleus and the screening of the Coulomb nucleus field by the electron cloud with the energy of the projectile. Several extensions of this model co-exist, notably to describe the process cross section in case of large energy transfer, e.g. for cosmic muons. Among these extensions, the model of Kelner, Kokoulin and Petrukhi [91] is often used, which includes the bremsstrahlung contribution from the atomic electrons. Note that the cross section is approximatively proportional to Z^2 for nuclear bremsstrahlung and to Z for electronic bremsstrahlung.

Energy loss via pair production

The direct production of an e^-/e^+ pair arises from the conversion of a virtual photon emitted by a muon while deflected in the Coulomb field of a nucleus or an electron. It is the dominant process for high energy muons in the TeV range. An overview of the models describing the cross section via pair production can be found in [92, 93].

The formula of Kokoulin and Petrukhin is the most widely used for muon transport calculations. It includes a simple parametrization of the screening functions. Similarly to the emission of a real photon via bremsstrahlung, the cross section for pair production is proportional to Z^2 in the field of a nucleus and to Z in the field of an atomic electron.

Energy loss via muon nuclear interaction

The muon nuclear interactions can be modelled with the absorption of a virtual photon by the nucleus as shown in fig. 3.3, and is therefore also referred to as photonuclear muon interaction. For a large energy transfer between the muon and the nucleus, the high energy virtual photon interacts with a single nucleon rather than with the whole nucleus. The process is then similar to photodisintegration, described by the absorption of high energy γ by a nucleus which is brought to an excited state. Thus, muon nuclear interaction is also referred to as muon spallation in analogy to nuclear spallation. Muon nuclear interactions have a significant contribution to the muon stopping power at high muon energies $E_\mu > \mathcal{O}(\text{GeV})$ and relatively high fractional energy transfers $\nu/E_\mu > \mathcal{O}(10^{-2})$, especially for light materials [85]. The contribution from this process should be known precisely for the simulation of muon propagation through matter. Indeed, muons interacting via nuclear interaction can loose a significant part of their energy and scatter at large angles. In addition, this process is the main source of nuclear showers and therefore strongly contributes to the hadron (and thus to the neutron) background.

A combination of models is needed to describe the muon nuclear interaction, which depends on the nucleon structure functions, as well as on the energy and four-momentum transfer ν and Q^2, respectively. Most of the interactions are characterized by low $Q^2 \leq 0.1\,\text{GeV}^2$, for which perturbative QCD cannot be applied for the calculation of nuclear structure functions [94]. Instead, non-perturbative phenomenological models have to be used, in which the parametrization of the nucleon structure function is a free parameter, determined by fitting experimental data [95]. The most widely used model to calculate the muon nuclear interaction is based on the Weizsäcker-Williams approximation as formulated by Bezrukov and Bugaev, which gives consistent results with other calculations within 30%. Virtual photons are treated according to the Weizsäcker-Williams approximation [96], namely the passage of a charge particle in matter is considered to have the same effect as a beam of quasi-real photons. In this model, it is assumed that the γ-N cross section is the same for real and virtual photons. This approximation breaks down at low muon energies, when the virtuality of the photon can not be neglected any more. In addition, at low energy transfers $<0.3\,\text{GeV}$ [97], the virtual photon does not interact any more with a single nucleon but induces collective excitation of nucleons. The interaction cross section is therefore enhanced by several resonances, depending on the energy transfer i.e. the wavelength of the virtual photon. The contribution to the neutron yield of these resonances is still negligible compared to neutrons produced by the electromagnetic showers, and consequently adds only a minor contribution to the total neutron yield [98].

In the range of large four-momentum transfer between the muon and the nucleon, $Q^2 \geq 3\,\text{GeV}^2$, the nucleon structure functions can be derived from pertubative QCD [94].
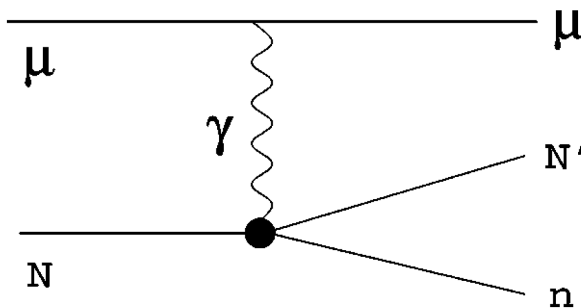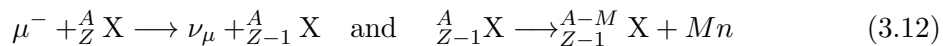

Figure 3.3. – Feyman diagram of the muon photonuclear interaction. Extracted from [98].

3.1.3. Production of neutrons by muons

Neutrons produced by cosmic muons have two origins: they are either directly induced by muon interactions with matter (negative muon capture or muon nuclear interactions), or indirectly in the interaction of the μ-induced electromagnetic or hadronic showers. A hadronic shower is dominantly generated by pions produced in photonuclear interactions of a muon with a nucleus. The individual contribution of direct and indirect processes depends on the mean energy of muons at the studied depth. In terms of neutron production in underground laboratories, the production of secondary neutrons by the hadronic shower outnumbers the direct production of neutrons by muon-nuclear interaction [33].

Negative muon capture on nuclei

Low energy negative muons gradually loose their energy via scattering on electrons until being captured by an atomic nucleus in a high atomic orbit, forming a muonic atom. Because of its large mass, the muon undergoes a cascade through the electron cloud to the innermost electron orbit, ejecting Auger electrons and emitting electromagnetic radiation [99]. In light nuclei, the muon mostly decays into an electron and two neutrinos: $\mu^- \to e^- + \bar{\nu}_e + \nu_\mu$. In heavy nuclei, it is usually captured by the nucleus: $\mu^- + p \to n + \nu_\mu$. The mass of the muon appears in nuclear excitation and in neutrino kinetic energy. The excited nucleus then emits one or two evaporation neutrons of kinetic energy $\sim 8\,\text{MeV}$. This process can be written as:

$$\mu^- +^A_Z \text{X} \longrightarrow \nu_\mu +^A_{Z-1} \text{X} \quad \text{and} \quad ^A_{Z-1}\text{X} \longrightarrow^{A-M}_{Z-1} \text{X} + Mn \tag{3.12}$$

where the number of evaporated neutrons M does not exceed 2.
The muon capture cross section strongly varies with the energy of the muon: it steeply decreases for kinetic energies greater than the binding energy of an electron in the atomic nucleus. This process is dominant at shallow depths of about $80\,\text{m}$ w.e. (at which $\langle E_\mu \rangle \sim 30\,\text{GeV}$), where it contributes to $\sim 50\%$ to the total neutron yield [97]. Its contribution at large depths e.g. at the LSM depth of $1800\,\text{m}$ w.e. is less than 1%.

Muon nuclear interactions

On a short time scale after the nucleus spallation ($10^{-22} - 10^{-21}\,\text{s}$), nucleons are knocked out of the nucleus with various energies, depending on ν and Q^2 [97]. The nucleus releases later on its residual excitation energy by emitting photons or evaporation nucleons, with kinetic energies of approximatively the binding energy of a nucleon. For $E_\mu > 1\,\text{GeV}$ and a high energy transfer $\nu \geqslant 0.3\,\text{GeV}$, pion photonuclear production starts via Δ resonance and leads to the creation of hadronic showers, which then generate neutrons [97].

In the electromagnetic and hadronic showers

Hadronic showers are mostly initiated by pions produced via muon photonuclear interaction. Neutrons are notably produced by intranuclear cascades with a large angular distribution with respect to the muon track. These neutrons themselves induce intranuclear cascades and produce more neutrons. Evaporated neutrons are also produced during intranuclear cascades and emitted isotropically. On the contrary to cascade neutrons, they are not able to breed because of their low energy. The dependence of the total number of neutrons produced in hadronic showers on the muon energy was measured to be $\propto E_\mu^{0.7}$ [98].
Electromagnetic showers are initiated by the decay of uncharged mesons, δ-electrons, e^-/e^+ pairs and burst of bremsstrahlung photons from muon interaction with matter

which have enough energy to trigger the cascade mechanism. At large depths greater than 2000 m.w.e., muons loose energy pre-dominantly via pair-production and bremstrahlung photons, dominating the electromagnetic showers. Neutrons are mostly produced in photonuclear reactions similar to muon photonuclear reactions but involving a real photon. In the same way, a dominant contribution to the neutron production comes from the low energy transfer resonances, leading to neutron evaporation.

Another smaller contribution to the neutron background arises from inelastic charge exchange reactions of real photons $\gamma p \to n\pi^+$ and $\gamma A \to (A-1)n\pi^+$ and pion photoproduction reactions $\gamma A \to A\pi^+\pi^-$ followed by the capture process $\pi^- A \to (A-2)np$. Because of their high energy threshold of $\sim 140\,\text{MeV}$, these reactions do not contribute much to the total neutron background but make the neutron energy spectrum harder.

The neutron yield from electromagnetic showers is larger than the neutron yield from hadronic showers. But the hadronic showers induce neutrons with a harder energy spectrum because of the energy thresholds [97].

3.2. Detection of muons at LSM with the muon-veto system

Despite the muon flux at LSM is reduced by a factor 10^6 compared to the flux at the Earth's surface, the rare remaining muons should be tagged to reject the potential μ-induced neutrons interacting in the bolometers. The μ-veto system installed for this purpose is described in this section.

3.2.1. Description of the setup

General setup

The μ-veto is made of 46 plastic scintillator modules, which acts as an active shield to reject bolometer events which can be attributed to the passage of a muon. As shown in fig. 3.4, the μ-veto is divided into two levels: an upper level (*Level 1*) made up of 30 modules which surrounds the external shield in the clean room and a lower level called *Level 0* composed of 16 modules. Each module is labelled with a number, from 1 for the easternmost module of the top to 48 [2] for the southernmost module of the bottom. Each wall of the muon veto system is labelled according to the geographical orientation.

The modules M7, M8, M15 and M16 were added in July 2010 as part of the upgrades towards EDELWEISS-III. They cover the empty space in the junction of the two movable parts, and will be referred as extra-top modules hereafter. They are equipped with LEDs along their axis [3] to monitor more easily the ageing of the modules. Note that the lateral modules M15 and M16 are $\sim 1.041\,\text{m}$ long and therefore cover only the upper $\sim 1/3$ of the lateral gap between the two parts of the shielding. However, the probability that a muon crosses the setup via the two lateral gaps is negligible as muons with such high zenith angle are rare.

For the cryostat to remain easily accessible, the upper level is positioned on rails and can be opened into two symmetric parts. Two lasers are used to monitor the position of the muon veto wagons, as the μ-veto efficiency is reduced when the system is open. Since the installation of the extra-top modules, one laser measures the distance between the western wall of the clean room and the near edge of M6 while another measures the distance between the western wall and the near edge of M8. By subtracting the two, the relative gap size can be derived. Both distances are measured five times every 15 minutes, and the measurements are written in a log file. In the offline analysis, the average position and its

---

2. There is no module labelled 23 and 24.

3. M7 and M8 are 2.1 m long and equipped with three LEDs: one at the center and the other two at 0.45 m distance from either of the two ends, all at the center of the module width. As for M15 and M16, they are 1.041 m and 1.033 m long. Both are equipped with one LED at the very center of the module.
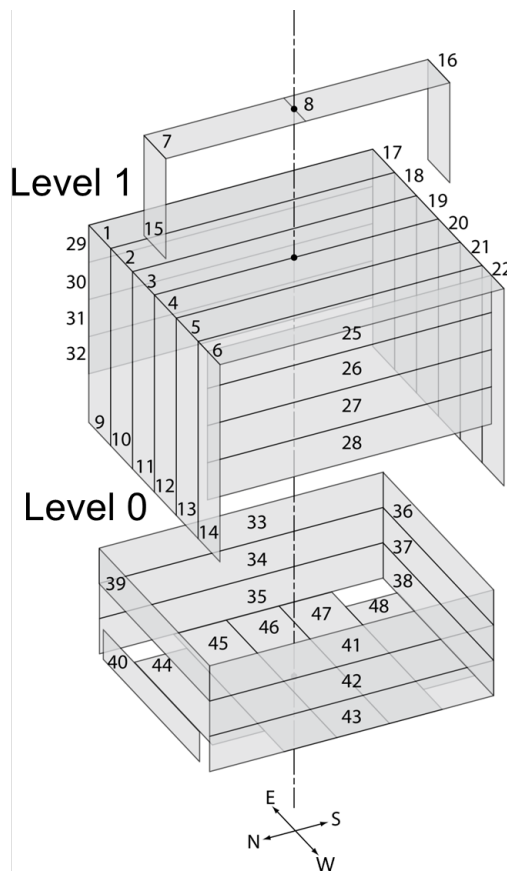
Figure 3.4. – Schematic view of the muon-veto, divided into a lower and an upper part, called *Level 0* and *Level 1*, respectively.

uncertainty ($< 1\,$mm) are calculated from the five measurements.

The plastic scintillator modules were previously used as muon-veto in the KARMEN experiment [100]. They have a width of $65\,$cm and a thickness of $5\,$cm, with a length that varies from $2\,$m up to $4\,$m (see fig. 3.5). At each module end, a group of four 2 inch Photomultiplier Tubes (PMT) collects the scintillation photons. As can be seen in fig. 3.5, $6\,$cm thick scintillator bars are used as light guides at both module ends in order to fix the PMTs on the inside of the module. Thus, there is no loss of detection volume at the junctions once the modules are combined to make up the μ-veto. Each group of PMTs is individually biased by a high voltage (HV). Individual HV settings were fixed for each group during the module calibration using muons at the Earth's surface [101]. The HV values are around -1500 V and have been tuned slightly since their installation at the LSM in order to reduce sparks on the PMTs or to compensate ageing effects of the modules [102]. This has been made before the start of bolometer data taking in EDELWEISS-III.
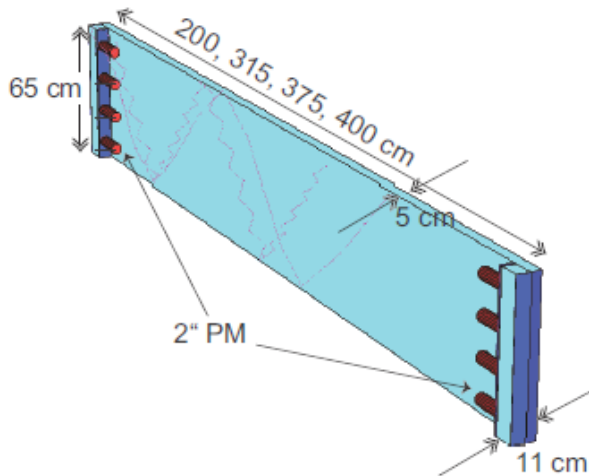
Figure 3.5. – Schematic view of a μ-veto module with its readout by two groups of 4 PMTs at both module ends.

Geometric efficiency

Despite the efforts to enclose the experimental setup almost hermetically, some gaps remain: a module on the north side of *Level 0* was left out to enable the passage of pipes needed for the operation of the cryogenic system. The module M40 is a 3.75 m long module which was used as no more 4 m module was remaining. Additionally, the modules M44 and M48 are shorter as there are the steel pillars of the EDELWEISS clean room. On the *Level 1*, in the east and west directions, a space was left below the modules M28 and M32 because of the rails on which the upper parts move. Lastly, a notch of 75 cm^2 was cut in the module M20 to enable the passage of the cryoline. Due to these gaps, the geometrical efficiencies from one side to the other vary from 99.7% for the top side down to 65.7% for the north side of *Level 0* [33]. However, due to the enclosed geometry, an overall geometric efficiency of $\sim 98\%$ is achieved requiring a muon to be detected in at least one module [103, 33, 32], as the detection of the muon is redundant. The remaining $\sim 2\%$ of muons going through gaps can still partly be detected by measuring their electromagnetic and hadronic showers. Requiring that two modules are hit decreases the efficiency to 81%.

Muon energy deposit in a module

High energy muons at LSM with $\langle E_\mu \rangle_{\mathrm{LSM}} \approx 280\,\mathrm{GeV}$ deposit approximatively $2\,\mathrm{MeV/cm}$ in the μ-veto modules of density $\rho \simeq 1\,\mathrm{g/cm^3}$ (eq. 3.11). It allows separation of muons (deposing an energy typically above $10\,\mathrm{MeV}$) from background events arising from natural radioactivity (deposing energy mostly below $4\,\mathrm{MeV}$), which enables to reduce the dead-time induced by vetoing bolometer events. The fluctuations in energy loss for a given path length of a muon in a μ-veto module are described by a Landau-Vavilov distribution [88, 104, 105]. The width of the Landau depends on the detector thickness and material as well as on the energy of the incoming particle [88]. This distribution is recognizable by its long tail arising from rare but existing collisions with a large energy transfer up to E_{max} (defined in eq. 3.9). The mean energy loss as formulated by Bethe (eq. 3.8) is therefore less technically adapted to describe the distribution, as most energy deposits are below the mean deposit. To avoid taking into account large energy deposits from the tail, it is more relevant to use the most probable value (MPV) to characterize the distribution. The mean μ track length in a module and its spread depend on the geometrical orientation of the module as well as on the angular distribution of the muon flux induced by the mountain

profile. Different groups of modules can be distinguished according to their orientation. The energy deposit is minimal in the horizontal modules from the bottom and top of the μ-veto, where a mean energy deposit [4] of $\langle E_{\mathrm{dep}} \rangle = 12.2\,\mathrm{MeV}$ and $\langle E_{\mathrm{dep}} \rangle = 11.8\,\mathrm{MeV}$, respectively, are expected from simulation [33]. Indeed, as muons reaching the laboratory mostly have a small zenith angle, the average track length in a module is of the order of the module thickness. The other modules are oriented vertically along their length or their width, leading to a higher mean energy deposit for low zenith angle muons as they have a longer path length. As the mountain axis is approximatively in the east/west direction, the muon flux with high zenith angle is higher for the north/south direction. Consequently, an average energy deposit of $\langle E_{\mathrm{dep}} \rangle \simeq 20\,\mathrm{MeV}$ in the north and south groups of modules is expected from the simulation, whereas an average of $\langle E_{\mathrm{dep}} \rangle \simeq 24\,\mathrm{MeV}$ is expected for the east and west. However, if a muon goes through a module at its extremity (so-called *grazing muons*), it does not cross the entire thickness of scintillator and deposits an energy well below the MPV.

To conclude, most muons deposit energy in the μ-veto modules well above the radioactive background, at the exception of muons going through gaps and of *grazing muons*. In the latter cases, low energy deposits from the muon itself or from its showers should be detected in order to tag the muon, and veto the eventual bolometer events it induced. The efficiency to detect small energy deposits is determined by the trigger threshold value of each μ-veto module.

Threshold

As will be explained in section 3.2.2.2, a trigger threshold of $150\,\mathrm{mV}$ on the amplitude of the pulses is set for all PMT groups to control the dead-time of the system. The effective trigger threshold in MeV depends on the individual gain of the PMT groups and the position of the interaction (see section 3.2.2.3). The modules were calibrated individually before the installation of the μ-veto in 2006 to ensure approximatively a uniform gain [101]. However, they aged significantly and inhomogeneously so that by now, the trigger threshold strongly varies from one PMT group to the other.

The trigger threshold value on the pulse amplitude was chosen to be much below the expected amplitude for an MPV in the plastic scintillators, mainly to detect *grazing muons* and muons passing through gaps by detecting their shower. A high detection efficiency at low energies also allows to extend the efficiency of the μ-veto to muons passing by the system via the detection of their showers. Consequently, the μ-veto overall rate in EDELWEISS-III is of $\sim 1.5\,\mathrm{Hz}$ whereas the expected rate of through-going muons hitting at least one module of the upper and lower levels is $\sim 3.5 \times 10^{-4}\,\mathrm{Hz}$ [32].

3.2.2. Working principle of the muon-veto modules

3.2.2.1. Production of scintillation light

The scintillators used for the μ-veto are organic plastic scintillator of type BC-412 chosen for their long attenuation length. The base of the BC-412 scintillator is the polyvinyl-toluene (PVT), an organic polymer containing benzenic rings responsible of the luminescence [106]. To further increase the light output, the PVT is additionally doped with aromatic rings of anthracene $C_{14}H_{10}$. The luminescence arises for given configurations of the valence electrons shared between two carbon atoms. In case of simple bound, the two shared electrons are participating to a strong σ bound (axial overlap of the orbitals). In the case of a double or triple bound, two of the valence electrons occupy a σ molecular

---

4. Despite the MPV is more relevant to characterize a Landau distribution, the mean value of the simulated energy deposit in each group of module is given in [33].

orbital whereas the others occupy one or two π molecular orbitals respectively. The π orbitals extend outside the axial region, leading to the delocalization of the electrons, as they are no more associated to a particular atom. Transitions of these π electrons from the first excited state to the ground state are responsible for the production of UV scintillation photons.

Because of the overlap between emitted and absorbed energy spectra, the attenuation length of the primary scintillation photons is short (few mm). Organic fluors are therefore added in high concentration to the PVT base to shift the scintillation light to a more convenient wavelength where the attenuation is less significant [17]. The mechanism responsible of the shift in wavelength is shown in fig. 3.6. First, the energy is transferred from the base to the fluor by non-radiative dipole-dipole resonance, also called Förster energy transfer [107]. This type of energy transfer is possible if the distance between two molecules is small and if there is an overlap between the emission spectrum of the base and the absorption spectrum of the fluor. It partly excites the electrons of the π bounds between carbon molecules from the ground state S_0 to the base state or a vibrational state of S_1, S_2 or S_3, on a time scale of $\mathcal{O}(10^{-14}\,\mathrm{s})$. In the case of electrons on the S_1 state, they decay radiation-less to the base state S_{10} by thermal equilibration in $\mathcal{O}(10^{-10}\,\mathrm{s})$. Once in the base state S_{10}, two decays can take place: either the electron decays back with a short decay time $(10^{-9}-10^{-8}\,\mathrm{s})$ to one of the vibrational states of S_0 by emitting a so-called fluorescence photon; or it undergoes a spin flip and passes non-radiatively to a triplet excited state [108]. After this intersystem crossing process, the excited electron is no longer paired with the ground state electron as required from the Pauli principle. When an electron in a triplet state decays back to the ground state, it emits a so-called phosphorescence photon with a much longer decay time than the fluorescence photon [109]. To conclude, because the photons emitted by fluorescence and phosphorescence have a lower energy than the minimum required for exciting electrons, scintillators are mostly self-transparent. The wavelength difference between the emitted and absorbed photons is the so-called *Stokes shift*.

Despite the doping, only a few % of the energy deposit in the module are actually converted into scintillation. The remaining energy is dissipated via non radiative processes, mainly via vibrations or heat. If the ionization density $\mathrm{d}E/\mathrm{d}x$ is small, the relation between the number of scintillation photons L and the energy deposit E by the ionizing particle in the scintillator is linear [110]. However, if the ionization density is large, the excited π-electrons are quenched i.e. the fast component is reduced because of overlapping excitations interfering with each other. Consequently, the energy response is non-linear with energy:

$$L = S(E - Q) \tag{3.13}$$

where Q includes the ionization quenching and S is the absolute light output. Due to the light quenching for heavy particles with a high ionisation density, pulse shape discrimination is possible by comparing the fast and the slow components. More details on the quenching will be given in section 4.3.2 when its implementation on simulated data will be discussed.

The scintillation photons propagate within the module via reflections on a highly reflective aluminium foil in which the modules are wrapped and are guided to the PMTs. Depending on the quantum efficiency of each PMT, a fraction of these photons are converted into electrons at the photo-cathode, which are then amplified by a system of dynodes. The electric signal at the output of each PMT group is then sent to be processed by the acquisition chain.

3.2.2.2. Electronic chain for the scintillation light readout

The acquisition of the μ-veto is totally independent from the bolometer data acquisition. It runs continuously, even when no bolometer data is acquired. The HV applied on the
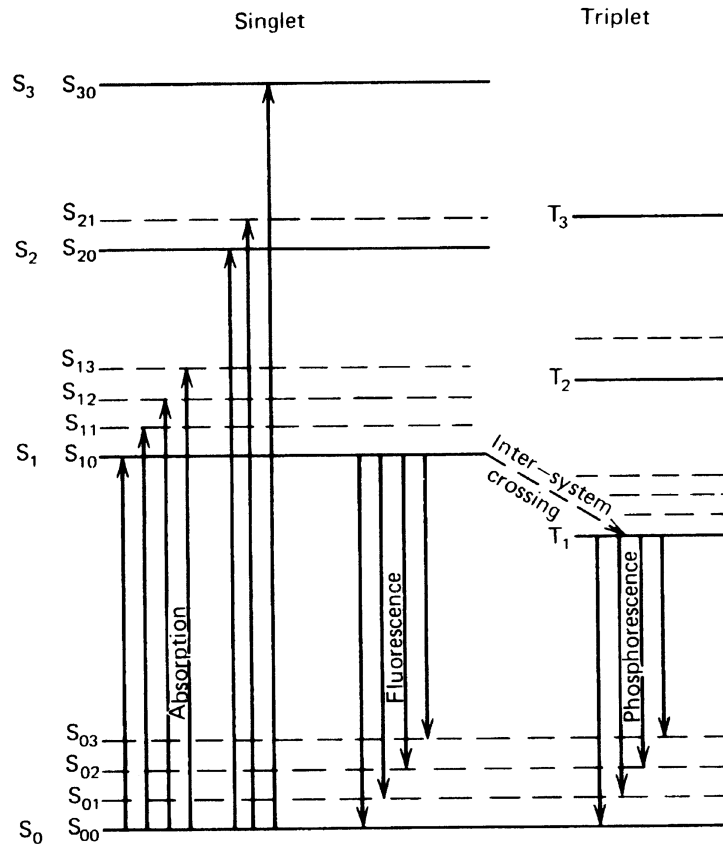
Figure 3.6. – Energy levels of π electrons in an organic molecule. Extracted from [110].

PMTs are switched off rarely, when some operations are ongoing in the clean room, for the safety of the people working there but also to protect the μ-veto from disturbances. Indeed, a strong increase of the rate can be seen when the light and the air conditioning in the clean room are turned on or when the μ-veto wagons are opened.

A chart of the electronic chain used for the μ-veto data acquisition is given in fig. 3.7. First, the signal coming from each PMT group is split in a so-called splitter card. One copy is sent to an Analog-to-Digital Converter (ADC) card. When a trigger decision is taken, it integrates the signal to estimate the energy deposit in the module (in units of ADC channels). The other copy is sent to a discriminator card, which further spreads the signal if its amplitude is higher than a trigger threshold, set to 150 mV for all the discriminator cards. This value was chosen to ensure the best compromise between dead-time and detection efficiency of low energy deposits, expected from electromagnetic and hadronic showers induced by muons or by muons crossing only a fraction of the module thickness. If the signal amplitude is above the threshold, three copies of the logical signal are made. One is sent to a scaler card which simply counts the number of signals per channel per 15 min, and records it in a scalar data file used to monitor the system. Another copy of the logical signal is sent to a Time-to-Digital Converter (TDC) card, which stores the arrival time of the signal. This information is used in the offline analysis to reconstruct the mean position of the energy deposit along the module axis. And finally, a third copy is sent to a Logical Unit (LU) card: if there is a coincidence between the 2 PMT groups on each end of a module within a 100 ns time window, it sends a command to the central veto logic card to store all non-zero signals in all μ-veto modules. The veto card sends a gate window to all the ADC cards for the signal integration, as well as a special TDC channel (common stop) which triggers back all TDC cards. It also makes the interface with the external clock, adding a timing with a 10 μs precision from the bolometer DAQ to the μ-veto event to

Figure 3.7. – Schematic of the electronic chain of the muon-veto. The logical signals from both module ends are checked to be in coincidence within a 100 ns time window by the logic unit cards (LU). If it is the case, the analogue data is recorded as one event.

reconstruct coincidences between the μ-veto and the bolometer array offline. Considerable improvements have been made between the EDELWEISS-II and EDELWEISS-III phases to ensure the delivery of a reliable and precise clock to all the systems. In the former system, each of the three acquisition computers had its own clock, which was reset at each run independently from the others. Only one of these clocks was connected to the veto time board. Therefore, considerable work had to be performed offline to reconstruct a common time basis for the bolometers and the μ-veto [102]. In EDELWEISS-III, the $10\,\mu s$ clock signal is attached to the bolometer data in the IPE crate (introduced in section 2.1.4), which redistributes it to the acquisition computers. In parallel, the clock signal is delivered via optical fibre to the μ-veto central card. A reliable reconstruction of muon-induced events is thus achievable, as will be shown in chapter 5.

Whenever a module triggers the acquisition, all non-zero TDC and ADC information of every group of PMTs, as well as the timing of the event (a $10\,\mu s$ precision clock delivered by the DAQ crate and the local computer time) are stored as one event. A dead-time follows the trigger during which no energy deposit can be detected. It was measured in EDELWEISS-III to be $\tau = (0.161 \pm 0.002)\,\mathrm{ms}$ with a spread $\sigma = (0.020 \pm 0.001)\,\mathrm{ms}$ and checked to be independent of the number of modules triggering [111].

The events are stored in an event data file lasting for a period of 8 hours per file. These files are grouped together in so-called Runs, each Run made of up to 99 event files. The entire data taken during a Run is converted in a single ROOT [112] file for an easy analysis of the data using the ROOT structure. In addition, it is converted in a single so-called *KData file*. KData is a data structure and analysis framework developed at KIT, notably designed to hold in a single event-based structure both the bolometer and μ-veto events [113]. It allows to automatize the data management (e.g. data backups and transfers) and create an interface with all the metadata stored in CouchDB databases collecting e.g. the radon level in the clean room, the μ-veto wagon position or the μ-veto HV settings. In addition, it provides tools for the analysis of the bolometer data [32]. For the work

detailed in this thesis, KData was not used as an analysis pipeline but as a data format to hold the μ-veto data. As the KData pipeline was not approved by the collaboration, the joint event builder of bolometer and μ-veto events was not implemented.

3.2.2.3. Position-dependent light output

For large scintillators, longer or of the order of the spectral attenuation length, the light output is dominated by the light attenuation from self-absorption. In the μ-veto modules, the scintillation light must be transported up to 4 m from the interaction point to the furthest PMT group. Consequently, the light output depends on the position of the interaction along the module axis. The light yield measured by a PMT group decreases exponentially with the path length d of the photons between the interaction and the PMTs and can be approximated by the empirical Beer-Lambert formula:

$$I(d) = I_0 \times e^{-\frac{d}{\Lambda_{\text{eff}}}} \tag{3.14}$$

with Λ_{eff} the effective attenuation length in meters. This Λ_{eff} should not be mistaken with the wavelength-dependent spectral attenuation length $\Lambda(\lambda)$, which gives a measure of the transparency of the scintillator and therefore only depends on the material. As for Λ_{eff}, it gives the scintillator transparency for a given geometry and is therefore detector specific. A better description of the light output than the one introduced in eq. 3.14 can be achieved by using a sum of exponential functions with different values of Λ_{eff} [114]. Indeed, the scintillation photons are either directly detected by the PMT group or indirectly after further reflections on the module boundaries. Note that Λ_{eff} actually depends on the emission wavelength, described with a broad spectrum.

Earlier measurements of Λ_{eff} are briefly reviewed below as this parameter will be needed to determine the μ-veto module response in chapter 4. The light output and the self-absorption of the μ-veto modules were originally optimized by the KARMEN collaboration with respect to the detector geometry using MC simulations [100]. Λ_{eff} was then first measured using two independent methods. One, called the *muon paddles method*, follows the principle of a muon telescope using two scintillator paddles. The paddles are located on the top and the bottom of the module to select muons with a given interaction position in the module. The other method is the so-called *free running method*: data is taken with the internal coincidence between the two PMT groups as trigger. Muons going through the whole module surface are thus measured and their position is selected offline by using the difference in arrival time of the photons at each module ends. The two methods showed consistent results on a test module, with an effective attenuation length $\Lambda_{\text{eff}} \sim 600$ cm in agreement with the specification of the provider BICRON [100]. The $\mu - \gamma$ separation of the 136 KARMEN μ-veto modules was then checked using the *free running method*, deriving a Λ_{eff} for each PMT group of a module. Indeed, due to inhomogeneities in the quantum efficiency of the PMTs or their gluing, the Λ_{eff} value is not necessary the same for both PMT groups. A gaussian distribution with a maximum at (595 ± 10) cm was found.

However, these measurements were performed in 1997/1998 and the modules have considerably aged since then. They were first transported from England to KIT, responsible for setting up the μ-veto, and stored above the freezing temperature [101]. Before the installation in Modane, every module has been checked by eye for possible damages. The module surfaces were cleaned with cotton gloves in order to remove oil from fingerprints which can cause micro-cracks on the module surface. Most of the PMTs were not glued on the light guide any more and were re-glued using the optical cement BC-600. Lastly, cracks in the aluminium foil were repaired. The modules were then transported to LSM. Since then, the modules aged further, leading to several effects [115]: first, the primary light

yield is reduced because of radiation damages from near UV and ionizing particles, which notably destroy double bounds between carbon atoms. Additionally, a decrease of the self-transparency is observed: plastic scintillators as well as crystals containing anthracene become yellow when exposed to radiation and to oxygen. The light propagation to the PMT can also degrade because of micro-cracks on the module surface which deteriorate the light reflection at the module boundaries. Lastly, the light detection may change due to the new coupling of the PMTs to the light guide.

These effects led to a decrease of the effective attenuation length. Two 4 m long modules were measured in 2003/2004 using the two methods described above and in [101]. The effective attenuation length of module M5 was measured using the *free running method*. The measured light yields for the individual PMT group and for the sum of both for this module are displayed in fig. 3.8. The total light output is minimal at the center and rises exponentially towards the module ends according to the effective attenuation length. By fitting the individual yields with an exponential, Λ_{eff} was found to be (343 ± 1.5) cm for the south side and (330 ± 1.4) cm for the north side [101]. For another module (M1) measured using the *muon paddle method*, Λ_{eff} was found to be (189 ± 0.8) cm for the south side and (204 ± 0.2) cm for the north side, where the uncertainties denote the statistical uncertainty on the exponential fit [101]. Another more recent measurement was performed in 2010 using a spare module available at KIT. An effective attenuation length $\Lambda_{\text{eff}} = 324$ cm was measured according to [83]. From these three measurements, a significant decrease of Λ_{eff}, dependent on the PMT group, can be apprehended compared to the initial values measured in 1997/1998. A smaller effective attenuation length means worse μ-γ discrimination and more importantly, less detection efficiency at low energies near the threshold, especially towards the module ends.
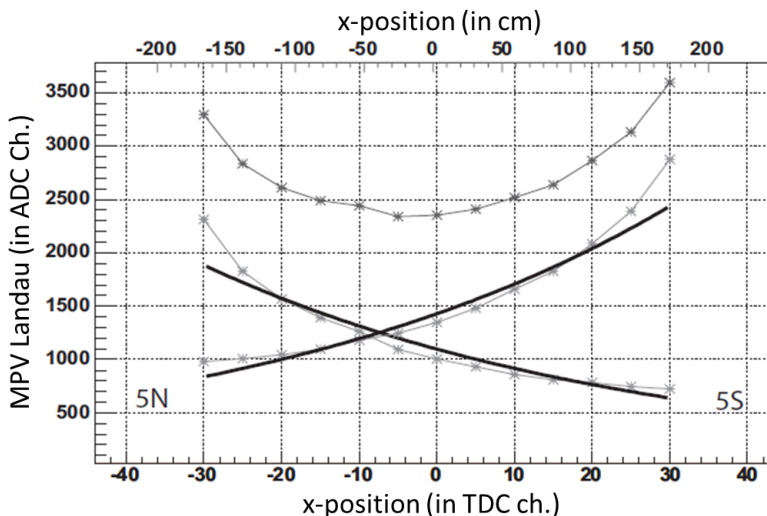
Figure 3.8. – Light yield curves for the north PMT group (5N, rising) and for the south PMT group (5S, decreasing) of the module M5 with exponential fits and the sum of the light yield curves. Extracted from [101].

3.2.3. Comparison of the module response to low and high energy deposits

The influence of the interaction position along the module axis can be significant or negligible depending on the amount of energy deposited in a module. This can notably be

illustrated by comparing the distributions of energy and position for muons and ambient background. As explained in section 3.2.2.2, the following information is stored for each energy deposit in a module (see fig. 3.5) of the μ-veto: the energy measured by each group of PMTs E_1 and E_2 in units of ADC channels, and the arrival time of the signal at each PMT group t_1 and t_2 in TDC units. The position of an energy deposit along the axis of a module can be reconstructed using the difference in arrival time $\Delta t = t_1 - t_2$. The energy and position distributions in the top modules of the μ-veto are plotted in fig. 3.9 for ambient background and for muon candidates. Muon candidates were selected by requiring a coincidence between the top module and at least one other module with full TDC and ADC information to reduce the probability of accidental coincidences.

As shown in fig. 3.9a, the energy spectrum of muons, fitted by a Landau distribution, is mostly above the energy distribution from ambient background. The separation is even more pronounced in the lateral modules as the mean energy deposit of muons in the top modules, together with the bottom modules, is lowest. The small tail towards lower energies either arises from fake muon candidates (random coincidence of backgrounds fulfilling the muon candidate selection), or from muons crossing only a fraction of the module thickness. Energy calibration of the modules is performed by comparing the MPV from the fit of the data with the expected MPV from simulation. A mean calibration coefficient of $5.44\,\mathrm{keV/ADC}$ channel was calculated in EDELWEISS-II.

Similarly, the interaction position distributions are shown in fig. 3.9b for ambient background and muon candidates. The distribution of muons is flat within statistical uncertainties and ends sharply at the module ends at around ± 40 TDC channels, equivalent to $32\,\mathrm{ns}$. Such a distribution can also be used to calibrate the event position along the module axis. Indeed, all interaction positions are equally probable to happen and to trigger the acquisition as the energy deposit is far above the threshold. As for ambient background, the distribution strongly varies with the position. It is the highest for the center and decreases towards the extremities. The two bumps on each side arise from the double thickness of scintillator on the module extremities on which the PMT groups are glued. Events with a larger, unphysical $|\Delta t| > 30\,\mathrm{ns}$ are due to low energy deposits with a worse time resolution.

It was shown in section 3.2.2.3 that the light yield measured by a PMT group is exponentially decreasing with the distance to the energy deposit due to light absorption. Consequently, the total light output is smallest at the center and rises exponentially towards the module extremities (see fig. 3.8). However, due to the trigger condition requiring that both PMT groups have a time signal amplitude above threshold, low energy deposits at the center are more likely to trigger. Indeed, the distance the scintillation photons have to cross is minimal at the center. The longer the distance to the further PMT group is, the less probable is the trigger as the absorption increases exponentially with the distance. Consequently, the effective threshold is the lowest for the center and exponentially rises towards the extremities. The PMT group the furthest from the energy deposit is the one responsible for the trigger.

To conclude, a muon fully crossing the scintillator will in general trigger the acquisition regardless of the position of the interaction. However, a muon crossing only a fraction of the module thickness and therefore depositing an energy close to the threshold (*grazing muons*) will be sensitive to the position dependence of the trigger. The detection of the electromagnetic and hadronic showers, used to improve the detection efficiency of missed muons, is also affected. In additional rare cases, a high energy neutron produced in the rock can reach the Ge bolometers and the muon passing next to the μ-veto. The detection will then only be possible via the showers. Therefore the determination of the position-dependent effective threshold is a key to determine the efficiency to detect low energy muons. The new method set up to extract it will be presented in chapter 4.
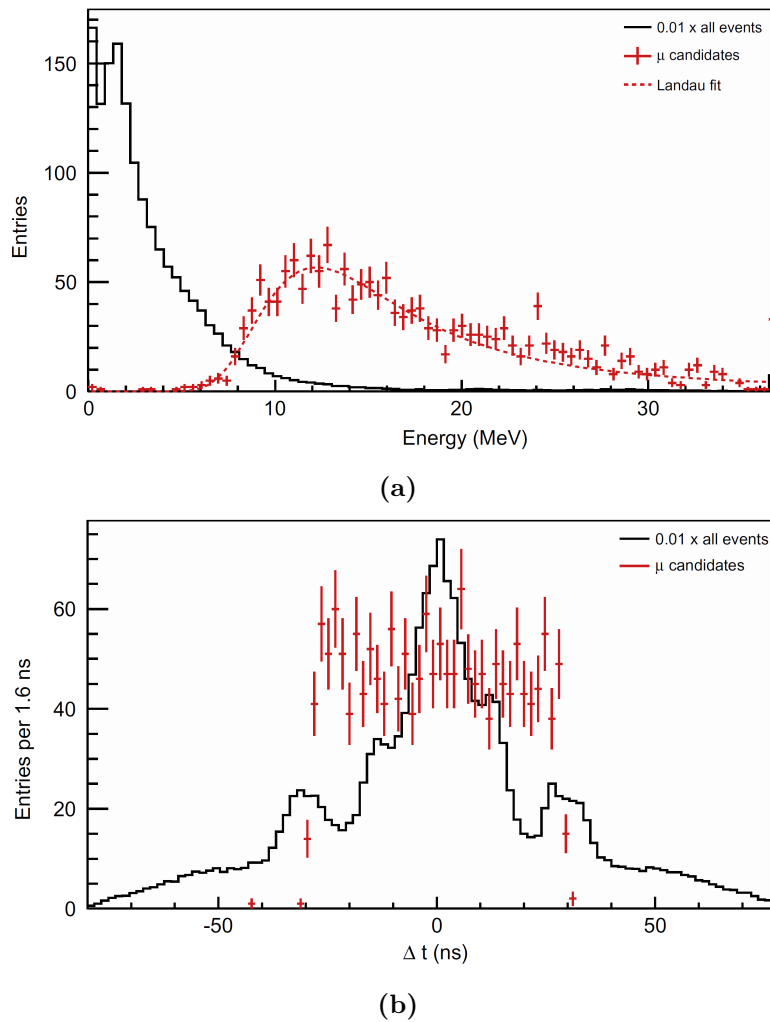
(a)

(b)

Figure 3.9. – Comparison of the energy and time distributions in a module from the top of the μ-veto between the muon candidates, selected by requiring full non-zero ADC and TDC information in another module of the μ-veto (red data points), and the background events recorded for a standard trigger condition (solid black histograms). **(a)** Distribution of energy deposits. The background distribution is scaled by 0.01 for visibility. The energy distribution of muon candidates are fitted by a Landau distribution (red dotted line). **(b)** Time difference between the two PMT signals for a module from the top. Extracted from [32].

3.2.4. Muon detection in EDELWEISS-II

The part of the μ-veto data analysis performed in EDELWEISS-II [78, 32], of interest in the framework of this thesis, is summarized in the following. First, the methods applied to derive the μ-veto efficiency and their limitations are explained. Secondly, the determination of the muon flux, useful for the normalization of the simulation, is described.

3.2.4.1. Determination of the muon-veto efficiency

The definition of the μ-veto efficiency varies with the context. One can define the μ-veto efficiency to be the probability of detecting a muon entering the volume enclosed by the μ-veto system. It includes muons going through the outermost corners of the μ-veto, which are not likely to produce secondaries interacting in the bolometers. These muons have a higher probability to be missed because of the gaps in the mounting structure in the corners or because they might deposit an energy below threshold. It therefore provides a lower limit of the actual efficiency of the μ-veto to trigger μ-induced events. A more realistic estimate can be done by determining the probability of detecting muons passing in the external lead shield where most of μ-induced neutrons are produced. This efficiency can be derived either from MC simulations or from a bolometer data sample by selecting events clearly induced by muons. The μ-veto efficiency definition can also be extended to the detection of muons passing outside the veto volume but detectable through their secondaries. Indeed, there is an extremely rare but existing probability that a neutron created in the rock reaches the bolometers without the muon crossing the μ-veto system. Two different methods were used in EDELWEISS-II to extract the μ-veto efficiency. One is based on a detailed MC simulation of muons in the experimental setup including the individual module trigger responses. The other is based on a sample of bolometer data clearly induced by muons. Both methods will be reviewed here.

μ-veto efficiency from the MC simulations

In order to determine the detection efficiency of a given simulated energy deposit in a module, the trigger thresholds of all individual modules were extracted using low energy μ-veto data. Although the trigger threshold depends on the position of the interaction along the module axis, only an averaged efficiency over all hit positions could be measured. Indeed, the cosmic muon flux is so low that the methods used to derive the position-dependent response described in section 3.2.2.3 cannot be applied *in situ* at LSM. Once a single module triggered the acquisition, all non-zero ADC and TDC values of all modules of the μ-veto were stored to disk. To derive the trigger efficiency of a module, events in this module for which an energy deposit were measured (non-zero measured ADC values) but which were not responsible of the trigger are selected. If one or both TDC signals in this module were equal to zero, then the energy deposit would not have triggered the acquisition itself and would have been missed. The fraction of potential triggers over all events versus the uncalibrated energy gives the energy dependent trigger efficiency $\varepsilon_i(E)$ of a module i. To derive the trigger efficiency in MeV, the μ-veto modules were calibrated by comparing the MPV from the data fit (in ADC units) with the one extracted from simulations (in MeV). However, the accuracy of the data fit was estimated to be 20% because of the limited number of muon candidates. This accuracy depends on the module as the muon flux varies with the orientation of the module. In addition, it is worse for the lateral modules, in which the spread of muon path length is large due to the muon angular distribution. Consequently, the measured energy distribution is a sum of Landau distributions spread over a large energy range.

By averaging the modular detection efficiencies derived from this method, a mean efficiency of $\langle \varepsilon_i^\mu \rangle = 95\%$ was found with a standard deviation of $\sigma(\varepsilon_i^\mu) = 4\%$. The modular detection

efficiency was then implemented in the simulated data to derive the overall μ-veto efficiency to detect muons. The error on the efficiency was determined by shifting the individual calibration coefficients by $\pm 20\%$ and extracting the corresponding efficiency. Consequently, the μ-veto efficiency to detect a muon entering the veto volume was estimated to be:

$$\varepsilon_{\text{tot, MC veto-volume}} = (93.6 \pm 1.5)\% \tag{3.15}$$

Over the 6.4% undetected muons, 2.4% passed through gaps in the structure; 0.9% were missed because of a malfunctioning module during a small part of the data taking, for which the trigger efficiency was set to zero for the appropriated amount of time; the remaining 3.1% were missed due to the module inefficiencies. Additionally, the μ-veto efficiency to detect muons passing within a $1\,\text{m}$ distance from the center of the cryostat was derived from simulation to be:

$$\varepsilon_{\text{tot, MC central-sphere}} = (97.7 \pm 1.5)\% \tag{3.16}$$

As explained earlier, this value gives a better estimate of the μ-veto efficiency to tag muon-induced bolometer events. The selection bias to muons passing close to the cryostat was shown to be negligible, using both measured and simulated data. Among the 234 coincidence events between the μ-veto and the bolometers measured in EDELWEISS-II, the tracks of 109 muons could be reconstructed unambiguously as information on the position of the muon interaction was recorded in two modules. It was found that more than 90% of these μ-induced bolometer events are induced by muons passing within a distance of less than $1\,\text{m}$ from the cryostat's center. It was also shown from simulations [33] that 90% of the neutrons depositing an energy $E_{rec} > 1\,\text{keV}$ in the bolometers are produced in the lead shield and in the cryostat. Even for neutrons produced in the rock outside the shielding, it is possible though rare that they reach the bolometers due to their high penetration depth. This contribution was estimated from simulation to be $\sim 0.05\%$. To conclude, most μ-induced bolometer events in EDELWEISS-II were caused by muons crossing the cryostat or the lead shield and could therefore potentially be vetoed with the μ-veto system.

μ-veto efficiency derived from a sample of bolometer data

Another, fully independent, method to derive the μ-veto efficiency relies on the selection of a bolometer data sample, which is unambiguously induced by muons. The efficiency is then derived by checking how many bolometer events are seen in coincidence with the μ-veto. The advantage of this method is that it avoids uncertainties on the calibration and on the simulations. However, it is limited by statistics as strict requirements are applied to select a pure sample of μ-induced events excluding all ambient radioactivity. With a selection of events satisfying $E_{\text{heat}} > 7\,\text{MeV}$ and a bolometer multiplicity $m_{bolo} \geqslant 2$, 34 muon candidate events were extracted from the bolometer data. All were found in coincidence with the μ-veto in a time window of $[-15,+1]\,\text{ms}$, leading to a best estimate of the efficiency of 100%. The lower limit at 90% C.L. on the efficiency was derived according to binomial statistics as follows:

$$P(k, n, \varepsilon_{\mu\text{-veto}}) = 10\% \quad \text{with} \quad P(k, n, \varepsilon_{\mu\text{-veto}}) = \binom{n}{k} \varepsilon_{\mu\text{-veto}}^{k} (1 - \varepsilon_{\mu\text{-veto}})^{n-k} \tag{3.17}$$

where n is the number of μ-induced bolometer events selected ($n = 34$), k the number of events tagged by the μ-veto ($k = 34$) and $\varepsilon_{\mu\text{-veto}}$ the probability of a μ-induced bolometer to be detected in the μ-veto. Consequently, the μ-veto efficiency was derived to be:

$$\varepsilon_{\mu\text{-veto}} \geq \sqrt[34]{0.1} = 93.5\% \text{ at } 90\% \text{ C.L.} \tag{3.18}$$

The systematic uncertainty on this efficiency calculation was estimated to be less than 1%.

3.2.4.2. Determination of the muon flux at LSM

The muon flux through a horizontal surface was determined using the EDELWEISS-II data and the corresponding MC simulations. This work is only summarized below, more details can be found in [78, 32]. Considering the complex geometry of the experiment, there is no straightforward way to determine the muon flux. First, muon-candidates were selected from the data by requiring at least one module of two distinct surfaces of the μ-veto to be hit, leading to a rate of muon candidate of $\Gamma_{\mu-\mathrm{cand}} = (108.7 \pm 0.8)/\mathrm{day}$. The simulation including the individual trigger responses was then used to translate the measured muon rate in flux. By applying the same muon selection criteria on the simulated data, the proportion of these muons crossing a virtual horizontal surface at the center of the μ-veto gives an acceptance of $a_{MC} = (20 \pm 0.4)$ candidates$/(\mu/\mathrm{m}^2)$. Consequently, the muon flux at LSM through a horizontal surface was estimated to be:

$$\Phi_\mu^{\mathrm{horizontal}} = \Gamma_{\mu-\mathrm{cand}}/a_{MC} = 5.4 \pm 0.2 \ (\mathrm{stat})^{+0.5}_{-0.9} \ (\mathrm{syst}) \ \mu/\mathrm{m}^2/\mathrm{day} \qquad (3.19)$$

The systematic uncertainties can be explained by three contributions. Firstly, the muon-candidate sample is not pure i.e. background events can contaminate the selection, notably in case of energy deposits in the corner of the μ-veto. Their influence was checked by deriving the efficiency excluding adjacent surfaces. It led to a reduction of the muon flux of 10%. Secondly, the uncertainties of $\pm 20\%$ on the individual module calibration described above led to another 10% uncertainty on the μ flux. Lastly, the contribution of muon bundles to the total muon flux, measured by the Fréjus experiment to be of 5% of the total muon flux [116] was not simulated. This flux will be compared with an earlier measurement performed by the Fréjus experiment in section 3.4.2.2 when the normalization of the muon simulations will be discussed.

3.3. Online monitoring of the muon-veto system

A central task to minimize the μ-induced background for dark matter search is to ensure that the μ-veto system is continuously running and that the recorded data is of good quality. Therefore daily shifts were performed in the framework of this thesis to detect as early as possible problems with the μ-veto system or with individual modules. This monitoring gets even more important with time because the system is suffering from ageing. The current electronic chain was also in use to read-out the KARMEN μ-veto but some electronic components are even older.

To detect problems as early as possible, the online monitoring of the μ-veto was significantly improved. Until the end of EDELWEISS-II, the monitoring of the μ-veto was done using raw data from the scaler cards. These cards basically count the number of hits per PMT group without any requirement of coincidence within the same module. In the framework of this thesis, the scripts to monitor the data used for the analysis were developed. This data gives a more complete overview of the proper functioning of the overall μ-veto and of single modules, and allows to better identify the source of problems. Several monitoring plots are produced by these scripts for each μ-veto run, every couple of hours and uploaded to an html webpage. The overall μ-veto functioning is controlled by plotting the overall event rate, which is approximatively of $1.5\,\mathrm{Hz}$. The time distribution between two consecutive events is also displayed to monitor the dead-time of the system. Indeed, it happened that the dead-time increased without any obvious reason. This problem could be solved by simply restarting the acquisition. In addition, the ratio of single over total number of events in each module is calculated as it gives an estimate of the trigger threshold. Four plots are displayed per module: an illustration for a well-working module is given in fig. 3.10, and for a malfunctioning module in fig. 3.11. The plot on top left corner displays the event rate in the module per hour. In case of stable run condition, this rate is

approximatively flat. A drop of the rate would indicate a malfunctioning of the electronics whereas a strong increase is due to noise and should be monitored to ensure an acceptable dead-time. The plot on the top right shows the position distribution relative to the center Δt versus time without condition on the TDCs. The projection of this distribution is shown on the bottom right plot for events satisfying the trigger condition (both TDC's >0). As for the distribution on the bottom left, it shows the sum of the energies measured by the two PMT groups versus time. Together, these plots give a good overview of the module stability. As can be seen in fig. 3.10, the module M18 was working perfectly during Run115 with a stable rate and energy distribution, and a symmetric response from both PMT groups. As for the module M30 (fig. 3.11), its event rate increased by a factor ~ 2 on the 13th of October 2014. From the energy and position distributions, it can be attributed to some low energy noise able to trigger the module at the center, where the threshold is the lowest. In addition, this module was strongly asymmetric: the south PMT group had such a high threshold that only rare events of high energy (e.g. muons) interacting on the north side of the module can be detected. The HV applied to the south PMT group was increased by steps, but no improvements could be achieved for this module.
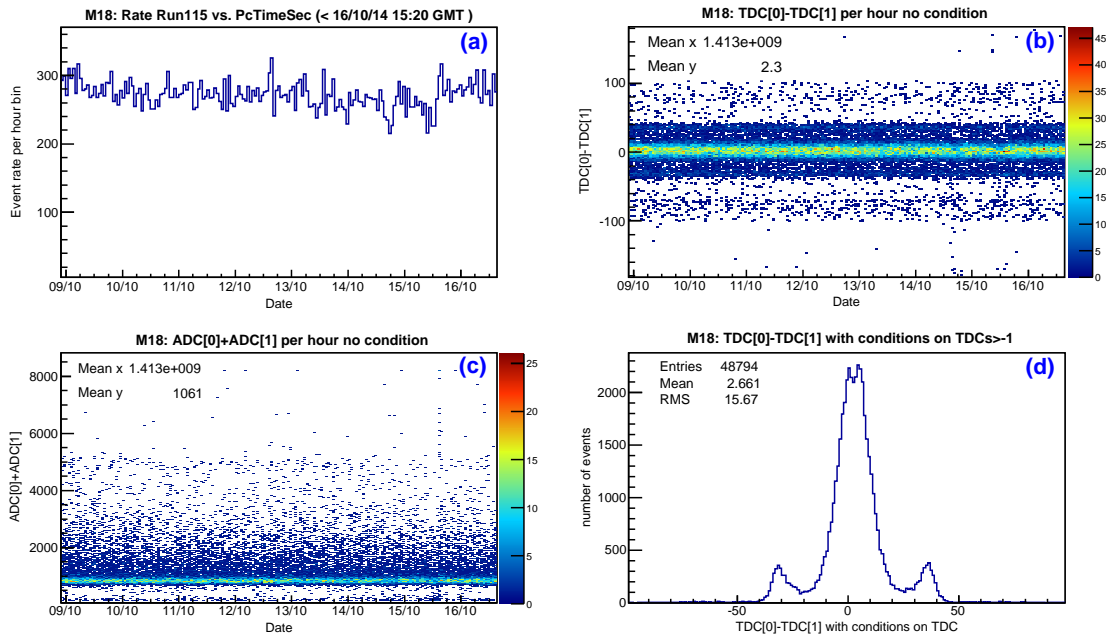
Figure 3.10. – Example of monitoring plots for a well functioning module (M18) during the μ-veto Run115: (a) event rate versus time per hour bin; (b) position distribution Δt versus time; (c) total measured energy versus time; (d) position distribution Δt for events satisfying the trigger condition.
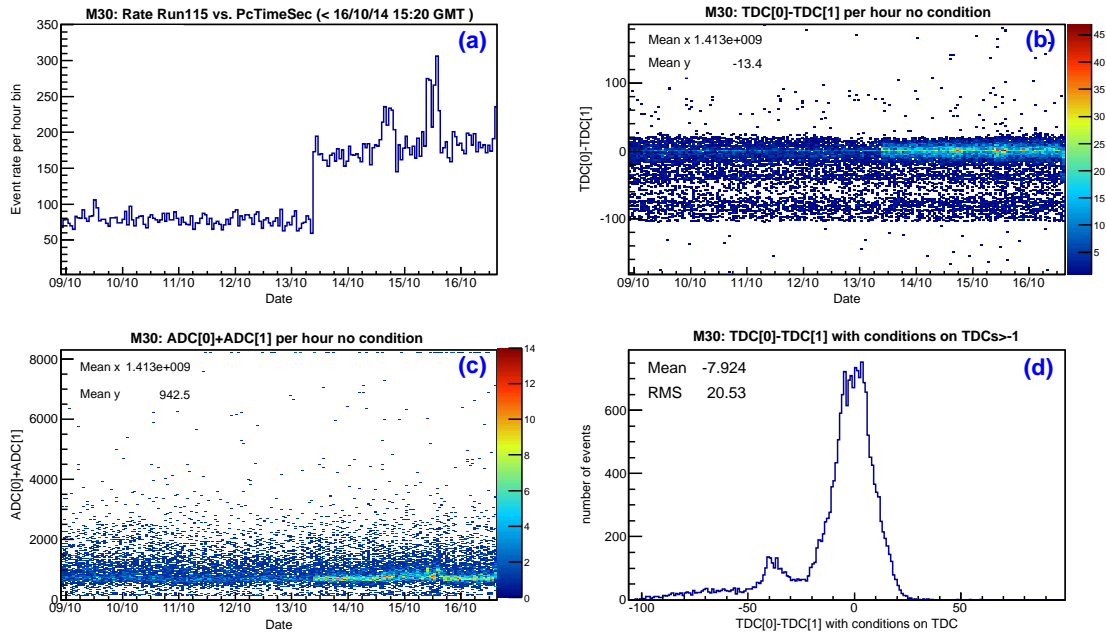
Figure 3.11. – Example of monitoring plots for a malfunctioning module (M30) during the μ-veto Run115: (a) event rate versus time per hour bin; (b) position distribution Δt versus time; (c) total measured energy versus time; (d) position distribution Δt for events satisfying the trigger condition.

3.4. Simulation of muons at LSM with the GEANT4 software

The GEANT4-based simulation software further developed for EDELWEISS-III simulations is presented here. A special emphasis is placed on the muon simulations, which will be used in the following chapters.

3.4.1. The GEANT4 simulation software used in EDELWEISS-III

GEANT4 is an object-oriented toolkit to simulate the passage of particles through matter using a Monte Carlo algorithm [66]. It was designed in a modular way so it can be adapted to a wide range of applications from the simulation of particles in a complex detector geometry to medical or military purposes. It is based on an object-oriented structure, made of a set of classes and libraries, which can be used independently from each other. As it is designed as a toolkit, the user must define its own main program as well as three mandatory classes:

— **the physics list** describing the physics processes and their modelling for the particles of interest, chosen according to the application of the simulation code. Each physics process is defined by its cross section and a model defining its final state. Which model describes the best the data depends on the energy range and the type of particle studied. Therefore different models should be combined to cover a large energy range. This is described in the physics list, which is set up carefully by the user to describe the best his application. Some pre-defined reference physics lists are developed by the GEANT4 collaboration but recommended only for specific tasks.

— **the geometry of the experimental setup**, implemented with the help of visualization tools. For the simulations in EDELWEISS, the full setup including the experimental hall with its concrete walls and the rock surrounding the laboratory have been implemented. This is especially needed for a precise simulation of the muon shower development in the rock and shielding of the setup. A high level of details is also required to simulate the radiogenic and gamma backgrounds. Even, small components close to the detectors such as connectors are described.

— **a primary particle generator** defining the energy, position and angular distribution of the initial simulated particles, e.g. a muon generator.

In the past years, independent simulation codes have been developed within the EDELWEISS collaboration, either optimized for radioactive background or muon-induced background simulations. Towards EDELWEISS-III, the different codes were merged to provide a common framework for all EDELWEISS-III simulations. Significant work has been done to set up a coding convention, unify the geometry and physics list, provide a single output, and clean the code from useless classes. In addition, the code has been implemented such that so-called *macro files* can be used as input of the simulation to change the particle generator without recompiling the code. These macro files are typically text files including a list of commands, which are given as input of the simulation code and interpreted by GEANT4. This makes it easy to change between neutron-, γ- and muon- sources and change the parameters of the initial particles without any modification of the code and compilation.

The simulation code for EDELWEISS-III was updated to run with the GEANT 4.9.6 version [117] (in comparison to GEANT 4.9.2 used in EDELWEISS-II simulations). Important changes were made between the two versions on the physics processes and models involving neutrons at all energy scales. The complete list of standard evaluated neutron data libraries is now accessible. Concerning the hadronic physics, the changes implemented lead to a lateral profile of hadronic showers narrower in heavier absorbers such as lead. The detailed list of updates can be found in [117].
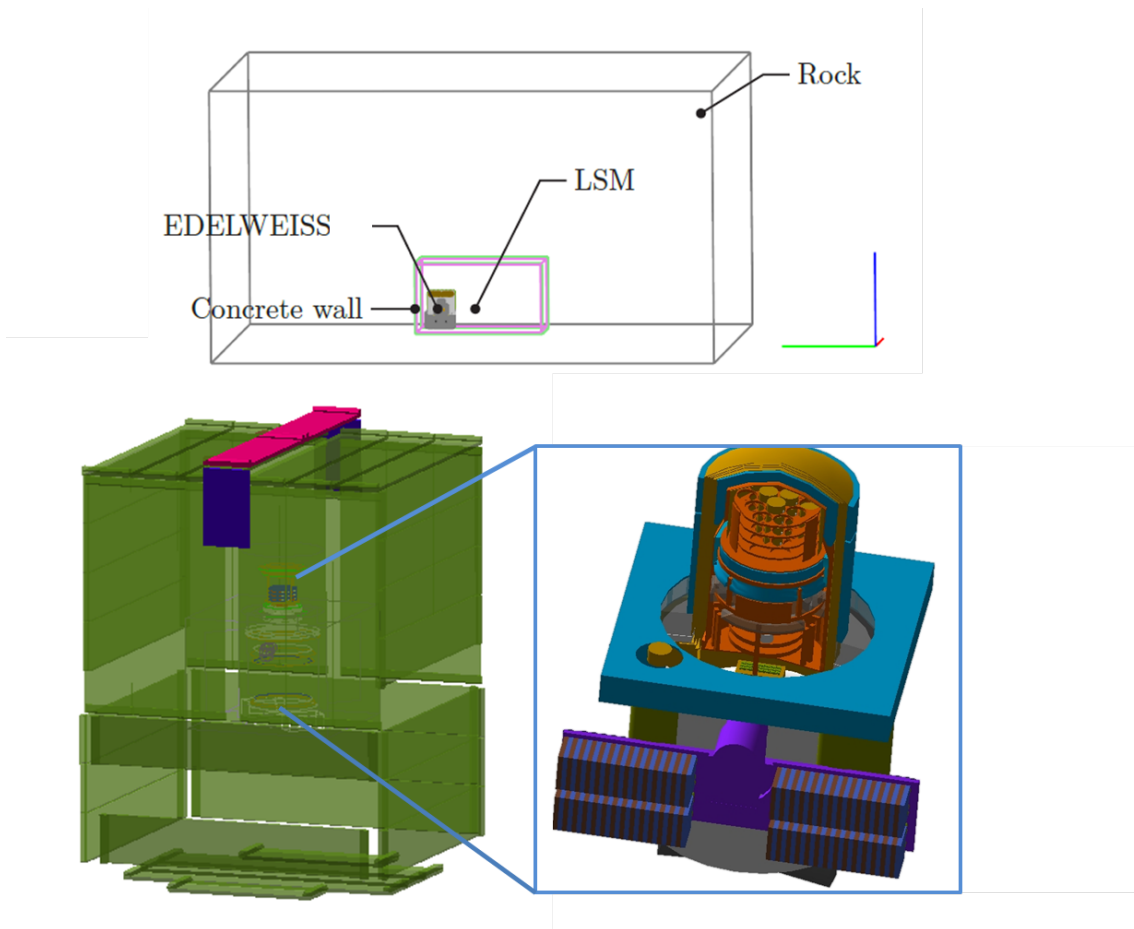
Figure 3.12. – Visualization of the EDELWEISS-III geometry as implemented in the simulation code. The μ-veto system, with the newly implemented modules covering the gap between the two chariots, and the cryostat together with the warm electronics are shown.

In addition to the upgrade to GEANT 4.9.6, the physics list was changed. In EDELWEISS-II, the `low energy electromagnetic interactions` physics list [75] was used for radioactive background simulations, whereas a custom physics list has been developed for the muon simulations. For the EDELWEISS-III simulations, the `Shielding` physics list [68], recommended by the GEANT4 collaboration for shielding applications, is now in use. The implications of the change in physics list in terms of μ-induced neutron background will be discussed in the next section.

Aside from the new code, the new version of GEANT4 and the new physics list, significant modifications have been made to the implemented geometry to include the EDELWEISS-III upgrades detailed in chapter 2.1. The main changes concern the addition of the new internal and external PE shields; the 1 K and 10 mK areas with the new structure of the experimental chamber of the cryostat, the cabling, the new shape of the 1 K copper cryogenic screen and the electronics; the FID800 geometry with its casing, PTFE clamps and connectors; and the electronics at 300 K. In the framework of this thesis, the μ-veto geometry was implemented with the 4 additional modules installed at the junction between the two part of the shields. Part of these changes are illustrated in fig. 3.12.

The debugging and tests of the new simulation code for muon simulation were performed in the context of this thesis.

3.4.1.1. Physics list for hadronic interactions

The description of hadronic interactions in the simulation software has a significant influence on the simulated neutron yield. Indeed, the physics of muon-nuclear interactions and the production of secondary neutrons in the hadronic shower are not yet understood; numerous models co-exist, which are valid in specific energy ranges. Depending on the models used, large variations of the simulated neutron yield in lead have been observed, with a discrepancy up to a factor 2 between different MC codes [118].

For the EDELWEISS-II simulations of μ-induced neutron background, a custom physics list was developed especially for a high precision modelling of μ-induced neutron production by M.Horn [33]. This physics list has been replaced by the reference `Shielding` physics list recommended since 2012 by the GEANT4 collaboration for shielding application, high energy physics and space physics. The list used in EDELWEISS-III is based on the `FTFP_BERT_HP` reference list with improved neutron cross sections from the Japanese Evaluated Nuclear Data Library (JENDL) [119] and better description of ion interactions. The high precision (`HP`) low energy neutron transport package describes neutron interaction below 20 MeV using data-driven models. The hadronic interactions are modelled using the Bertini-style cascade (`BERT`) for hadrons below 5 GeV and using the FriTioF string model (`FTF`) at high energies above 4 GeV together with the Precompound model to handle the fragmentation of the excited nucleus. It also contains the description of all standard electromagnetic processes and includes neutron capture. As illustrated in fig. 3.13 for inelastic neutron scattering, this list significantly differs from the one used in EDELWEISS-II: at high energies, the quark-gluon string model (`QGS`) was used, together with the Precompound model for nuclear fragmentation (the combination is known as the `QGSP` model). The intra-nuclear binary cascade (`BiC`) model was used for low energies. The intermediate gap was covered by the low energy parametrization model (`LEP`). This physics list was based on the reference physics list `QGSP_BIC_HP` provided by the GEANT4 collaboration: only the energy ranges in which each model was used varied.

A detailed study of the implications of these changes in terms of μ-induced neutron background was beyond the scope of this work. Therefore, the associated uncertainties on the μ-induced neutron background have been evaluated from literature. Most neutrons scattering in the Ge bolometers are produced by interactions of the electromagnetic or hadronic showers induced by a muon in the external lead shield surrounding the experiment. The uncertainty on the simulated neutron background in EDELWEISS-III is largely dominated by the uncertainty on the simulated neutron yield in lead.

A comparison of the μ-induced neutron yield for different versions of GEANT4 and physics lists has been done in [118] using a mono-energetic μ-beam at 260 GeV directed on a lead block. It was notably shown, using the GEANT version 4.9.5p01, that the `Shielding` list produces a higher neutron yield of about 15% compared to the `QGSP_BIC_HP` list. More generally, the `Shielding` list exhibits the largest neutron yield compared to the other lists and shows the biggest increase in yield going from the GEANT4 v9.4 to v9.5. The increase is mainly due to the increased of neutrons produced in inelastic scattering of hadrons and in particular neutrons. This is also explained by the muon-nucleus interaction model: the scattering cross sections in both cases are the same but the π^+/π^- produced in the final state in earlier versions of GEANT4 is now replaced by a π^0 interacting further via Bertini intra-nuclear cascade. From these results, one expects a higher neutron yield produced in lead in the EDELWEISS-III simulation compared to the EDELWEISS-II one, leading to a higher μ-induced neutron background.

The question arises which physics list describes the data better. Several studied have been performed to assess the accuracy of the GEANT4 simulation to estimate the neutron yield in lead (see [83] for a review and references herein). Two recent measurements have been performed at a large slant depth, for the mean muon energies, which are of interest for this work. Firstly, a long-term measurement campaign of the neutron yield in lead using
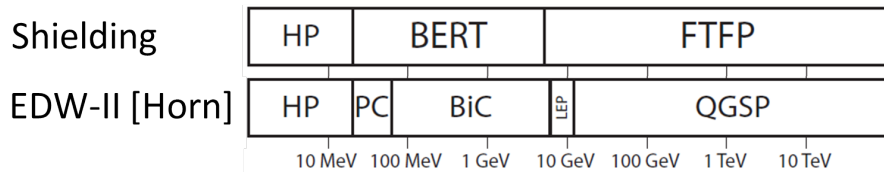
Figure 3.13. – Comparison of the models used to describe neutron inelastic scattering between the custom physics list used in EDELWEISS-II and the reference `Shielding` physics list used in EDELWEISS-III. The models used are: data driven high precision model `HP`; Bertini cascade `BERT`; FriTioF string model (`FTF`) using the Precompound (`PC`) model for nuclear deexcitation `FTFP`; Binary cascade `BIC`; low energy parametrization model `LEP`; quark-gluon string model (`QGS`) using the Precompound `QGSP`. Based on [83].

a dedicated neutron detector was performed at LSM, in the context of the EDELWEISS experiment [83]. The GEANT4 version 4.9.2p01 and the custom physics list defined in [33] were used to simulate the neutron yield. A deficit of 16% of the measured yield compared to the simulated one was obtained. Another comparison between simulated and measured data was performed using the ZEPLIN-III dark matter detector, located at the Boulby Underground Laboratory at a depth of 2850 m w.e.. The mean muon energy of 260 GeV [120] is similar to the mean energy of muons at LSM. The GEANT4 version 4.9.5p01 together with this `Shielding` physics list were used in [118] to compare the neutron yield in lead measured with the simulated one. An excess of 26% of the measured neutron yield compared to the simulated one was derived. In the following, these two values will be used as systematic uncertainty $\left(\begin{smallmatrix}+26\%\\-16\%\end{smallmatrix}\right)$ on the simulated neutron yield in EDELWEISS-III.

3.4.2. Simulations of muons in the EDELWEISS-III experiment

3.4.2.1. The muon generator

The role of the muon generator is to provide the starting position $\vec{r_{\mathrm{s}}}$, direction $\vec{w_{\mathrm{s}}}$ and energy E_{s} of the simulated muons. In the case of EDELWEISS, a custom generator developed in [33] and improved in [83] is used and will be briefly reviewed here.

The muon generation follows three steps. Firstly, the local muon flux is parametrized considering the energy loss in the rock and the angular distortion due to the Earth's curvature. Secondly, the probability density function associated with the muon flux parametrization are constructed and sampled. In a third step, the actual position $\vec{r}$, direction $\vec{w}$ and energy E of the muon are chosen. The muon is then started from a hemisphere $\mathcal{H}$ of $h_0 = 30$ m radius centred on the LSM hall (see fig. 3.14) and propagated through the rock and the experimental setup using GEANT4. Each of these steps is briefly described below. The parametrization of the muon flux on the hemisphere $d\Phi_r/dE_r d\Omega$ (where the index r stands for rock) can be related to the muon flux $d\Phi_0/dE_0 d\Omega_0$ at the Earth's surface via the coordinate transformation:

$$\frac{d\Phi_r}{dE_r d\Omega} = \frac{d\Phi_0}{dE_0 d\Omega_0}\frac{dE_0}{dE_r}\frac{d\Omega_0}{d\Omega} \tag{3.20}$$

As input of the simulations, the energy range of muons at their starting position on the hemisphere $\mathcal{H}$ and a number of energy bins to be considered have to be provided. For each local energy bin E_r, the corresponding energy at the Earth's surface is calculated by applying the CSDA approximation introduced in eq. 3.6. The validity of such approximation has been shown in [83] by comparing the results of the muon generator with the Fréjus measurement [116]. The rock thickness crossed by a muon with a given direction is
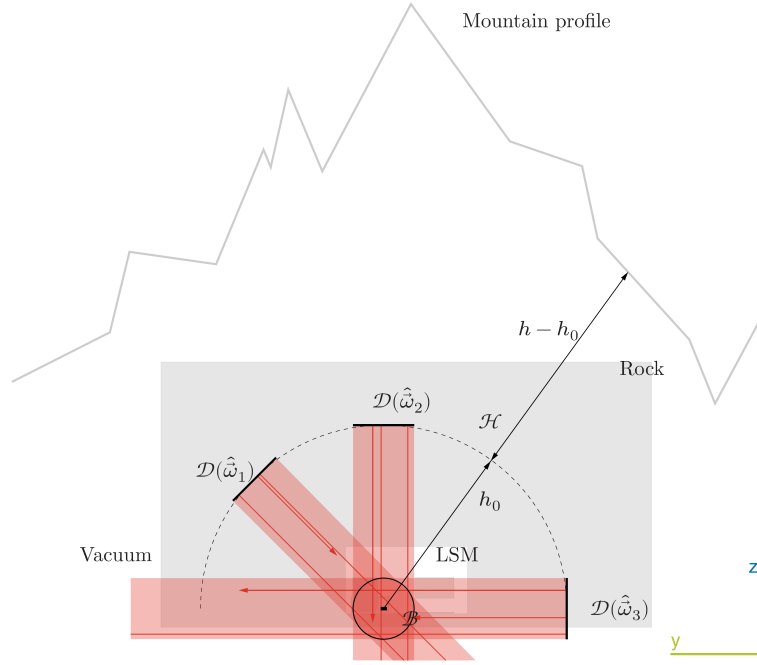
Figure 3.14. – Illustration of the muon generator in the $y-z$ plane. The implemented rock is shown as a light gray shaded area and the LSM hall in white shaded area. The muons are started on a plane disk $\mathcal{D}$ lying on an hemisphere $\mathcal{H}$ of radius h_0. As example, 3 muons are shown (red lines) for three directions w_1, w_2 and w_3 (red shaded areas). The intersections of all muons illuminate homogeneously a ball $\mathcal{B}$ in which the μ-veto system is included. At the exception of the illustrative mountain profile, the dimensions are to scale. Extracted from [83].

derived from the mountain profile map $h(\theta, \phi)$ with $1°$ angular resolution provided by the Fréjus collaboration [121]. As muons reaching the LSM are relativistic, the deflection of a muon in the rock is neglected and the muon direction at the Earth's surface is considered to be the same as the direction at LSM. Knowing E_0 and $d\Omega_0$, the differential muon flux at the Earth's surface $d\Phi_0/dE_0 d\Omega_0$ can be described using the Gaisser parametrization introduced in eq. 3.2, corrected for the Earth's curvature by introducing the zenith angle θ^* of primary particles on the top of the atmosphere. θ^* transfers to a zenith angle θ on Earth by considering the Earth's curvature following $\sin(\theta) = \sin(\theta^*)\frac{R_E+H_{int}}{R_E}$ with the Earth's radius $R_E = 6600$ km and the mean interaction height of primary particles in the atmosphere of $H_{int} = 18.6$ km. The subsequent correction in the element of solid angle $d\Omega_0 = \sin\theta_0 d\theta_0 d\phi$ is implemented in the local muon flux parametrization.

Once the muon flux has been parametrized, a probability density map is constructed by integrating the differential muon flux over each energy and angular bin, their binning parameter defined as input by the user.

Lastly, the start parameters of the muon E_s, Φ_s and of zenith angle Θ_s are derived randomly according to the probability density distribution. To increase the efficiency of the simulation, the volume homogeneously illuminated by the incident muons is restricted from the LSM experimental hall to a ball $\mathcal{B}$ of radius $d = 5$ m centred on the setup, as can be seen in fig. 3.14.

The correctness of the muon generator has been verified in [83] by comparing the data of the Fréjus experiment [116] and the output of the generator folded with the Fréjus detector response. As can be seen fig. 3.15, the zenith and azimuthal angular distributions obtained from both show good agreement. These distributions reflects the profile of the mountain

above the LSM, which is located inside the Fréjus tunnel crossing the Alps almost from north to south. The maximum of the zenith angle distribution at $\Theta = 35°$ corresponds to the smallest rock overburden at the mountain flanks. The azimuthal distribution is expressed in the coordinate system of the laboratory, corresponding to an offset of $\Phi = 16°$ to the north direction. As can be seen, more muons reach the lab from the north-south direction i.e. from the valleys, where the rock thickness is minimal. Along the mountain range in the east-west axis, the muon flux is the smallest. Note that an additional cross-check of the muon generator output using the EDELWEISS-II data was performed in [32] and also showed a good agreement between the two.

(a)

(b)
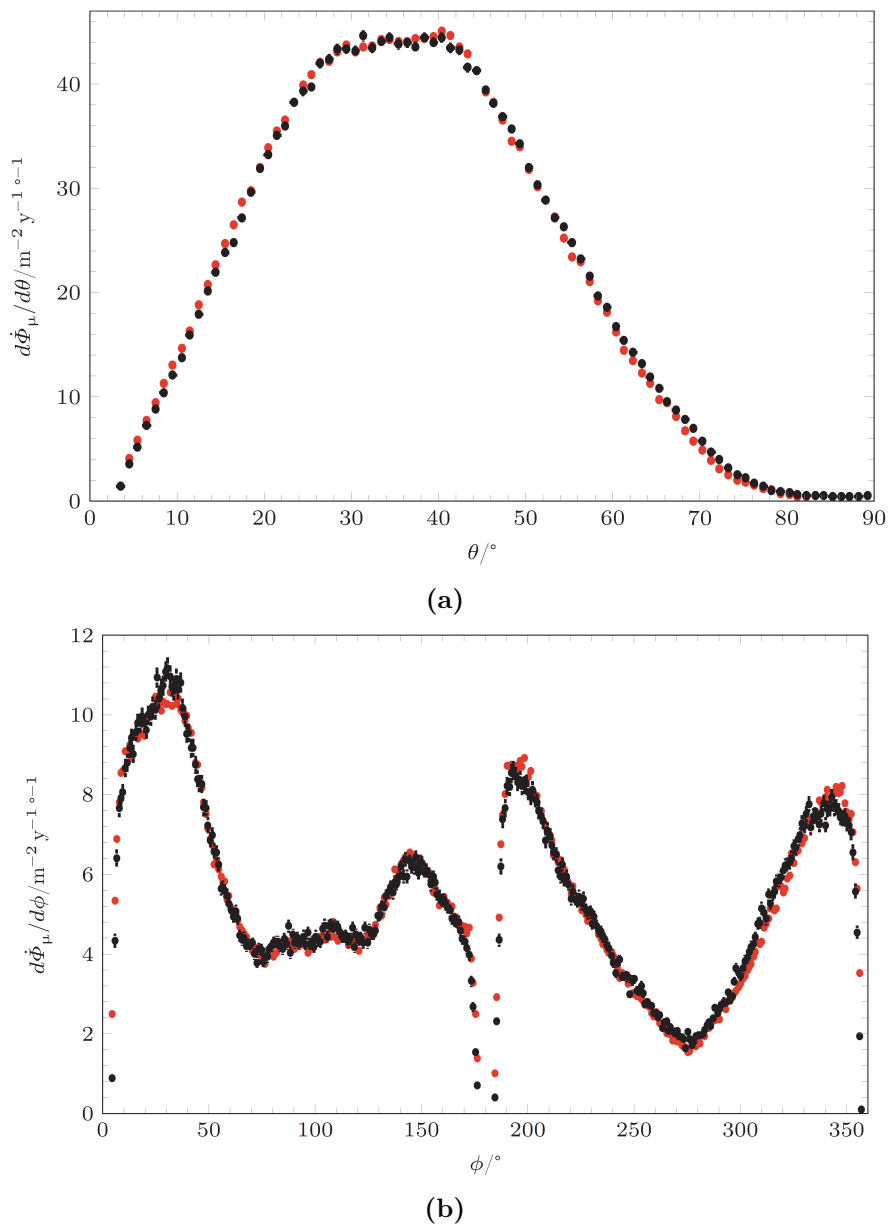
Figure 3.15. − Differential muon flux (a) versus the zenith angle Θ and (b) versus the azimuthal angle Φ, as simulated with GEANT4 with the muon generator described in [33, 83] (black) and as measured by the Fréjus experiment (red) [116]. See text for more details. Extracted from [83].
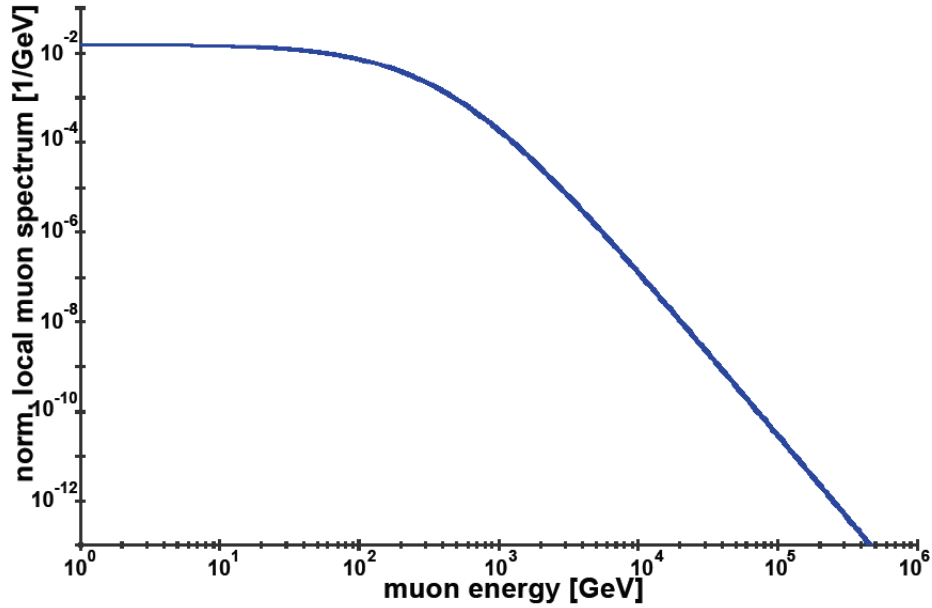
Figure 3.16. − Local energy spectrum of muons at LSM normalized to unity. Extracted from [33].

3.4.2.2. Simulation of the local muon flux and its normalization

The method applied to simulate the local muon flux in the framework on this thesis follows the method described in [83].

Local muon flux at LSM

As explained in section 3.1.3, μ-induced neutrons can be both produced by low energy muons via capture of μ^- on a nucleus, as well as by high energy muons interacting with matter via muon-nuclear interactions. The simulated muon spectrum should therefore cover a wide range of energies to ensure a proper estimation of the μ-induced neutron background. However, the energy spectrum of muons underground is a steeply falling spectrum (see fig. 3.16) following the energy distribution of primary cosmic rays. To ensure enough statistics over the whole energy range, the simulation of muons is split into 4 sub-ranges from 2 GeV up to 20 TeV as listed in table 3.1. Muons below 2 GeV do not contribute to the muon spectrum at LSM as they get captured in the rock or decay before reaching the experimental hall. The contribution of muons above 20 TeV is well below 0.01% and is therefore neglected. Note that the initial energy of muons given as input of the simulation, is the energy range of muons at their starting point, i.e. on the hemisphere of 30 m radius centred on the LSM hall.

For each sub-range of energies, both μ^+ and μ^- are simulated as the neutron production via muon capture on nuclei depends on the charge of the muon. A ratio $\mu^+/\mu^- = 1.37$ is considered at the depth of LSM, as it is the measured ratio for atmospheric muons with a minimal energy of 2.5 TeV, necessary for a muon to reach the LSM [84].

The contribution of each sub-range of energies and each muon type to the muon flux at LSM was derived in [83]. It was calculated by multiplying the contribution of each energy range to the total energy spectrum, with the muon charge ratio and the muon transmission probability from the hemisphere to the LSM cavern. The results of these calculations are listed in table 3.1.

Table 3.1. – Partition of the initial energy spectrum of muons into 4 energy sub-ranges. The contribution of each energy range to the total muon flux is given. Based on [83].

Muon type	Energy range (in GeV)	Contribution to the μ flux (in %)
μ^-	$2 - 20$	2.0
	$20 - 200$	24
	$200 - 2 \times 10^3$	15.7
	$2 \times 10^3 - 2 \times 10^4$	0.4
μ^+	$2 - 20$	2.7
	$20 - 200$	33.0
	$200 - 2 \times 10^3$	21.5
	$2 \times 10^3 - 2 \times 10^4$	0.5

Normalization of the simulation

For each simulation, the measurement time corresponding to the number of simulated muons should be derived. This is possible by counting the number of muons through a surface and by dividing it with the expected muon flux at LSM. Two published measurements of the muon flux at LSM exist: one derived using data from the Fréjus experiment and the other using EDELWEISS-II data.

First, it should be noticed that several definition of a particle flux co-exist. One can calculate it by counting the number of particles crossing a plane of either direction, per unit area da and unit of time dt. On the other hand, the ICRU defines it as the quotient of the number of particles dN incident on a sphere of cross section area da during the time interval dt [122]. Using a sphere as reference is the simplest way to always consider an area perpendicular to the direction of a particle independent of its incoming direction. In addition, the effective detection area, which is equal to the sphere cross section da, is the same for all zenith angles. This approach is equivalent to take a horizontal plane as reference and project it on the incoming direction of the particle. In this case, the effective detection surface decreases with increasing zenith angle θ.

Knowing that different definitions of the flux exist, we should be particularly careful when comparing flux values of different experiments. The number of particles crossing a plane is proportional to $|\cos(\theta)|$ with θ the angle between the direction of the particle and the direction perpendicular to the plane. Therefore, the muon flux through a sphere is higher than the muon flux through a plane for all angular distributions of particles. In the case of the muon flux determination at underground laboratories, choosing a sphere as reference is more relevant as the angular distributions vary significantly according to the mountain profile, as shown in fig. 3.15a and fig. 3.15b.

The first muon flux measurement at LSM was performed in 1989 by the Fréjus experiment [123]. This proton decay experiment had the particularity that its horizontal surface of $6\,\text{m} \times 12.3\,\text{m}$ was bigger than the typical average distance of $3.3\,\text{m}$ between a muon and its shower axis. Due to a position resolution of $5\,\text{cm}$ [123], it allowed separation of closed pack muons and correction for detector size effects. A high statistic of 407 775 single muons and 12 559 so-called *muon bundles* has been achieved. Muons with a zenith angle $\theta < 60°$ were cut from the data set as a precise knowledge of the mountain topography could not be guaranteed above this angle [116]. The detector threshold of $300\,\text{MeV}$ was excluding most of secondary muons produced by the hadronic shower of the muon in the rock. Thus, the measured rate of $\mu - \text{event}$ was:

$$\phi_{\text{Fréjus}}^{\mu\text{-event}} = 4.98\,\mu\text{-events/m}^2/\text{day} \tag{3.21}$$

This rate gives the number of triggers per day which can be attributed either to single muons or to muon bundles, and can be distinguished due to the high spatial resolution of the detector. The rate of single muons was derived to be $4.73\,\mu/m^2/$day and the rate of all muons, defined as $\dot{\phi} = \sum_{i=1}^{10} m_n \times \phi_n$, was derived to be $5.31\,\mu/m^2/$day [116]. However, it was not possible to state with certainty which reference surface was used to determine these fluxes, despite discussions with former members of the Fréjus collaboration and attempts of reverse engineering summarized in [83]. The favoured hypothesis is that the Fréjus flux was derived through a sphere.

An additional estimation of the flux was done using the EDELWEISS-II μ-veto data, as described in section 3.2.4.2, giving a muon flux through a horizontal surface of:

$$\Phi^{\mu}_{\text{EDW-II}} = 5.4 \pm 0.2 \text{ (stat)}^{+0.5}_{-0.9} \text{ (syst) } \mu/\text{m}^2/\text{day} \qquad (3.22)$$

A comparison of the EDELWEISS-II measured flux with the Fréjus value was performed in [32]. As it is not possible to distinguish between single and multiple muons with EDELWEISS-II, the measured flux has to be compared with the rate of μ-events measured by the Fréjus experiment. Simulations were performed to correct the Fréjus measurement for the zenith angle cut $\theta < 60°$. The correction for the energy threshold of $300\,\text{MeV}$ was not necessary as the probability that a secondary muon of such low energy satisfies the muon selection criteria used in EDELWEISS-II is low. Assuming the Fréjus result was derived for a horizontal surface, the correction for the zenith angle cut increases the total μ-event rate $5.2\,\mu$-events/m^2/day, to be compared with the value given in eq. 3.22. The EDELWEISS-II flux is 3.7% higher than the Fréjus flux but the two values agree within uncertainties. Now, assuming that the Fréjus flux of $5.2\,\mu$-events/m^2/day was obtained using a sphere, it can be converted in a flux through a horizontal surface using a conversion factor derived in [32] from simulations. The flux then decreases down to 4.13 μ-events/m^2/day. The muon flux measured in EDELWEISS-II exceeds the Fréjus flux by 23.5%. Considering the strong indications that the Fréjus flux was derived using a sphere as reference surface [83], the discrepancy between the two values remains and is considered as a systematic uncertainty.

For the simulations performed in the framework of this thesis, the Fréjus rate of μ-event given in eq. 3.21 was chosen to normalize the simulations. Indeed, the Fréjus result is based on a high statistics of muons and the detector response has been extensively studied to correct its effects on the measured flux. As explained in section 3.2.4.2, large systematic uncertainties on the EDELWEISS-II flux arise from the uncertainties on the detector response and the selection criteria, as the experiment was less adapted for the study of the muon flux.

3.4.2.3. Implementation of the bolometer response

The output of each simulation is written in a ROOT file [112] containing information about each single interaction in a sensitive volume, i.e. in the μ-veto system and in the Ge detectors. However, the responses of the detectors are not included in the simulation and have to be applied afterwards. The implementation of the position-dependent response of the μ-veto modules will be described in chapter 4. Therefore only the implementation of the bolometer response is discussed in the following.

GEANT4 splits each particle track in multiple steps, the step length depending on the particle type and its cross section in the crossed material. For each single energy deposit by a particle, the following information is recorded: the 3D position of the single energy deposit; the name of the bolometer in which the particle interacted; the type of particle interacting; the process responsible for the energy loss; and the relative time compared to the beginning of the event. This information is then used to build the total energy deposit

Table 3.2. – Number of simulated muons for each energy sub-range and type of muons and corresponding simulated time in years using the Fréjus as reference for the normalization of the simulation.

Muon type	Energy range (in GeV)	Nb simulated μ (in 10^6 events)	Simulated time (in years)
μ^-	$2 - 20$	3	380.9
	$20 - 200$	4	109.0
	$200 - 2 \times 10^3$	6	249.7
	$2 \times 10^3 - 2 \times 10^4$	0.59	971.1
μ^+	$2 - 20$	3	259.2
	$20 - 200$	4	79.4
	$200 - 2 \times 10^3$	5.95	180.9
	$2 \times 10^3 - 2 \times 10^4$	0.6	721.4

in the bolometer, distinguishing between electronic and nuclear recoils. To compare the simulated data with the measurement, the output of the simulation needs to be modified to imitate the bolometer response: first, the single energy deposits in each bolometer are summed according to their recoil type. Then, the heat and ionization energies are calculated taking into account the ionization quenching (parametrized as in eq. 2.6) and the Neganov-Luke effect (defined in eq. 2.9) induced by the applied electric potential, as well as random fluctuations with the energy-dependent resolution of each channel. Another key point needed to compare the simulation with measurement is the fiducialization of the detector volume. As the electrodes and the electric field configuration are not implemented in the GEANT4 simulation [5], a geometric definition of the fiducial volume is used to classify an event. For this, the fiducial volume is approximated by a cylinder, whose size can be chosen independently for each detector as input of the event building software. While the mass of a detector varies between $820\,\mathrm{g}$ and $889\,\mathrm{g}$, all the bolometers have been simulated with the same mass of $817\,\mathrm{g}$. The size of the cylinder delimiting the fiducial volume was adapted to the measured fiducial mass, which varies from 68% to 89% of the total detector volume.
An energy deposit in a bolometer is considered to trigger when the total heat energy is above the average trigger threshold $\langle E_{th} \rangle$.

The EDELWEISS-III simulation package presented here will be used to derive the results described in this thesis: first, to extract the individual responses of the μ-veto modules using an AmBe source, by comparing the simulated and measured energy spectra (chapter 4); secondly, to compare the topology of μ-induced bolometer events between data and simulation, as well as the rate of coincidences between the μ-veto and the bolometer array (chapter 5); lastly to estimate the μ-induced background for dark matter search in the standard and low mass WIMP analyses (chapter 6).

---

5. The simulation of charge migration, from which fig. 2.4 was derived, is performed independently using a custom MATLAB-based simulation software.

4. Determination of the muon-veto efficiency using an AmBe source

To estimate the untagged muon-induced background for dark matter search, the efficiency of the μ-veto has to be derived accurately. This estimation relies on the detailed knowledge of the trigger threshold of the 46 individual modules making up the μ-veto. These modules have been calibrated at the Earth's surface using cosmic muons in 2003 [101]. Since then, the plastic scintillator as well as the signal read-out electronics have aged significantly. Despite attempts to correct for ageing effects, the individual trigger thresholds may worsen inhomogeneously with time and have to be monitored. One of the drawbacks of going underground to shield the experiment against cosmic rays is that muons cannot be used for monitoring anymore, as their flux is too low to give sufficient statistics. Therefore new alternative methods had to be developed.

In EDELWEISS-II, the module response was extracted from low energy μ-veto data, mostly arising from radioactive backgrounds in the μ-veto [32]. Although the response strongly depends on the position of the interaction along the module axis, this method only gives an average over all hit positions. In addition, it is limited by 20% systematic uncertainties assumed on the energy calibration (see section 3.2.4.1). Therefore a new method using an AmBe source was set-up in the framework of this thesis to derive the position-dependent trigger threshold. The goal of this method is to extract the unknown parameters characterising the module response for a given position along the module axis. This can be achieved by comparing the measured energy spectrum obtained with the AmBe source, with the simulated spectrum convoluted with the module response. A maximum likelihood analysis is used to derive the set of parameters giving the best match between the two. By repeating it for several positions along the module axis, the trigger threshold can be extrapolated. The modular muon detection efficiency can then be derived by applying the position-dependent response on the simulated energy spectrum of muons.

The first section of this chapter (4.1) is dedicated to the measurement campaign of the μ-veto modules at LSM using an AmBe source. The strong position-dependent response of the modules to AmBe data is illustrated in particular. In the second section 4.2, the work performed to accurately simulate the AmBe measurements using the GEANT4 software is described. The modelling of the module response applied on the simulated data is detailed in section 4.3. The binned maximum likelihood analysis performed to derive the set of parameters describing the best the data is explained in section 4.4. To estimate the uncertainty on these parameters, a Monte Carlo Markov Chain was used and is described in section 4.4.6. The modular detection efficiency and its uncertainty are then derived. The

complete method is illustrated with one module of the μ-veto system. An outlook on how this method could be used to extrapolate the total μ-veto efficiency from the efficiencies of individual modules concludes this chapter.

4.1. Measurement of the AmBe data

4.1.1. Measurement campaign at LSM

The source used to probe the individual trigger thresholds is an AmBe source at disposal at LSM. It is usually used as a neutron source to study the response of Ge detectors to nuclear recoils, but is used in the context of this study for its high-energy γ's. A neutron is produced when an α produced by the ^{241}Am decay is captured by a ^{9}Be nucleus. The resulting ^{13}C is produced in an excited state such that a neutron is always evaporated. Depending on the energy carried out by the evaporated neutron, the resulting ^{12}C isotope is produced either in its ground state or in its first excited state. In the later case, a high energy γ of 4.4 MeV energy is emitted by the ^{12}C during the transition to its ground state. More details about the working principle of the AmBe source will be given in section 4.2.1 when discussing its implementation in the simulation.

The AmBe γ's are particularly suited to probe the trigger threshold, as its average over the module length was estimated in EDELWEISS-II to be around 4 to 5 MeV (position-dependence described in section 3.2.2.3 and 3.2.3). Note that the neutron contribution and the rather limited energy resolution of the plastic scintillator allow the detection of the source even if the γ-peak is below the threshold.

The weak point of the EDELWEISS source is its low activity, chosen on purpose not to activate the Ge crystals in a calibration measurement. It was measured with γ-spectroscopy using a NaI(Tl) detector [124]. The activity of the source was deduced by integration of the 4.4 MeV γ photopeak and the two escape peaks, and compared with simulation of the experimental setup to include the detection acceptance. Assuming a γ-ray to neutron ratio of 59.1±2.6% [125], the activity of the source was calculated to be:

$$\mathcal{A}_\gamma = 12 \pm 2 \ \gamma/\text{s, and} \ \ \mathcal{A}_n = 21 \pm 4 \ \ \text{neutrons/s} \qquad (4.1)$$

Note that the uncertainty on the γ-ray to neutron ratio is large considering the difficulty to measure low energy neutrons. The ratio used to derive the activity of the EDELWEISS source is in reasonable agreement with the results obtained by other groups and with the calculated ratio (56.6±5.7%) using cross section and stopping power data [125].

To determine the position-dependent module response, the source was mounted on three positions along the longer axis of the module: at the center and at 50 cm distance from each of the module ends, always in the center along the width of the module. The calibration at the central position requires $\sim$ 2 days of measurement and the calibrations near the ends $\sim$ 6 days, with significant variations from one module to another depending on the trigger threshold. The number of calibrated positions per module is limited by the long measurement time required and by the isotropy of the source. Some attempts were nevertheless made to collimate the source with a hollow lead cylinder of 4 cm thickness, open on the side facing the module and closed on the other, in which the source was placed. However, both the simulation and the test measurement showed that it does not significantly improve the collimation whereas it significantly prolongs the needed measurement time. For practical reasons, the final measurements were performed with the source placed inside a hollow stainless steel cylinder of 2 cm thickness. The cylinder was fixed on a camera tripod, with the opening facing the module. With this installation, all modules could thus be reached, including those on the top of the μ-veto. In addition, it allowed approximately the same source orientation for all measurements. Note that for the calibration of the modules of the top of the μ-veto, the cylinder was placed lying on its side.

The calibration campaign took place from the end of the year 2012 until the end of July 2015. Despite this long campaign, calibration data could not be acquired for all modules of the μ-veto for several reasons. First, due to the low activity of the source, two weeks are needed in average to calibrate one of the 46 modules of the μ-veto. It was attempted to buy a more active source (with a higher activity in α's) but its transportation to LSM as well as its storage would have been problematic. Moreover, for an underground laboratory like the LSM, the limitation on the α activity is too strict to allow a significantly more active source than the one in use: in case of fire, the ^{241}Am of the source could be evaporated in the laboratory air and would present a danger for the fire brigades. A second reason is linked to constraints associated to operations in the special environment of the LSM, which explains in part why the calibration time on some modules was extended to ~ 3 weeks. And lastly, calibration with a neutron source in the vicinity of the cryostat is of course not possible while WIMP search data is acquired. Therefore not all modules close to the cryostat have been calibrated (*Level 1* of the μ-veto system). These constraints on the calibration planning led to the following outcome: 23 out of the 46 modules of the μ-veto have been fully calibrated. The remaining modules were not calibrated at all or only partly for various reasons: four out of the five modules making up the floor of the μ-veto were not accessible. Three modules had such a high trigger threshold that the source could not be detected. Due to a lack of time, seven modules in the clean room could not be calibrated and nine modules only partly.

4.1.2. Module response to the AmBe source

To show why measurements with an AmBe source are suited to determine the effective trigger thresholds, the energy spectra measured for the three positions of the source are compared below. For illustration, the data taken with the module M42 (long side of the module along the north-south axis) is studied. This module shows a homogeneous response of both its PMTs groups and a low trigger threshold, and is therefore used as illustration. The source was placed at the center of the module for ~ 2 days and at $50\,\mathrm{cm}$ from the north and south ends for ~ 6 days each. The side positions will be called hereafter *north* (*south*) position for simplification. The arrival time of the PMT pulse and the energy measured by each group of PMTs will be hereafter denoted according to the geographic orientation of the PMT group i.e. t_N (t_S) and $\mathrm{ADC_N}$ ($\mathrm{ADC_S}$) respectively.

First, the distributions of the difference in arrival time of the signal $\Delta t = t_N - t_S$ for the three positions of the source are shown in fig. 4.1. A TDC channel, corresponding to $0.8\,\mathrm{ns}$, has been measured to be equivalent to $(5.6 \pm 0.1)\,\mathrm{cm}$ [101]. The distributions for the side positions are normalized to the measurement time for the center position. Note that the center of the module does not coincide with $\Delta t = 0$. There is a shift of 6 TDC channels (corresponding to $4.8\,\mathrm{ns}$) which can be explained by a systematic delay of the signal from the north PMT group in the electronics chain. The contribution of background particles to the Δt spectrum is negligible.

The number of measured events strongly varies with the position of the source. For the same measurement time, it is 9 (7) times larger for the center position than for the north (south) position. This behaviour is due to the position-dependent effective threshold, discussed in section 3.2.3. Due to the trigger conditions, the count rate is highest for the center position where the threshold is lowest, and decreases towards the module ends as the threshold rises exponentially. As the energy of the AmBe γ's is close to the trigger threshold, a slight variation of the threshold induces a strong variation in the number of triggered events. As for the difference in trigger number between the two module ends, it reflects the inhomogeneity of the response from one PMT group to the other. As explained in section 3.2.3, the PMT group which is the furthest away from the energy deposit is responsible for the trigger. One can then deduce that the PMT group on the north side has a lower threshold or a worse energy resolution than the PMT group at the south side.
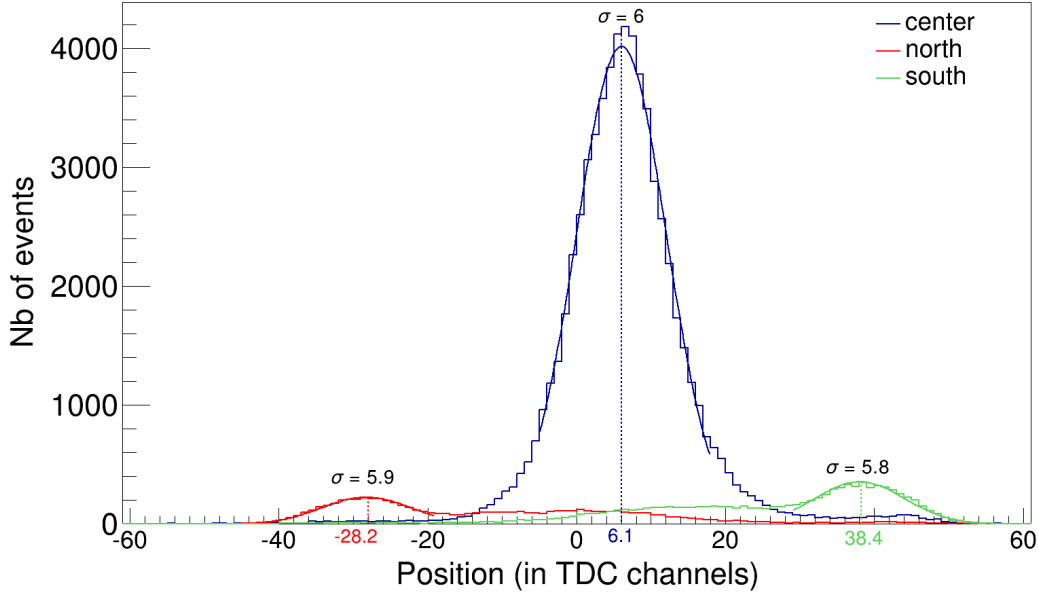
Figure 4.1. – Distributions of the difference in arrival time of the two PMT signals $\Delta t = t_N - t_S$ for the source at the center (blue histogram), at the south end (green histogram) and at the north end (red histogram) of the module M42. The distributions for the side positions are scaled to the measurement time at the center (2 days). For each position, the spread of the source is fitted with a gaussian distribution. Errors on the fit parameters are <1% and therefore not quoted.

To conclude, the number of events triggering the acquisition is a strong indicator of the effective trigger threshold.

Concerning the shape of the Δt spectrum shown in fig. 4.1, each distribution is made of a Gaussian component centred at the source position, with a width of $\sigma \simeq 6$ TDC channels corresponding to 33 cm [101]. For the side positions, there is an additional shoulder of events going towards the furthest PMT group. Despite fewer particles deposit energy that far, the trigger probability is higher as the distance to the furthest PMT group (which is leading the acquisition) is smaller. This effect is not seen for the center source position: the probability to trigger is highest at the center (as the distance to both PMT groups is minimal) and diminishes exponentially with the distance to the furthest PMT group. In addition, the threshold curve is steeper at the module ends than at the center, leading to larger threshold variations for the side positions of the source.

To derive the effective trigger threshold for a given position of the source, the energy distribution of AmBe events in the module will be fitted and therefore need to be understood beforehand. Fig. 4.2a shows the energy distributions ADC_N, ADC_S and $ADC_N + ADC_S$ for the data taken with the AmBe source at the module center. The peak structure of the energy distributions should not be mistaken with the 4.4 MeV photopeak. As will be illustrated in section 4.3, it arises from the convolution of the smeared AmBe energy spectrum with the trigger threshold. The difference in shape between ADC_N and ADC_S distributions shows once more the inhomogeneities of the PMT group responses. The distribution of $ADC_N + ADC_S$ exhibits a low energy tail down to ~ 1200 ADC channels, a gaussian-like peak structure centred on ~ 1500 ADC channels and a high energy tail. This shape can be understood by plotting the total measured energy $ADC_N + ADC_S$ versus the position of the interaction along the module axis, as shown fig. 4.2b. The clear peak at ~ 1500 ADC channels mostly arises from energy deposits of the source at the center of

the module, with a spread for a given Δt driven by fluctuations of the energy deposit and energy resolution effects. The high energy tail is due to energy deposits closer to one of the PMT group, where the light output is larger. One can notably perceive the exponential rise in energy towards the PMT groups. Events with unphysical Δt outside of the physical boundaries of the module ($\Delta t \lesssim -40$ TDC channels or $\Delta t \gtrsim 50$ TDC channels including reflections) are mostly due to low energy background events with limited time resolution. The event population with $\Delta t \sim 45$ TDC channels is also arising from noise in the south PMT group.

Similar spectra are shown for the source positioned at the north end (fig. 4.3) and at the south end (fig. 4.4) of the module. As shown on the Δt distribution fig. 4.1, a burst of events at the source position and a tail towards the furthest PMT group can be distinguished. To understand their contribution to the energy distribution, the energy deposit measured by each PMT group individually is plotted versus the mean position of the interaction in figures fig. 4.3 and fig. 4.4 (see (b) and (c) for both figures). For both source positions, the energy distribution measured by the furthest PMT group (fig. 4.3a south and fig. 4.4a north) shows a peak structure at $E \sim 700$ ADC channels similarly to what was seen at the center. It arises from localized energy deposits at the source position, but also from energy deposits towards the center of the module. The spread in energy mostly characterizes the energy resolution of the PMT group. As for the high energy tail, it is clearly induced by rare events depositing energy close to the PMT group. The energy distributions measured by the PMT groups the closest from the source differ significantly. The spread in energy deposit at the source location is large (from ~ 1000 up to ~ 4000 ADC channels). This is due to the exponential decrease of the light output with the distance to the PMT group, plus the fluctuations in the path length of the light and energy resolution effects. Energy deposits towards the center suffer more from absorption and therefore contribute to the lower energy part of the spectrum. To conclude, the scintillation and collection efficiency are dominating the measured energy when an energy deposit occurs close to a PMT group, whereas the absorption is leading in the opposite case.
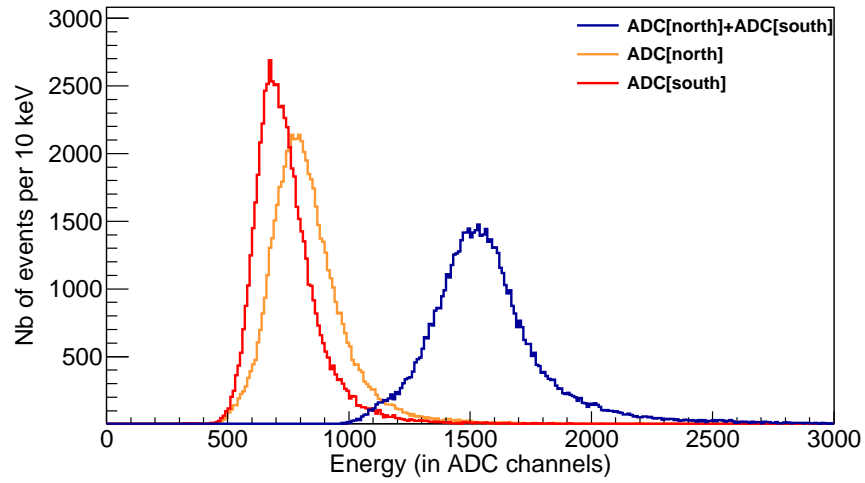
(a)
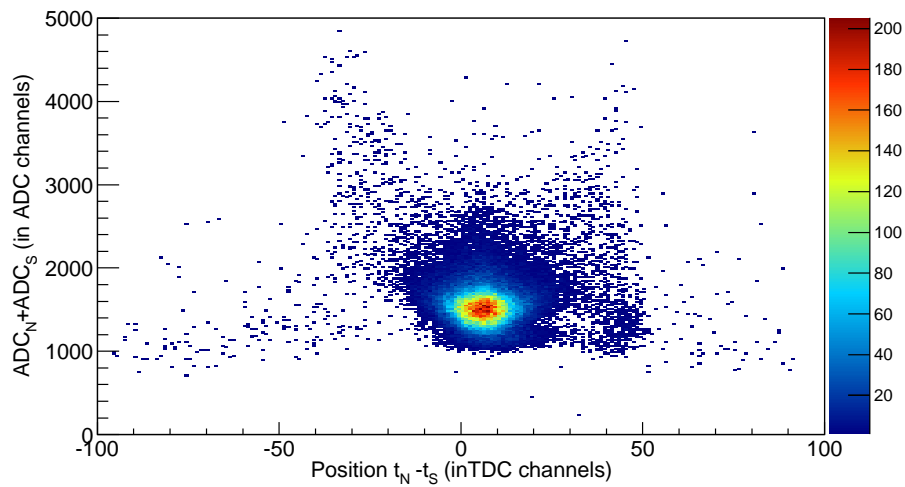
(b)

Figure 4.2. – AmBe data taken at the center of the module M42: (a) Distributions of the energy measured by the north PMT group (red), by the south PMT group (orange) and the sum of energies event by event (blue); (b) Total measured energy versus the mean position of the interaction along the module axis.

(a)

(b)

(c)
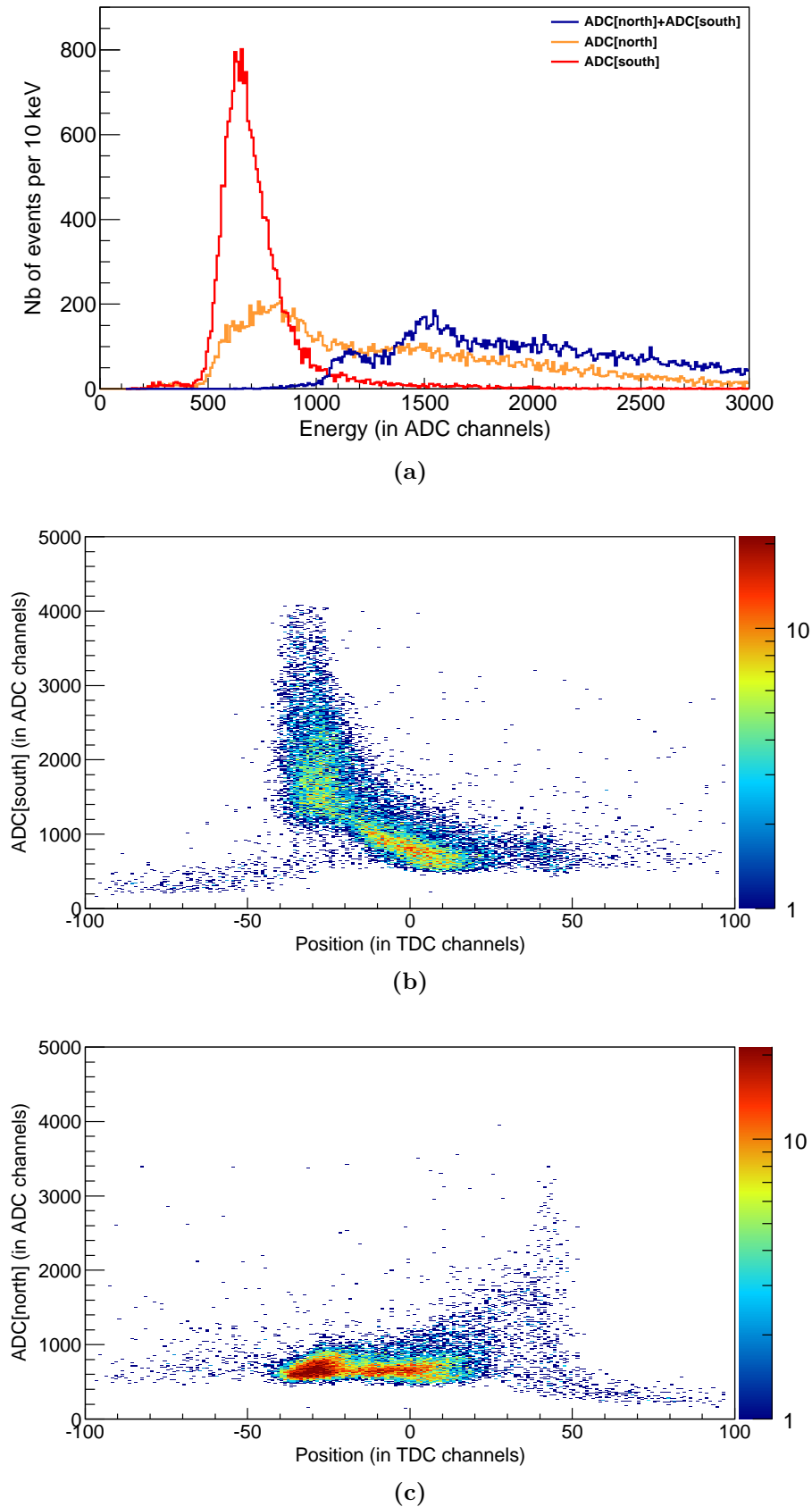
Figure 4.3. – AmBe data taken at 50 cm from the north end of the module M42: (a) Distributions of the energy measured by the north PMT group (red), by the south PMT group (orange) and the sum of energies event by event (blue); (b) Energy measured by the north PMT group versus the mean position of the interaction along the module axis; (c) Energy measured by the south PMT group versus the mean position of the interaction along the module axis.

(a)

(b)

(c)
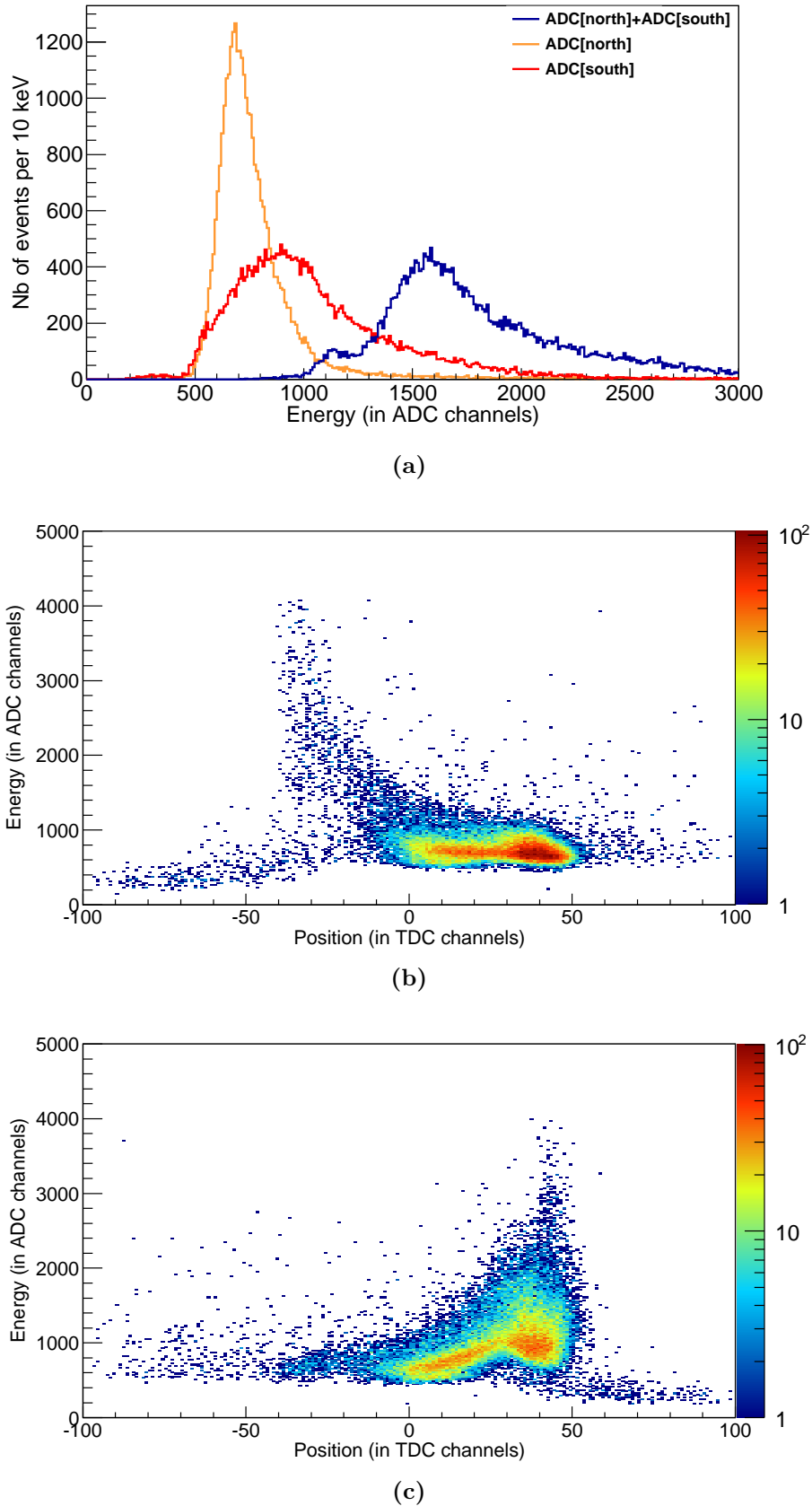
Figure 4.4. – AmBe data taken at 50 cm from the south end of the module M42: (a) Distributions of the energy measured by the north PMT group (red), by the south PMT group (orange) and the sum of energies event by event (blue); (b) Energy measured by the north PMT group versus the mean position of the interaction along the module axis; (c) Energy measured by the south PMT group versus the mean position of the interaction along the module axis.

4.1.3. Selection of data

The first step of this method is to derive an energy distribution characteristic of the position of the source. For this purpose, a cut is applied on the Δt distribution to remove energy deposits occurring away from the source position. This step is particularly important for the side positions, where the contribution from energy deposits towards the module center is significant. The spread of the uncollimated source is derived from the Δt distribution and can be approximated by a gaussian distribution centred on the source position. Events occurring outside of a $\pm 2\sigma$ interval from the source position are cut from the energy distribution.

Background and noise events also contribute to the measured energy spectrum with the AmBe source. They notably induce structures at low energies which can not be fitted by the simulated spectrum. The background energy distribution is extracted using a time period before or after the calibration, generally twice longer than the calibration time. It is then scaled to the measurement time and subtracted from the energy distribution measured with the AmBe source.

4.2. Simulation of the AmBe measurements

4.2.1. Implementation of the source in the simulation

The neutrons and γ's emitted by the AmBe source are correlated in time and energy. A simplified description of the source was already implemented in the EDELWEISS simulation package. Within this simulation, neutrons are created isotropically with energies between 0 and 11 MeV, and in 59.1% of the cases accompanied by a 4.4 MeV γ without restriction on the neutron energy. That means that a γ could be emitted in coincidence with a high energy neutron even if the sum of both energies violates the principle of energy and momentum conservation. This simplification is sufficient when the probability to measure a neutron and a γ in the studied detector is negligible. However, with the μ-veto, there is a significant probability to measure both as a large solid angle is covered by a scintillator panel. Consequently, the high energy tail of the simulated energy spectrum is not well reproduced. It is particularly important in this study as only high energies above the trigger threshold are measured. Therefore, a more accurate description of the AmBe decays has been implemented as part of this work. As various, and sometimes contradicting, descriptions of the AmBe source can be found in the literature, it is described in details in the following.

Description of the AmBe source

The AmBe source is an example of a $^9\mathrm{Be}(\alpha, n)$ neutron source which is based on a mixture of a radioactive isotope decaying via α emission and a low Z material with a high α capture cross section. The nature and properties of such sources have been widely studied since the early 1930's, mainly for two reasons. Firstly, the second excited state of $^{12}\mathrm{C}$ plays a key role in the nucleosynthesis in stars via multi-body breakup processes [128]. Secondly, these sources are widely employed as neutron sources, notably for detector calibration.

$^{241}\mathrm{Am}$ is an α emitter with a half-life $T_{1/2} = (432.7 \pm 0.5)$ years [129]. The α of 5.48 MeV kinetic energy is captured in approximately $1/10^4$ cases by a $^9\mathrm{Be}$ nucleus forming a $^{13}\mathrm{C}$ nucleus in an excited state [130]:

$$\alpha + {}^9\mathrm{Be} \rightarrow {}^{13}\mathrm{C}^* \tag{4.2}$$

The energy available in the final state is the sum of the Q-value of the capture process ($Q = 10.65$ MeV) and the remaining kinetic energy of the incoming α. Depending on this
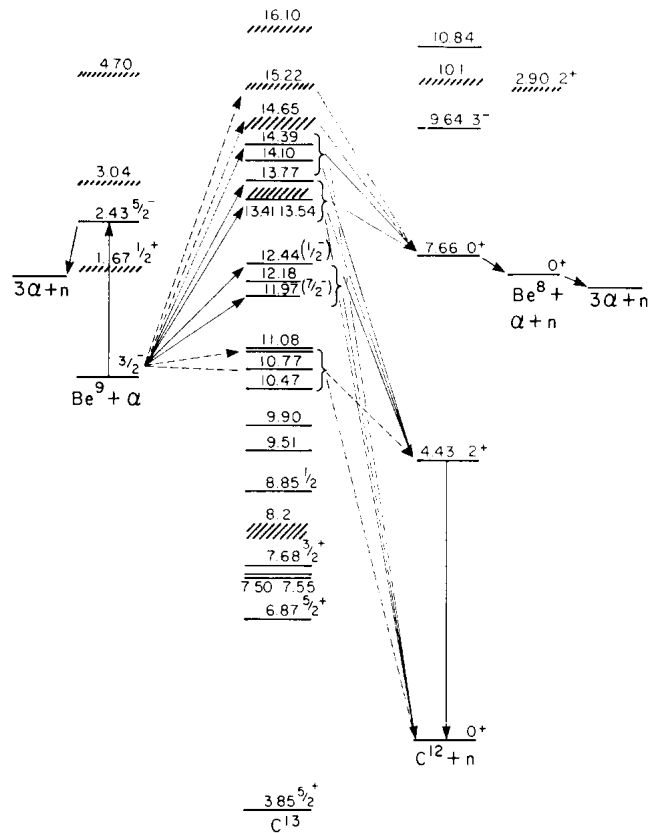
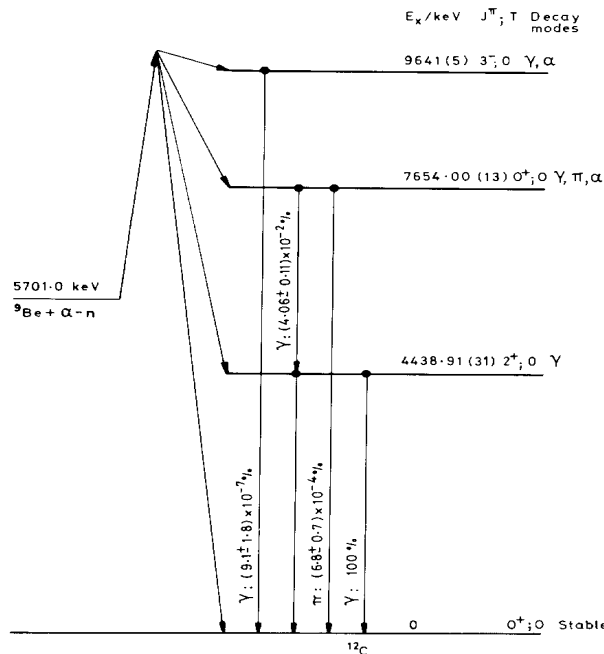**Figure 4.5.** – Excited nuclear states in the ^{9}Be(α, n) reaction. Extracted from [126].

Figure 4.6. – Energy level diagram for ^{12}C indicating electromagnetic transitions. Extracted from [125], based on [127].

energy, the ^{13}C nucleus is produced in an excited state with energies from 10.77 MeV to 15.22 MeV [126], as shown in fig. 4.5. As the excitation energy of the ^{13}C nucleus is always higher than the binding energy per nucleon (E_b=7.47 MeV), a neutron is emitted:

$$^{13}\text{C}^* \to {}^{12}\text{C}^{(*)} + n \tag{4.3}$$

Depending on the excited state of ^{13}C, the neutron production reaction will populate either the ground state, the first excited state (4.439 MeV) or the second excited state (7.654 MeV) of the residual ^{12}C nucleus [125]. Note that populating the third state (9.641 MeV) requires an α energy of at least 5.690 MeV, and therefore cannot be reached in case of the AmBe source. Consequently, 3 discrete neutron groups n_0, n_1 and n_2 can be distinguished, populating the ground state, the first excited state or the second excited state of the ^{12}C nucleus respectively (see fig. 4.5). The group of neutrons n_1 is always accompanied at a time $t = 61$ fs later, by a γ-ray of 4.4 MeV arising from the transition of the ^{12}C nucleus from its first excited state to its ground state (see fig. 4.6). The ^{12}C nucleus in the second excited state goes back to the ground state either directly via internal conversion, or by a cascade of two γ's at 3.2 and 4.4 MeV. However, it undergoes in ~99.96% of the cases a multi-body breakup [128]: the carbon nucleus decays into a ^{8}Be nucleus, a neutron (referred to as group n_b hereafter) and an α particle [131, 132].

$$^{9}\text{Be}(\alpha, \alpha^{'})^{9}\text{Be}^* \to {}^{8}\text{Be} + n \tag{4.4}$$
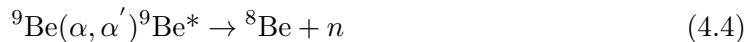
The energy distribution of each of the neutron groups n_0, n_1, n_2 and n_b is displayed in fig. 4.7 for several ^{9}Be(α, n) sources. The breakup neutrons n_b mainly contribute below 1.5 MeV. The importance of the multi-body breakup process is due to the fact that the direct transition between the second excited state and the ground state of the ^{12}C nucleus is forbidden because of spin conservation (both states are 0^+). The excited ^{12}C nucleus still has a low probability of $(4.06 \pm 0.01) \times 10^{-2}$% to decay to the ground state via the first excited state by emitting a cascade of two γ's of 3.2 and 4.4 MeV (see fig. 4.6. Additionally, it has a $(6.08 \pm 0.07) \times 10^{-4}$% probability to return to the ground state by internal conversion [127]. These rare but existing de-excitation processes explain why carbon is the fourth most abundant element in the Universe [128]. To explain the formation of carbon in stars, the astronomer F.Hoyle predicted the existence of resonances of the triple α process leading to the second excited state of the ^{12}C nucleus, also called the *Hoyle state*. Due to these de-excitation processes, the excited ^{12}C nucleus can decay to its ground state in ~0.04% of all cases instead of undergoing multi-body breakup reactions [128].

The neutron-alpha and neutron-gamma angular correlations in X(α,n)Y reactions have been studied to distinguish between different modelling of such interactions. They can notably be described by the compound nucleus model, or by stripping of the incident α-particle considered as a combination of a ^{3}He and a neutron, or stripping of a neutron of the target nucleus or by knock-on collision of the incident α on a loosely bound neutron of the target nucleus [133].

Implementation in the simulation

Within the framework of this thesis, an improved version of the AmBe source was implemented in the simulation. In the earlier simplified description of the source, the simulated energy was overestimated when a neutron n_0 was emitted in coincidence with a γ and underestimated when a neutron n_1 was not. Now, the neutron group of highest energy n_0 is never simulated in coincidence with a γ. On the contrary, the group of neutrons n_1 is always simulated in coincidence with a 4.4 MeV γ. For simplification, the angular correlation between the two is neglected here. The effect of this simplification might be small as neutrons scatter in the extended source of 3 cm long or in the surrounding materials, e.g.
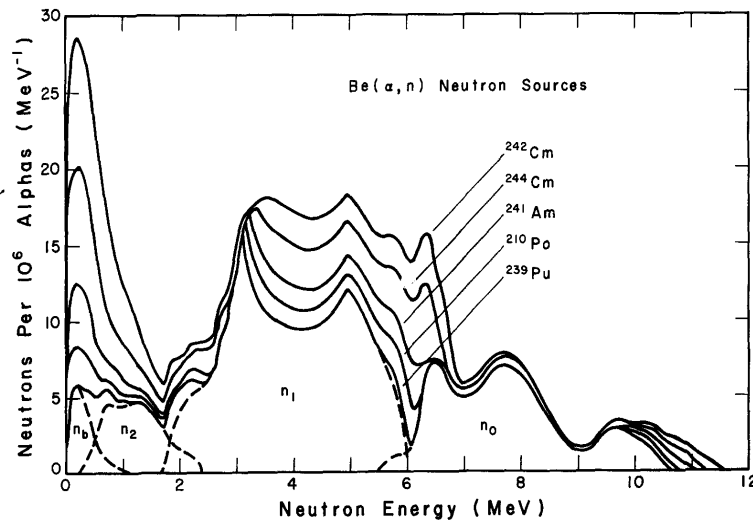
Figure 4.7. – Energy spectrum of neutrons from various $^9\text{Be}(\alpha, n)$ sources with the contribution from individual neutron groups. Extracted from [134].

in the lead capsule or in the steel cylinder holding the source, before being detected in the module.

The decay from the second excited state of the ^{12}C nucleus to the ground state via emission of a γ cascade and a low energy neutron n_2 is negligible in comparison to multi-body breakup reactions [135, 136, 137]. Therefore this decay was not implemented in the simulation for simplification.

References giving the individual energy distributions of the neutron groups were difficult to find in literature, whereas it is easy to find the overall energy distribution. For this study, it was estimated that a graphical extraction from [132] of the energy ranges in which each neutron group is dominant is sufficient. The energy range boundaries for neutrons n_1 in coincidence with the γ were adjusted for the γ/n ratio of 59.1±2.6% [125], used to determine the activity of the EDELWEISS source in [124]. The n_1 neutrons were therefore simulated between 1.8 and 6.2 MeV and the n_0 neutrons between 6.2 MeV and 11 MeV. This is summarized in fig. 4.8 showing the normalized energy spectrum of the simulated neutrons.

4.2.2. Simulation procedure

The AmBe source is simulated as a point source as its dimensions are small compared to the size of the module, isotropically emitting γ's and neutrons according to the description in section 4.2.1. The source is placed at the center of the hollow steel cylinder which is used to hold it during the measurements. The simulation source code was implemented to allow the 3D positioning of the source using an external macro file, simplifying the simulation of the hundred different possible positions of the source.

Each position of the source is simulated to derive the corresponding energy spectrum. In order to reduce computation time, the conversion of the energy deposit into scintillation light, as well as the light propagation until the module ends and the PMT response are not implemented in the simulation. Therefore the effects of the module response need to be modelled and applied to the simulated data (see section 4.3). Thus, no module response is taken into consideration in the simulation. The simulated energy in a module is only the sum of all energy deposits. Consequently, there is no significant difference between the energy spectra obtained at different positions along the module axis. The only factor of difference is the proximity of a material near the module which gets activated by the source. This is notably the case for the steel mounting structures.
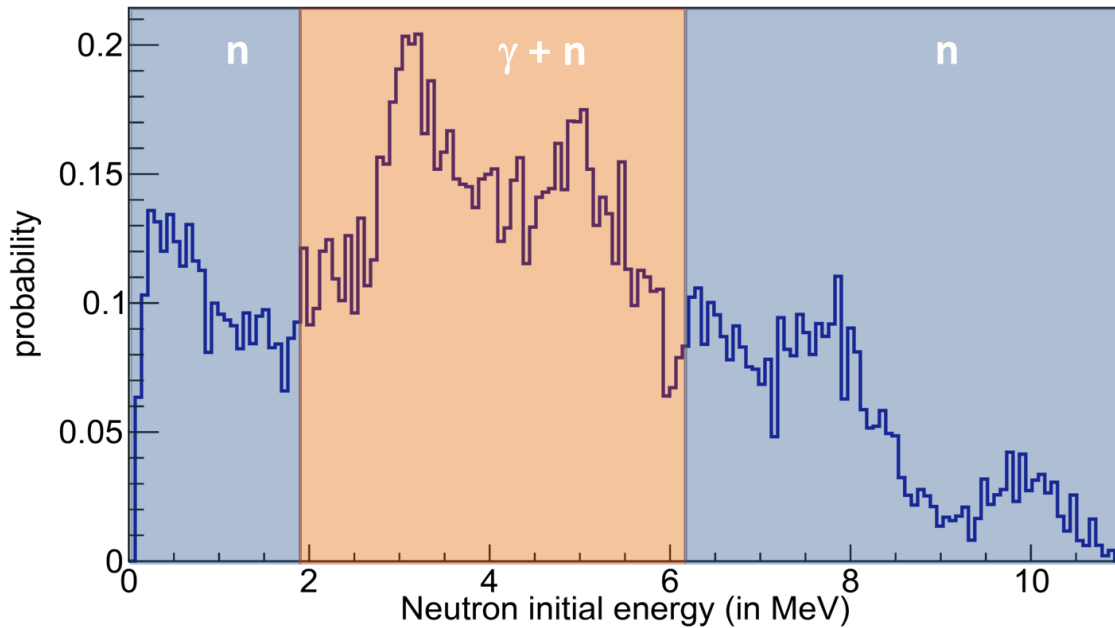
Figure 4.8. – Normalized energy distribution of AmBe neutrons as implemented in the simulation, with in red the energy range where a γ and a neutron are simulated in coincidence and in blue a neutron only.

The number of simulated neutrons and γ's is calculated for each position of the source from the known measurement time, the source activity in neutrons given eq. 4.1 and the branching ratio. As the measurement time is of few days, the number of simulated γ's and neutrons is of few million per position of the source. The dead-time associated to a particle trigger is neglected as only few per cents of the emitted particles actually trigger the acquisition.

4.2.3. Simulated energy spectrum without module response

An example of energy spectrum of total energy deposit (γ and neutron), obtained by simulating the AmBe source at the center of module M42, is shown fig. 4.9. Features of both γ and neutron energy deposits are visible. As illustration, fig. 4.10 gives the measured and calculated total cross sections for photon interactions on carbon with contributions from individual processes such as photoelectric effect, incoherent and coherent Compton scattering or pair production. In the MeV range and in light materials, the energy loss of γ's is dominated by incoherent Compton scattering, contributing to a continuous spectrum from 0 up to 4.4 MeV. As can be seen in fig. 4.10, photoelectric effect on carbon is negligible in the MeV range. More generally, the photoelectric effect cross section increases for high Z materials and rapidly decreases with the energy of the γ. Therefore, organic scintillator panels are particularly inefficient to stop high energy γ's from the AmBe source via photoelectric effect. However, as the module has a 5 cm thickness, there is still a high probability that a γ loses all its energy in the scintillator via successive Compton scatterings. It shows up as a pronounced shoulder at $E \simeq 4.4$ MeV in fig. 4.9. On the top of this shoulder, a peak at $E \simeq 4.15$ MeV can be distinguished, arising from backscattered γ's (Compton edge). The maximal energy loss of a γ of energy $E = 4.4$ MeV interacting with the medium occurs for a scattering angle of 180°and is given by the following formula:

$$E' = \frac{E}{1 + 2E/m_e c^2} \simeq 241.5 \, \text{keV} \tag{4.5}$$
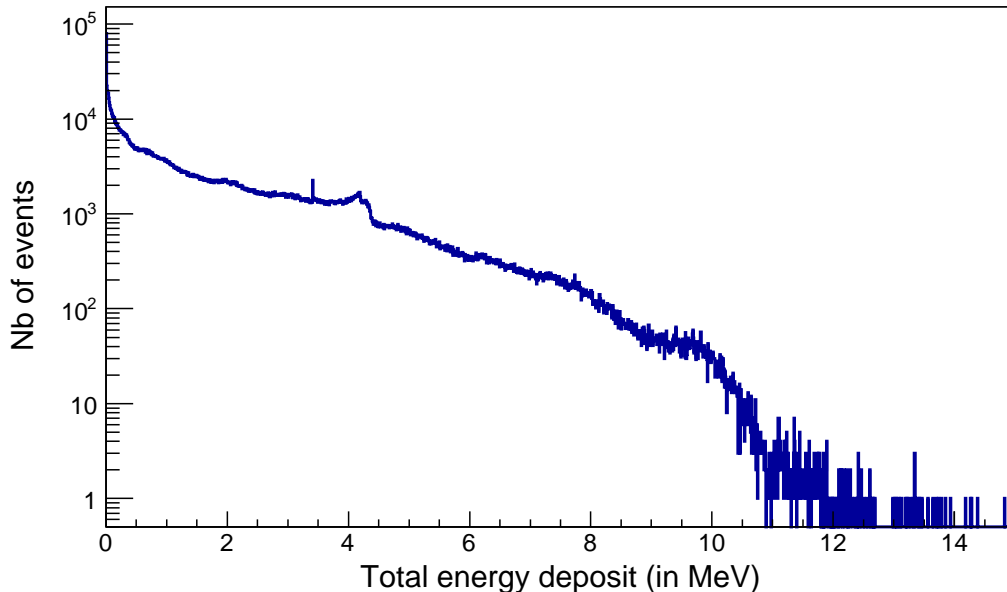
Figure 4.9. – Distribution of the total energy deposit in module M42 at the output of the
simulation for the AmBe source at the center of the module, summing all
energy deposits of an event. See text for more details.

where E' is the energy of the scattered γ and $m_e c^2$ the electron energy at rest. As can be
seen in fig. 4.11 bottom, a significant part of the interactions occurs close to the module
boundary. In this case, the scattered γ can escape the detection and total measured energy
is of 4.15 MeV.

Another feature in the energy spectrum fig. 4.9 is a narrow peak at 3.417 MeV. This energy
is typical of a proton capture by a ^{58}Ni, producing a ^{59}Cu in an excited state, which decays
by emitting a 3.417 MeV prompt γ [138]. This isotope is present in the steel of the cylinder
holding the source and in the mounting structure of the μ-veto modules. However, the
cross section of such process is extremely low and therefore cannot explain the observed
peak. In addition, such a narrow peak is not expected from γ's. As the initial energy
of the neutrons responsible of this feature is below the experimental threshold, the exact
origin of this feature was not further investigated. It could be due to an unsolved issue in
the GEANT4 package.

The contribution from neutrons of the AmBe shows up on all the energy range of energy
deposits but dominate at high energies. Fast neutrons mainly lose energy by a succession of
elastic scatterings on the nuclei of the scintillator until they are thermalized and eventually
captured. Organic scintillators are particularly efficient to thermalize fast neutrons as they
contain mainly light elements like hydrogen, carbon and oxygen. Hydrogen is the most
efficient moderator because neutrons can lose up to all their energy in a single collision,
as the mass of the two particles are almost identical. In addition, hydrogen exhibits the
highest neutron scattering cross section. Once fast neutrons have kinetic energies below
1 MeV, the energy transfer per scattering becomes smaller and few hundreds of nanosec-
onds are needed until they reach thermal equilibrium with the medium. Thermalized
neutrons finally get captured by a proton of the scintillator, accompanied with a γ of 2.2
MeV. The single energy deposit at 11.8 MeV arises from the sum of a high energy neutron
fully thermalized in the module and of the 2.2 MeV γ induced by its capture.
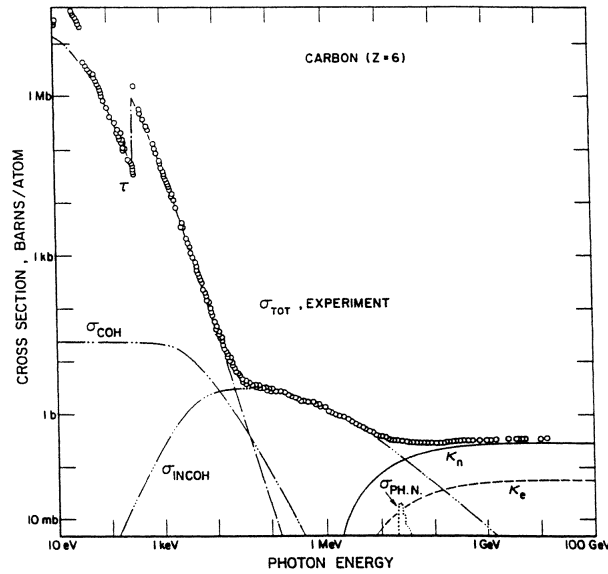
Figure 4.10. – Contributions of atomic photo-electric effect τ; coherent scattering σ_{COH}; incoherent (Compton) scattering σ_{INCOH}; nuclear-field pair production κ_n; electron-field pair production κ_e; and nuclear photoabsorption $\sigma_{\mathrm{PH.N.}}$ to the total measured cross section σ_{TOT} (circles) in carbon over the photon energy range 10 eV to 100 GeV. The measured σ_{TOT} points, taken from 90 independent literature references, are not all shown in regions of high measurement density. Extracted from [139].
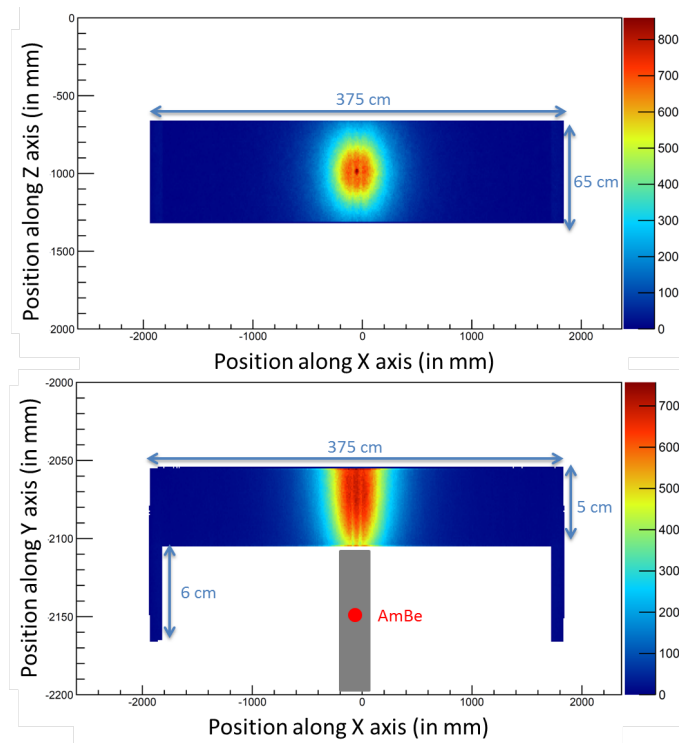
Figure 4.11. – Distribution of the interaction positions inside the module of γ's and neutrons from the AmBe source, placed at the module center. The top plot gives the position along the module width (Z axis in the simulation) versus the position along the module length (X axis). The bottom plot shows the position along the module thickness (Y axis in the simulation) versus the position along the module length.

4.3. Modelling of the module response

Before fitting the measured energy spectrum with the simulated one, the module response has to be implemented on the simulated data. As explained above, the simulation only gives the energy deposit in a module without conversion in scintillation photons, their propagation towards the module ends and their detection by the electronics chain. The implementation of these effects is discussed below and illustrated using the simulated energy spectrum for the AmBe source at the center of module M42.

4.3.1. Acquisition time window

The data acquisition chain was designed such that the total energy deposit in a module is measured by integrating the two pulses from both PMT groups over a 100 ns time window after the trigger. The width of the integration window was chosen to ensure a full collection of the scintillation light including reflections. A dead-time of $\tau = (0.157 \pm 0.001)$ ms [111] follows each trigger, during which the electronic chain is reset and the event stored to disk.

When measuring AmBe data, the integration time window is not wide enough to sum
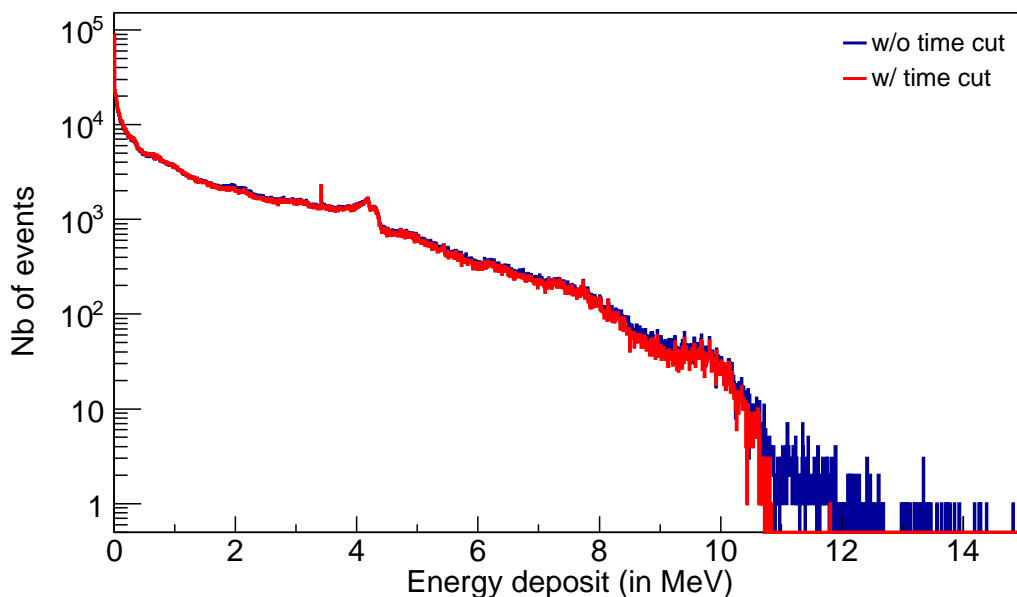
Figure 4.12. – Distribution of the total energy deposit in module M42 without (blue histogram) and with (red histogram) the acquisition time window.

all energy deposits. As explained in section 4.2.3, γ's deposit their energy in only a few ns via Compton scattering. But neutrons, once quickly slowed down by hydrogen, take time to be thermalized and captured. Consequently, part of energy deposits from neutrons is not measured, notably the 2.2 MeV γ which is emitted during the neutron capture by hydrogen. The acquisition window width was therefore implemented in the simulation by summing the energy deposits which occur in a 100 ns time window after the first hit. The comparison between the energy spectrum with time cut and without time cut is shown in fig. 4.12. The distribution with time cut ends more sharply at the highest neutron energy produced by the source ($\sim$11 MeV), as there is no more coincidence with the associated 2.2 MeV γ produced by neutron capture. In overall, there is a slight reduction of the high energy neutron tail as well as the 2.2 MeV γ peak, accompanied with a slight increase of the low energy below 1.5 MeV. As expected, the γ peaks at 4.2 and 4.4 MeV are not affected by this time cut because $\gamma's$ deposit their energy in few ns.

4.3.2. Quenching of the energy deposit

It is well known that the response of organic scintillator depends on the incoming particle: for a given energy deposit, the light output arising from nuclear recoils is significantly diminished compared to the light output induced by electronic recoils. This effect is similar to the ionization quenching of nuclear recoils in the Ge detectors described in section 2.1.2.1. In scintillators, the quenching arises from the non-linear response of the material to the ionization density dE/dx. Various theories exist to explain this non-linear behaviour, all based on the assumption that a high ionization density along the particle track results in a quenching of the primary fluorescence process [140]. This non-linear response has been attributed by J.B.Birks to *damaged* molecules dissipating their excitation via non radiative processes instead of primary scintillation light [110]. By assuming that the light output is proportional to the energy loss excluding this quenching mechanism, he derived the following semi-empirical model giving the light output per unit of path length:

$$\frac{\mathrm{d}L}{\mathrm{d}x} = \frac{A\frac{dE}{dx}}{1 + kB\frac{dE}{dx}} \tag{4.6}$$

where A is the absolute scintillation factor, dE/dx the ionization density, $B\frac{\mathrm{d}E}{\mathrm{d}x}$ the density of *damaged* molecules and k the fraction of scintillation light which is quenched. kB is treated as a single parameter which is adjusted to fit the experimental data for a specific scintillator. The scintillation quenching factor Q can then be expressed as the ratio of the light yield produced by nuclear recoils L_n and by electronic recoil L_γ:

$$Q = \frac{L_n(E)}{L_\gamma(E)} = \frac{\int_0^E \frac{dE}{1 + kB\left(\frac{dE}{dx}\right)_\gamma}}{\int_0^E \frac{dE}{1 + kB\left(\frac{dE}{dx}\right)_n}} \tag{4.7}$$

Various other parametrizations co-exist in the absence of theory describing the scintillation quenching. Some work has been undertaken to better describe the quenching at low energies in [141] and [142]. Indeed, Birks' assumption that the light yield is proportional to the energy deposit is true for high energy deposits but large deviations have been measured at lower energies [143]. It was shown in [144] that Birks' parametrization describes well the light output for $(\mathrm{d}E/\mathrm{d}x) < 100\,\mathrm{MeV}/(\mathrm{g}\cdot\mathrm{cm})$. As it is mostly the case of the energy deposits from AmBe in the μ-veto plastic scintillator, Birks' parametrization will be used to quench the simulated energy deposits.

Many studies on the non-linear response of plastic scintillator have been done using general purpose plastic scintillator of type NE-102 (equivalent to BC-400), for different particles of different energies. Most of the results agree with a kB value of $10\,\mathrm{mg}/(\mathrm{cm}\cdot\mathrm{MeV})$ [144]. No reference could be found for the plastic scintillator used in the EDELWEISS experiment (Bicron BC-412, equivalent to NE-110) as its usage is more specific (long strips or large areas of detectors). Nevertheless, they both have the same base and only differ by the type of wavelength shifter and their concentration [106]. Consequently, the ionization density $\mathrm{d}E/\mathrm{d}x$ is approximatively the same in both scintillators. In addition, the Birks' parametrization concerns the quenching of the primary scintillation, so that the type or the concentration of the wavelength shifter should not matter, except for a slight change in the average $\mathrm{d}E/\mathrm{d}x$. Therefore the average kB value of $10\,\mathrm{mg}/(\mathrm{cm}\cdot\mathrm{MeV})$ [144] obtained for the NE-102 scintillators will be used to parametrize the scintillation quenching.

As information about single energy deposits E_h are stored in the output of the simulation, the quenching of the energy deposit can be implemented a posteriori. The total energy deposit in a 100 ns window is now calculated as the sum of single energy deposits quenched individually:

$$E_{\mathrm{tot}} = \sum_{h=1}^N E_h \times \frac{1}{1 + \frac{kB}{\rho} \cdot \frac{dE_h}{dx_h}} \quad \text{with} \quad \frac{kB}{\rho} = 9.69 \times 10^{-2}\,\mathrm{MeV}^{-1} \tag{4.8}$$

Fig. 4.13 shows the average scintillation quenching $\langle Q \rangle$ versus the total energy deposit in the module M42 in a 100 ns time window. The population with $\langle Q \rangle \simeq 1$ arises from electromagnetic interactions induced by γ's from the AmBe source and from neutron capture by hydrogen. Neutrons show up with $0.1 < \langle Q \rangle < 0.5$, where two populations can be distinguished. The prominent line at higher $\langle Q \rangle$ is due to neutrons depositing their energy via one scattering on a hydrogen atom. The lower distribution is due to neutrons depositing their energy via multiple scatterings, leading to a lower average $\langle Q \rangle$ value. The events between the γ and the neutron populations arise when part or all the energy of the 4.4 MeV γ is summed with a neutron. The dropping parabolic population from 4.4 MeV up to 10 MeV can notably be distinguished. It corresponds to the coincidence of a neutron depositing part of its energy with a low quenching and the 4.4 MeV γ depositing all its energy with a quenching $\simeq 1$. The average quenching factor over the time window decreases when the neutron contribution to the total energy deposit increases. The population at low energies with $\langle Q \rangle \simeq 0$ is inherent to the energy production thresholds implemented in GEANT4. Below this threshold, no secondary particle will be generated to avoid infrared divergence of some electromagnetic processes and the energy will be locally deposited.

The total energy spectrum is compared in fig. 4.14 before and after the implementation of the energy quenching. The neutron contribution is strongly reduced, emphasizing the characteristics of the Compton spectrum. The high energy tail is reduced and ends more sharply around ~ 7 MeV. These high energy neutrons as well as the γ's from the photopeak allow to probe the trigger threshold as they will trigger the acquisition. Extracting the quenched energy spectrum of fig. 4.14 is time consuming as a loop over each single energy deposit in the module from the simulated particle and its secondaries is required. However, as the kB value is fixed, the energy spectrum including the acquisition window and the quenching of the scintillation light is produced once and stored on disk for further use.
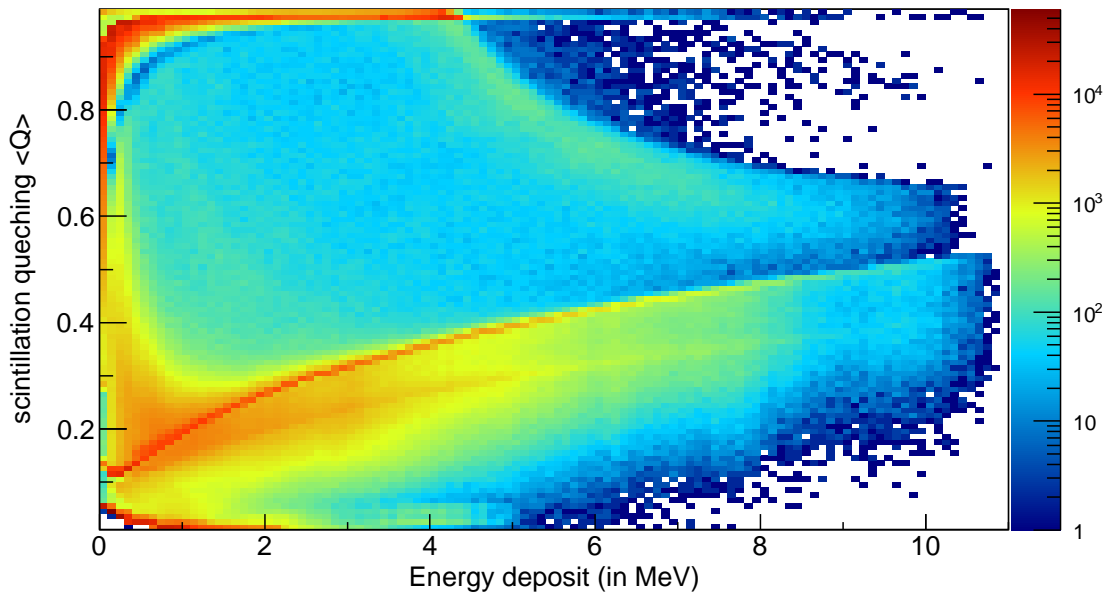
Figure 4.13. – Average scintillation quenching $\langle Q \rangle$ in a 100 ns time window after the first hit versus the total energy deposit in module M42 during this time window.
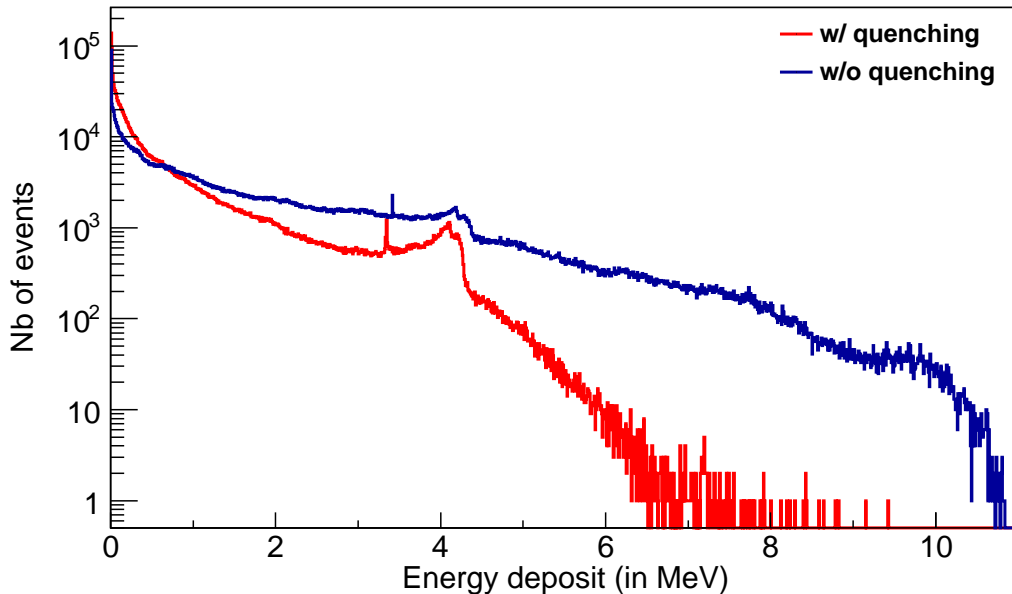
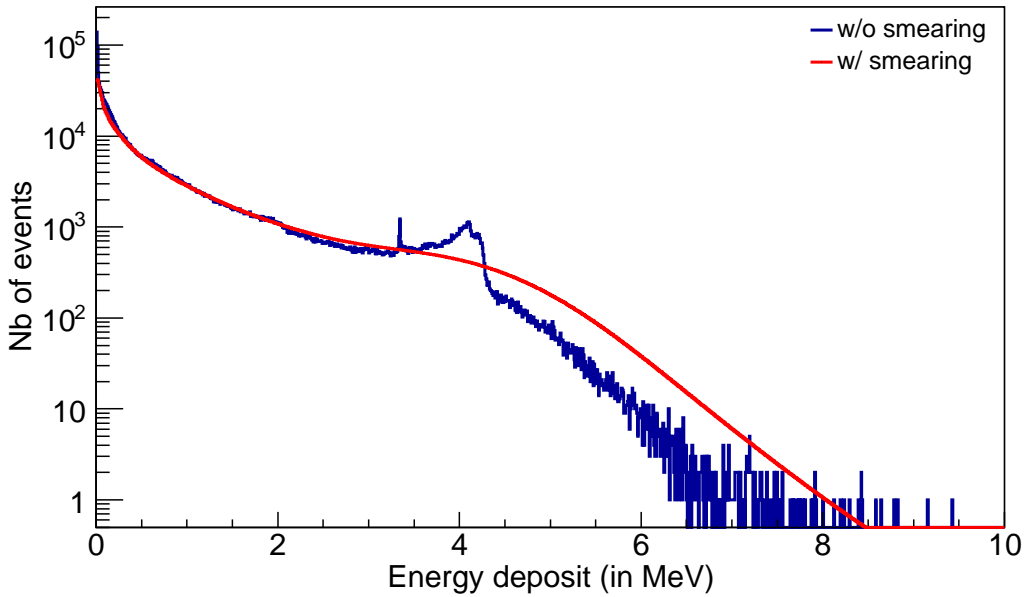**Figure 4.14.** – Distribution of the total energy deposit in module M42 without (blue histogram) and with (red histogram) the scintillation quenching.

4.3.3. Energy resolution

The total energy deposit in the module is additionally smeared to take into account the statistical fluctuations in the production of scintillation photons, their absorption on their way to the PMT groups, and their detection (depending on the quantum efficiency) and amplification by the PMTs. The baseline resolution is negligible compared to the statistical fluctuations of the energy deposit. In order to reduce the computation time, the smearing is not performed event-by-event: the energy spectrum including the acquisition window and scintillation quenching effects is convoluted bin per bin with a gaussian distribution, centred on the bin i and of width $\sigma_i = \sigma_E \sqrt{E_i}$ with σ_E being the width of the gaussian at 1 MeV. σ_E is an unknown parameter which should be determined by fitting the measured energy spectrum. Note that the energy resolution of the two PMT groups is not the same, notably because of inhomogeneous ageing effects. Consequently, the energy distributions of both PMT groups should be fitted independently.

A comparison of the energy spectrum before and after energy smearing is given in fig. 4.15 for $\sigma_E = 0.37\,\text{MeV}$, close to the best fit value once the module response is completely implemented. The photopeak is smeared, leading to a rise of the high energy tail of the distribution above the trigger threshold. Consequently, σ_E is constrained by the shape of the high energy tail.

4.3.4. Effective trigger threshold

As explained in section 3.2.2.2, a hardware threshold of 150 mV is applied on the pulse amplitude of the two PMT groups for the acquisition to be triggered. For a given position of the energy deposit, the effective trigger threshold in MeV units depends on the gain of the PMT group. It can therefore vary significantly from one module to another due to inhomogeneous ageing of the plastic scintillator and the electronics. In addition, the effective threshold varies for a given energy deposit as the pulse shape fluctuates depending on the location of the energy deposition, the light propagation and collection. This shape depends on the path of the scintillation photons and notably on their reflections on the
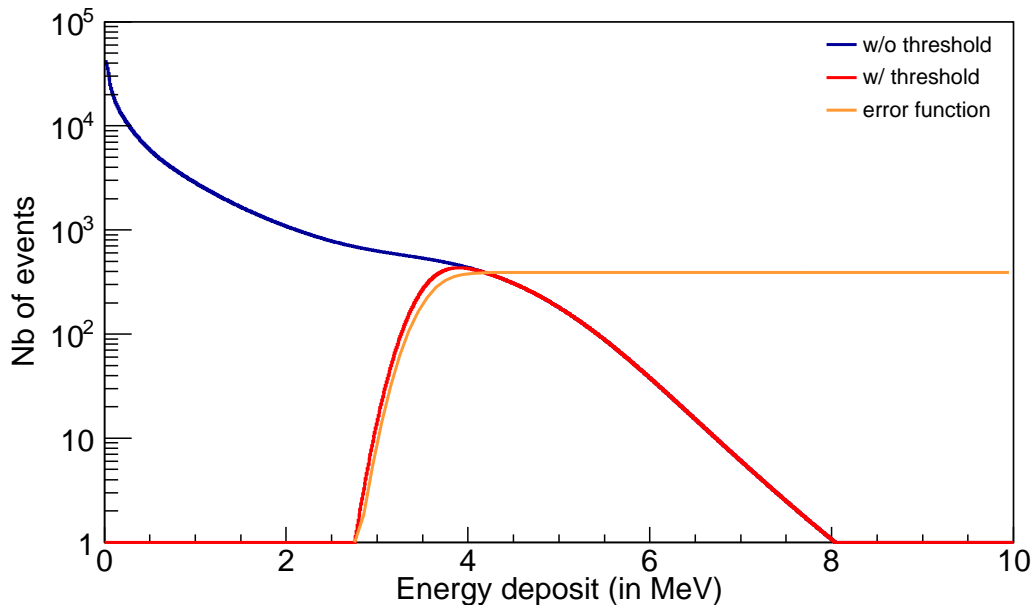
Figure 4.15. – Distribution of the total energy deposit in module M42 without (blue histogram) and with (red histogram) energy smearing. An energy smearing of $\sigma_{\mathrm{E}} = 0.37\,\mathrm{MeV}$ is used here for illustration.

module boundaries and in the light guides. Consequently, the height of the pulse measured for a given energy deposit can be below or above the trigger threshold of $150\,\mathrm{mV}$. The trigger efficiency as a function of energy is thus not a step function but a smooth curve. It is well described by a so-called *error function* $\mathrm{erf(x)} = \frac{2}{\pi}\int_0^X e^{-t^2}\,dt$, which is equivalent to a Heaviside function $\Theta(E - E_{\mathrm{thr}})$ at the energy E_{thr}, convoluted with a gaussian of resolution σ_0. The effective trigger threshold E_{thr} is defined as the energy for which the module efficiency is 50%. E_{thr} and σ_0 are both unknown and will be derived from the fit of the measured energy spectrum.

The implementation of the trigger threshold is illustrated in fig. 4.16 for a threshold value of $E_{\mathrm{thr}} = 3.6\,\mathrm{MeV}$ and $\sigma_0 = 0.25\,\mathrm{MeV}$, given by the best fit once the module response is completely implemented. As it was shown in section 4.1.2, a slight increase of the effective threshold induces a strong variation in the number of events triggering the acquisition. Consequently, the threshold value E_{thr} is strongly constrained by the number of measured events. Note that, of the 1.5×10^6 simulated γ's and neutrons interacting in the module, only 6.4×10^4 remain after implementation of the module response, corresponding to 4.3% survival probability. As for trigger width σ_0, this is well constrained by the rise of the measured energy spectrum.

4.3.5. Energy calibration

The last unknown parameter is the calibration coefficient C_{cal} to convert, event by event, the measured energy in ADC channels into MeV units given as output of the simulation. Contrary to common practice, the scaling is not applied on the model (simulation) but on the measured energy and this for practical reasons: the binned energy spectrum including the scintillation quenching is used as input of the maximum likelihood method. Hence, information about single energy deposits is lost. Scaling the simulated spectrum would imply to calculate how the content of each bin is distributed over a range of bins. It is therefore easier, faster and more accurate to scale each of the measured events.

Figure 4.16. – Distribution of the total energy deposit in module M42 without (blue histogram) and with (red histogram) effective trigger threshold. The trigger efficiency function is displayed in orange and was scaled for visibility by a factor ~ 400.

To conclude, the module response is modelled with 4 unknown parameters: the energy smearing σ_E, the effective trigger threshold E_{thr}, the smearing of the threshold σ_0 and the scaling in energy C_{cal}. The set of parameters $\vec{\theta} = \{\sigma_\mathrm{E}, E_\mathrm{thr}, \sigma_0, C_\mathrm{cal}\}$ characterizes the response of a module for a given position of the AmBe source.

4.4. Efficiency determination of individual module using a likelihood analysis

The set of parameters $\vec{\theta} = \{\sigma_\mathrm{E}, E_\mathrm{thr}, \sigma_0, C_\mathrm{cal}\}$ giving the best match between the measured and simulated energy spectra has to be extracted for the three positions of the source along the module axis. By extrapolation between the three positions, the position-dependent trigger threshold can be derived and implemented in the simulation to finally derive the μ-veto efficiency.

The best set of parameters is extracted using a binned maximum likelihood analysis: a 4D likelihood function is defined and maximized according to the Bayes' inference. In the following, the method will be introduced and the likelihood function derived including statistical uncertainties on the simulated spectrum. It will then be illustrated using a simplified example before being applied to the full problem.

4.4.1. Bayes' theorem

Given the measured energy spectrum, the probability that a set of parameters $\vec{\theta}$ describes the measured spectrum is the so-called *conditional* or *posterior* probability $P(\vec{\theta}|\mathrm{data})$. It is given by the Bayes theorem, which relates the *a priori* probability distribution (PDF) of a parameter set before the data taking $P(\vec{\theta})$ with the *a posteriori* probability distribution $P(\vec{\theta}|\mathrm{data})$ as follows:

$$P(\vec{\theta}|\mathrm{data}) = \frac{P(\mathrm{data}|\vec{\theta})P(\vec{\theta})}{P(\mathrm{data})} \tag{4.9}$$

$P(\text{data}|\vec{\theta})$ is the conditional PDF of the data given the input parameters $\vec{\theta}$ and is also called the likelihood function $\mathcal{L}(\text{data}|\vec{\theta})$.

$P(\vec{\theta})$ is the best estimate of the probability of $\vec{\theta}$ prior to data taking. It combines all the information gathered from past experiments or intuition. Multiplying it with the likelihood function gives information about the posterior PDF of the unknown parameters $\vec{\theta}$. The choice of the prior PDF is a key part of Bayesian inference. It can be informative i.e. give specific information which impacts the posterior distribution and dominates over the likelihood; or it can be uninformative, that means have minor effects on the posterior PDF of the unknown parameters.

As for $P(\text{data})$, it is the *a priori* PDF to observe the data. It is independent from the unknown parameters $\vec{\theta}$ and is therefore a normalization factor for the posterior distribution $P(\vec{\theta}|\text{data})$ to be a valid PDF. In order to calculate it, the parameter space available for the fitting should be integrated. It is necessary to calculate if the likelihood needs to be normalized to the accessible parameter space, e.g. to compare different models.

As $P(\vec{\theta})$ is considered uniform, the posterior PDF can be rewritten as follows for fixed $P(\text{data})$ and $P(\vec{\theta})$:

$$P(\vec{\theta}|\text{data}) \propto \mathcal{L}(\text{data}|\vec{\theta}) \tag{4.10}$$

Consequently, the parameter set $\vec{\theta}$ for which the posterior PDF is maximal can be determined by maximizing the likelihood function $\mathcal{L}(\text{data}|\vec{\theta})$:

$$\frac{dP(\vec{\theta}, \text{data})}{d\vec{\theta}} = \frac{d\mathcal{L}(\text{data}|\vec{\theta})}{d\vec{\theta}} = 0 \tag{4.11}$$

4.4.2. Determination of the binned logarithmic likelihood function

The likelihood function is defined as the conditional probability to measure the data knowing the set of parameters $\vec{\theta}$. It can be constructed using binned or unbinned data. To reduce the computation time, a binned likelihood function was chosen for this work: the time needed for the likelihood maximization is then proportional to the number of bins rather than to the number of events. The binned likelihood function was constructed taking into account systematic uncertainties on the simulation. First, the following variables are introduced:

— $N_i^D(C_\text{cal})$ the number of measured events in bin i after energy scaling

— $N_i^S(\sigma_\text{E})$ the number of events actually simulated in bin i after smearing in energy

— $\mu_i(\sigma_\text{E})$ the expected number of simulated events in bin i after smearing in energy

— $\widetilde{\mu}_i(E_\text{thr}, \sigma_0)$ the expected number of simulated events in bin i after the implementation of the module response.

For better readability, the dependence of these variables on the parameters are left out in the following.

The likelihood function can be written as the product of the probability for each bin i to observe N_i^D events whereas $\widetilde{\mu}_i$ events are expected from simulation after implementation of the module response. To take into account the systematic uncertainty due to the limited number of simulated events N_i^S in bin i, the probability to simulate N_i^S events whereas μ_i were expected is added as an extra factor to the likelihood. Both probabilities follow a Poisson distribution of mean value $\widetilde{\mu}_i$ and μ_i respectively. Consequently, the likelihood can be written:

$$\mathcal{L}(\text{data}|\vec{\theta}) = \prod_{i=1}^{N} P(N_i^D \mid \widetilde{\mu}_i) \times P(N_i^S \mid \mu_i) \tag{4.12}$$

$$= \prod_{i=1}^{N} \frac{(\widetilde{\mu}_i)^{N_i^D} \exp(-\widetilde{\mu}_i)}{N_i^D!} \times \frac{(\mu_i)^{N_i^S} \exp(-\mu_i)}{N_i^S!} \tag{4.13}$$

The $\widetilde{\mu}_i$ can be related to μ_i and to the trigger efficiency ε_i for this bin via the following expression:

$$\widetilde{\mu}_i = \mu_i \times \varepsilon_i \quad \text{with} \quad \varepsilon_i = \frac{1}{\Delta E_{\text{bin}}} \int_{i-}^{i+} \text{erf}(E_{\text{thr}}, \sigma_0) dE_i \tag{4.14}$$

with ΔE_{bin} the width of a bin in MeV units and $\text{erf}(E_{\text{thr}}, \sigma_0)$ the trigger efficiency function as defined in section 4.3.

As it is more convenient to work with the natural logarithm, the likelihood in eq. 4.13 can be rewritten:

$$\log \mathcal{L}(\text{data}|\vec{\theta}) = \sum_{i=1}^{N} N_i^D \log \widetilde{\mu}_i + N_i^S \log \mu_i - \widetilde{\mu}_i - \mu_i - \log(N_i^S!) - \log(N_i^D!) \tag{4.15}$$

Using the Stirling formula at the first order approximation:

$$\log x! \approx x \cdot log(x) - x \tag{4.16}$$

and assuming $N_i^D > 0$ and $N_i^S > 0$, $\log \mathcal{L}(\text{data}|\vec{\theta})$ (eq. 4.15) can be approximated by:

$$\log \mathcal{L}(\text{data}|\vec{\theta}) = \sum_{i=1}^{N} N_i^D (\log \widetilde{\mu}_i - \log N_i^D + 1) + N_i^S (\log \mu_i - \log N_i^S + 1) - \mu_i - \widetilde{\mu}_i \tag{4.17}$$

where μ_i is chosen to maximize the logarithmic likelihood function:

$$\frac{d \log \mathcal{L}(\text{data}|\vec{\theta})}{d\mu_i} = \frac{N_i^D}{\mu_i} + \frac{N_i^S}{\mu_i} - \varepsilon_i - 1 = 0 \tag{4.18}$$

and is therefore derived to be:

$$\mu_i = \frac{N_i^D + N_i^S}{1 + \varepsilon_i} \tag{4.19}$$

The likelihood function can be derived even more generally including cases where N_i^S or N_i^D are equal to 0.

$$\log \mathcal{L} = \begin{cases} \text{if } N_i^S = 0, \ \sum_{i=1}^{N} N_i^D (\log \widetilde{\mu}_i - \log N_i^D + 1) - \mu_i - \widetilde{\mu}_i \\[2mm] \text{if } N_i^D = 0, \ \sum_{i=1}^{N} N_i^S (\log \mu_i - \log N_i^S + 1) - \mu_i - \widetilde{\mu}_i \\[2mm] \text{else,} \ \sum_{i=1}^{N} N_i^D (\log \widetilde{\mu}_i - \log N_i^D + 1) + N_i^S (\log \mu_i - \log N_i^S + 1) - \mu_i - \widetilde{\mu}_i \end{cases} \tag{4.20}$$

4.4.3. Application to a simplified problem

The performance of the maximum likelihood analysis is illustrated here using a simplified problem with two unknown parameters $\vec{\theta} = \{E_{\text{thr}}, \sigma_0\}$. Fake simulated and measured energy spectra are generated using the parameters derived for the center of module M42, namely $E_{\text{thr}} = 3.6 \text{ MeV}$ and $\sigma_0 = 0.25$. A binning of 100 keV per bin and a number of entries per bin of 1000 are first chosen. The measured energy spectrum is randomly generated from the trigger efficiency function introduced in section 4.3, characterized by $\vec{\theta}$. The simulated energy spectrum is generated flat, each bin being filled by a random number drawn from a Poisson distribution with a mean value of 1000. An example of the resulting histograms is displayed fig. 4.17.

Due to the fast convergence of this likelihood analysis, this simplified example is used to test if the likelihood function gives the expected results and to study the variations of the standard deviation σ of each parameter with the number of entries per bin. This study
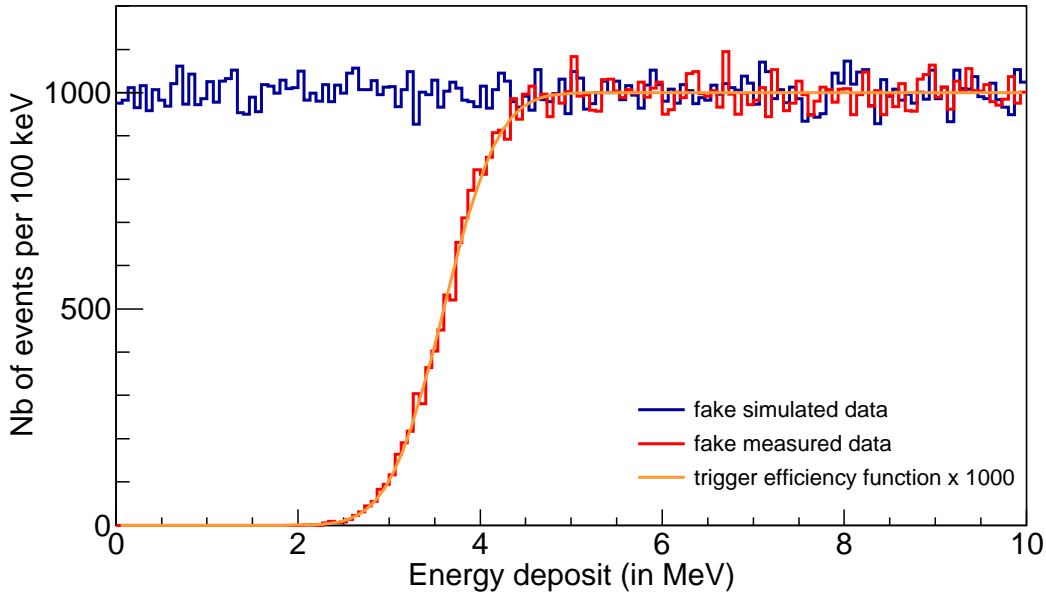
Figure 4.17. – Histograms of the fake simulated energy spectrum (blue) and fake measured energy spectrum (red), generated from the trigger efficiency function (orange).

is impossible to perform on the full problem as few hours are needed for the likelihood function to converge. Following the frequentist approach, 2×10^4 sets of measured and simulated data have been generated (as described above) including statistical fluctuations, for a binning of $100 \, \text{keV/bin}$ and 1000 entries per bin. For each set, the parameter set $\vec{\theta}$ maximizing the likelihood is derived and plotted in fig. 4.18. Firstly, one can deduce from this test that there is no systematic bias of the likelihood function: the mean value of each parameter is equal to the input value as expected. Secondly, the two variables E_{thr} and σ_0 are correlated: if the effective threshold E_{thr} increases, the smearing of the threshold should also increase to match the number of entries in the measured energy spectrum. The parameter E_{thr} is more constrained than σ_0 with a measured variance of 0.3% and 1.9% of their input value respectively. This test shows that the likelihood function has been correctly defined and implemented.

Fig. 4.19 shows the standard deviation (expressed in % of the input values $E_{\text{thr}} = 3.6 \, \text{MeV}$ and $\sigma_0 = 0.25 \, \text{MeV}$) versus the number of entries per bin, for a binning fixed at $100 \, \text{keV}$ per bin. Each value of σ was derived using 5000 sets of fake simulated and measured data. Two contributions to the uncertainties on the two parameters can be distinguished: at low number of entries per bin, the statistical uncertainty on the number of measured events dominates. This contribution decreases with the number of entries per bin but does not approach zero: for large number of entries per bin, the parameters uncertainty is dominated by the systematic uncertainty on the simulation arising from the limited statistics. Indeed, the second term in the likelihood function in eq. 4.12 was included to take into account the systematic uncertainty on the model. It is then not worth further increasing the statistics of the measured spectrum as the parameter uncertainty stagnates at $\sigma = \sigma_{\text{sys.}}$, with $\sigma_{\text{sys.}}(\sigma_0) = 1.8\%$ and $\sigma_{\text{sys.}}(E_{\text{thr}}) = 0.3\%$.
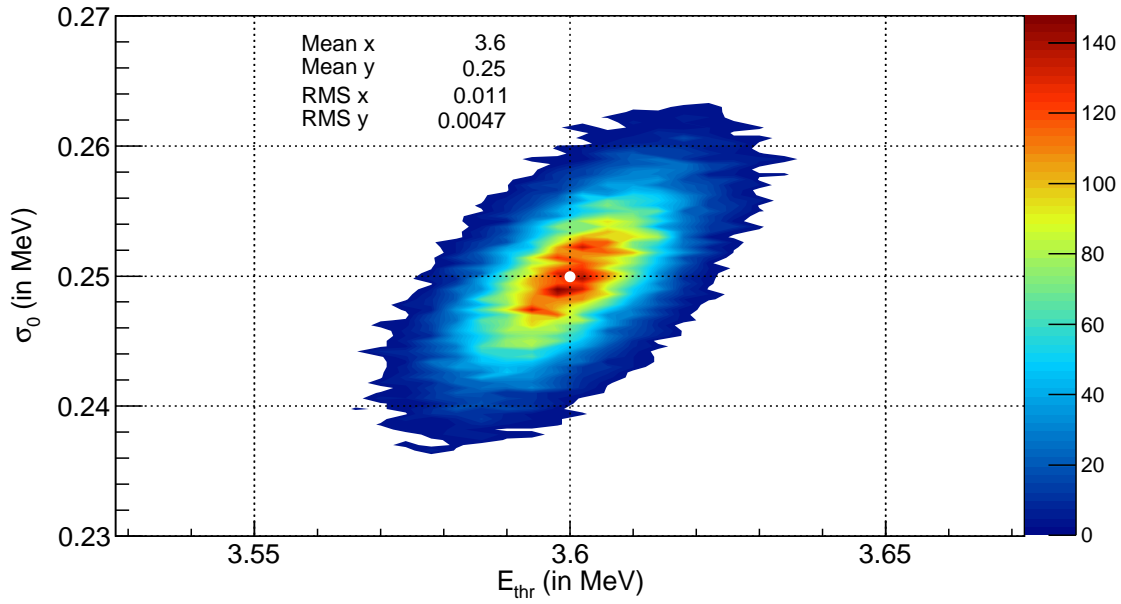
Figure 4.18. – Distributions of the best fit parameters E_{thr} versus σ_0 for 2×10^4 sets of fake measured and simulated data, generated using as input the parameters $E_{\mathrm{thr}} = 3.6\,\mathrm{MeV}$ and $\sigma_0 = 0.25\,\mathrm{MeV}$ (white marker). These results were obtained for a binning of $100\,\mathrm{keV/bin}$ and with 1000 entries per bin.
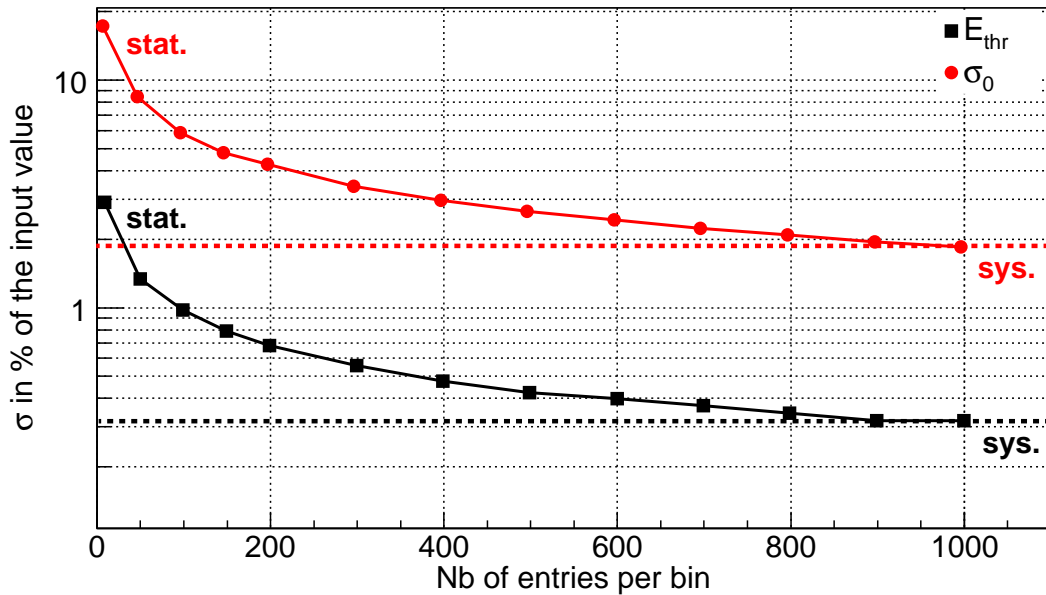
Figure 4.19. – Standard deviation σ in % of the input values ($E_{\mathrm{thr}} = 3.6\,\mathrm{MeV}$ and $\sigma_0 = 0.25\,\mathrm{MeV}$) of the two fit parameters versus the number of entries per bin in the fitted energy spectrum, for a binning of $100\,\mathrm{keV/bin}$. The dashed lines display the systematic uncertainties on the parameters.

4.4.4. Application to the module response determination

In this section, the parameter set maximizing the likelihood function defined in eq. 4.20 is derived for each position of the source. For the center position, the energy spectrum measured by each PMT group can be used to extract the best set of parameters. For the side positions, only the energy spectrum measured by the PMT group which is the furthest away from the source can be used. Indeed, it was shown in section 4.1.2 that the large spread in energy measured by the PMT group the closest from the source is not only due to energy resolution effects: the position-dependent light collection and the propagation of the scintillation photons need to be implemented in the response parametrization or in the simulation to describe this energy spectrum. On the contrary, the energy spectrum measured by the furthest PMT group is dominated by the light absorption and varies weakly with the position of the interaction (see section 3.2.2.3).

As explained in sections 3.2.3 and 4.1.2, the PMT group the furthest from the energy deposit is responsible for the trigger, which requires both PMT groups to measure a signal. As the light absorption increases exponentially with the distance to the PMT, the furthest PMT group dominates the acquisition. Thus, the parameter set derived from the data taken on the north end PMT group of the module gives the response of the south PMT group and vice versa. For the center position calibration, both PMT groups participate to the trigger if the module response is rather symmetric.

The simulated energy spectrum convoluted with the module response is shown together with the measured spectrum for the set of parameters given by the best fit in fig. 4.20a and fig. 4.20b for the source at the center of the module, in fig. 4.21a for the source at the north end and in fig. 4.21b for the source at the south end. The fit parameters derived for each of the source positions are summarized in table 4.1. First of all, a good agreement between the simulated spectrum with module response and the measured spectrum is achieved: the simple response parametrization described in section 4.3 is shown to describe the data well. The agreement is less good for the side than for the center position. There are two reasons for this: first, the number of 9000 measured events is much lower, than the 6×10^4 measured in the center. Secondly, it was shown in section 4.1.2 that for the side positions, not only events occurring at the location of the source trigger the acquisition, but also events depositing energy towards the center. Indeed, despite fewer particles depositing energy that far, the trigger probability is higher as the distance to the furthest PMT group is smaller. In addition, the threshold curve is steeper at the module ends than at the center, leading to larger threshold variations for the side positions of the source. These events were partly cut by selecting only energy deposits occurring within $\pm 2\sigma$ around the source location (see section 4.1.3), but they still contribute to the energy spectrum.

From the values in table 4.1, it can be deduced that the module has a symmetric position-dependent threshold. As a reminder, a slight asymmetry between the two PMT groups was seen in fig. 4.1: for a given measurement time, more triggers were seen when the

Table 4.1. − Overview of the sets of parameters characterising the best fit for the three position of the sources (the uncertainties on the parameters will be derived in the next section using a Monte Carlo Markov Chain analysis).

| source position	North	Center		South
PMT group	ADC[south]	ADC[south]	ADC[north]	ADC[north]
E_{thr} (MeV)	5.70	3.6	3.6	5.75
σ_0 (MeV)	0.60	0.30	0.26	0.59
σ_{E} (MeV)	0.26	0.33	0.35	0.42
C_{cal} (keV/ADC ch.)	8.1	5.1	5.9	8.1

source was placed at the south side compared to the north side. This is consistent with the energy smearing values given in table 4.1, showing that the energy resolution at $1\,\mathrm{MeV}$ of the north PMT group[1] is worse by a factor 1.6 compared to the south PMT group, for a similar threshold. The value of σ_0 increases from the center to the side positions, with the distance between the energy deposition and the PMT group. Indeed, the dispersion of the path length for longer distances stretches the measured pulse shape.

Using the threshold values extracted for the three positions of the source, the parameter of interest in this analysis, i.e. the position-dependent effective threshold curve, can be extrapolated. This is possible knowing the light yield dependence with the position of the interaction. As explained in section 3.2.2.3, the light yield measured by a PMT group decreases exponentially with the path length d of the photons between the interaction and the PMTs according to the empirical Beer-Lambert formula, characterized by the effective attenuation length Λ_{eff}. As the threshold variation reflects the position-dependent light output, the threshold dependence with the mean position x of the interaction along the module length, relative to one of the module end, is extrapolated following:

$$E_{\mathrm{thr}}(x) = A\exp(-x/\Lambda_{\mathrm{eff}}^{S1}) + B\exp((L-x)/\Lambda_{\mathrm{eff}}^{S2}) \tag{4.21}$$

with L the length of the module, $\Lambda_{\mathrm{eff}}^{S1}$ and $\Lambda_{\mathrm{eff}}^{S2}$ the effective attenuation length for each group of PMTs. As the module M42 studied here shows a symmetric behavior, one attenuation length is used as free parameter $\Lambda_{\mathrm{eff}} = \Lambda_{\mathrm{eff}}^{S1} = \Lambda_{\mathrm{eff}}^{S2}$. By extrapolating between the three measured threshold values (see fig. 4.22), an effective attenuation length of $\Lambda_{\mathrm{eff}} = (134.4 \pm 13)\,\mathrm{cm}$ can be derived for this module. This value is consistent with the latest measurement of Λ_{eff} performed on two modules before the installation of the μ-veto system (see section 3.2.2.3), considering the variations between modules and the ageing of the system since these measurements in 2007. Using the threshold curve together with the energy smearing, the response of module M42 can be implemented in the simulation and the muon detection efficiency can be derived.

---

1. measured when the source was located at the south end of the module
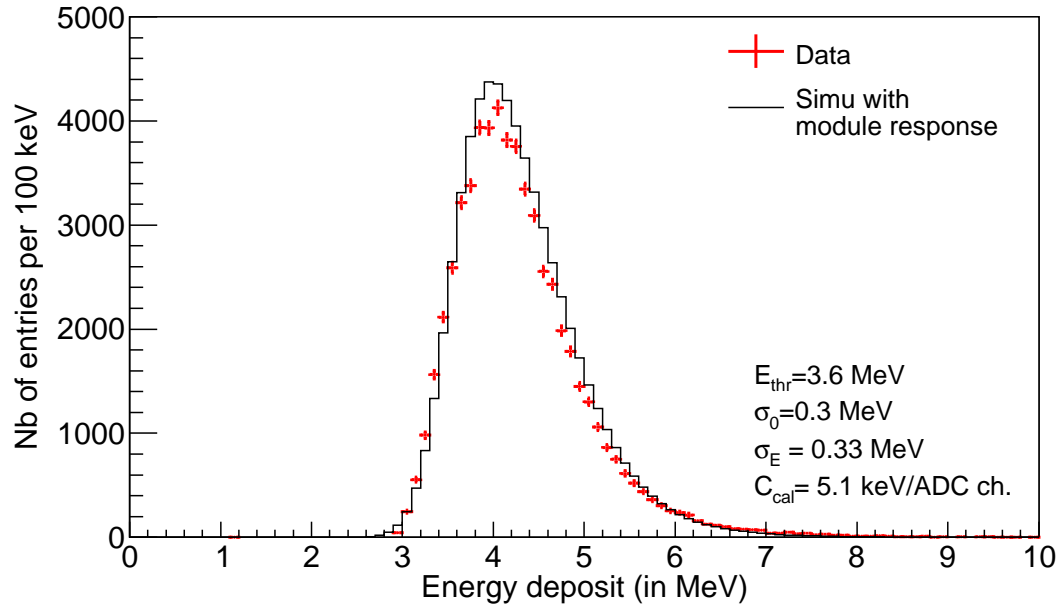
(a)
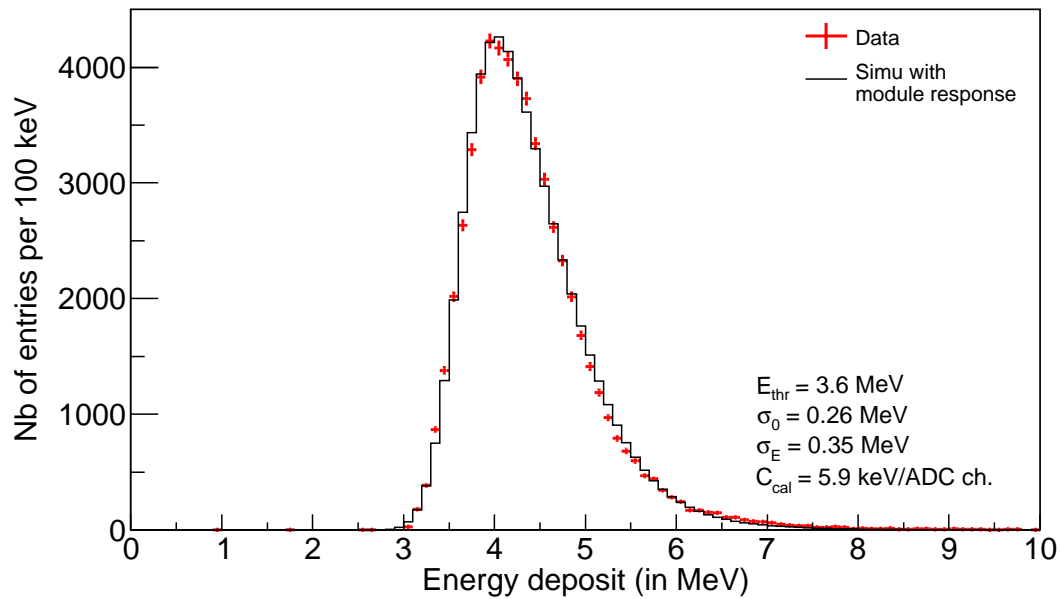
(b)

Figure 4.20. – Energy distributions of the AmBe source located at the center of module M42. The red markers shows the measured energy spectrum. The black histogram shows the simulated energy spectrum including the module response, obtained using the set of parameters giving the best match with the measured spectrum (written in the right bottom corner).
(a) source at the **center** measured by the **south PMT group**;
(b) source at the **center** measured by the **north PMT group**.
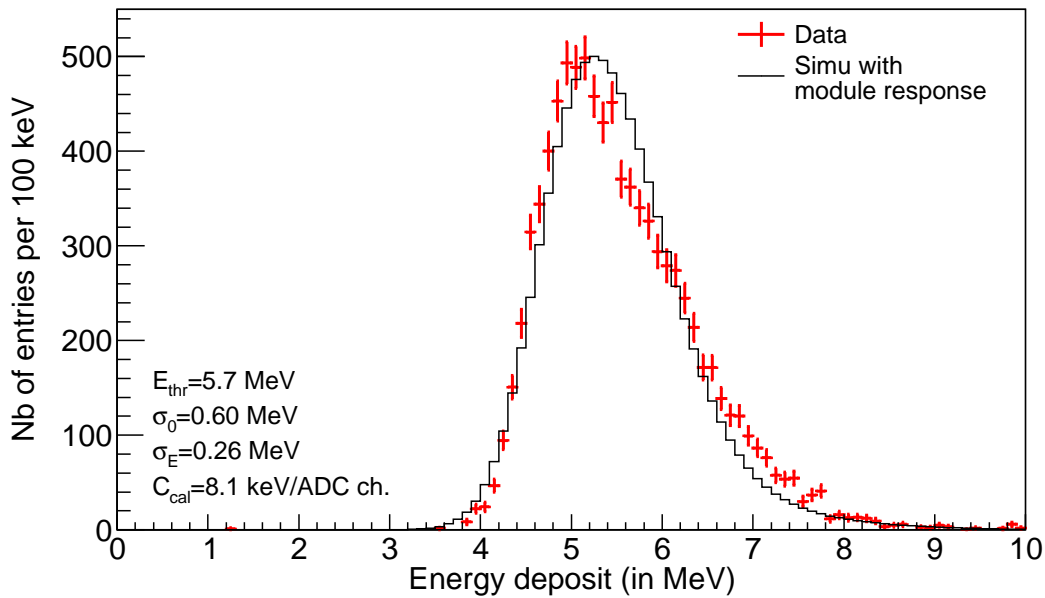
(a)
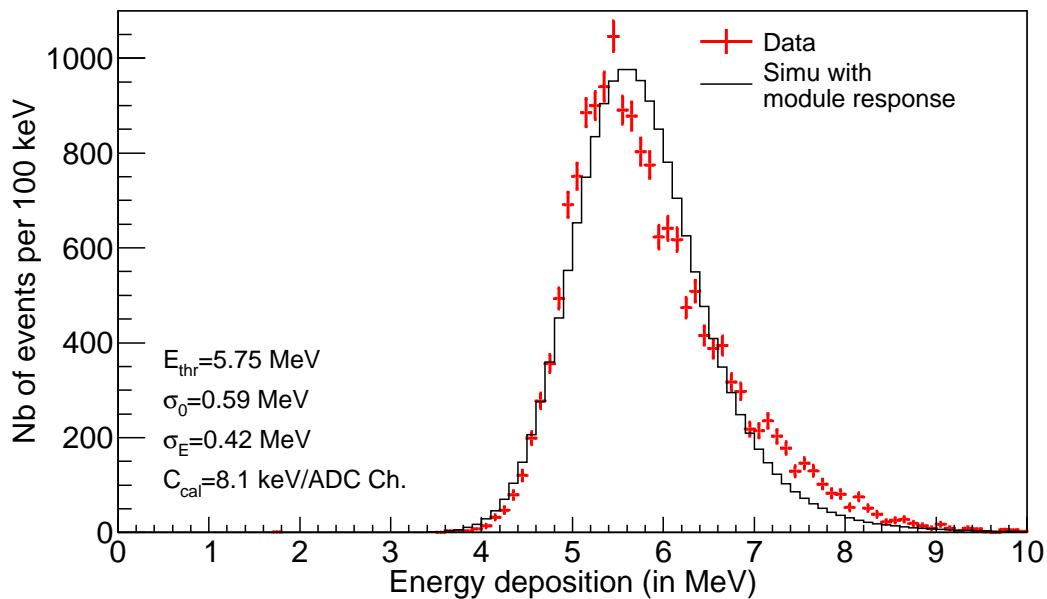
(b)

Figure 4.21. – Energy distributions of the AmBe source located at different ends of the module M42. The red markers shows the measured energy spectrum. The black histogram shows the simulated energy spectrum including the module response, obtained using the set of parameters giving the best match with the measured spectrum (written in the right bottom corner).
(a) source at the **north** end measured by the **south PMT group**;
(b) source at the **south** end measured by the **north PMT group**.
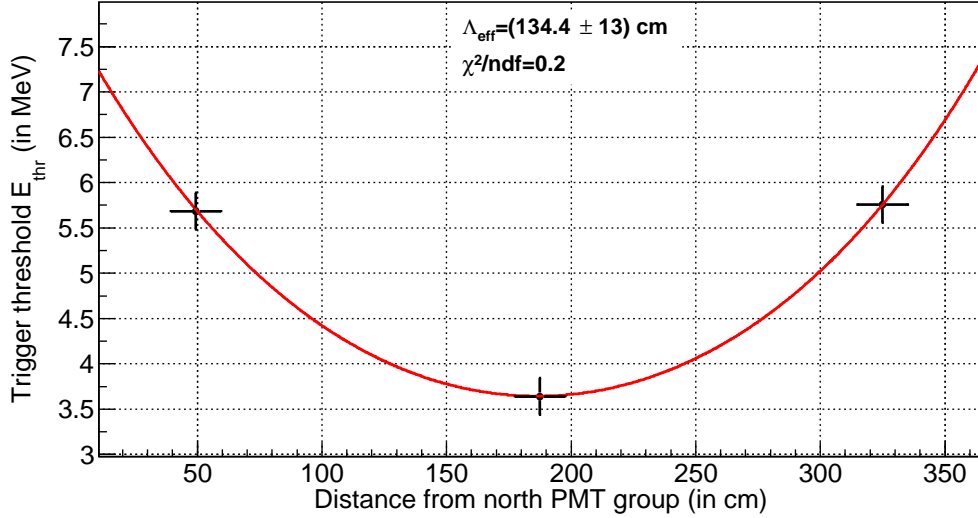
Figure 4.22. – Effective trigger threshold versus the distance from the north PMT group in module M42. The black markers show the threshold values extracted for the best fit for each position of the source. The horizontal error bars represent the uncertainty of ± 10 cm considered on the positioning of the source. The vertical error bars represent the uncertainty of ± 0.2 MeV considered on the threshold values. The red curve shows the fit function used for extrapolation defined as $E_{\mathrm{thr}}(x) = A \exp(-x/\Lambda_{\mathrm{eff}}) + B \exp((L - x)/\Lambda_{\mathrm{eff}})$.

4.4.5. Determination of the module efficiency

The muon detection efficiency of a module can be derived by implementing the module response on simulated data. The simulations of muons in the experimental setup described in section 3.4 are used to extract, for each simulated muon interacting in module M42, the total energy deposit by the muon and its shower and the mean location of the energy deposit [2]. Then, the module response described in section 4.3 is applied on the simulated data, knowing the unknown parameter values from the likelihood analysis. First, each energy deposit is smeared with a gaussian distribution of width $\sigma_i = \sigma_{\mathrm{E}}\sqrt{E_i}$. The effective trigger threshold at the mean location of the energy deposit is then derived using the extrapolated threshold curve shown in fig. 4.22. As explained in section 4.3.4, the trigger efficiency function is modelled using an error function, equivalent to a Heaviside function at $\Theta(E - E_{\mathrm{thr}}(x))$, convoluted with a gaussian of width σ_0. The value given by the threshold curve is the threshold value for which an efficiency of 50% is reached. For each energy deposit, the corresponding detection efficiency is derived. To make the decision if the energy deposit actually triggers, a random number r is generated uniformly between 0 and 1. If $r < \varepsilon(x, E_{\mathrm{thr}}(x))$, the energy deposit is considered to be detected. The muon detection efficiency of the module is then derived by doing the ratio of the number of simulated events which are considered to be detected over the total number of simulated events.

The question arises which values of the parameters σ_0 and σ_{E} should be applied on the simulated data. Contrary to the effective threshold, no obvious extrapolation between the σ_0 and σ_{E} values derived for the three positions of the source can be performed. In theory, 50% of the energy deposit is collected by each PMT group, such that the simulated energy deposit should be divided in two and smeared according to the parameters measured for each PMT group. However, the variation in efficiency derived by using

---

2. Note that the mean position of the energy deposit is calculated by weighting the position of each single energy deposit by the amount of energy deposit.

different combinations of these parameters was determined to be less than 0.1%. Therefore average values of these parameters are used to modify the simulation.

Applying this method, the muon detection efficiency of the module M42 including the position dependent response is found to be:

$$\varepsilon_{\text{M42}} = 95.0\% \tag{4.22}$$

This value can be compared with the efficiency derived in EDELWEISS-II using the average threshold value over the module length as described in section 3.2.4.1. Averaging over the module detection efficiencies, a mean value of 95% was derived with a spread of $\sigma = 4\%$ [32]. Thus, the efficiency extracted using the method developed in the framework of this thesis is consistent with the average module response in EDELWEISS-II.

One of the limitations of the method used in EDELWEIS-II was the large uncertainties of $\pm 20\%$ on the module calibration and the lack of knowledge of the module response at low energy, leading to an uncertainty on the total efficiency of the μ-veto of $\pm 1.5\%$. To evaluate the gain of the method developed here, a precise calculation of the systematic uncertainty on the module detection efficiency is needed. This is performed in the following section using a Monte Carlo Markov Chain analysis.

4.4.6. Uncertainty determination using a Monte Carlo Markov Chain

In the previous section, the set of parameters maximizing the likelihood function was derived and the detection efficiency extracted. To derive the uncertainty on this efficiency, the uncertainty on each parameter of the fit should be determined. For this purpose, a grid calculation of the likelihood function around the best set of parameters could be performed. However, this technique is time consuming as it scales with x the number of points to sample for each parameter and D the number of parameters following x^D. Moreover, this method is particularly inefficient as the parameter space of interest represents only a small fraction of the total tested parameter space. A Monte Carlo Markov Chain (MCMC) analysis is a faster and more efficient alternative to the grid calculation, as the likelihood function is randomly sampled only in the region of interest. In addition, a batch of MCMC can be calculated in parallel as the independent data sets can be added together to get a more accurate description on the posterior distribution.

First, a general description of the working principle of a MCMC is given based on [145, 146, 147]. This method is then used to derive the uncertainty on the muon detection efficiency of the μ-veto module M42.

4.4.6.1. Principle of a Monte Carlo Markov Chain

Let's consider a parameter set of n dimensions $\vec{\theta} \equiv \{\theta^{(1)}, \theta^{(2)}, ..., \theta^{(n)}\}$ describing the measured data. In order to derive the uncertainties on each parameter $\theta^{(\lambda)}$, the probability density distribution $P(\theta^{(\lambda)}|\text{data})$ of each of them has to be sampled. According to the Bayesian approach, the posterior PDF of each parameter $\theta^{(\lambda)}$ can be calculated by integrating $P(\vec{\theta}|\text{data})$ over the other parameters, so-called *marginalization*:

$$P(\theta^{(\lambda)}|\text{data}) = \int_{\Omega_\beta, \forall \beta \in [1,m] \setminus \{\lambda\}} P(\vec{\theta}|\text{data}) d\theta^{(\beta)} \tag{4.23}$$

As seen in section 4.4, $P(\vec{\theta}|\text{data})$ is given by the Bayes' theorem 4.9 and can be written as follows as $P(\text{data})$ is considered as a normalization factor:

$$P(\vec{\theta}|\text{data}) \propto \mathcal{L}(\text{data}|\vec{\theta}) P(\vec{\theta}) \tag{4.24}$$

The mean value and the confidence intervals of each parameter are then extracted from the 1 dimension PDF. This implies to derive with precision the posterior PDF $P(\vec{\theta}, \text{data})$,

which will be noted $P(\vec{\theta})$ in the following for simplification. For this purpose, a MCMC was used to generate random points in the n dimension space where the posterior PDF is evaluated.

The Metropolis-Hastings sampling algorithm is one possible choice to generate a Markov chain with a sequence of points $\{\vec{\theta}_i\}_{i=1,...,n} \equiv \{\vec{\theta}_1, \vec{\theta}_2, ..., \vec{\theta}_n\}$ in the n dimension space, converging towards the posterior distribution. A Markov chain is defined as a sequence of independent points i.e. $\vec{\theta}_{j+1}$ is sampled from a distribution $p(\vec{\theta}, \vec{\theta}_j)$ which only depends on the current parameter $\vec{\theta}_j$. It requires a starting value, which should be chosen as a feasible $\vec{\theta}$ in the parameter space, e.g at the parameter sets given by the best fit derived from the likelihood method previously described. The step $\vec{\theta}_{j+1}$ is deduced from the previous step $\vec{\theta}_j$ according to the following procedure:

1. a new step $\vec{\theta}_{trial}$ is proposed given the current step $\vec{\theta}_j$ according to a proposal function $q(\vec{\theta}_{trial}|\vec{\theta}_j)$. The choice of the proposal distribution is crucial. It should be as close as possible from the target distribution $P(\vec{\theta})$. If it is too wide, the acceptance will be low and the chain will stagnate. If the proposal function is too narrow, the correlation between consecutive steps is large.

2. the new step $\vec{\theta}_{trial}$ is accepted or rejected by calculating the acceptance probability $a(\vec{\theta}_{trial}|\vec{\theta}_j)$ defined as:

$$a = a(\vec{\theta}_{trial}|\vec{\theta}_j) = \min\left(1, \frac{P(\vec{\theta}_j)}{P(\vec{\theta}_{trial})} \frac{q(\vec{\theta}_{trial}|\vec{\theta}_j)}{q(\vec{\theta}_j|\vec{\theta}_{trial})}\right) \tag{4.25}$$

If the proposal distribution is symmetric, $q(\vec{\theta}_{trial}|\vec{\theta}_j) = q(\vec{\theta}_j|\vec{\theta}_{trial})$, the expression of the acceptance probability is simplified, as given by the Metropolis algorithm (1953). The extension to non-symmetric proposal function was introduced by Hasting in 1970 [146]. This condition ensures the convergence of the random walk towards the target distribution.

3. if $a = 1$, the point is accepted i.e. $\vec{\theta}_{j+1} = \vec{\theta}_{trial}$

4. if $a < 1$, there is a probability a for the point to be accepted. Otherwise, the chain stagnate at the same point i.e. $\vec{\theta}_{j+1} = \vec{\theta}_j$

As explained earlier, the goal of the Monte Carlo Markov Chain is to generate random variables according to the posterior distribution. However, the sequence of n points in the parameter space generated with the Metropolis-Hastings algorithm are not all independent: the parameter set $\vec{\theta}_{j+1}$ is by definition strongly correlated to the previous set $\vec{\theta}_j$. When the chain stagnates, the same set of parameters is stored until the chain finally moves. All these correlated sets should be cut to ensure a relevant MCMC. For this purpose, the following characteristics are studied:

— The burn-in length b, which corresponds to the number of iterations at the beginning of the chain which should be excluded as depending on the starting value $\vec{\theta}_0$. If the chain converges towards $p(\vec{\theta})$, the dependence between $\vec{\theta}_j$ and $\vec{\theta}_0$ diminishes as j increases. The burn-in length is defined as the first iteration b for which $p(\vec{\theta}_b)$ reaches the average value of the posterior distribution:

$$p(\vec{\theta}_b) > \frac{1}{N}\sum_{i=0}^{N} p(\vec{\theta}_i) \tag{4.26}$$

— The correlation length $l^{(\alpha)}$, calculated for each parameter $\theta^{(\lambda)}$, which is the minimal distance in number of iterations between two sets of the chain for them to be considered

independent. The degree of correction is estimated using the auto-correlation function $c_j^{(\lambda)}$ between the step $\theta_i^{(\lambda)}$ and $\theta_{i+j}^{(\lambda)}$, which is defined as [145]:

$$c_j^{(\lambda)} = \frac{E\left[\theta_i^{(\lambda)}\theta_{i+j}^{(\lambda)}\right] - \left(E\left[\theta_i^{(\lambda)}\right]\right)^2}{E\left[\left(\theta_i^{(\lambda)}\right)^2\right] - \left(E\left[\theta_i^{(\lambda)}\right]\right)^2} \tag{4.27}$$

These values are calculated using a fast Fourier transformation [145, 148]. The $l^{(\lambda)}$ are defined as the smallest value of j satisfying the condition $c_{j=l^{(\lambda)}}^{(\lambda)} < 1/2$. The choice of this auto-correlation value is arbitrary and follows [145, 149]. The total correlation length l is defined as the longest length among $l^{(1)}, l^{(2)}, ..., l^{(n)}$.

— The convergence of all the MCMC chains, to ensure that all chains are sampling the same target distribution $p(\vec{\theta})$. The probability that a chain converge increases with the length of the chain, together with the precision on the target distribution.

For a batch of chains obtained using the Metropolis-Hastings, the chains which did not converge are excluded and the remaining chains are sub-sampled by keeping the set of parameters satisfying $\vec{\theta}_{\text{sub-sample}} = \vec{\theta}_{i=b+kl}$. To reject a minimum of parameter sets, the correlation and burn-in lengths should be as small as possible. To do so, the proposal function should be as close as possible from the target distribution $p(\vec{\theta})$.

4.4.6.2. Uncertainty on the module detection efficiency

Determination of the uncertainty at one position of the source

Applying the method described before, a batch of MCMC was produced to estimate the uncertainty of the module detection efficiency due to the best fit determination. It was performed for the center position of the source using the energy spectrum measured by the north PMT group.

Positive and uniform priors were used for the 4 parameters of the model. The proposal function was chosen to be a multivariate gaussian based on the covariance matrix:

$$\vec{\theta}_{trial} = \vec{\theta}_i + PC\vec{x} \tag{4.28}$$

where C is the matrix of eigenvalues of the covariance matrix and P the matrix of eigenvectors, and $\vec{x}$ is a vector of n random variables between 0 and 1. The covariance matrix was given by the minimizer algorithm used to minimize the $-log(\mathcal{L})$.

A batch of 120 chains of length $n = 1.2 \times 10^5$ were started around the best fit parameters given in section 4.4.4, taking into account small gaussian fluctuations around these values to generate independent chains. Consequently, the burn-in length varies from 78 to 261 iterations. As for the correlation length, it varies between 34 and 880 iterations. An example of the correlation functions derived for each fit parameter is given in fig. 4.24, where the correlation length varies from $l = 22$ for σ_E to $l = 52$ for C_{cal}. In most cases, the correlation length is maximal for the calibration coefficient parameter C_{cal}. This can be explained as the marginal distribution of this parameter is not smooth but peaked at given values. Each chain has been sub-sampled according to its burn-in and correlation lengths and the remaining 19990 independent sets have been added together. The distribution of the $log(\mathcal{L})$ of these independent parameter sets is plotted in fig. 4.25. Three distinct $log(\mathcal{L})$-peaks can be distinguished: a clear global maximum at $log(\mathcal{L}) \simeq 750$ and two local maxima at $log(\mathcal{L}) \simeq 450$ and $log(\mathcal{L}) \simeq 540$. This shows that the sampling algorithm maps the parameter space in a wide enough region around the best fit. Despite the existence of multi-maxima, there is a clear global maximum for which the likelihood value is 5.3 times higher than for the next highest local maximum. Chains which did not converge towards
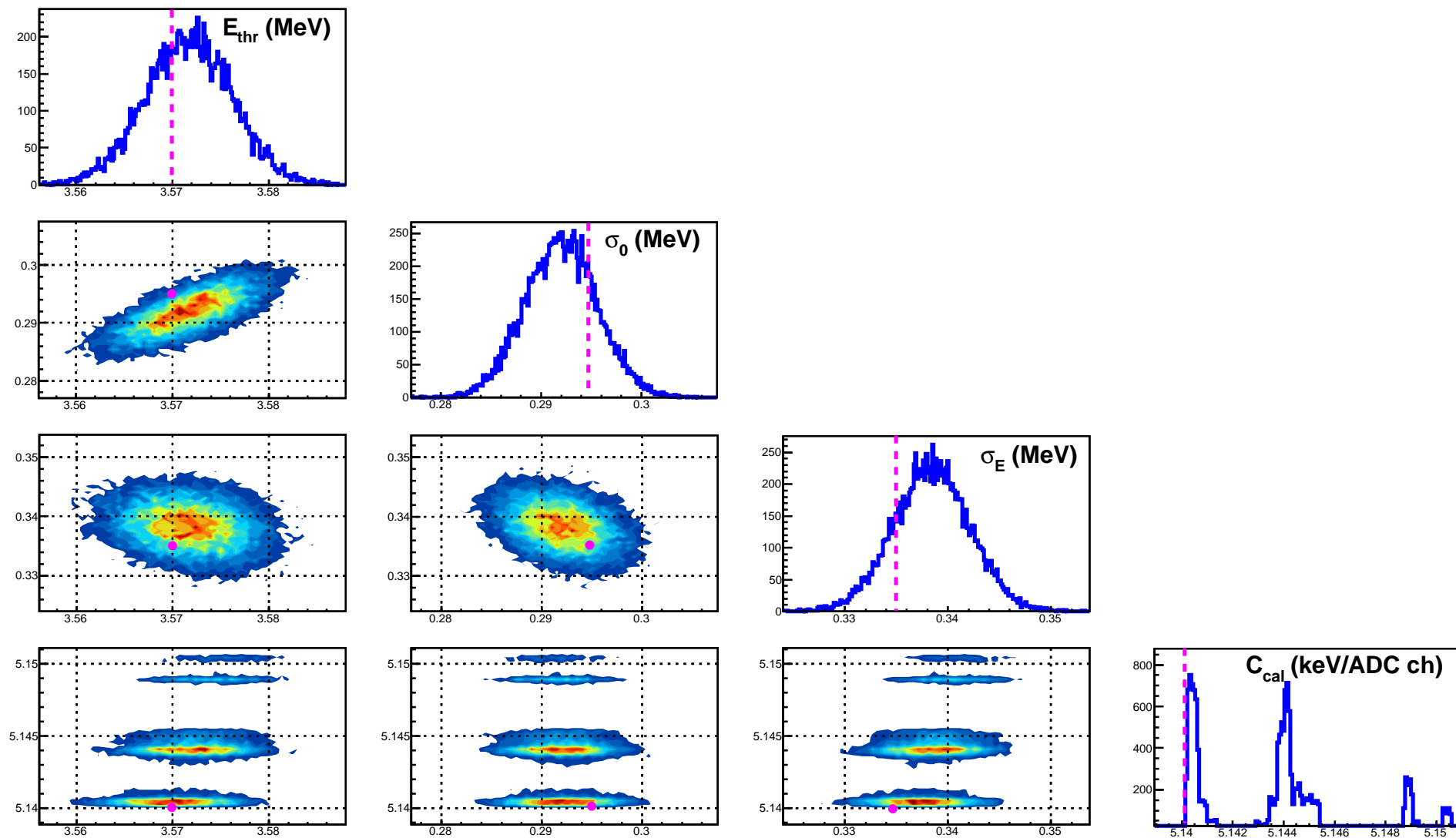
Figure 4.23. – Marginal distributions (diagonal) and 2D correlations (off-diagonal) of the 4 fit parameters describing the response of the μ-veto module M42 after MCMC analysis. The pink markers and the vertical dashed lines display the best fit values obtained from the maximum likelihood analysis performed in section 4.4.4.

the global maximum are cut. Thus, out of the 1.44×10^6 generated parameter sets, only 14155 are kept, corresponding to a sampling efficiency of 1%.

Using these independent parameter sets, the marginal distributions of each of the 4 fit parameters as well as the 2D correlations were derived and are plotted in fig. 4.23. From the marginal distributions, the median values as well as the 68% C.L. uncertainty on each parameter were found to be:

$$E_{\text{thr}} = 3.5770^{+0.0044}_{-0.0044} \text{ MeV} \quad (68\% \text{ C.L.}) \tag{4.29}$$

$$\sigma_0 = 0.2921^{+0.0035}_{-0.0037} \text{ MeV} \quad (68\% \text{ C.L.}) \tag{4.30}$$

$$\sigma_{\text{E}} = 0.3383^{+0.0037}_{-0.0036} \text{ MeV} \quad (68\% \text{ C.L.}) \tag{4.31}$$

$$C_{\text{cal}} = 5.1439^{+0.0012}_{-0.0035} \text{ keV/ADC ch.} \quad (68\% \text{ C.L.}) \tag{4.32}$$

The relative uncertainty on each parameter varies from $\approx 0.1\%$ for the calibration coefficient C_{cal} up to $\approx 1\%$ for the energy deposit and threshold smearing parameters σ_0 and σ_{E}. Using the method described in section 4.4.5, the muon detection efficiency at the center of the module is calculated for each of the parameter sets of the sub-sampled MCMC. The distribution of efficiencies is plotted in fig. 4.26. The median efficiency a the module center and its uncertainty at 68% C.L. was derived to be:

$$\varepsilon_{\text{center}} = 96.56^{+0.04}_{-0.04} \tag{4.33}$$

Thus, the uncertainty on the module detection efficiency at the module center due to the parameter uncertainties is less than 0.4%. This can be understood considering that most muons deposit energies according to a Landau distribution of most probable value $E_{\text{MPV}} = 19.8 \text{ MeV}$, which is well above the trigger threshold E_{thr} of the module.

In addition, the uncertainty on the AmBe source activity needs to be taken into account. The source activity is used to calculate the number of γ's and neutrons which should be simulated for a given measurement time. It was measured in [124] to be of $\mathcal{A}_n = 21 \pm 4$ neutrons/s, corresponding to a relative uncertainty of $\pm 20\%$. To determine the associated uncertainty on the detection efficiency, a MCMC has been generated using the lower and the upper limit on the activity to normalize the simulation. The median of each of the 4 fit parameters as well as of the detection efficiency have been derived and are listed in table 4.2:

$$E_{\text{thr}} = 3.58^{+0.19}_{-0.18} \text{ MeV} \quad (68\% \text{ C.L.}) \tag{4.34}$$

$$\sigma_0 = 0.29^{+0.05}_{-0.05} \text{ MeV} \quad (68\% \text{ C.L.}) \tag{4.35}$$

$$\sigma_{\text{E}} = 0.34^{+0.02}_{-0.01} \text{ MeV} \quad (68\% \text{ C.L.}) \tag{4.36}$$

$$C_{\text{cal}} = 5.14^{+0.19}_{-0.12} \text{ keV/ADC ch} \quad (68\% \text{ C.L.}) \tag{4.37}$$

$$\varepsilon_{\text{center}} = 96.56^{+0.15}_{-0.20} \% \tag{4.38}$$

The uncertainty on the fit parameters is thus dominated by the lack of knowledge of the AmBe source activity.

Extrapolation to the uncertainty on the module efficiency

The uncertainty on the muon detection efficiency of module M42 can be derived by scaling the threshold curve displayed in fig. 4.22 to higher or lower values according to the uncertainty measured on E_{thr}. It has been shown above that this uncertainty is largely dominated by the unprecise source activity. Therefore, the uncertainty on E_{thr} from the
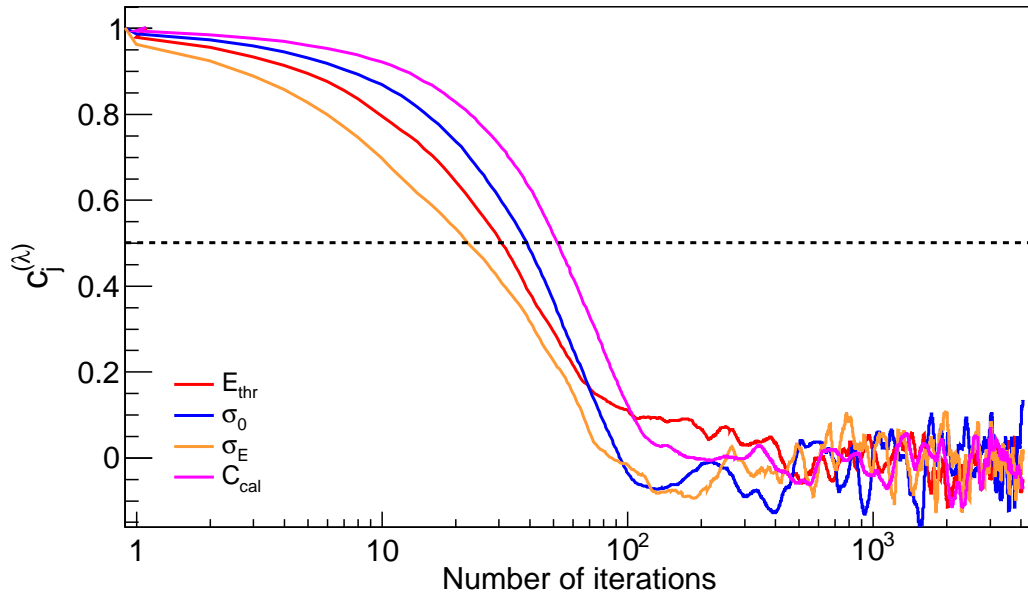
Figure 4.24. – Example of the correlation functions of the 4 fit parameters using a multivariate gaussian distribution based on the covariance matrix as proposal function. The horizontal dashed line indicates the correlation value chosen to derive the correlation length.
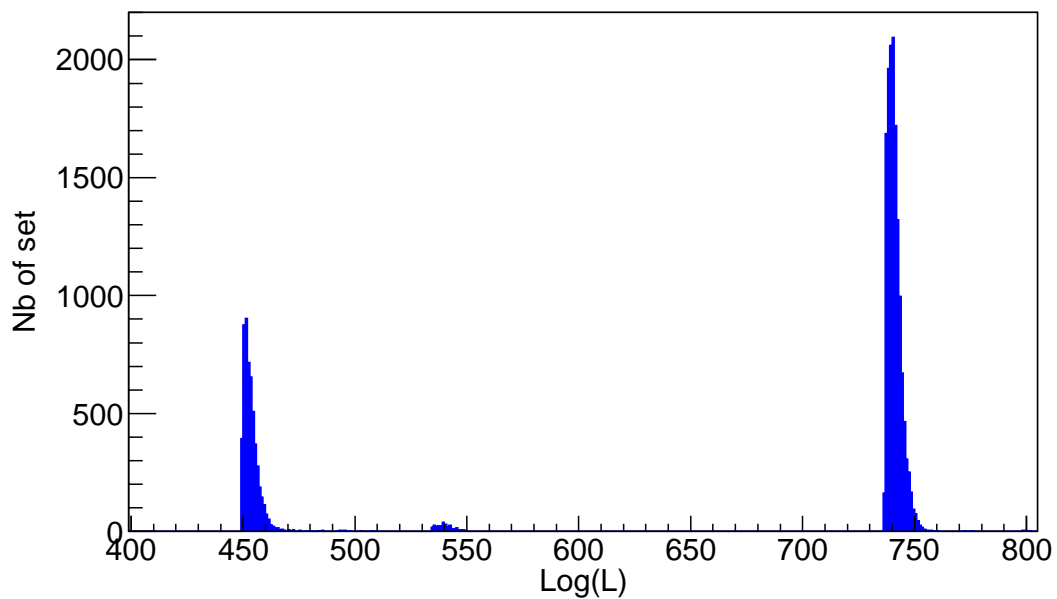

Figure 4.25. – Distribution of the $\log(\mathcal{L})$ values of the 19990 independent sub-sampled MCMC. The largest peak, showing the global maximum, is populated by 14155 sets.
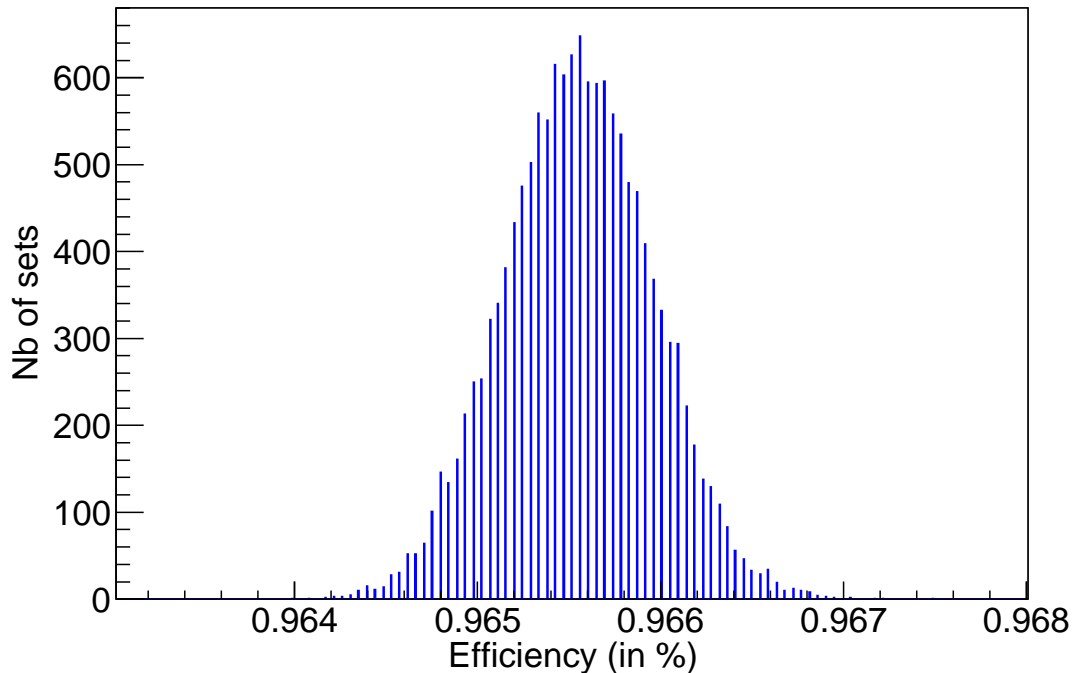
Figure 4.26. − Distribution of the muon detection efficiency of module M42 obtained from folding the simulated muon energy spectrum with the module response using each of the 14155 independent parameter sets from the MCMC.

best fit determination is neglected.

Due to a lack of time, the uncertainties on E_{thr} for the side positions could not be determined. They are expected to be larger than at the center for two reasons: the number of particles from the source triggering the acquisition is lower and the model is less adequate to describe the measured energy spectrum (see section 4.1.2). To be conservative, the uncertainty on the threshold value is considered twice larger than the one estimated for the module center. As for the σ_0 and σ_{E}, the values measured for the center are used, as it was found that the detection efficiency only weakly depends on these parameters.

By scaling the threshold curve by $\pm 0.4\,\text{MeV}$, the upper and lower limit on the efficiency are derived. In addition, the contribution from the uncertainty on the attenuation length, determined by fitting the three values of the threshold to be $\Lambda_{\text{eff}} = (134.4 \pm 13)\,\text{cm}$, was calculated to be of $\pm 0.1\%$. By adding quadratically both contributions, the muon detection efficiency of module M42 and its uncertainty are estimated to be:

$$\varepsilon_{\text{M42}} = 95.0 \pm 0.5 \ \% \tag{4.39}$$

Thus, a good precision on the muon detection efficiency of individual modules can be derived, the uncertainty will be largely dominated by the uncertainty of $\pm 20\%$ on the source activity.

4.5. Outlook: extrapolation of the method to the muon-veto efficiency

The method described above allows to extract the position-dependent response of individual μ-veto modules in situ at LSM, where muons are too rare to be used in this purpose. In particular, the trigger threshold curve was extracted, allowing to precisely estimate the detection efficiency of muons. By applying the position-dependent module response on the

Table 4.2. – Median values and uncertainty at 68% C.L. for each of the fit parameter obtained using either the lower limit (left), median value (center) or the upper limit (right) of the AmBe source activity, for the source at the center of module M42.

$\mathcal{A}$ in n/s	17	21	25
E_{thr} (MeV)	$3.40^{+0.01}_{-0.01}$	$3.58^{+0.01}_{-0.01}$	$3.77^{+0.01}_{-0.01}$
σ_0 (MeV)	$0.237^{+0.004}_{-0.003}$	$0.292^{+0.003}_{-0.004}$	$0.337^{+0.004}_{-0.004}$
σ_{E} (MeV)	$0.327^{+0.007}_{-0.006}$	$0.338^{+0.004}_{-0.004}$	$0.362^{+0.004}_{-0.004}$
C_{cal} (keV/ADC ch.)	$5.025^{+0.021}_{-0.007}$	$5.144^{+0.001}_{-0.004}$	$5.326^{+0.002}_{-0.002}$
ε (%)	96.71 ± 0.04	96.56 ± 0.04	96.36 ± 0.04

simulated energy spectrum of muons and its shower, the modular detection efficiency can be extracted.

In the context of this thesis, it was possible to estimate the responses of the modules listed in table 4.3. The extrapolation from detection efficiencies of single modules to the overall μ-veto efficiency could not be achieved due to time constraints. In addition, the method presents several limitations: first, using a neutron source in the vicinity of the bolometers is not compatible with dark matter search. Thus, considering the low activity of the source at disposal, AmBe data was taken for 23 modules out of the 46 making up the μ-veto modules. Secondly, the trigger threshold of the module on the side or even at the center is sometimes too high for the source to be detectable. Another problem arising for modules of the upper level of the μ-veto is that the amplitude of the measured signal is below the ADC converter threshold. Consequently, the energy spectrum is sharply cut at low energies. Depending how much is cut from the spectrum, it is then difficult or even impossible to derive σ_0 and E_{thr}. This problem could be solved by simply lowering the ADC converter threshold. Lastly, the minimization of the $-\log(\mathcal{L})$ to derive the best set of parameters for each position of the source is time consuming due to the presence of multi-minima. The minimizer is sometimes stuck in a local minimum and a MCMC is then necessary to provide a better starting value to the minimizer.

Apart from these limitations, the method which has to be applied to determine the μ-veto efficiency is straightforward: for each simulated muons crossing the experimental setup, one or two modules are crossed by a muon, whose shower might be additionally detected in neighbouring modules. For each of the module with some energy deposit, the trigger threshold associated to the mean position of the energy deposit is derived, knowing the position-dependent threshold curve of each module. If the energy deposit is above this threshold, it is then considered as triggering the module. Thus, the number of modules which could trigger the acquisition is derived from each muon. By doing the ratio of "detected" muons over the total number of simulated muons crossing the veto volume, the μ-veto efficiency to detect muons can be derived. As explained in section 3.2.4.1, this efficiency represents a lower limit of the actual efficiency of the μ-veto to trigger μ-induced events. It includes muons going through the outermost corner of the μ-veto , which are not likely to produce secondaries in the bolometers. These muons are more likely to be missed because of gaps in the mounting structure in the corners, or because they cross only a fraction of the module thickness and might deposit an energy below the trigger threshold. As most of μ-induced neutrons are produced in the external lead shield, a more realistic estimate can be performed by extracting how many muons crossing a virtual sphere of 1 m radius centred on the cryostat are actually detected.

Table 4.3. – Summary of the parameters E_{thr} (upper line) and σ_0 (lower line), given in MeV units, extracted from AmBe data. The absence of value indicates that the value was not yet extracted. The X mark indicates that the fit did not converge to a global maximum.

module	side 1	center ADC[1]	center ADC[2]	side 2
M5		6.5	6.7	
		1.32	1.5	
M18		3.1	3.1	
		0.25	0.25	
M21		5.0	4.8	
		0.86	0.93	
M22	too high	too high	too high	too high
M27	5.7	4.2	4.2	6.7
	0.56	0.43	0.47	0.83
M29		4.7	4.9	
		0.34	0.43	
M33	too high	too high	too high	too high
M34	too high	5.8	4.7	6.5
		1.08	0.24	1.18
M35	5.5	3.8	3.8	5.1
	0.56	0.46	0.34	0.56
M36	6.0	X	4.45	5.70
	1.13	X	1.29	1.04
M37	5.0	4.7	4.7	5.3
	0.58	0.42	0.34	0.52
M39		5.4	5.4	
		0.89	0.94	
M40	too high	5.4	5.5	too high
		0.76	0.70	
M41	7.4	3.9	3.9	7.40
	0.97	0.56	0.47	0.40
M42	5.7	3.6	3.6	5.75
	0.60	0.3	0.26	0.59
M44		3.8	3.9	
		0.35	0.24	

5. Analysis and simulation of coincidences in Run308

In this chapter, the dedicated analysis performed to study coincidences between the μ-veto system and the bolometers using the Run308 data is presented. A different approach is used compared to the usual veto analysis, where the coincidences are reconstructed from a selection of bolometer events by associating the closest μ-veto event. Here the opposite is done, i.e. a selection of μ-veto events is associated to the closest bolometer hit. This analysis has multiple goals: first, coincidences should be identified by deriving the typical time difference between the energy deposit of a muon and/or its shower in the μ-veto system and the potential bolometer hits it induces. This way, the time window used to veto bolometer events in the WIMP search analysis is determined. Secondly, the coincidence rate is sensitive to the synchronization between the different acquisition computers and the μ-veto, as well as to the number of bolometers actually taking data. Thus, it serves as a powerful tool to detect possible synchronization problems or data processing issues such as missing data from a bolometer.

Once the coincidences will be identified, the signatures of μ-induced events in the Run308 configuration will be extracted. Knowing the topology of μ-induced bolometer events, the μ-veto efficiency will be derived using a sample of bolometer data clearly induced by muons.

The measured rate of coincidences and of WIMP-like events will be extracted and compared to simulation results. For this purpose, strict cuts are applied on the μ-veto and bolometer data to ensure stable experimental conditions, which can be reproduced in the simulations.

5.1. Nomenclature

The meaning of the words "event" and "hit" often varies depending on the context in which it is used within the EDELWEISS collaboration. As these words will be used extensively in this chapter, they are explicitly defined to avoid any misunderstanding:

> **A bolometer hit** is defined as a physical interaction in a single bolometer, leading to an energy deposit.

> **A bolometer event** is the ensemble of bolometer hits within a given time window, which can be attributed to the same physical origin (e.g. a muon or a multiple γ scattering). In Run308, each hit which is less than 10 ms after the previous hit is considered to be part of the same event. That means that the width of the time

window is not fixed e.g. 6 hits each 9 ms after each other are considered as a single event.

A muon-veto event is the ensemble of all interactions occurring in a time window of 100 ns after a module triggered the μ-veto acquisition, which are read-out as a single event.

The bolometer multiplicity is defined as the total number of bolometer hits which make up one event.

The μ-veto multiplicity, as used in the framework of this thesis, is the number of μ-veto modules with at least one non-zero time (TDC) or energy (ADC) information (see section 3.2.2.2).

5.2. Data selection and live-time

As the acquisition chains of the μ-veto system and the bolometer array are independent, it happens regularly that while one is taking data, the other is off for technical reasons. Therefore the live-time for the combined analysis has to be calculated off-line. Before the live-time determination, cuts are applied on the bolometer and μ-veto data to ensure stable conditions of data taking which can then be reproduced in the simulation. These cuts select time periods during which a full efficiency of both systems to detect μ-induced coincidences is achieved. The set of cuts as well as the live-time calculation are detailed in the following sections.

5.2.1. Selection of the μ-veto data

Time periods during which the upper part of the μ-veto was open were cut: if the system is not hermetically closed, the muon detection efficiency decreases. Indeed, there is a high probability to miss the muon exiting the veto volume in the lower part due to the numerous gaps on the structure (see section 3.2.1). The position of the μ-veto wagons is monitored using laser measurements performed every 15 min. Time periods during which the deviation from the fully closed state is more than 3 cm or during which the measurements failed were cut. This condition is strict but the μ-veto is often either widely opened during interventions or in a close position. The acceptance of this cut is 93.2% and is mostly reduced because the μ-veto was open at the beginning of the run after an intervention on the cryostat.

As the coincidence analysis requires a precise timing determination of the μ-veto and bolometer events, time periods were cut during which the clock delivered to both systems was unreliable. These periods can be found by searching for timestamp values close to 0 or for positive or negative jumps of the timestamp of more than 10^{10} stamps between two consecutive μ-veto events. In addition, there was an update of the DAQ crate delivering the clock on the 10th of October 2014 which led to timing issues during 2.5 days. The newly implemented timestamp, based on the unixtime, was too long to be always correctly read by the μ-veto time board. The acceptance of this cut is of 98%.

Early September 2014, the upper part (Level 1) of the μ-veto was powered down during 2 days for safety reasons as work was ongoing in the clean room to install a PE shield around the cryostat. Consequently, the μ-veto rate and detection efficiency dropped. These two days were cut from the analysis as well.

In addition, time periods during which the μ-veto rate increased abnormally because of noise in some modules were also cut. These increases of the rate are mostly correlated with the opening or closing of the shields (mechanical stress) or electromagnetic interference due to the light and the ventilation ON in the clean room. They are not problematic but are cut for security as they might induce additional dead time and artificially increase the accidental coincidence rate between the μ-veto and the bolometer array. Thus, 10 min bins
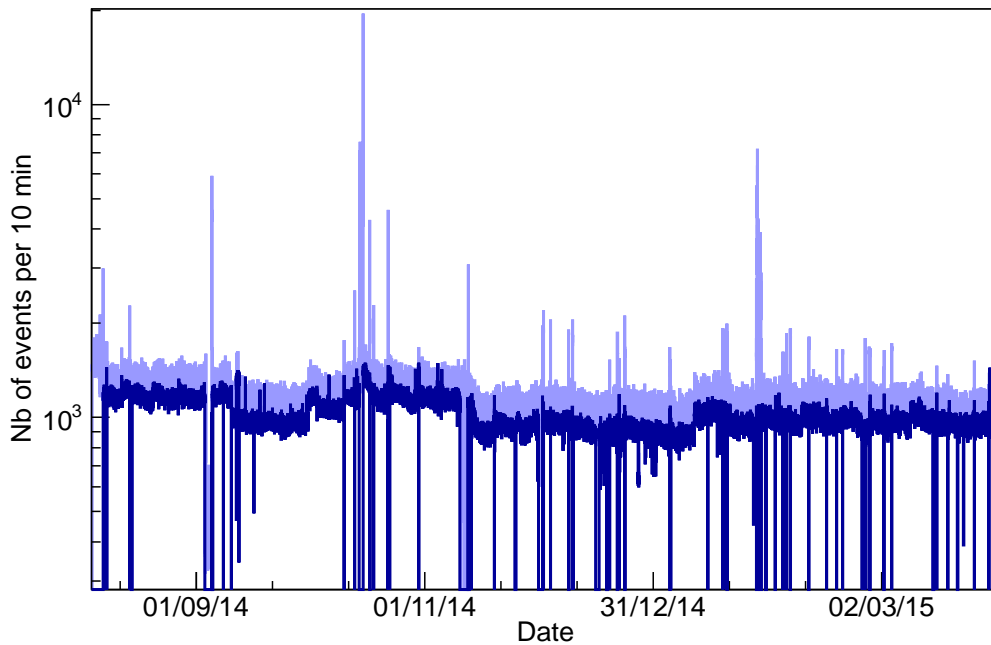
Figure 5.1. – Muon-veto event rate per 10 min bin versus time before (light blue) and after (dark blue) quality cuts.

for which the averaged rate is above $2.5\,\mathrm{Hz}$ before the 12th of November 2014 and above $2\,\mathrm{Hz}$ after this date were cut.

In addition, there is a periodic increase of the μ-veto rate of $\sim 20\%$ due to the LEDs inside the 4 additional modules covering the gap between the two μ-veto wagons. They are fired one after the other every 8 hours for 1 min each. These events are flagged in the data and cut on an event-by-event basis, therefore not inducing any dead-time.

Finally, the live-time of the μ-veto was determined by plotting the overall event rate per 10 min bin, as can be seen in fig. 5.1. In the studied period of 253 days, the μ-veto was taking data during 250.1 days i.e. 98.5% of the time. After applying the quality cuts described above, the remaining live-time is 228.2 days i.e. 91.2% of the data taking period.

Note that these periods during which the μ-veto efficiency cannot be guaranteed are taken into account in the determination of the μ-induced neutron background in chapter 6.

5.2.2. Selection of the bolometer data

The rate of coincidences between the μ-veto and the bolometer array varies with the number of bolometers taking data. As described in section 2.1.3.1, the acquisition is performed using 3 independent Mac computers [1], on which the data acquisition is started independently. Most of the time, the data taking is started on one Mac after the other within a minute but it happens that for technical reasons, only a sub-set of these Macs is actually taking data. Similarly, it often happens that one or more bolometers are dismissed because of energy saturation. This is not an issue for the WIMP search where we expect single nuclear recoil events. However, it is problematic for comparing the measured and simulated coincidence rate between the μ-veto and the bolometers. These time periods are therefore identified and cut.

To derive the number of active bolometers versus time, the hit rate per bolometer per hour is determined applying a $2\,\mathrm{keV}$ cut on the total ionization energy. This cut ensures that

---

1. Mac S1, S2 and S3 read out 8, 4 and 12 bolometers, respectively.
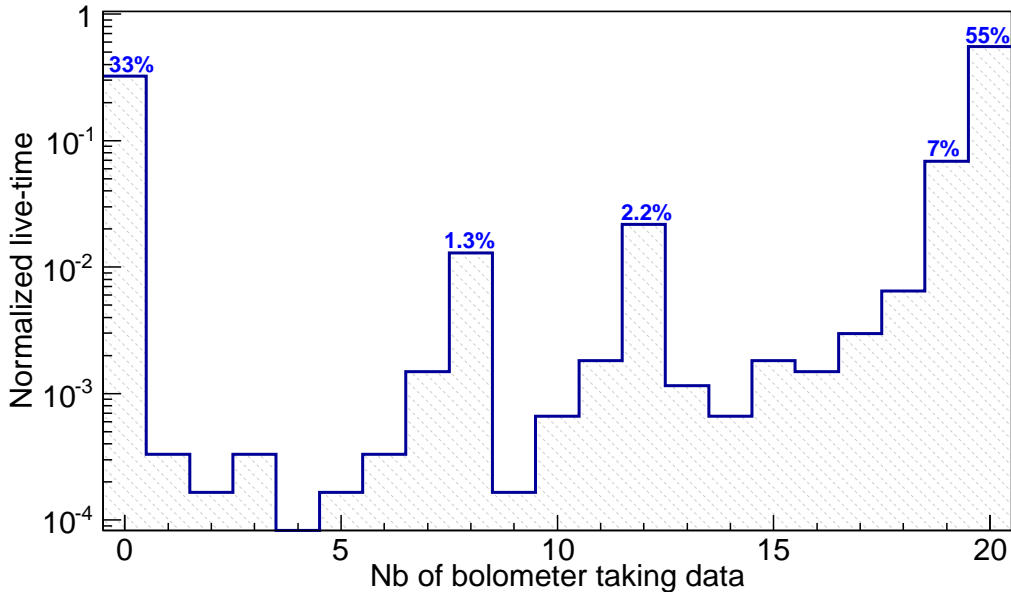
Figure 5.2. – Distribution of the number of active bolometers during the studied period in percent of the total live-time. A bolometer is considered active is there is at least one hit per hour with $E_{\mathrm{ion}} > 2\,\mathrm{keV}$.

both heat (presence of a trigger) and ionization measurements are functioning and cuts most of the noise-induced events. It means that physical data is taken, which can be used to search for dark matter or for coincidences. With this condition, the measured hit rate varies between 9 and 16 hits/hour/bolometer depending on the detector response at low energy and the radiopurity of the materials in proximity of the bolometer.

However, the hourly binning does not allow to cut the so-called *maintenance* periods. During this procedure, the data taking is interrupted and the bias voltages on the bolometer electrodes are set back to their default values. This operation is necessary to ensure a constant electric field through the detector volume over time. Indeed, as the bolometers have a floating voltage, the bias on the electrodes decreases due to the accumulated charge carriers. A first maintenance is performed $100\,\mathrm{s}$ after the start of the run and repeated automatically. It was done every $5000\,\mathrm{s}$ at a length of $174\,\mathrm{s}$ before the 1st of October 2014 (inducing a dead-time of 3.5%), and every $10000\,\mathrm{s}$ for $110\,\mathrm{s}$ afterwards with the aim to reduce the associated dead-time down to 1.1%. As the bolometer data taking is started independently on the 3 acquisition Macs, the maintenance periods are either overlapping in time or totally desynchronized depending on how the run was started. The number of bolometers actually taking data therefore varies depending on which Mac was in maintenance.

To ensure a precise comparison between the measured and simulated coincidence rate, the maintenance periods of individual Macs were identified and cut from the data. For this purpose, the hit rate per Mac per $30\,\mathrm{s}$ has been extracted. The start and end of the maintenance periods were derived by searching for at least 2 and up to 5 consecutive empty bins. However, this technique is not applicable for Mac S2 which reads-out only 4 bolometers. Indeed, the probability to have two consecutive empty bins due to statistical fluctuations of the rate is significant and would artificially decrease the live-time. Therefore the 4 bolometers read out by Mac S2 were excluded from the coincidence analysis. The expected decrease of the coincidence rate was estimated from simulations to be of $\simeq 8\%$.

Once the maintenance cut was applied, the number of active bolometers per hour in Mac

S1 and S3 was derived. A bolometer is considered active if it measures at least one hit per hour with $E_{\text{ion}} > 2\,\text{keV}$. As can be seen in fig. 5.2, for 88% of the studied time period, the bolometer array is either entirely ON or OFF. The increase of live-time for 8 or 12 active bolometers corresponds to hours during which only Mac S1 or Mac S3 were working. The 7% of live-time with 19 bolometers taking physical data is mostly due to two bolometers, FID832 (11.1 days) and FID821 (3.8 days), whose electronics were suffering from energy saturation. Typically, each hour bin with less than 20 active bolometers should be cut. Nevertheless, in order to increase the live-time and consequently reduce the statistical uncertainties on the coincidence rate, hour bins during which only FID821 or FID832 were off are kept in the data selection. That implies that the simulated coincidence rate will be determined by simulating 3 configurations (full array ON or FID821 OFF or FID832 OFF) which will be scaled according to the contribution of each configuration to the live-time. Note that the contribution of individual bolometers to the coincidence rate depends on its position in the cryostat: a bolometer on the outer part of the array contributes more than a bolometer inside it.

After the selection cuts have been applied, a precise live-time determination of the selected data is required. The cut on the number of active bolometers per hour ensures that at least one physical hit per bolometer has been registered. The contribution of each remaining hour is then weighted by the number of minutes during which the acquisition was ON. This is the case when there is at least one bolometer hit registered in one of the 20 studied bolometers without any requirement on the energy. In addition, time periods were cut during which the μ-veto system was not running. Last, the dead-time induced by the reset of the FET boxes needs to be implemented. During this time, the capacitors contained in these pre-amplifiers are discharged to avoid saturation. It occurred every 32 s for 2 s before the 1st of October 2014 (6.2%), and every 64 s for 2 s afterwards (3.1%), with the aim to reduce the associated dead-time. The dead-time following an energy deposit is neglected: most events triggering the acquisition are single events, meaning that the rest of the bolometer array is sensitive to coincidences.

The effect on the live-time of each of the cut described above is detailed in table 5.1. Concerning the systematic uncertainty on the live-time, a detailed study on the influence of the bin size used to calculate the live-time was performed in [150]. Indeed, a large time interval leads to an overestimation of the live-time as time periods during which the acquisition was off are counted. On the contrary, a small time interval can lead to an underestimation of the live-time if, due to the limited trigger rate, no event are observed in the time interval. From this study, a conservative systematic uncertainty of $\pm 5\%$ was derived for a bin size of one hour. In the coincidence analysis performed here, each hour bin is weighted by the number of minutes during which the acquisition was on. Thus, the associated uncertainty on the live-time is smaller. A conservative value of $\pm 2\%$ is considered hereafter. To summarize, the accumulated live-time for the coincidence analysis is:

$$t^{B+V} = (133.6 \pm 2.7)\,\text{days} \tag{5.1}$$

Table 5.1. – Live-time in days remaining after each cut. See text for more details.

cut	live-time (in days)
none	161.1
maintenances	157.8
nb of bolo ON	145.0
μ-veto	139.2
FET resets	133.6

5.3. Characteristics of coincidences between muon-veto and bolometers

After selection of the bolometer and μ-veto data, each μ-veto event is associated to the closest bolometer hit in time. Together, they form a potential physical coincidence, later on referred to as candidate. To be considered a physical coincidence, the time difference between the two, $\Delta t = t_{bolo} - t_{veto}$, should be included within a certain range. Candidates outside this window are considered to be accidental coincidences. The first step in this analysis is to find the adapted time range for the coincidence region, which depends on the goal of the analysis. With the view of comparing the measured and simulated coincidence rate, the window should be as narrow as possible to maximize the signal to noise ratio and therefore reduce the statistical uncertainties on the measured coincidence rate. On the contrary, in the WIMP search, this window will be chosen wider to veto bolometer events to conservatively reject potential μ-induced events.

The expected value of Δt for real coincidences can be deduced as follows: from a physics point of view, the μ-veto event comes earlier than the potential induced bolometers hits. First, the muon deposits energy in the μ-veto system which is converted into an electric signal within tens of nanoseconds. The two signals on each module end are then sent to an electronic chain (described in section 3.2.2.2) which induces an additional delay of $\mathcal{O}(100\,\text{ns})$ [101]. As the longest possible muon track in the setup is covered in 80 ns, the energy deposit induced by the muon exiting the μ-veto will be registered in the same event. Thus, the delay between the physical interaction in the μ-veto system and the event timing is of the order of 100-200 ns. As for the bolometer timing, it is determined with respect to the maximum of the ionization signal (see section 2.1.3.2). It is known from simulations of charge migration that the ionization rise time for an FID800 detector varies between a few hundreds of ns for surface events up to $1\,\mu\text{s}$ for bulk events [151]. Consequently, a small positive time difference $\Delta t = t_{bolo} - t_{veto} \simeq 1\,\mu\text{s}$ is expected from physics point of view. Nevertheless, the coincidence peak in EDELWEISS-II was measured at $\Delta t \simeq 50\,\mu\text{s}$. This delay was induced by the bolometer acquisition chain, notably by the pulse filtering in the online processing. As this part of the acquisition was not updated, the same delay is expected in the EDELWEISS-III phase. This shift is not an issue for the coincidence analysis if it is constant over time.

With the aim of analysing the characteristics of the coincidence events, a cut on the multiplicity of the μ-veto event was applied in favour of a good signal to noise ratio. As the μ-veto system is a hermetically closed system, most of muons ($\sim 85\%$) deposit energy in at least 2 modules. Therefore the following cut is applied on the μ-veto multiplicity M_{veto}:

$$M_{\text{veto}} \geq 2 \tag{5.2}$$

It requires at least a non-zero time (TDC) or energy (ADC) information in 2 distinct modules. It is thus less strict than requiring an energy deposit with full information in two

modules. It reduces the number of μ-veto events selected for the analysis by two orders of magnitude down to 2.4×10^5 events.

Note that this requirement biases the determination of the coincidence rate as it excludes muons crossing a single module. However, it is only used to determine the coincidence window and study the characteristics of the μ-induced events without significant bias from accidentals. It will be later discarded to determine the coincidence rate (see section 5.3.4). The question may arise whether these selection criteria bias the shape of the Δt distribution, from which the coincidence window is determined. This would be the case if the μ-veto multiplicity directly influences the bolometer multiplicity. Indeed, the probability to miss a coincidence because Δt is outside the coincidence window gets lower with increasing bolometer multiplicity. However, no direct correlation between the μ-veto and bolometer multiplicity was found.

5.3.1. Determination of the coincidence window

The distribution of the time differences Δt between the closest bolometer hit and the μ-veto event is plotted in fig. 5.3a. A peak at small positive Δt arising from physical coincidences is clearly distinguishable from the plateau of accidental coincidences. These true coincidences are spread homogeneously in time, as can be seen in fig. 5.3b, showing the Δt distribution versus real time. The interruptions of the continuous line arising from the physical coincidences are due to interruptions of the μ-veto or bolometer data taking. A zoom on the coincidence peak is displayed in fig. 5.3c: two coincidence peaks can actually be distinguished, which are fitted by gaussian distributions. The black distribution shows the Δt values for the 56 coincidences measured before the 11th November 2014. The gaussian fit gives a mean value of 54.6±0.4 μs as expected from the EDELWEISS-II coincidence analysis. The red distribution shows the Δt values for the 82 coincidences measured after the 11th November 2014, for which the gaussian fit gives a mean value of 64.5±0.4 μs. This unexpected shift of one 10 μs timestamp of the coincidence peak is correlated with an update of the DAQ crate (described in section 2.1.4) delivering the common clock to both bolometer and μ-veto system. After being identified, this shift can be taken into account and does not pose an issue for the coincidence analysis. As its origin is not clear, the shift is not corrected but two coincidence windows are defined as the $\pm 3\sigma$ regions centred on the Gaussian mean value obtained before or after the 11th November 2014. To be conservative, the σ of the wider coincidence peak including uncertainty is used, namely $\sigma = 4\,\mu$s. Thus, the coincidence regions are defined as follow:

$$\Delta t = 54 \ \mu s \pm 12 \ \mu s \quad \text{from } 25^{\text{th}} \text{ July } 2014 \text{ to } 11^{\text{th}} \text{ November } 2014 \tag{5.3}$$

$$\Delta t = 64 \ \mu s \pm 12 \ \mu s \quad \text{from } 11^{\text{th}} \text{ November } 2014 \text{ to } 3^{\text{rd}} \text{ April } 2015 \tag{5.4}$$

Thus, the width of the coincidence windows is $\pm 3\sigma = 24\,\mu$s. It is reduced in comparison to the time window used in the EDELWEISS-II analysis of Run12, which was of $300\,\mu$s width due to a faulty time board in the μ-veto system, and of $60\,\mu$s once this board was replaced [78]. The consequence of a narrower window is a larger ratio of physical coincidences over accidental ones. This progress is due to the installation of an integrated DAQ system developed at the IPE, providing a reliable common clock for both bolometer and μ-veto system.

Despite the flatness of the accidental event distribution outside the two peaks, there might be missed coincidences due to a faulty time reconstruction of bolometer events with high energy deposits. As described in section 2.1.3.2, a μs precision on the bolometer hit timing is not always achievable, notably for high energy deposits saturating the bolometer ADC. In most cases, a pulse is found in the 100 kHz window, from which the bolometer hit timing is derived with a μs precision. However, in case of energy saturation or pile-up events, the pulse might be missed in the short 100 kHz time window: the 1 kHz ionization trace
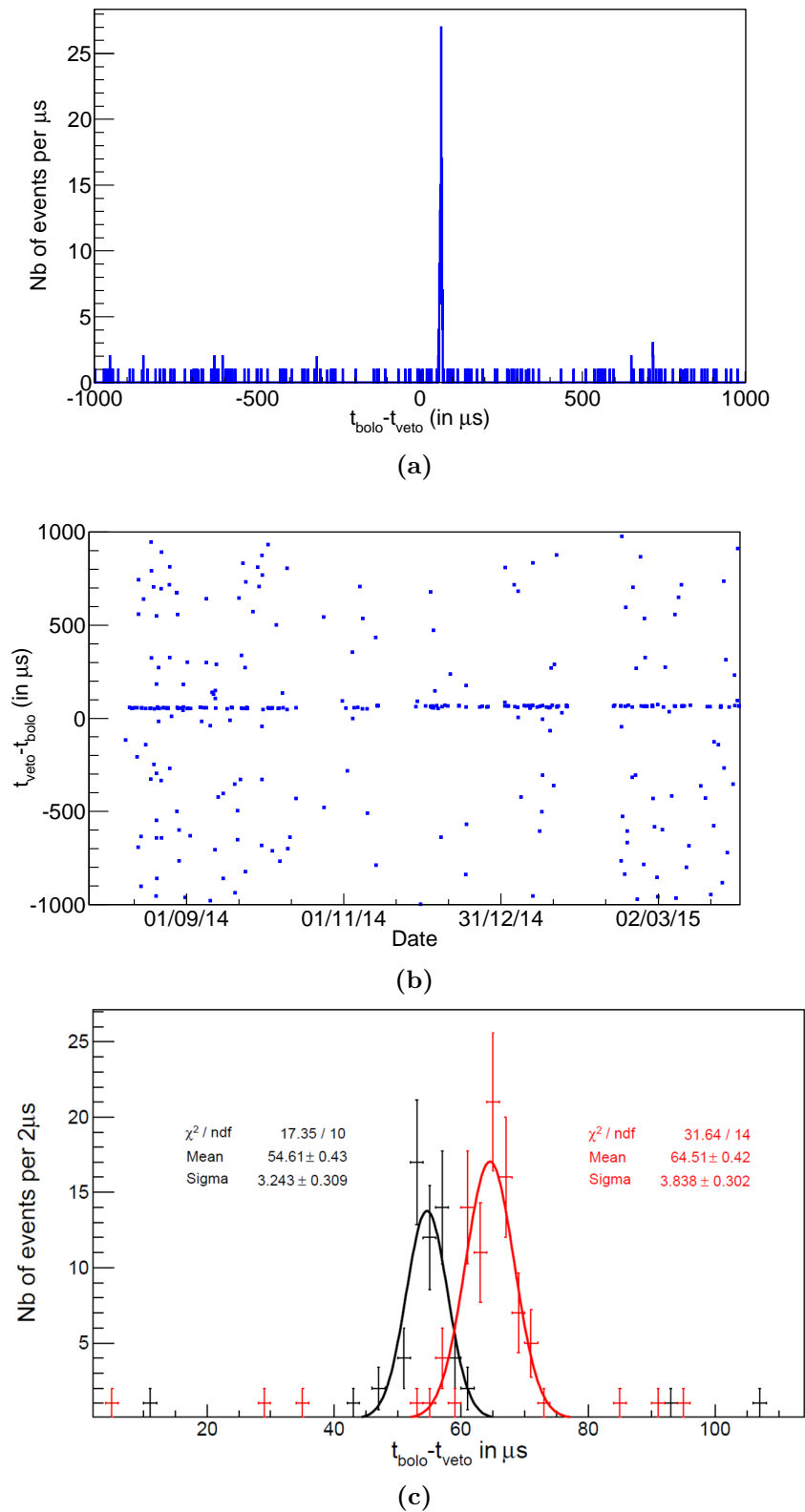
(a)

(b)

(c)

Figure 5.3. – (a) Distribution of the time differences between the closest bolometer hit and the μ-veto event Δt. (b) Δt versus the real time. (c) Zoom on the coincidence peak in the Δt distribution. The black data points arise from data taken before the 11th of November 2014 whereas the red data points arise from data taken after this date. Both distributions are fitted by a gaussian distribution.

is then used to derive the timing, with a precision varying from ms to μs depending on the pulse amplitude. Consequently, some coincidences might be missed because of a worse time resolution. Nevertheless, a saturating μ-induced bolometer hit often comes along with lower energy deposits in other bolometers, for which a precise timing reconstruction is achieved. The narrow coincidence window of $24\,\mu$s width defined in eq. 5.3 and eq. 5.4 is then sufficient to identify the coincidence. The problem arises for rare but existing bolometer events including only saturated hits, that is mostly single saturating energy deposits. The coincidence window is not chosen wider to include these potentially missed coincidences, as it is necessary to achieve the best signal-to-noise ratio in order to study μ-induced bolometer events. An estimation of their number is performed in the following and will be used as systematic uncertainty on the number of measured coincidences.

First, the time window where the potential missed coincidences are expected should
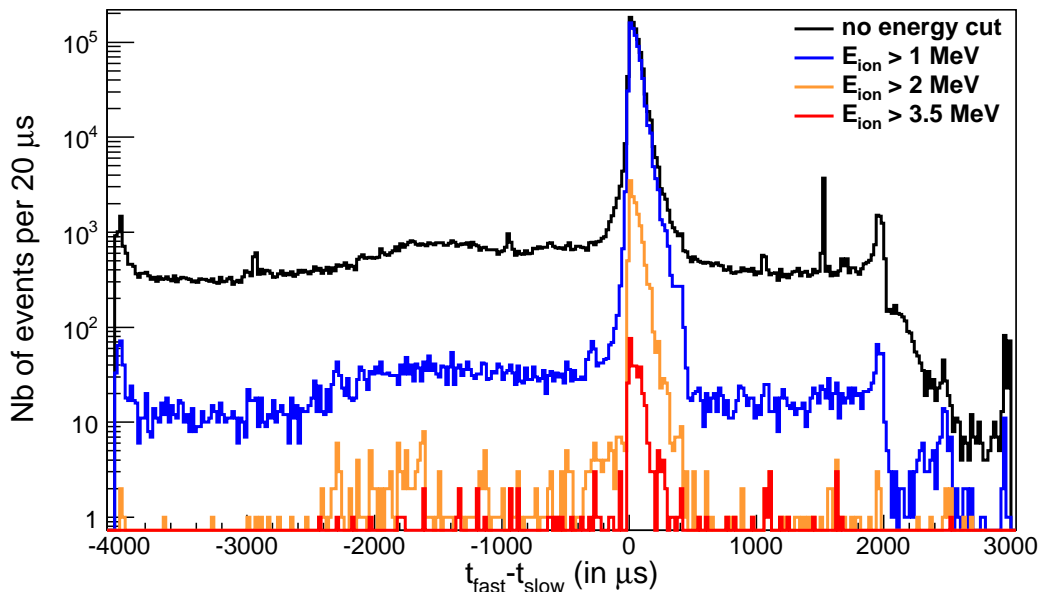
Figure 5.4. – Distribution of $t_{\text{fast}} - t_{\text{slow}}$ for different cuts on the ionization energy deposit for bolometer hits for which a trigger time could be derived both from the $100\,$kHz ionization trace (t_{fast}) and from the $1\,$kHz ionization trace (t_{slow}). See text for more details.

be determined. The timing resolution of the $1\,$kHz channel depending on the bolometer hit energy is therefore studied: bolometer hits with both $100\,$kHz timing t_{fast} and $1\,$kHz timing t_{slow} are selected. The timing difference $\Delta t_{\text{reso}} = t_{\text{fast}} - t_{\text{slow}}$ is plotted in fig. 5.4 for different cuts on the hit ionization energy E_{ion}. The features on this distribution are related to the post-processing algorithm, which will not be detailed here. Without energy cut, the time resolution of the $1\,$kHz channel varies between -4 ms and +3 ms, 75% of all hits being included in a range $\Delta t_{\text{reso}} = [-10, 140]\,\mu$s. The majority of the hits outside this range arises from low energy deposits below $30\,$keV. By selecting bolometer hits with $E_{\text{ion}} > 1\,$MeV, the number of hits included in a $\Delta t_{\text{reso}} = [-10, 140]\,\mu$s range increases up to 91%. Indeed, the steeper the pulse rise is, the more precise is the timing determination. By applying a cut $E_{\text{ion}} > 3.5\,$MeV to reject most γ's, the proportion of μ-induced hits in the selected events rises. 75% of them are included in a time window $\Delta t_{\text{reso}} = [-10, 140]\,\mu$s. The window should be extended to $\Delta t_{\text{reso}} = [-2.5, 3.0]\,$ms to include all hits. In the following, one considers the time resolution of μ-induced events to be included in this window. Knowing the expected time resolution of the $1\,$kHz channel for high energy events, the number of potential coincidences missed because of a worse time resolution can be es-

Table 5.2. – Information about the 3 bolometer hits with a timing determined from the 1 kHz channel in the coincidence window $\Delta t = [-2.5, 3.0]$ ms. The parameters given in the table are Δt the time difference between the bolometer hit and the μ-veto event, E_{ion} the measured ionization energy, E_{rec} the measured recoil energy, the bolometer multiplicity, the name of the detector and the run and event numbers characterising the hits.

Δt (in μs)	E_{ion} (in keV)	E_{rec} (in keV)	bolometer multiplicity	FID	run number	event number
54.3	149.6	156.1	1	840	3052402	9586
168.4	257.4	235.4	1	810	1031800	17560
149.0	640.8	666.7	3	822	3082100	717

timated. For this purpose, bolometer hits in coincidence with a μ-veto event for which $t_{bolo} - t_{veto}$ is included in the time window $[-2.5, 3.0\,\text{ms}]$ have been selected. Out of the 588 bolometer hits in potential coincidence, 3 have their timing determined from the 1 kHz channel and could be physical coincidences missed because of a worse timing resolution. Information about these bolometer hits are given in table 5.2. Contrary to what was expected, the energy deposited is far from saturating the electronics. One hit is included in the coincidence window of 24 μs. Looking at the traces of these 3 hits, it can be determined that the online trigger time determined in the acquisition software is not properly reconstructed despite clear and well shaped pulses. It could be due to a trigger on noise shortly before the energy deposit. Even if these hits look like typical γ interaction, it is not possible to determine with certainty whether these hits are μ-induced or not. To be conservative, we consider that these hits are μ-induced events and that 2 are missed because of a too narrow coincidence window.

To conclude, there is no indication that high energy events typically induced by muons are affected by a worse timing resolution. For WIMP search, a conservative coincidence window of ± 1 ms is therefore considered wide enough.

5.3.2. Rate of coincidences with a multiplicity cut on the muon-veto

The rate of coincidences is determined by simply integrating the number of events in the coincidence regions defined in eq. 5.3 and eq. 5.4. First, the coincidence rate is calculated considering only μ-veto events with a multiplicity $M_{\text{veto}} \geq 2$. A total of $N_{\text{tot}} = 138$ events are measured in the coincidence windows, which are made up of physical coincidences and of accidental coincidences, whose contribution has to be subtracted.

The contribution of accidentals was estimated by selecting the same μ-veto events, but searching for the closest bolometer hit a few seconds before or after: all reconstructed coincidences are then accidentals. The number of accidentals is calculated using a reference window and for a given live-time t^{B+V}, and is averaged over the window width to extract the number of accidentals per unit of μs of coincidence window. To minimize the statistical uncertainties, a wider window than the one used for the coincidence analysis is used. However, the window width should be carefully chosen such that the contribution from accidentals can be considered uniform. Indeed, as each μ-veto event is associated to closest bolometer hit in time, the number of accidental coincidences decreases exponentially with the width of the coincidence window, the slope depending on the trigger rate of the bolometers. A window of 230 μs width is chosen here. To further reduce the statistical uncertainties, the accidental coincidence estimation is performed for several positive and negative delays of the μ-veto event.

By applying the method described above, the number of accidental coincidences per μs is found to be $\Gamma_{\text{acc}} = 0.081 \pm 0.001$ events/μs for a live-time $t^{B+V} = 133.6 \pm 2.7$ days

(eq. 5.1), resulting in an expected number of accidentals in the coincidence regions of $N_{acc} = 1.94 \pm 0.02$ events. The number of physical coincidences can therefore be written as:

$$N^{\mu}_{M_{veto} \geq 2} = N_{tot} - N_{acc} = 136.1 \pm 11.7 \text{ (stat) } {}^{+2.0}_{-0.0} \text{ (sys) events} \qquad (5.5)$$

where $N_{tot} = 138$ events is the total number of events in the coincidence region, and N_{acc} the expected number of accidental coincidences in the coincidence region, as defined above. The statistical uncertainty on $N^{\mu}_{M_{veto} \geq 2}$ is calculated by error propagation and is dominated by the scarce number of coincidences. The systematic uncertainty is derived conservatively by considering that the two coincidence candidates with a timing determined from the 1 kHz ionization window are missed μ-induced events. With a signal-to-noise ratio of $N^{\mu}_{M_{veto} \geq 2}/N_{acc} = 71$, the coincidence selection is almost background free using the cut on the μ-veto multiplicity.

Knowing the live-time of the analysis $t^{B+V} = 133.6 \pm 2.7$ days (eq. 5.1), the coincidence rate can be derived:

$$\Gamma^{\mu}_{M_{veto} \geq 2} = 1.02 \pm 0.09 \text{ (stat) } {}^{+0.03}_{-0.02} \text{ (sys) events/day} \qquad (5.6)$$

Note that no selection is applied on the bolometer data except a 2 keV cut on E_{ion}. That means that no distinction is made between single and multiple events, the type of recoil, the location of the recoil energy deposit (surface or fiducial) and the amount of energy deposited. Thus, only a small fraction of these measured μ-induced events are a potential background for WIMP search.

The comparison of the measured coincidence rate given in eq. 5.6 with the simulated one cannot be performed as the multiplicity cut applied on the data (either one ADC or TDC value non-zero in two modules) is very specific to the electronic data acquisition and thus cannot be reproduced straight forward in the simulation. Indeed, some electronic noise or a background particle interacting simultaneously with the muon passage will artificially bring up the event multiplicity. A more reliable comparison can be performed once the multiplicity cut is discarded, as will be shown in section 5.3.4.

Coincidence rate using the KData analysis pipeline

Parallel to this work, an independent analysis of the coincidence rate between the μ-veto and the bolometers was performed in [152], in the framework of a bachelor thesis. This analysis is based on data files produced with a different analysis pipeline called KData, shortly introduced in section 3.2.2.2. Both analyses share the same raw data but the post-processing is independent and partly different, potentially leading to different reconstructions of the energy and timing for a given bolometer hit.

This coincidence study was performed on the data taken between August 8th and December 1st, 2014. The accumulated live-time when both systems were running is $t^{B+V} = (55.90 \pm 0.02)$ days. This analysis has few specifics: first, the bolometer hits were not already merged into events using a given coincidence window, thus only data per bolometer were available. Therefore the coincidence analysis was performed for each bolometer individually, i.e. each selected μ-veto event was associated to the closest hit in each bolometer. The Δt distributions obtained for each bolometer were summed and the number of bolometer hits in coincidence with the μ-veto determined. The number of coincidence events was derived in a second step by studying the spread in time of the bolometer hits. Another particularity of this analysis is that the timing with a μs precision determined from the 100 kHz ionization trace was available for only part of the data, taken before the 5th of October 2014. At this date, the width of the recorded 100 kHz trace was increased from 20.48 ms to 40.96 ms. As the data processing algorithm was not updated with this change, the timing derived from the 1 kHz ionization trace could only be used after this date. Therefore the 1 kHz timing was used to perform the coincidence analysis. Note that for

the data taken before the 5th of October, a coincidence peak was found at $\Delta t{=}51.7{\pm}0.8\,\mu\text{s}$ using the 100 kHz timing. The slight difference compared to position of the peak position found in fig. 5.3c before the 11th of November, is due to the fact that each hit of a bolometer event contributes to the Δt in the KData analysis, whereas only the closest bolometer hit contributes to the distribution in fig. 5.3c.

The same multiplicity cut as in eq. 5.2 was used to select μ-veto events, which are then associated to the closest hit of each bolometer. The Δt distribution obtained using the bolometer trigger time determined from the 1 kHz window is plotted in fig. 5.5. The origin of the multiple coincidence peaks seen in the Δt of the data taken before the 5th of October could not be established in the framework of this bachelor thesis. It might be explained by the different filters applied on the data. By studying the resolution of the 1 kHz channel in a similar way as described in section 5.3.1, the coincidence window was determined to be $\Delta t = [-430, 690]\,\mu\text{s}$. Thus, because the timing of the bolometer hits could not be derived with a μs precision, the coincidence window is much wider than the 24 μs window used in the analysis developed in this thesis (see eq. 5.3 and eq. 5.4). A total of 300 hits are included within the wide coincidence window, distributed over 120 bolometer events with an estimated number of accidentals of 63.6 events. With such a wide window, the signal-to-noise ratio is of 0.9 i.e. the selection is dominated by accidental coincidences. The following coincidence rate has been deduced:

$$\Gamma^{\mu}_{\text{M}_{\text{veto}}\geq 2} = 1.01 \pm 0.24 \text{ (stat)} \pm 0.01 \text{ (sys) events/day} \tag{5.7}$$

This rate is in good agreement with the results described in this thesis (eq. 5.6), obtained with an independent analysis pipeline. It confirms that the number of coincidences potentially missed by the narrow window of 24 μs is negligible.
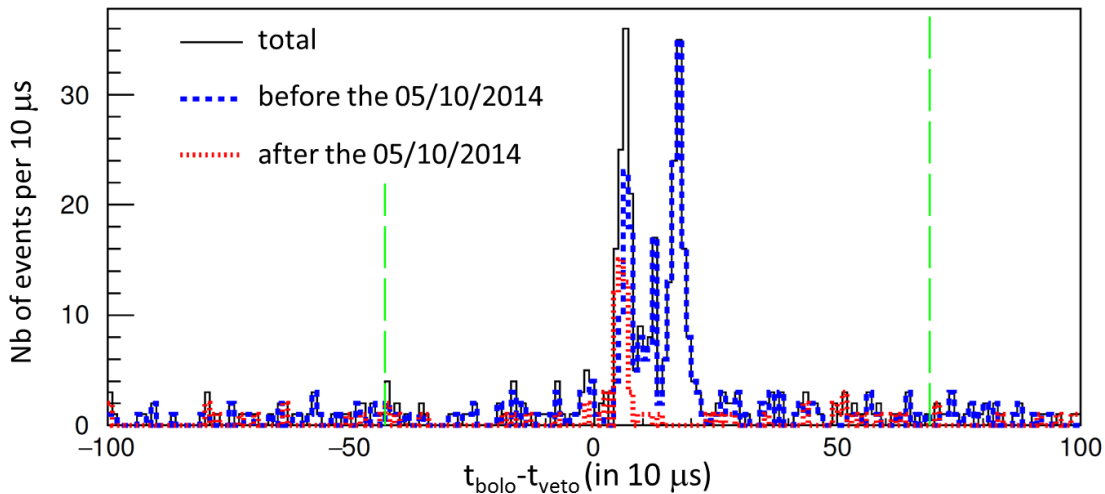
Figure 5.5. – Distribution of $\Delta t = t_{\text{bolo}} - t_{\text{veto}}$ for all bolometer hits in coincidence with a μ-veto event satisfying $M_{veto} \geq 2$, obtained using the KData analysis pipeline. The bolometer trigger time used here was extracted from the 1 kHz ionization channel. The vertical dashed lines indicate the boundaries of the coincidence window as used in the KData analysis. The coincidence window defined using the KData analysis pipeline is wider than the 24 μs window derived with the other analysis pipeline used in this thesis, as a μs precision on the bolometer timing could not be achieved with the KData pipeline. Extracted from [152].

5.3.3. Signatures of muon-induced bolometer events

Due to the narrow coincidence window of 24 μs (see eq. 5.3 and eq. 5.4) and the cut of the μ-veto multiplicity, an almost background free selection of coincidences is achieved. Thus,

the signatures of μ-induced bolometer events can be studied with only a negligible bias from accidental coincidences.

Multiplicity distribution

Although only 20 bolometers are considered in this analysis, all the 24 read out bolometers are used to determine the bolometer event multiplicity for a more efficient rejection of single events. Note that the multiplicity condition $M_{veto} \geq 2$ applied to select μ-veto events does not influence the multiplicity distribution of the bolometer events.

The multiplicity distribution of events included in the coincidence windows (i.e. mostly physical coincidences) is drawn in fig. 5.6, together with the multiplicity distribution for accidental coincidences. For the latter one, a mean multiplicity of $M_{\text{bolo}}^{\text{acc}} = 1.2$ is derived. More precisely, 84.4% of the events are single and 99.6% have an interaction in 3 bolometers or less. Large multiplicities are only occasionally reached when the bolometers collectively trigger on electronic or mechanical noise. The mean multiplicity of physical coincidences is significantly higher with $M_{\text{bolo}}^{\mu} = 4.6$. Out of the 136 physical coincidences, $(75 \pm 0.07)\%$ have multiple interactions within the bolometer array. The coincidence analysis performed in [152] (summarized in the previous section) using the KData analysis pipeline gives a similar mean multiplicity of $M_{\text{bolo}}^{\mu} = 4.2$ for a reduced data set and with slightly stricter cuts on the bolometer data [2]. In addition, the time window used to determine if two bolometer hits are considered as one event is not the same: whereas a variable window [3] is used in this analysis, a study of the spread in time of the coincident hits was performed with KData, as it did not include any event building. Considering these differences, the results are in good agreement.

The multiplicity distribution of events occurring in the 20 selected bolometers was also derived from simulations of muons through the experimental setup, described in section 3.4. The multiplicity in the simulation is defined as the number of bolometer hits with E_{heat} above the bolometer-dependent trigger threshold. Note that only average trigger values over Run308 are applied on the simulated data, whereas the actual triggers are adaptive in order to regulate the trigger rate. The measured and simulated multiplicity distributions are compared in fig. 5.7. A lower multiplicity of 3.1 hits is expected from simulations, with 60% of the μ-induced events inducing multiple scattering. There are 15% more single scattering events in the simulation than were actually measured, and the measured spectrum at higher multiplicity is higher than the simulated one. Probable reasons to explain the discrepancy are: first, the measured multiplicity is artificially increased due to accidental coincidences between unrelated bolometer hits. Considering the averaged trigger rate of the bolometer array of about few Hz and the variable coincidence window, there is a probability of few percent that two unrelated bolometer hits are considered as one event. This percentage significantly varies depending on the trigger threshold and the noise conditions. Another reason is that the bolometer response implemented on the simulation is only the averaged one, although the detection of low energy deposits is strongly sensitive to the bolometer threshold and energy resolutions at a given time. More on the comparison between simulation and data will be given in section 5.3.4.2 where the two coincidence rates will be compared.

Compared to the mean multiplicity of physical coincidences $M_{\text{bolo}}^{\mu} = 4.6$, the value measured in EDELWEISS-II with 12 detectors was significantly lower with $M_{\text{bolo}}^{\mu} = 2.27$, where $(46.6 \pm 0.6)\%$ of the coincidence events were multiple interactions [78]. In EDELWEISS-III, 75% of the μ-induced background can be rejected by requiring that a WIMP scattering would produce a single recoil. Indeed, due to the higher granularity and density of the

---

2. In the analysis performed with KData, a cut of $2\,\text{keV}$ on E_{ion} and E_{heat} was applied whereas a single cut of $2\,\text{keV}$ applied on E_{ion} is required in the analysis performed in this thesis

3. Each hit which is less than $10\,\text{ms}$ after the previous hit is considered to be part of the same event i.e. the coincidence window is a multiple of $10\,\text{ms}$
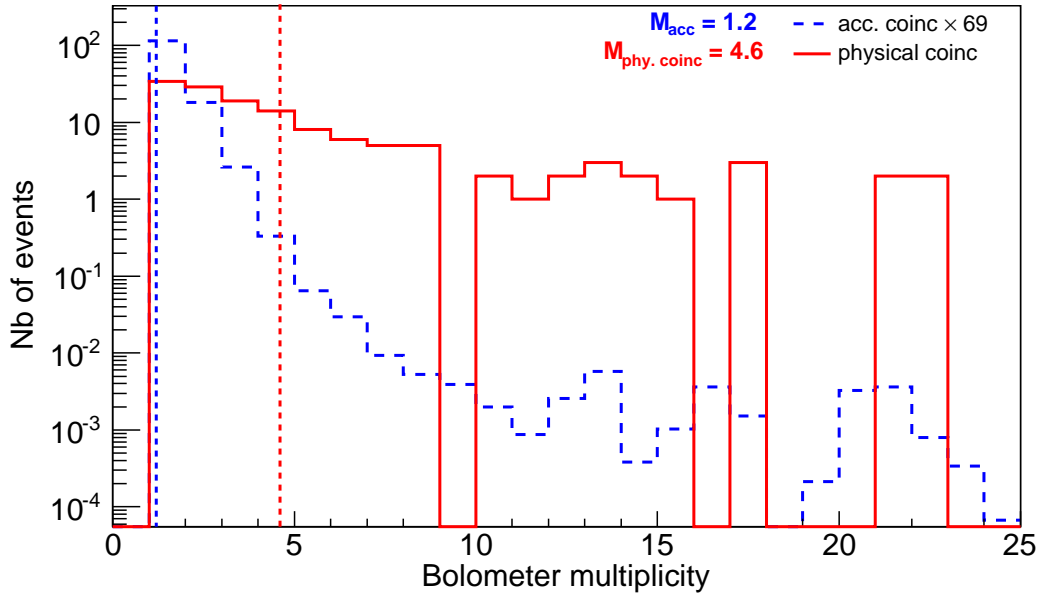
Figure 5.6. – Bolometer multiplicity distribution for physical coincidences (red) and for accidental coincidences (blue). The distribution for accidental coincidences was normalized to the number of measured physical coincidences. Vertical dashed lines indicate the mean multiplicity of each distribution.
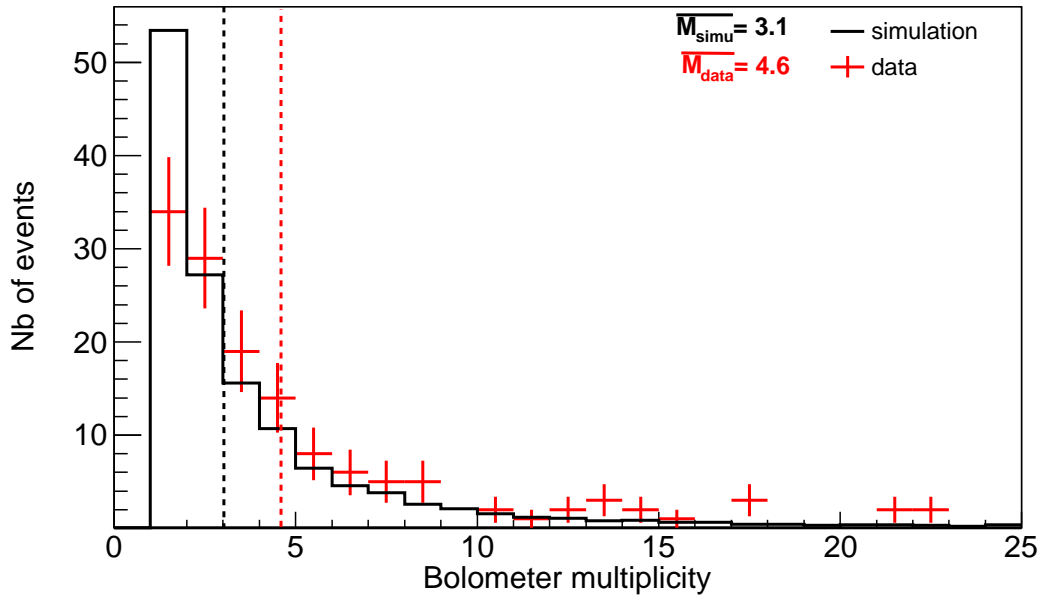

Figure 5.7. – Bolometer multiplicity distributions from the data (red) and from simulation normalized to the measuring time of $t^{B+V} = 133.6$ days (black). Vertical dashed lines indicate the mean multiplicity of each distribution.

bolometer array, the mean multiplicity of μ-induced events is higher. Note that it is further reduced by requiring hits to occur in the fiducial volume, depositing energy only in a ROI and in the 90% C.L. nuclear recoil band considered for WIMP search.

Recoil energy spectrum

To further study the characteristics of μ-induced events, the sum of the recoil energy (derived as shown in section 2.1.2.1) of all bolometer hits in coincidence is plotted for accidental coincidences in fig. 5.8 and for physical coincidences in fig. 5.9. Several features can be recognized in the shape of the accidental energy spectrum, which extends mostly up to 10 MeV. The steep decrease up to 3 MeV is due to $\gamma's$ from natural radioactivity which dominate the trigger rate with 70 measured events/(kg · day). They are produced by the decays of ^{60}Co, ^{40}K and ^{238}U/^{232}Th daughter nuclei, and lose their energy via photoelectric effect or Compton scattering in the bolometers. As shown in fig. 5.8, they mostly interact in a single (86%) or in two bolometers (13.7%). The peak at 5.1 MeV is due to the interaction of α-particles of energy $E_\alpha = 5.3$ MeV produced by the decay of ^{210}Po (a radon daughter). As expected, 95% of α-particles are single scattering events. The remaining 5% with multiplicity 2 are most probably due to accidental coincidences with another bolometer hit. The high energy tail in the spectrum can be explained by several contributions: first, by the interaction of high energy α's from the decay of polonium isotopes (produced by the U/Th decay chains, see appendix A) with a Q-value of 9.0 MeV and 7.7 MeV, respectively. However, their contribution should be relatively small as no clear α peak can be seen. Another possible explanation for the high energy tail with $M_{\text{bolo}} > 2$ are accidental coincidences between an α and a high energy γ. But the most probable explanation is the wrong estimation of the heat energy for large energy deposits as the heat pulse is saturated. In this case, the pulse template used to determine the heat energy does not describe the pulse well, which can lead to an overestimation of the heat energy. The estimate of the ionization energy is therefore more reliable for large energy deposits as the ionization pulse is a Heaviside function.

The summed energy spectra of accidental and real coincidences are compared in fig. 5.9. The accidental spectrum has been scaled by a factor $1/(2 \times 10^4)$ in comparison to its actual contribution ($N_{\text{acc}} = 1.94$ events as derived in section 5.3.2). In comparison to the accidental coincidences, the energy spectrum of real coincidences extends to much higher energies, up to $\sim$70 MeV. Such large energy deposits occur when a muon crosses the detector, depositing on average 10 MeV/cm. A broad peak centred at 35 MeV is expected from simulations due to the favoured path length of muons inside the crystal induced by the zenith angle distribution of the muon flux. However, due to the limited statistics, this peak cannot be seen in the measured spectrum. Energy deposits at lower energies come from the hadronic and electromagnetic showers induced by the muon in the materials of the setup.
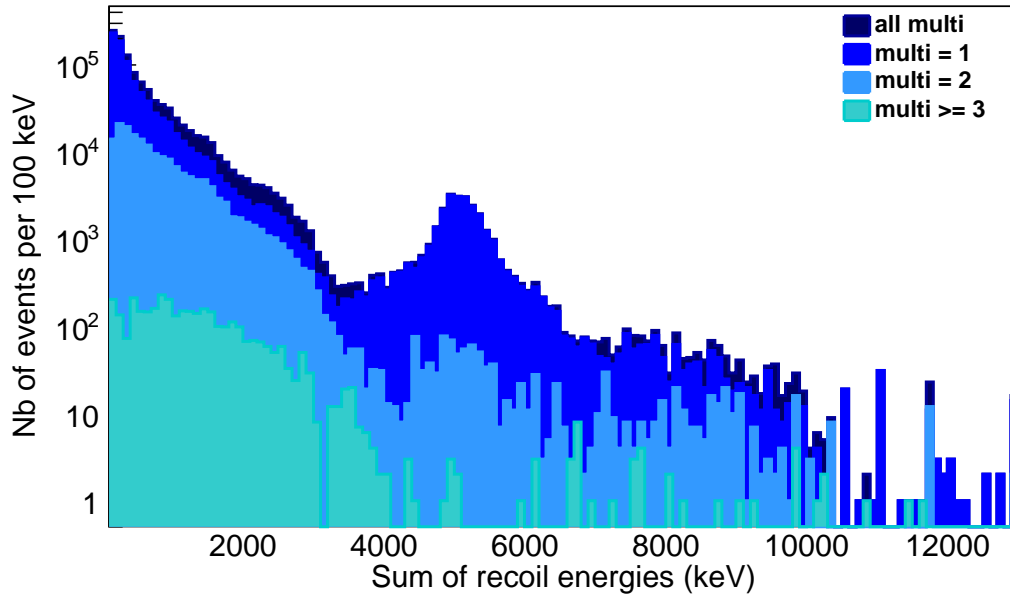
Figure 5.8. – Distribution of the sum of the recoil energies in the bolometer array for accidental coincidences. The color code indicates the multiplicity of the event following the legend.
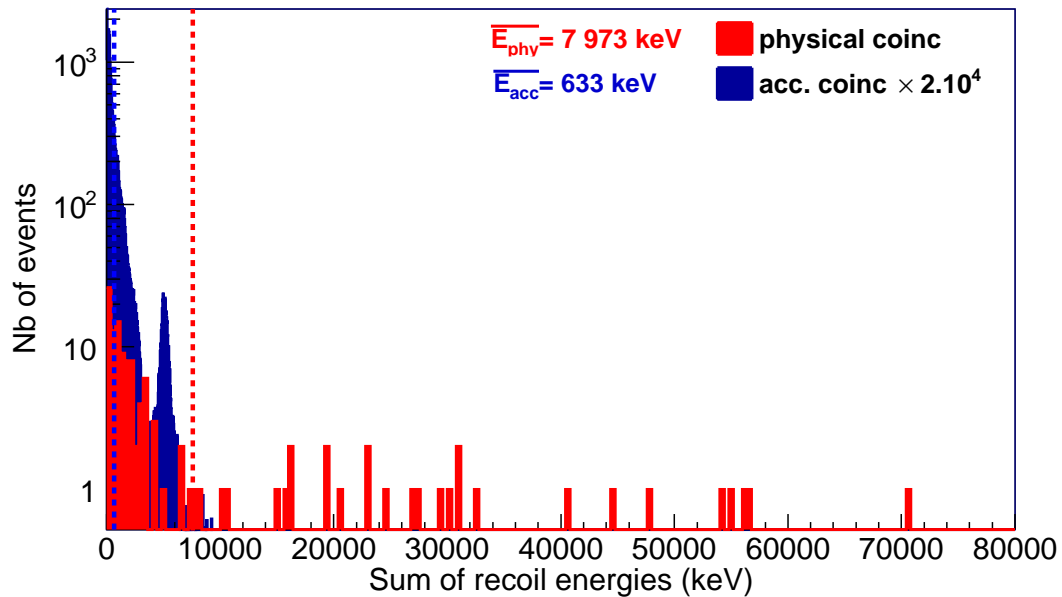
Figure 5.9. – Distribution of the sum of the recoil energies in the bolometer array for the physical (red) and accidental (blue) coincidences. The energy spectrum of accidentals has been scaled by a factor of $1/(2 \times 10^4)$ in comparison to its expected contribution to the physical coincidences energy spectrum ($N_{\mathrm{acc}} = 1.94$ events). The vertical dashed lines indicate the mean total recoil energy for each spectrum.

Distribution of the μ-veto multiplicity

The multiplicity of the μ-veto events M_{veto}^{2TDCs} in coincidence with the bolometer array is shown in fig. 5.10. Here it is required that each fired module has at least its 2 TDC signals non-zero, i.e. satisfies the trigger condition. This cut is stricter than the $M_{veto} \geq 2$ cut applied to select μ-veto events, where only one ADC or TDC signal should be non-zero for a module to be counted. It is more appropriate to reflect the real multiplicity of the μ-veto event without influence of possible noise in one or several modules. In fig. 5.10, the μ-veto multiplicity for physical coincidences is compared to the multiplicity of all μ-veto events, which are mostly arising from ambient radioactivity and noise. The mean multiplicity varies from $M_{veto}^{\text{2TDCs}} = 3.3$ for physical coincidences down to $M_{veto}^{\text{2TDCs}} = 1.4$ for all μ-veto events. 98.5% of the μ-veto events have a μ-veto multiplicity 1 or less. Surprisingly, 7.5% of all events have a multiplicity 0, i.e. no module has both its TDC non-zero, despite this condition should be required for the acquisition to be triggered. Most probably, the discriminators responsible of the trigger decision are working correctly but one of TDC cards, reading one discriminator output, is certainly malfunctioning (see fig. 3.7). These events are characterized by one or more non-zero TDC values in different modules. They do not represent an issue for the coincidence analysis as they are correctly stamped. Note that none of the physical coincidences are of multiplicity 0. More than 90% have a multiplicity above 1 but this number will decrease once the cut on the μ-veto multiplicity (eq. 5.2) will be discarded, as will be shown in the following section.

5.3.4. Comparison of the measured and simulated coincidence rates

In the previous section, the coincidence region has been determined by applying a cut on the μ-veto multiplicity (eq. 5.2) minimizing the bias from accidental coincidences. This cut is now discarded to additionally include coincidences for which only one module of the μ-veto was hit and thus determine the total rate of μ-induced events.

5.3.4.1. Measured rate of muon-induced bolometer events

The Δt distribution obtained after removing the cut on the μ-veto multiplicity is plotted in fig. 5.11. The number of events included in the coincidence windows defined in equations 5.3 and 5.4 increases from $N_{M_{\text{veto}} \geq 2}^{tot} = 138$ with multiplicity cut to $N^{tot} = 190$ events without. The number of expected accidental coincidences per μs unit of the coincidence window is calculated as described in section 5.3.2, using all μ-veto events. It increases by a factor 16 up to $\Gamma_{acc} = 1.34 \pm 0.06$ events/μs for a live-time $t^{B+V} = 133.6 \pm 2.7$ days (eq. 5.1). The expected number of accidentals in the coincidence region is thus $N_{acc} = 32.1 \pm 1.4$ events. The number of physical coincidences in the coincidence windows is:

$$N_{M_{\text{veto}} \geq 1}^{\mu} = N_{tot} - N_{acc} = 157.9 \pm 14.0 \text{ (stat) } ^{+2.3}_{-0.0} \text{ (sys) events} \qquad (5.8)$$

The statistical uncertainties are derived by error propagation on the number of measured events in the coincidence windows and on the expected number of accidental coincidences. The systematic uncertainty comes from the number of bolometer hits in coincidence with the μ-veto, whose trigger time was determined using the 1 kHz time window (see section 5.3.1). It was extrapolated from the number of measured events with the multiplicity cut on the μ-veto, considering that it scales with the live-time. Note that the signal-to-noise ratio decreases from 71 to 5 by discarding the cut on the μ-veto multiplicity. Using the live-time $t^{B+V} = 133.6 \pm 2.7$ days, the overall rate of μ-induced events in the 20 bolometers selected in this analysis is:

$$\Gamma_{M_{\text{veto}} \geq 1}^{\mu} = 1.18 \pm 0.10 \text{ (stat) } ^{+0.03}_{-0.02} \text{ (sys) events/day} \qquad (5.9)$$
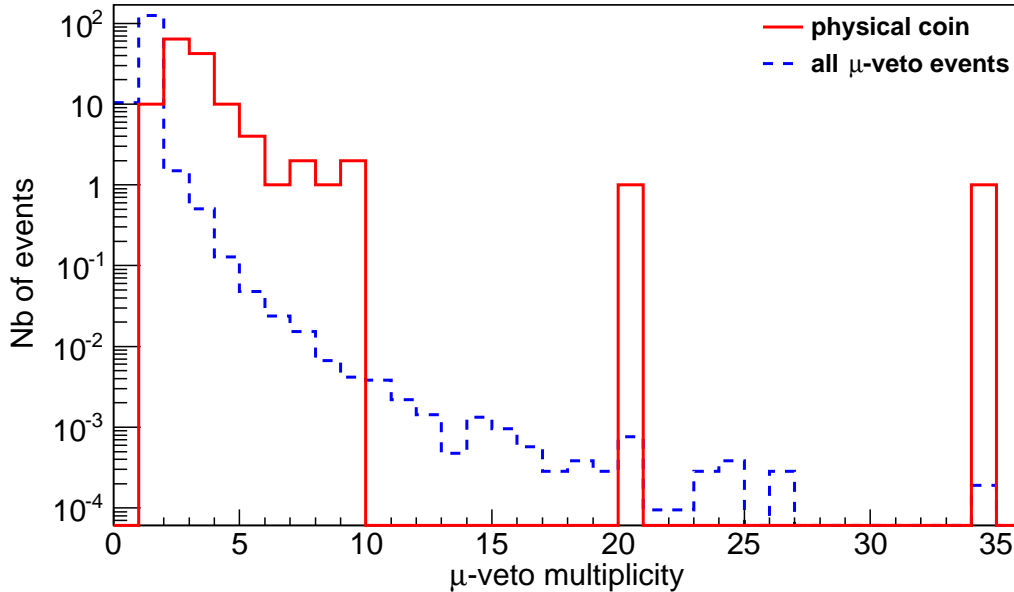
Figure 5.10. – Muon-veto multiplicity distribution for physical coincidences (red) and all events in the μ-veto system (blue) normalized to the number of measured physical coincidences, requiring each fired module to have at least 2 non-zero TDC signals.

By comparing this rate with the one obtained with a multiplicity cut in eq. 5.6, one can deduce that 15.7% of muons inducing a bolometer event deposit energy in only 1 module of the μ-veto. This result can be compared with the simulated geometric efficiency of the μ-veto to detect muons going through the lead shield calculated in [103], requiring at least either one or two modules to be hit. Without taking into account any module response (i.e. assuming the modules to be 100% efficient), an efficiency of $\varepsilon \geq 85.7\%$ was found by requiring at least two modules to be hit, whereas an efficiency of $\varepsilon \geq 99.7\%$ was achieved by requiring at least one module to be hit. As this simulation does not include secondary particles produced by muons, the 15% increase in geometric efficiency (and thus in coincidence rate) is an upper estimation of the expected rise. This rise should be additionally lowered as some μ-veto events are artificially considered as multiplicity 2 because of noise simultaneous to the muon passage. However, this 15% difference expected from the simulation is derived considering all modules to be 100% efficient. With more realistic efficiencies, the contribution of events with multiplicity 1 will increase. Therefore, the measured difference of 15.7% is in the range of expectation.

As explained earlier, the rate in eq. 5.9 includes nuclear recoils as well as electronic recoils in the whole detector volume and without any condition on the deposited energy. The rate of WIMP-like events limiting the sensitivity for dark matter search is determined by selecting single nuclear recoils in the 90% C.L. nuclear recoil band occurring in the fiducial volume and depositing energy in the region of interest. To estimate the number of such events in the selected data set in this analysis, the ionization yield Q versus the recoil energy is plotted in fig. 5.12 for all bolometer hits in coincidence with a μ-veto event. Note that a dedicated analysis of the number of μ-induced WIMP-like events in the standard and low mass WIMP analyses of the EDELWEISS-III data will be given in the next chapter for the selected bolometers. For the data selected in this analysis, 4 single nuclear recoil events with $Q<0.6$ are measured in $E_{\rm rec} = [10, 200]$ keV and are listed in table 5.3; 2 of them are located in the 90% nuclear recoil band of their respective detector, defined using the average resolutions of each bolometer over the Run308. The cleaner
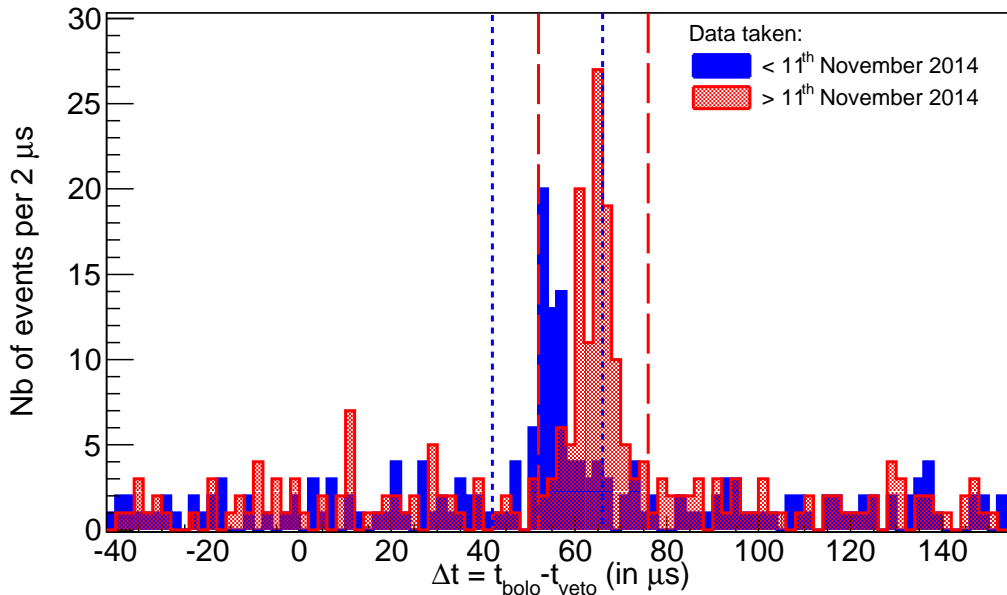
Figure 5.11. – Distribution of $\Delta t = t_{\text{bolo}} - t_{\text{veto}}$ before (blue) and after (red) the 11$^{\text{th}}$ of November 2014 without cut on the μ-veto multiplicity (all μ-veto events were associated to the closest bolometer hit). The vertical dashed lines indicate the coincidence region for each data taking period.

way to determine whether they are inside the nuclear recoil band is to use the hourly resolutions of the individual bolometers. However, this information was not accessible in the data files used in this analysis. It has not been further investigated, as all 4 hits have a significant signal on the veto electrodes and are therefore clear surface events. In addition, 3 of them have been measured in detectors known to have issues, which are excluded from dark matter search. They are therefore most probably wrongly reconstructed electronic recoils. Thus, no WIMP-like event has been measured in the 20 bolometers selected for the analysis live-time of $t^{B+V} = 133.6 \pm 2.7$ days. The 90% upper limit on the rate of μ-induced WIMP-like events can then be deduced:

$$\Gamma_{\text{M}_{\text{veto}} \geq 1}^{\text{WIMP-like}} < 0.017 \text{ events/day} \quad \text{at 90\% C.L.} \tag{5.10}$$

The μ-induced bolometer event rate varies significantly with the geometry of the bolometers inside the cryostat. It does not depend much on the volume occupied by the array but more on the covered surface. Indeed, adding more detectors in a given volume increases mostly the mean multiplicity but does not significantly increase the rate of coincidences dominated by the muon flux. The latest coincidence analysis for EDELWEISS-II [78, 32] was performed using 12 ID detectors installed in 4 towers holding 4 detectors each and arranged cylindrically (towers T1, T2, T3, T8 in fig. 2.5). From the total accumulated live-time of 307 days, a coincidence rate of $\Gamma_{\text{M}_{\text{veto}} \geq 1}^{\mu}(\text{EDW-II}) = 0.84 \pm 0.06$ events/day was derived. The measured coincidence rate in EDELWEISS-III (eq. 5.9) is thus 40% higher than in EDELWEISS-II for an increase of mass of about a factor 3.3. Indeed, the 20 selected FID detectors for the coincidence analysis are located in 5 towers, containing 4 detectors each and covering the total cross section of the cryostat (towers T2, T3, T4, T8 and T9 in fig. 2.5). As for the rate of WIMP-like events measured in EDELWEISS-II, it was determined to be $\Gamma_{\text{M}_{\text{veto}} \geq 1}^{\mu} = 0.013 \pm 0.007$ events/day before vetoing. The μ-induced WIMP-like event rate in EDELWEISS-III could not be measured for the accumulated live-time of this analysis. Only an upper limit as given on eq. 5.10 can be set. Two upgrades performed on the setup indicate that this rate should indeed be smaller than

FID	Q	E_{rec} (keV)	Δt (in μs)	remark
807	0.37	13.02	5.7	surface + leakage current
810	0.15	13.31	6.2	surface + unstable heat channel
845	0.41	24.47	7.4	surface
840	0.30	124.97	6.1	surface + missing ionization channel

Table 5.3. – Details on the 4 single nuclear recoils measured with $Q < 0.6$, with the name of the detector, the ionization yield Q, the recoil energy E_{rec}, the time difference with the closest μ-veto event $\Delta t = t_{bolo} - t_{veto}$. The first two hits are inside the 90% nuclear recoil bands of their respective detector, defined using the individual time-averaged detector response.
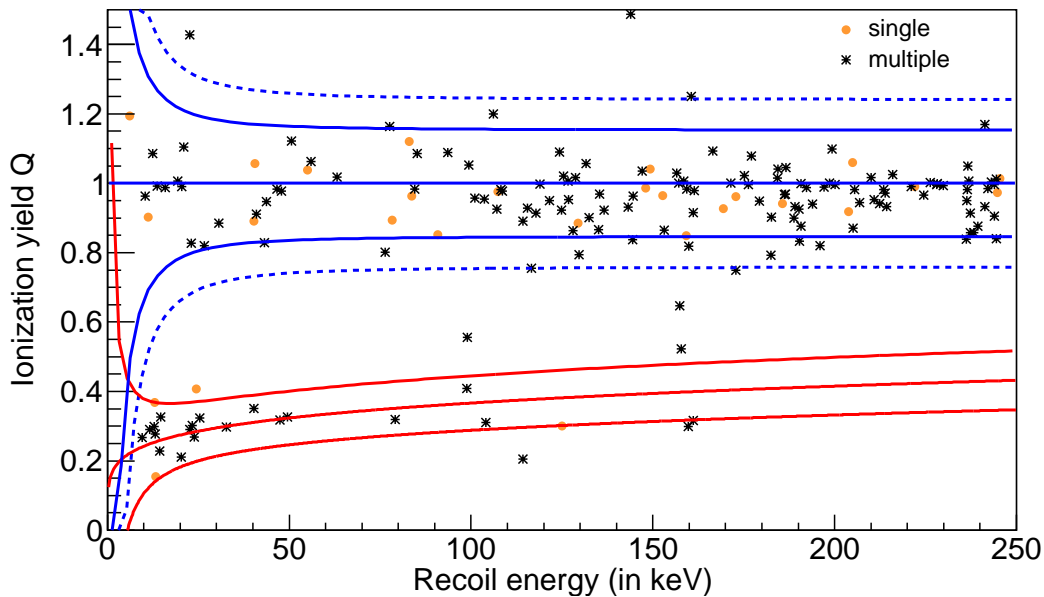
Figure 5.12. – Ionization yield versus recoil energy for μ-induced bolometer hits. The full lines represent the 90% electronic (blue) and nuclear (red) recoil bands. The dashed blue lines represent the 99% electronic recoil band. These bands are plotted using the average energy resolutions of the bolometer array.

the one measured in EDELWEISS-II. First, as the FID detectors are twice higher than the ID detectors, the space between detectors is also reduced i.e. the array is of higher density. Muon-induced neutrons are therefore more likely to scatter multiple times, which makes them distinguishable from WIMPs. Secondly, it was derived from simulations that the newly installed PE shields (see section 2.2.2.2) attenuate the μ-induced neutron background by a factor 2.7. To determine the WIMP-like event rate for the EDELWEISS-III configuration, the simulation should be used.

5.3.4.2. Simulation of the coincidence rate

In order to derive the simulated coincidence rate, the simulations presented in section 3.4 are used. To briefly summarize, a total of 27.2 million of muons and antimuons with initial energies between 2 GeV and 20 TeV has been simulated for the Run308 detector configuration and setup. To make up for the steep fall of the differential energy spectrum, the muon initial energy range was split in 4 sub-ranges to ensure enough statistics in each of them. The contribution of each energy range and each muon type to the coincidence rate was then weighted accordingly to its contribution to the total muon flux.

The coincidence rate was calculated for the 20 selected bolometers, considering the time periods during which either FID832 (11.1 days) or FID821 (3.8 days) were OFF. The simulations were normalized using the muon flux measured by the Fréjus experiment of 4.98 μ-event/m^2/day through a spherical surface [4]. As explained in section 3.4.2.2, this value is not in agreement with the muon flux measured in the EDELWEISS-II experiment of 5.4 ± 0.2 (stat)$^{+0.5}_{-0.9}$ (syst) μ/m^2/day through an horizontal surface. This discrepancy gives rise to a significant systematic uncertainty on the coincidence rate.

Note that all bolometers are simulated as a cylinder with fixed size (3.5 cm radius and 4 cm height) and density ($\rho = 5.31$ g/cm^3), corresponding to a fixed mass of 817 g. However, the actual measured masses vary between 820 and 889 g, with an average of 872 g. As the coincidence rate depends on the effective surface covered by the array, the increase of bolometer size necessary to simulate the real mass gives an assessment of the error induced by a fixed detector size. As germanium has a high density, the missing 55 g cover only a volume of 10.3 cm^3, achievable by increasing the radius or the height of the crystal of less than 0.3 cm. Therefore the uncertainty on the simulated mass is considered negligible.

The multiplicity of a simulated event is determined by the number of bolometers in which the deposited heat energy is above its average heat threshold. A single cut of 2 keV is applied on the ionization energy $E_{\rm ion}$, to reproduce the cut applied on the data. This way, the following simulated rate of μ-induced bolometer events has been extracted:

$$\Gamma^{\mu}_{\rm simu} = 1.09 \pm 0.01 \text{ (stat) } ^{+0.24}_{-0.00} \text{ (sys) events/day} \qquad (5.11)$$

As the individual responses of the 46 μ-veto modules are not all known, this rate was derived without any requirement on the energy deposited in the μ-veto module. That means that the efficiency of the μ-veto is not taken into account. In theory, the comparison between the measured and simulated rates could give an estimate of this efficiency. In practice, the uncertainties on both rates are too large to conclude. The measured rate is 7.6% higher than the simulated one, but in agreement within uncertainties. The simulated rate is dominated by the systematic uncertainty arising from the normalization of the simulated muon flux. No systematic uncertainty on the total number of simulated events is considered. The measured rate is dominated by the statistical uncertainties on the scarce number of μ-induced bolometer events in the accumulated live-time of 133.6 days. No conclusion can be drawn from this comparison in terms of efficiency. The higher measured coincidence rate is a further indication that the muon flux measured with EDELWEISS is indeed higher than the one measured by the Fréjus experiment. For indication, the coincidence rate derived using the EDELWEISS-II muon flux would be $\Gamma^{\mu}_{\rm simu} = (1.33 \pm 0.01$ (stat) $^{+0.12}_{-0.22}$ (sys)) events/day.

Using the simulation, the rate of WIMP-like events expected for the 20 selected bolometers of this analysis can be extracted. Fiducial events were selected by requiring less than 1.5 keV deposited energy in the surface volume. Despite bolometers being simulated with a fixed total mass, the size of the fiducial volume was chosen to match the measured fiducial mass. The rate of single nuclear recoil in the 90% nuclear recoil band in the energy range $E_{\rm rec} =$[10,200] keV was estimated to be:

$$\Gamma^{\rm WIMP-like}_{\rm simu} = (7.6 \pm 0.1 \text{ (stat) } ^{+2.6}_{-1.7} \text{ (sys)}) \times 10^{-3} \text{ events/day} \qquad (5.12)$$

The positive systematic uncertainty is calculated as the quadratic sum of the uncertainty on the simulation normalization and on the neutron yield in lead estimated from [118] to be 26%. The negative systematic uncertainty arises from the negative uncertainty on the neutron yield in lead, estimated from [83] to be 16%, and considering the 15% excess of single events in the simulation compared to the data, shown in fig. 5.7. Discussion on the systematic uncertainties on the simulation normalization and on the neutron yield can

---

4. No statistical or systematic uncertainties are given on this flux in the publication [116]

be found in section 3.4.1.1. Taken the rate in eq. 5.12 for the accumulated live-time of $t^{B+V} = 133.6 \pm 2.7$ days, the expected number of WIMP-like events is:

$$N_{\text{simu}}^{\text{WIMP-like}} = 1.02 \pm 0.01 \text{ (stat) } {}^{+0.34}_{-0.22} \text{ (sys) events} \tag{5.13}$$

This result is compatible with the fact that no event has been measured (see eq. 5.10) considering statistical fluctuations.

5.4. Determination of the muon-veto efficiency

As shown in section 5.3.3, μ-induced bolometer events can be distinguished from other backgrounds on the basis of their bolometer multiplicity and their total energy deposit in the bolometer array. Thus, a sample of bolometer events clearly induced by muons can be selected. By studying how many are seen in coincidence with the μ-veto within the time window defined in eq. 5.3 and eq. 5.4, the μ-veto efficiency to detect muons passing inside or close to the array can be extracted. As explained in section 3.2.4.1, this efficiency is higher than the efficiency to detect muons entering the veto volume, which includes muons going through the outermost corners of the μ-veto. These muons have a higher probability to be missed because of the gaps in the mounting structure in the corners or because they might deposit an energy below threshold. However, they are not likely to produce secondaries interacting in the bolometers: it was shown using the EDELWEISS-II μ-veto data that more than 90% of μ-induced bolometer events are induced by muons passing within a distance of less than 1 m from the cryostat center [32]. Thus, extracting the μ-veto efficiency from bolometer data gives a good estimate of the ability of the μ-veto system to reject muons inducing background for dark matter search.

The difficulty of this analysis is to choose the proper cuts to select the sample of μ-induced bolometer events. The cuts have to be strict enough such that all events from natural radioactivity, including high energy α-particles, are rejected. At the same time, as the number of μ-induced bolometer events is scarce, it should not be too strict to ensure an acceptable statistics of μ-induced bolometer events. As shown in section 5.3.3, the event multiplicity is an efficient selection criterion to select μ-induced bolometer events. In addition, a cut on the energy should be applied with several choices, e.g. a cut can be applied either on heat, ionization or recoil energy, on the total energy deposit in the bolometer array or on the energy deposit per bolometer. From the findings obtained with the coincidence analysis, it was chosen to apply a condition on the ionization energy. As explained in section 2.1.3.2, the determination of the heat energy is not reliable for large energy deposits saturating the ADC, characteristic of μ-induced events. Indeed, the pulse template is not describing saturated pulses well, leading to either an overestimation or underestimation of the energy deposit. The estimate of the ionization energy is more reliable as the ionization pulse is described by a Heaviside function: in case of saturation, the steep rise is cut earlier leading to an underestimated energy estimation, but the shape of the pulse can still be well fitted with the template. Events with a bad energy reconstruction are partially cut by requiring the total recoil energy E_{rec}^{tot} to be positive. Another motivation to use the ionization energy is that the highest energy deposits from natural radioactive decay chains arise from α particles, whose ionization energy is quenched in the bolometers.

The cuts on the multiplicity and the energy deposit were chosen by studying the total ionization energy deposit in the bolometer array versus the bolometer multiplicity displayed in fig. 5.13, for bolometer events in accidental coincidence with a selection of μ-veto events. As explained earlier, accidental coincidences are derived by delaying each μ-veto event and associating it to the closest bolometer hit. It was ensured that all identified μ-induced bolometer events were previously cut from the data such that they cannot be associated to a μ-veto event and bias the cut determination. Once the cuts have been derived, they were
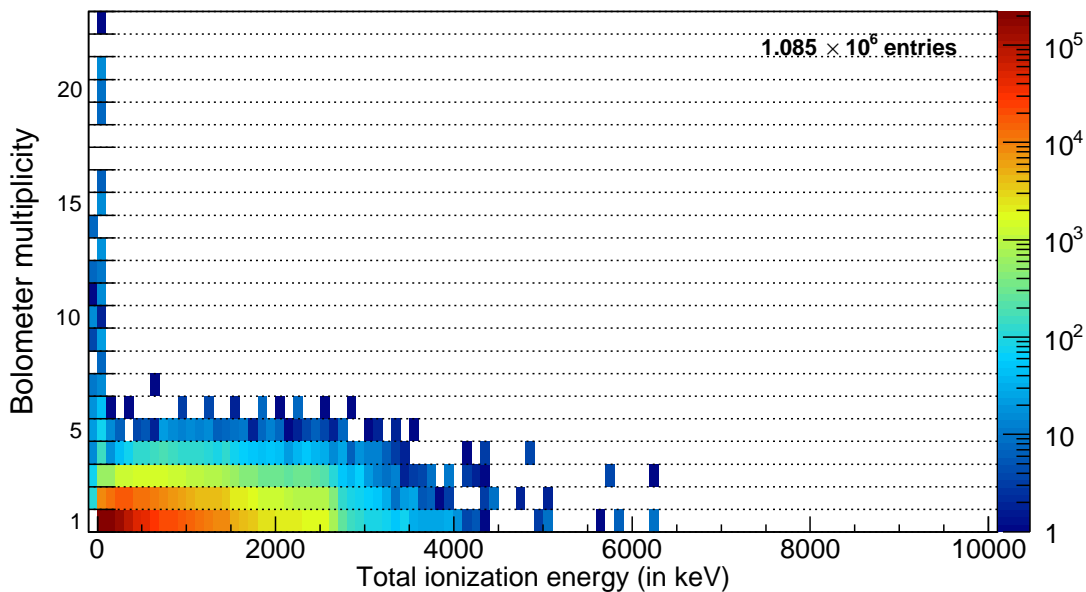
Figure 5.13. – Total ionization energy deposited in the bolometer array versus the multiplicity of bolometer events forming an accidental coincidence with a μ-veto event.

applied on the bolometer data to select a sample of μ-induced bolometer events. In order to determine the cuts, three regions have been distinguished in fig. 5.13: first a region of low multiplicity $M_{\text{Bolo}} \leqq 4$ where some rare coincidences between γ-rays extend the total ionization energy up to 6.3 MeV; a region of intermediate multiplicity $5 \leqq M_{\text{Bolo}} \leqq 6$; and a region of high multiplicity $M_{\text{Bolo}} \geq 7$ where events are induced by noise and relatively small energy deposit. The chosen cuts are the following:

$$1 \leqq M_{\text{Bolo}} \leqq 4 \qquad E_{\text{rec}}^{\text{tot}} > 0 \text{ MeV and } E_{\text{ion}}^{\text{tot}} > 7 \text{ MeV} \tag{5.14}$$

$$5 \leqq M_{\text{Bolo}} \leqq 6 \qquad E_{\text{rec}}^{\text{tot}} > 0 \text{ MeV and } E_{\text{ion}}^{\text{tot}} > 4 \text{ MeV} \tag{5.15}$$

$$M_{\text{Bolo}} \geq 7 \qquad E_{\text{rec}}^{\text{tot}} > 0 \text{ MeV and } E_{\text{ion}}^{\text{tot}}/M_{\text{Bolo}} > 200 \text{ keV} \tag{5.16}$$

The cut in eq. 5.16 on the mean ionization energy per bolometer was specifically chosen to reject high multiplicity events in coincidence with spike of temperature or due to the remainder of a reset pulse in one bolometer (maintenance procedure described in section 5.2.2). With this set of criteria, 32 μ-induced bolometer events have been selected. All are seen in coincidence with the μ-veto within a coincidence window of $\pm 12 \, \mu$s, as defined in eq. 5.3 and eq. 5.4. A lower limit of the μ-veto efficiency at 90% C.L. can then be determined, considering the probability for a muon to be detected to follow a binomial distribution:

$$P(k,n,\varepsilon_{\mu\text{-veto}}) = 10\% \quad \text{with} \quad P(k,n,\varepsilon_{\mu\text{-veto}}) = \binom{n}{k}\varepsilon_{\mu\text{-veto}}^{k}(1 - \varepsilon_{\mu\text{-veto}})^{n-k} \tag{5.17}$$

where n is the number of μ-induced bolometer events selected ($n = 32$), k the number of events tagged by the μ-veto ($k = 32$) and $\varepsilon_{\mu\text{-veto}}$ the probability of a μ-induced bolometer event to be detected in the μ-veto :

$$\varepsilon_{\mu\text{-veto}} \geq \sqrt[n]{0.1} = 93\% \text{ at } 90\% \text{ C.L.} \tag{5.18}$$

This result is in agreement with the μ-veto efficiency of $\varepsilon_{\mu\text{-veto}} > 93.8\%$ at 90% C.L., derived from EDELWEISS-II data using a similar method with different selection criteria

[32]. This method has the advantage to be completely independent of the systematics on the simulation or on the module responses, and is only limited by statistics. Concerning the systematic uncertainties, the bias to close muon tracks is negligible as discussed above. Thus, this method gives a reliable low boundary on the μ-veto efficiency to tag muons inducing bolometer events.

6. Muon-induced neutron background in EDELWEISS-III

Using the data taken during the cryogenic run called Run308, new limits on the WIMP-nucleon cross section have been derived by the EDELWEISS collaboration for both standard mass WIMPs in the mass range $[10, 1000]$ GeV and so-called low mass WIMPs in the mass range $[3, 30]$ GeV. These analyses are reviewed below, as well as the expected backgrounds in the region of interest. Particular attention is given to the estimation of the μ-induced neutron background since that was performed in the framework of this thesis. In comparison to the $\pm 12\,\mu$s coincidence window used in the previous chapter, a conservative window of ± 1 ms is used to veto μ-induced bolometer events in the dark matter search analyses.

6.1. Results of the standard WIMP mass analysis

6.1.1. WIMP search in Run308

From the 22nd of July 2014 until the 3rd of April 2015, WIMP search data was taken with the Run308 configuration shown in section 2.1.3.1. Data taken after the 5th of January 2015 was blinded, i.e. single bolometer events in the energy range $E_{\mathrm{rec}} = [0, 200]$ keV, with an ionization quenching $0 < Q < 0.5$ were excluded from the data set. Data taken before this blinding has been analysed in terms of dark matter search in the context of [150], in order to confirm the detector performance and the background level. The analysis of the data taken after the blinding has not yet been optimized, as priority was given to the low mass analysis. Therefore, only the data taken before the 5th of January is presented here. A subset of detectors, 17 out of the 24 which were read-out, was selected for the standard WIMP search analysis. Of the rejected detectors, four were excluded because of unreliable estimation of the energy deposit: two detectors had at least one missing ionization channel, leading to a partial charge collection, and the two others had unstable heat channels. The three other rejected detectors could not be operated at the standard fiducial voltage of 8 V, because of either leakage currents, or charge trapping or a failure of the electronics. Consequently, a sufficient discrimination between electronic and nuclear recoils could not be achieved for these 3 detectors.

From the available data, time periods were selected during which the baseline resolutions of the different channels were considered to be sufficiently low for dark matter search. For this purpose, a cut on the so-called *magic point* at 90% C.L. (denoted $M_p[90\%]$ in the following) was applied. Traditionally, the magic point is defined as the recoil energy E_{rec} at

which, in the standard ionization yield plot, the nuclear recoil band at 90% C.L. intersects with the electronic recoil band at 99.98%. The definition was extended in this analysis: if the nuclear recoil band at 90% C.L. intersects the trigger efficiency curve at 99.87% or the heat-only [1] cut at a higher recoil energy, then this energy is defined as the magic point. Hence, by selecting events with $E_{\rm rec} > M_p[90\%]$, a trigger threshold of at least 99.87% in the 90% C.L. nuclear recoil band is ensured as well as a discrimination of electronic recoils above 99.98%. $M_p[90\%]$ is calculated on an hourly basis using the corresponding baseline resolutions, detector per detector, requiring in addition $M_p < 20\,\rm keV$. Note that this single cut combines the cuts on the baseline resolutions of heat and fiducial ionization channels, as well as on the trigger threshold, which were performed individually in the EDELWEISS-II analysis [61]. By requiring in this analysis a magic point $<20\,\rm keV$, only 4.7% of the data is rejected. In overall, the mean trigger threshold was estimated to be $9\,\rm keV$, with a non-zero detection efficiency down to $6.6\,\rm keV$.

A fiducial cut was also applied to reject surface and mixed events which suffer from incomplete charge collection and can leak into the nuclear recoil band. For this purpose, cuts were applied on the measured energy of the veto electrodes A and C, as well as on the difference of the measured energies of the two collecting electrodes B and D. The fiducial volume of each detector is determined by the fraction of cosmogenic events in the $10\,\rm keV$ peaks (see section 2.2.2.1) passing the fiducial cut.

Lastly, pile-up events were rejected. These are two consecutive events following so close in time, that their recorded pulse traces partially overlap. The determination of the energy and timing of such a pile-up event is wrong as the pulse templates used for fitting the heat and ionization traces do not describe well the overlapping signals. These events can therefore be rejected by cutting on the normalized χ^2 of the fit of each individual heat or ionization channel.

The remaining exposure after quality cuts was calculated by summing all hours during which each individual bolometer was taking physics data. A bolometer is considered to be sensitive to WIMPs if there is at least one hit per hour, which satisfies the two requirements:

$$E_{\rm fid} > 2 \times {\rm FWHM}_{\rm fid} \tag{6.1}$$

$$E_{\rm heat} > 1.5 \times {\rm FWHM}_{\rm heat} \tag{6.2}$$

with the fiducial ionization (heat) energy $E_{\rm fid}$ ($E_{\rm heat}$) and the corresponding baseline resolution ${\rm FWHM}_{\rm fid}$ (${\rm FWHM}_{\rm heat}$), respectively. The dead-time caused by the maintenance procedures described in section 5.2.2 adds up to about 11% of the measurement time and was subtracted from the live-time. Due to the magic point cut, the trigger efficiency is always above 99.87%. Any efficiency loss due to the trigger is therefore neglected in the exposure calculation. The inefficiency of the fiducial volume cut is already included in the calculation of the fiducial mass. Considering a conservative fiducial mass of $600\,\rm g$ per detector, an exposure of $772\,\rm kg \cdot days$ was derived after quality cuts, for an analysis threshold of $20\,\rm keV$ or lower. After implementation of the dead-time cut, it is lowered to $690\,\rm kg \cdot days$ and finally to $600\,\rm kg \cdot days$ when taking into account the acceptance of the nuclear recoil band, estimated conservatively to be 86% [150].

 In the following, the definition of "hit" and "event" follows the nomenclature presented in section 5.1: a hit is an energy deposit in a single bolometer and an event is made up of all bolometer hits in coincidence. Bolometer hits passing the quality cuts are displayed in fig. 6.1, showing the ionization yield Q versus recoil energy $E_{\rm rec}$ of these events. The nuclear and electronic recoil bands are displayed using the average resolutions of the 17 selected detectors, but each hit is classified using the hourly resolutions. The nuclear recoil band is surprisingly populated with 17 hits measured in the energy range $E_{\rm rec} = [0, 200]\,\rm keV$.

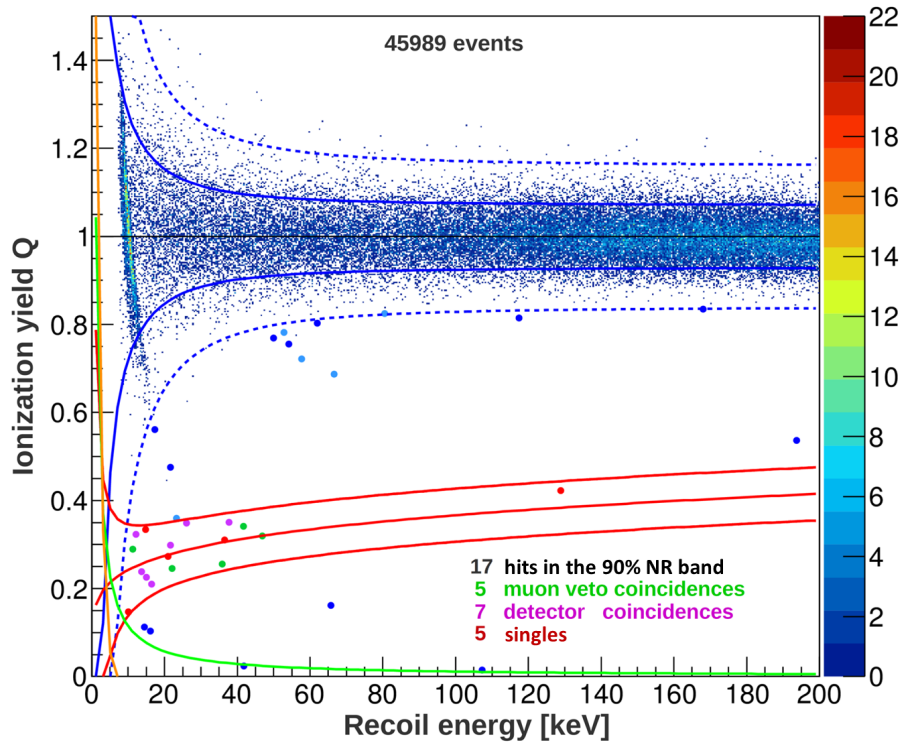1. Events for which the measured ionization signal arises from electronic noise.

Figure 6.1. – Ionization yield Q versus recoil energy for WIMP search data from 17 selected detectors passing all quality cuts. Solid lines indicate the 90% C.L. electronic recoil band (blue), and nuclear recoil band (red), as well as the average trigger threshold curve (green). The dashed blue lines show the 99.98% C.L. electronic recoil band. These bands were calculated for the average energy resolutions of the selected detectors. Dark and light blue points are outside the electronic recoil band at 99.98% C.L. and the nuclear recoil band at 90% C.L., the hits in coincidences with at least one other bolometer being shown in light blue. Green points are hits in coincidence with the muon-veto system. Pink points inside the nuclear recoil band show hits in coincidence with at least one other bolometer. 5 remaining single nuclear recoils, which are potential WIMP candidates, are marked in red.
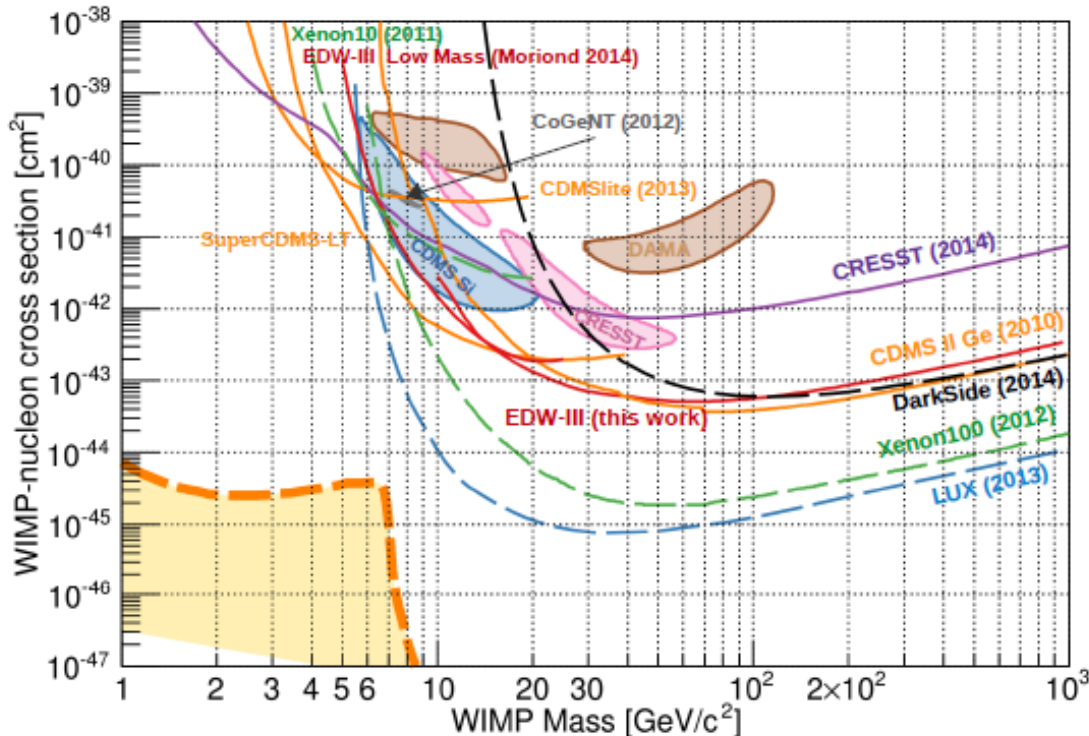
Figure 6.2. – Limit on the spin-independent WIMP-nucleon cross section for the
EDELWEISS-III standard mass analysis (red curves), using the data taken
until the 5th of January 2015. The exclusion limit labelled "this work" is ex-
tracted from the analysis described in this section [150]. The exclusion curve
at low mass labelled "Moriond 2014" shows the preliminary results of the low
mass analysis based on an exposure of $35 \, \text{kg} \cdot \text{days}$ presented in [153]. Ex-
tracted from [150].

Five of them are in coincidence with the μ-veto in the conservative coincidence window
of $\pm 1 \, \text{ms}$ used to veto bolometer events and also with several other detectors. Note that
these five events are still in coincidence with the μ-veto considering a more narrow window
of $\pm 12 \, \mu\text{s}$ width, as used in the previous chapter. Two hits among them are in coincidence
in time and can be attributed to a single muon. From the 12 remaining ones, 7 are seen
in coincidence with at least one other bolometer and will be referred as *multiple nuclear
recoils* hereafter. Note that 2 hits are in coincidence in time and can therefore be associ-
ated to the same bolometer event. The 5 remaining hits are considered as single events
and are thus potential candidates for dark matter.

As described in section 2.2.2.2, a total of 4.8 nuclear recoil events, including 1.4 single
events, is expected from simulations of the radiogenic background for one year of data
taking with 24 detectors (see table 2.3). Extrapolating to the accumulated exposure of
$690 \, \text{kg} \cdot \text{days}^2$, about 0.6 nuclear recoil events (single or multiple) are expected from ra-
diogenic neutrons. Thus, the observed neutron background cannot be explained by the
known radiogenic neutron sources which have been simulated.

The exclusion limit on the spin-independent WIMP-nucleon cross section determined in
this analysis is shown in fig. 6.2. The method of optimum interval [154] was used to derive
this limit, giving a limit on the cross section of $\sigma < 5.15 \times 10^{-7} \, \text{pb}$ at 90% C.L. for a WIMP
mass of $m_{\text{WIMP}} = 60 \, \text{GeV}$. As the origin of the measured background is unknown, it is not
possible to subtract it in order to improve the exclusion limit. Thus, this analysis revealed
the presence of an unknown neutron source, limiting the sensitivity of the EDELWEISS-III

---

2. The nuclear recoil band acceptance is not included in the calculation of the simulated exposure.

experiment for standard mass WIMPs. However, this neutron background is less of a limiting factor for the sensitivity to low mass WIMPs. Indeed, the spectral shape expected from radiogenic neutrons differs significantly from the exponentially decreasing energy spectrum expected from a WIMP signal. Together with the current context of direct dark matter search, this result motivated a change of strategy towards low mass WIMPs. The low mass WIMP analysis performed in this context will be presented in section 6.2.

Following this result, the question was raised whether these neutrons could have been induced by untagged muons, due to a possible inefficiency of the μ-veto system. The analysis described in chapter 5, which was performed to study coincidences between the μ-veto and the bolometer array already indicates that this is not the case. It has notably been shown that the measured and simulated coincidence rates are in agreement within uncertainties in section 5.3.4; moreover, the expected rate of WIMP-like events obtained from simulations for the 20 selected bolometers is low, of the order of 10^{-3} events/day before vetoing (eq. 5.11 in section 5.3.4.2); and lastly a lower limit on the μ-veto efficiency of 93% at 90% C.L was derived using bolometer data (section 5.4). Nevertheless, given the importance of this subject, a dedicated study for the bolometers selected in the standard mass analysis was performed in the framework of this thesis and is presented in the following section.

6.1.2. On the origin of the measured neutron background

Two studies were performed to find out whether the origin of the measured neutron background is radiogenic or cosmogenic. Firstly, a simulation was performed to estimate the expected number of single and multiple nuclear recoils in the ROI for the 17 selected bolometers with their average response. Secondly, the topology of the measured events is compared with the topology of μ-induced events.

Simulation of the expected μ-induced background

The muon simulations giving the results presented here have been detailed in section 3.4.2.2 and will therefore only be summarized here. More information on the simulation normalization and on the uncertainty calculation can be found in section 3.4.

In total, 27.2 million of muons and antimuons with initial energies between 2 GeV and 20 TeV have been simulated for the Run308 detector configuration and experimental setup. The initial energy range was split in 4 sub-ranges to ensure sufficient statistics in each of them despite the steeply falling muon differential energy spectrum. The equivalent simulated time varies between $t = 73.2$ years for the energy range contributing the most (μ^+ in the energy range 20-200 GeV) and $t = 898.5$ years for the one contributing the least (μ^- in the energy range 2-20 TeV).

First, the output of the simulation was modified to reconstruct events: the single energy deposits in each bolometer were summed, quenched according to the recoil type and smeared with the individual bolometer resolutions. The average heat and ionization resolutions determined for each detector, with the cuts described in section 6.1.1, were used as input.

As a reminder, the bolometer multiplicity of an event (i.e. the number of bolometers with an energy deposit in coincidence) is derived using all 24 read out bolometers. In the simulation, the multiplicity is defined in a similar way as the measured multiplicity: if the simulated heat energy deposit in a detector is above its average heat threshold, the energy deposit is considered to be detected. If the time between consecutive energy deposits is less than 10 ms, they are considered to be part of the same event. Fiducial events were selected in the simulation by requiring less than 1.5 keV deposited energy in the surface volume.

The simulation is normalized to the number of measured live-days for the three analysis thresholds (10, 15 and 20 keV) given in [150], assuming that all 17 detectors were taking

Table 6.1. – Rate of single $\Gamma_{\text{simu}}^{\text{WIMP-like}}$ and multiple $\Gamma_{\text{simu}}^{\mu-\text{multiple}}$ nuclear recoil hits in the fiducial volume, in the 90% nuclear recoil band, expected from simulation for an analysis threshold of 10, 15 and 20 keV, before vetoing. The rates are given in 10^{-2} events/day.

Threshold (keV)	live-time (days)	$\Gamma_{\text{simu}}^{\text{WIMP-like}}$ (10^{-2} event/day)	$\Gamma_{\text{simu}}^{\mu\text{-multiple}}$ (10^{-2} event/day)
10	41.2	0.62	3.8
15	20.6	0.42	2.8
20	5.9	0.32	2.2
(weighted) sum	67.7	0.53	3.4

data simultaneously. As shown in section 5.2.2, this was the case for more than 90% of the time. The calculated exposure chosen to normalize the simulation takes into account period cuts from the hourly quality cuts and maintenance procedures, but excludes the correction of the nuclear recoil band acceptance. Indeed, the μ-induced background is proportional to the live-time and not to the number of kg · days.

The number of single and multiple nuclear recoils is then extracted from the simulation by counting the number of events in the 90% C.L. nuclear recoil band (defined individually for each bolometer using its average energy resolution), with energy deposits above the analysis threshold and below 200 keV. To avoid any misunderstanding, a nuclear recoil is considered single if there is only 1 bolometer among the 24 with a simulated heat energy above the bolometer-dependent trigger threshold. If there is another bolometer with an energy deposit, then the nuclear recoil is considered as multiple. If, for a given simulated muon, two nuclear recoil hits occur, they are both counted as multiple nuclear recoils. The total number of expected single or multiple nuclear recoils is calculated as follows:

$$N_{\text{simu}}^{\mu-n} = \sum_{i=1}^{3} t_i \Gamma_i^{\mu} = \sum_{i=1}^{3} t_i \sum_{j=1}^{8} \frac{n_{ij}}{s_j} \tag{6.3}$$

with t_i the accumulated livetime for a threshold $i = \{10, 15, 20\}$ keV and Γ_i^{μ} the rate of μ-induced single or multiple nuclear recoil events for this threshold i. This rate is calculated for each of the 8 simulated data sets (4 energy ranges per muon type μ^+/μ^-) by calculating the ratio of n_{ij}, the total number of single or multiple nuclear recoils in the 17 bolometers in simulation j, for a given threshold i, in the 90% C.L. nuclear recoil band and in the ROI (<200 keV), over the simulated time s_j. The detailed results of the simulations with the contribution from each analysis threshold before vetoing are given in table 6.1. The total number of multiple nuclear recoils hits in the fiducial volume in the 90% nuclear recoil band without requirement on the μ-veto trigger is thus:

$$N_{\text{simu}}^{\mu-\text{multiple}} = 2.28 \pm 0.04 \text{ (stat)} \, _{-0.37}^{+0.85} \text{ (sys)} \tag{6.4}$$

and the number of single nuclear recoils is:

$$N_{\text{simu}}^{\text{WIMP-like}} = 0.36 \pm 0.02 \text{ (stat)} \, _{-0.08}^{+0.12} \text{ (sys)} \tag{6.5}$$

The systematic uncertainties arise from three contributions: the uncertainty on the simulated μ-induced neutron yield in lead, estimated to be +26% [118] and -16% [83] (see section 3.4.1.1); the reference muon flux used to normalize the simulation, estimated to be +22%; and the 15% excess of simulated single events compared to the data as described in section 5.3.3, considered as a negative systematic uncertainty for the rate of multiple nuclear recoils and as positive systematic uncertainty for the rate of single nuclear recoils.

The systematic uncertainty on the live-time determination is considered negligible.

Due to the low number of expected μ-induced WIMP-like events, it was decided that time periods during which the μ-veto is off are not cut from the analysis in order to maximize the exposure. The expected fraction of WIMP-like events actually limiting the sensitivity to dark matter search is calculated according to:

$$N_{\text{simu}}^{\text{WIMP-like}} = t^{B+V}\Gamma_{\text{simu}}^{\text{WIMP-like}}(1 - \varepsilon_{\mu-\text{veto}}) + t^B\Gamma_{\text{simu}}^{\text{WIMP-like}} \tag{6.6}$$

where t^{B+V} is the live-time when both acquisition systems of the μ-veto and the bolometers were running; $\Gamma_{\text{simu}}^{\text{WIMP-like}}$ the rate of WIMP-like events as determined in table 6.1; $\varepsilon_{\mu-\text{veto}}$ the μ-veto efficiency (see eq. 5.18); and t^B the accumulated live-time during which the μ-veto was either off or not fully efficient. The conservative cuts applied to determine if the μ-veto system is on were described in section 5.2.1. t^B was derived by extracting, for each hour with at least one bolometer hit, the number of minutes during which the μ-veto is considered off. t^B was estimated to be 3.9 days, corresponding to 5.8% of the accumulated live-time. A lower limit on the μ-veto efficiency $\varepsilon_{\mu-\text{veto}} > 93\%$ at 90% C.L. to detect μ-induced bolometer events was derived in section 5.4. By plugging these numbers in eq. 6.6 and taking into account the uncertainty on $\Gamma_{\text{simu}}^{\text{WIMP-like}}$, an upper limit on the number of expected unvetoed WIMP-like event in the standard WIMP mass analysis can be derived:

$$N_{\text{simu}}^{\text{WIMP-like}} < 0.06 \text{ events} \tag{6.7}$$

Thus, expected μ-induced neutron background is negligible in this analysis and is far from explaining the observed neutron background. Even with neglecting the μ-veto (eq. 6.5), μ-induced neutrons can not explain the observed single nuclear recoils.

Comparison of topology

Information about the 17 hits measured in the nuclear recoil band as shown in fig. 6.1 is given in table 6.2, separately for nuclear recoils not tagged by the μ-veto and μ-induced nuclear recoils. By comparing the experimental observables quoted in this table between the 5 tagged hits and the 12 untagged ones (4 and 11 events respectively), knowing the expected topology of μ-induced events (see section 5.3.3), an indication on the origin of the neutron background can be deduced.

First, from what can be seen in table 6.2, there is no significant difference between the energy deposit of the untagged nuclear recoils and the energy deposit of μ-induced nuclear recoils. However, the energy of neutrons produced by (α,n) reactions on light nuclei or by fission goes up to 10 MeV, whereas neutrons produced by muons have a harder energy spectrum extending up to a few GeV. As fast neutrons transfer larger energies to the recoiling nucleus, one could think that the recoil energy spectrum of μ-induced neutrons is harder. However, most of μ-induced neutrons interacting in the bolometers are produced in the external lead shield. As the neutron flux below 20 MeV increases with the atomic mass of the material following $A^{0.8}$ [155], the average neutron energy for high-A materials is lower than for low-A materials. In lead, the average energy of μ-induced neutrons for a muon energy of 260 GeV [3] has been simulated to be 8.8 MeV [156]. Consequently, most μ-induced neutrons have similar energies as radiogenic neutrons, leading to a similar recoil spectrum.

In the data listed in table 6.2, the bolometer multiplicity of the 11 untagged nuclear recoil events varies from 1 to 3 with an average of 1.7, whereas it varies from 3 to 13 with an average of 8.5 for a limited statistics of 4 μ-induced events [4]. Simulations of the radiogenic background give an expected mean multiplicity varying between 1.4 and 1.9 depending on

---

3. similar to the mean muon energy at LSM
4. 2 hits among the 5 are in coincidence in time and are therefore induced by the same muon

Table 6.2. – Overview of the 17 hits in the 90% C.L. nuclear recoil band with single hits in blue and multiple hits in black, ordered by event timing. The hits in coincidence with the μ-veto within a coincidence window of $\pm 1\,\mathrm{ms}$ are displayed at the bottom of the table in green, separately from the untagged neutrons. The columns give respectively the name of the detector, the time when the event occurred (in days since July, 1st 2014), the ionization yield Q, the recoil energy E_{rec} (in keV), the bolometer multiplicity $\mathrm{M_{bolo}}$, the time difference between the bolometer event and its closest μ-veto event $t_{\mathrm{bolo}} - t_{\mathrm{veto}}$ (in ms) and the μ-veto multiplicity $\mathrm{M_{veto}}$.

FID	Day	Q	E_{rec} (keV)	$\mathrm{M_{bolo}}$	$t_{\mathrm{bolo}} - t_{\mathrm{veto}}$ (ms)	$\mathrm{M_{veto}}$
823	40.3	0.34	14.90	1	299	1
842	43.0	0.35	37.68	2	62.2	1
838	45.2	0.42	128.8	1	196	1
828	48.4	0.24	13.96	3	2	1
839	50.4	0.27	20.97	1	133	1
823	61.6	0.21	16.68	2	159	1
824	91.6	0.14	10.06	1	-453	1
842	151.1	0.31	36.68	1	137	1
845	151.4	0.35	26.38	2	-86	1
828	152.3	0.30	21.71	3	270	1
821	185.8	0.23	14.99	2	-28	1
839	185.8	0.32	12.15	2	-28	1
846	54.9	0.25	22.07	12	0.055	2
841	122.9	0.26	35.68	6	0.056	2
841	128.4	0.34	41.87	3	0.058	7
823	128.4	0.29	11.3	3	0.058	7
823	157.6	0.32	46.94	13	0.060	6

the contaminated material and the decay chain. In comparison, it was shown in section 5.3.3 that the measured multiplicity of μ-induced bolometer events is 4.6 hits and that 75% of them are multiple events. Thus, the absence of single bolometer hits in coincidence with the μ-veto is not surprising.

The ratio between single nuclear recoils and the number of multiple nuclear recoils, referred to as *single-to-multiple ratio* hereafter, is also a useful hint concerning the origin of the background. The single-to-multiple ratio of nuclear recoil *hits* was calculated as output of the radiogenic simulation, such that 2 nuclear recoils in two different bolometers in coincidence in time are counted as 2 multiples. Following this definition, a single-to-multiple ratio of 0.45 in the energy range $E_{\mathrm{rec}} = [10, 100]\,\mathrm{keV}$, averaged over 8 bolometers, was extracted from the simulations. Note that this ratio depends on the energy threshold used as input of the simulation. The values quoted here were extracted using individual averaged trigger thresholds for each bolometer, estimated using the Run308 data. This ratio strongly varies of the order of $(\pm 20\%)$ depending on the position of the bolometer in the array. From one contaminated material to the other, the ratio varies from 0.33 for neutrons produced by (α,n) reactions in the CuBe contained in the connector sockets up to 0.48 for the contaminated Teflon isolation of the Axon cable. The single-to-multiple ratio was estimated in a similar way for μ-induced nuclear recoils to be of ~ 0.19, knowing the simulations of μ-induced events seem to overestimate the number of single events by $\sim 15\%$ as shown in section 5.3.4.2. These results have to be compared with the observed ratio of single-to-multiple nuclear recoils of $5/7 \simeq 0.71$. This is well above the expected ratio from μ-induced events. However, it could be explained by an unknown neutron source,

either far away from the bolometer and highly energetic, or close to the bolometers and of low energy.

The time difference $\Delta t = t_{\text{bolo}} - t_{\text{veto}}$ between a bolometer hit and its closest μ-induced event gives an indication whether the observed background is unvetoed because of an insufficiently wide coincidence window. The Δt value for each bolometer event is displayed in table 6.2. In case of multiple events, the coincidence search is not only performed using the bolometer hit in the ROI but using each hit of the event: if one of them is less than $\pm 1\,\text{ms}$ away from a μ-veto event, the event is considered to be a μ-induced event. The Δt value quoted in the table is the smallest difference observed for a given bolometer event. Note that the $\pm 1\,\text{ms}$ coincidence window is conservative compared to the $\pm 12\,\mu\text{s}$ window used in the previous chapter. Thus, it includes with certainty rare but existing events when a high energy neutron is produced outside the external shields, but still deposits energy in the bolometer array after a propagation of few μs through the shields. Looking at table 6.2, large variations of the Δt values can be seen for unvetoed hits whereas vetoed hits are clearly included in the $\pm 12\,\mu\text{s}$ coincidence windows defined in eq. 5.3 and eq. 5.4. In addition, the μ-veto multiplicity, defined as the number of μ-veto modules satisfying the trigger condition[5], significantly differs between vetoed and unvetoed bolometer hits. The closest μ-veto events associated to each unvetoed bolometer hits all have a multiplicity M_{veto} of 1, characteristics of noise and interaction of ambient background in the μ-veto. On the contrary, the 4 μ-veto events in coincidence with a bolometer event have a multiplicity varying from 2 to 7 with an average of 4 modules. This value is coherent with the mean multiplicity of 3 modules extracted from the coincidence analysis (section 5.3.3), even if a comparison with such low statistics is difficult.

To conclude, each of the observables described above indicates that the measured neutron background is of radiogenic origin. In an attempt to identify this unknown source, simulations of neutron sources with various energy spectrum, placed at various distances from the bolometer array, are planned to reproduce the single-to-multiple ratio observed in the data.

6.2. Results of the low mass WIMP analysis

As LHC results more and more disfavour the existence of standard mass WIMPs within the SUSY framework, interest for low mass WIMPS of $\mathcal{O}(\text{GeV})$ masses is restored. This is also partly motivated by measured excesses from several direct dark matter detection experiments compatible with a low mass WIMP signal $\mathcal{O}(\text{GeV})$ [157], [30] and the γ-ray excess in the center of the galaxy which could be interpreted in term of $\mathcal{O}(\text{GeV})$ dark matter annihilation [158]. In parallel, theoretical frameworks for low mass dark matter emerged [159].

Semi-conductor based experiments are natural candidates to search for low mass WIMPs as cryogenic detectors can offer low detection thresholds and good energy resolutions. For such low WIMP masses, the expected recoil energies from WIMP scattering in the EDELWEISS Ge detectors are near to the experimental threshold of $\mathcal{O}(1\,\text{keV})$. At these energies, new backgrounds may appear and the discrimination between nuclear and electronic recoils becomes more challenging. Indeed, the WIMP signal starts to overlap with the regions where various backgrounds are expected. More detailed models of these backgrounds as well as stricter data selection are required to improve the sensitivity to low mass WIMPs as well as a stricter data selection.

Two different low mass analyses were performed by the EDELWEISS collaboration using the Run308 data, which allows a cross-check of the results. The official analysis is based on a Boosted Decision Tree (BDT) [160] whereas a 2D profile maximum likelihood analysis was carried out in parallel. Only the official EDELWEISS analysis will be reviewed

---

5. Each module with its two TDC values non-zero is counted in the multiplicity

hereafter. Results from the likelihood analysis were shown to be consistent with the BDT analysis [161]. Note that the background models as well as most of the cuts applied to select the data are common to both analyses. The estimation of the μ-induced neutron background, performed in the framework of this thesis, will be detailed below.

After a brief description of the data selection cuts, the methods applied to extract the background models will be explained. More technical details for one specific detector can be found in [153]. The estimation of the μ-induced neutron background performed in the framework of this thesis will be discussed in more details in section 6.2.3. Lastly, a brief description of the BDT analysis and the results in terms of dark matter search will be presented.

6.2.1. Data selection

The data was selected with the aim to reach the lowest WIMP mass achievable but still aiming for a good sensitivity in the WIMP mass region ~ 20 GeV. The experimental parameter dominating the sensitivity at low mass WIMPs is the online trigger threshold E_{th}, monitored on an hourly basis. To select the bolometers used for the analysis, the live-time in days for $E_{\text{th}} \leq 1.5$ keV and $E_{\text{th}} \leq 1$ keV was calculated for each detector. The 9 detectors with E_{th} always below 1.5 keV and a large fraction of the time below 1 keV were pre-selected. One of them is FID826, which suffered from charge trapping at 8 V of applied fiducial voltage and was therefore partly operated at 16 V. This bolometer was discarded, because of indications that the electric field configuration was different from the usual one. In addition, it had only a small contribution to the combined sensitivity. Consequently, 8 detectors were finally selected for the low mass analysis. Four of them showed good efficiency ($\sim 80\%$) already at $E_{\text{heat}} = 1$ keV whereas the 4 others were mostly efficient starting from $E_{\text{heat}} = 1.5$ keV. The region of interest (ROI) for low mass WIMP search is defined as the fiducial energy $E_{\text{fid}} = [0, 8]$ keV and the heat energy $E_{\text{heat}} = [1, 15]$ keV or $E_{\text{heat}} = [1.5, 15]$ keV depending on the detector.

Cuts on time periods were applied on the hourly determined baseline resolutions of the combined heat channel, the fiducial ionization and the two veto electrodes. In addition, event-based cuts were performed on the χ^2 of the ionization and heat pulse fits of all channels to remove poorly reconstructed and pile-up events. Fiducial events were selected by requiring that the measured ionization energy of the veto electrodes, E_A and E_C, are within 5σ of the baseline fluctuations.

6.2.2. Background models

With the exception of the neutron background, the models used in the low mass analysis are data-driven, i.e. sidebands of the WIMP search data of Run308 were used to construct them. The data was first blinded, i.e. fiducial single energy deposit with an ionization quenching $0 < Q < 0.5$ in the energy range $E_{\text{rec}} = [0, 200]$ keV were excluded from the data set. Whenever possible, the model was cross-checked using calibration data.

Bulk gamma events

The bulk γ background is modelled by a Compton-like flat component and cosmogenic lines by fitting the data in the range $E_{\text{heat}} = [3, 15]$ keV$_{\text{ee}}$ (keV electronic recoil equivalent) and extrapolated down to 0 keV$_{\text{ee}}$. The biggest contribution arises from ^{65}Zn (8.98 keV), ^{68}Ga (9.66 keV) and ^{68}Ge (10.37 keV) with corresponding L-shell lines near the threshold at 1.10 keV, 1.19 keV and 1.30 keV, respectively. The L-shell cosmogenic line intensities are derived from the K-shell lines, knowing the relative intensity ratio of $\sim 11\%$. There are several other K-shell lines in the energy range $5 - 7.7$ keV which are not of importance for WIMP search. Note that a similar work has been done for surface γ's and 4 intermediate categories such as triple events or double veto events.

Events from β-decays and recoiling Pb nuclei

Using simulations, the main contribution to the β-background has been identified to come from radon in the vicinity and on the surface of the detectors. This background can vary significantly from one detector to the other. Simulations also showed that the shape of the measured energy spectrum strongly depends on the position of the source and its implementation depth. Considering the uncertainties on the simulations, sideband data has been used to derive a model. Surface events were first selected by requiring a clear signal on one of the veto electrodes ($> 5\sigma$). The β, ^{206}Pb and γ populations were separated according to their quenching for each detector, and their heat spectrum was extracted. The β spectra were fitted with a spline function in the energy range $E_{\text{heat}} = [4, 25]\,\text{keV}_{\text{ee}}$ and further extrapolated down to $0\,\text{keV}_{\text{ee}}$, inducing some systematic uncertainty on the model. As for the lead spectra, they are fitted by a gaussian peak at the energy corresponding to the recoil energy of a lead nucleus of $E_{\text{rec}} = 103\,\text{keV}$ with an underlying flat component in the range $E_{\text{heat}} = [10, 35]\,\text{keV}_{\text{ee}}$ and extrapolated down to $0\,\text{keV}_{\text{ee}}$. Surface calibration data were used to cross-check the spectra derived from the WIMP-search data. This calibration was performed in the so-called *Run305* between November 2013 and February 2014 using a ^{210}Pb source placed on the copper casing of two FID detectors. This data was only used for comparison as the radon background is highly depending on the detector and the run conditions. This comparison was performed for one detector (FID837) and a good agreement between the surface β spectra extracted from calibration and from WIMP search data was found [153].

Heat-only events

The dominating background at small recoil energies is the so-called heat-only background, i.e. events for which there is a trigger on one or both heat channels but only noise is reconstructed on each of the ionization channels. It is known from the EDELWEISS-II experiment that part of the heat-only events arise from internal radioactivity in the NTD sensor. These events can be easily rejected in EDELWEISS-III by applying a χ^2 cut on the heat pulse fit. Because of their distinctive pulse shape (due to a much faster decay time), the template used to fit these heat pulses is not adapted, leading to a bad χ^2 value of the fit. In addition, one expects both heat signals from the 2 NTDs to be equal within their respective resolutions. A cut on the difference of the measured heat energies can therefore further reduce such events. However, there is a new population of heat-only events in EDELWEISS-III which survive both cuts. Their origin is not yet understood and is under investigation. This population cannot be explained by the contribution from lead recoils in the collecting electrode, which would be of much lower intensity. Also, the rate of heat-only events after cuts shows the same time-dependent behaviour for all detectors. A burst of the rate followed by a slow exponential decrease was measured in coincidence with a cryogenic and hardware intervention on the 4$^{\text{th}}$ of September 2014, whereas the rate was low and approximatively flat before. Note that the measured decay time of 20 days cannot be related to any radioactive decay. Up to now, the origin of the heat-only events is still unknown. The hypothesis of mechanical noise such as friction between the crystals and their Teflon holders is the most favoured one. New holders were therefore designed and are currently under test at LSM.
The heat-only background for the low mass analysis was modelled by selecting events from the heat-only sideband with $E_{\text{ion}} < 0\,\text{keV}$. Above the analysis threshold of E_{heat} equal to 1 or 1.5 keV$_{\text{ee}}$, the possible contribution from a WIMP signal due to underfluctuation of ionization signal is negligible.

Radiogenic neutrons

Single fiducial neutrons are a potential background for low mass dark matter search. The energy spectrum of the radiogenic neutron background is derived from the simulation of all known neutron sources described in section 2.2.2.2. The dominant contribution comes from the Cu-Be sockets of the 10 mK connectors on the detector. A comparison of the simulated energy spectra for all the sources showed no significant change in the spectral shape in the range $E_{rec} = [2, 20]$ keV. Therefore a potential unknown neutron source should not deviate from the model. The energy spectrum of all simulated fiducial neutrons is fitted in the range $E_{rec} = [2, 20]$ keV using a double exponential function. The normalization of the neutron spectrum is derived from the number of observed multiple scatterings in the nuclear recoil band: 9 multiple events were found in $E_{rec} = [10, 100]$ keV$_{NR}$ (keV nuclear recoil equivalent) for a fiducial exposure of 1309 kg · days (see section 6.1.2). Using the expected single to multiple neutron ratio extracted from simulation, the number of expected single fiducial neutron was derived and the energy distribution was scaled for each bolometer.

6.2.3. Muon-induced neutrons

An estimation of the number of μ-induced neutrons in the low mass data was carried out before the data unblinding to decide whether it was necessary to perform a veto analysis before the data unblinding. The muon simulations used for this estimation were described in section 3.4.2.2 and summarized in section 6.1.2.

The simulation of muons in the experimental setup was split in 8 sub-simulations of muons and antimuons in 4 energy ranges. The output of each simulation is modified to take into account individual bolometer responses. The average heat and ionization baseline resolutions determined using the low mass data selection cuts were used here. In addition, the average trigger thresholds for each bolometer over the selected data period were used to determine whether an event is single or multiple. These parameters are summarized in table 6.3 for the 8 selected low mass detectors. Then, single events were selected by requiring only one bolometer with a simulated heat energy above the average trigger threshold. Fiducial events were selected by requiring $E_{rec} < 1.5$ keV in the volume delimiting the surface of the bolometer. A lower analysis threshold of 1 keV$_{ee}$ or 1.5 keV$_{ee}$ depending on the detector, and an upper threshold of 15 keV$_{ee}$ was applied on the simulated heat energy.

The number of single nuclear recoils expected in the data was calculated by deriving the number of simulated events in the 99% nuclear recoil band: contrary to the standard WIMP mass analysis, no 90% nuclear recoil band cut is applied on the data. An exact estimation of the μ-induced neutron background would require to take into account the BDT cut (described in the following section) which changes with the mass of the studied WIMP. Such level of precision is not necessary for a first estimation of the μ-induced background. Thus, using the 99% nuclear recoil band gives an upper limit on the number of expected μ-induced neutrons in the region of interest.

The total number of single nuclear recoils is calculated as follows:

$$N_{simu}^{WIMP\text{-}like} = \sum_{i=1}^{8\ (bolo)} t_i \left(\sum_{j=1}^{8\ (simu)} \frac{n_{ij}}{s_j} \right) \tag{6.8}$$

where t_i is the livetime for bolometer i among the 8 selected bolometers given in table 6.3; n_j the number of single events in the 99% nuclear recoil band, in the region of interest, in simulation j; and s_j the simulated time for the simulation j. The number of expected μ-induced single neutrons interacting in the fiducial volume before vetoing is:

$$N_{simu}^{WIMP\text{-}like} = 0.45 \pm 0.03\ (\text{stat})\ _{-0.09}^{+0.14}\ (\text{sys}) \tag{6.9}$$

Table 6.3. – Average bolometer heat $\langle \text{FWHM}_{\text{heat}} \rangle$ and ionization $\langle \text{FWHM}_{\text{ion}} \rangle$ baseline resolutions as well as trigger threshold $\langle E_{\text{th}} \rangle$ for the 8 low mass detectors over the selected time period $t_{\text{live-time}}$.

FID	824	825	827	837	838	839	841	842
$t_{\text{live-time}}$ (in days)	109	117.7	121	118.1	118.3	114.6	133.4	95.1
$\langle \text{FWHM}_{\text{heat}} \rangle$ (in keV)	0.55	0.46	0.52	0.52	0.54	0.54	0.49	0.60
$\langle \text{FWHM}_{\text{ion}} \rangle$ (in keV)	0.29	0.45	0.39	0.37	0.43	0.62	0.52	0.56
$\langle E_{\text{th}} \rangle$ (in keV)	0.60	0.84	0.81	0.83	0.90	1.14	0.98	1.09

Analog to the simulation for standard WIMPs, the systematic uncertainties arise from three contributions: the simulated μ-induced neutron yield in lead, estimated to be $+26\%$ [118] and -16% [83] (see section 3.4.1.1); the reference muon flux used to normalize the simulation, estimated to be $+22\%$ (see section 3.4.2.2); and the 15% excess of simulated single events compared to the data observed in section 5.3.3, considered as a negative systematic uncertainty for the rate of multiple nuclear recoils and as positive systematic uncertainty for the rate of single nuclear recoils. The systematic uncertainty on the live-time determination is considered negligible.

Considering the lower limit of the μ-veto efficiency of 93% (see eq. 5.18) and the uncertainty on the number of simulated events, the following upper limit on the number of untagged μ-induced WIMP-like events is calculated:

$$N_{\text{simu}}^{\text{WIMP-like, after } \mu\text{-veto}} < 0.04 \quad \text{events at 90\% C.L.} \tag{6.10}$$

The number of expected μ-induced WIMP-like events in the region of interest is thus far less than 1 event. It was therefore decided that time periods during which the veto was off (few % of the total live-time) are not cut from the analysis. A coincidence analysis was performed after the data unblinding, but none of the event in the WIMP box was seen in coincidence with the μ-veto.

6.2.4. Output of the BDT analysis and exclusion limits

In the BDT analysis, the following six variables are used: the four ionization channels of veto and collecting electrodes, the combined heat signal of the two NTD sensors and the time-dependent rate of heat-only events. The BDT combines these variables into a single discriminating variable called BDT score. Low BDT scores indicate that an event is more likely to be background whereas a high value indicates a signal-like event. For each detector and discrete WIMP mass values $m_{\text{WIMP}} \in \{3, 4, 5, 6, 7, 10, 15, 20, 30\}$ GeV, a separate BDT was used. First, each BDT was trained to distinguish background events from signals using toy MC events of known types. These toy events were generated from the background models described above and from the standard halo WIMP model. At the end of the training phase, the cut applied on the BDT output was chosen for each WIMP mass and each detector to maximize the signal to background ratio. The BDT analysis was then run over the unblinded WIMP search data. For illustration, the normalized BDT score distributions for two FID detectors (FID824 and FID825) and two WIMP masses (5 and 20 GeV) are plotted in fig. 6.3. The data points show good agreement with the predicted total contribution from all background sources. Events with a BDT score above the BDT cut are considered as WIMP candidates. For different WIMP masses, the background dominating above the BDT cut differs: while the radiogenic neutrons dominate at 20 GeV, the heat-only events and fiducial γ-events contribute most at 5 GeV. In both cases, surface events are a negligible background for the WIMP search due to the good rejection performance of the FID design. For the FID824 detector shown as illustration,
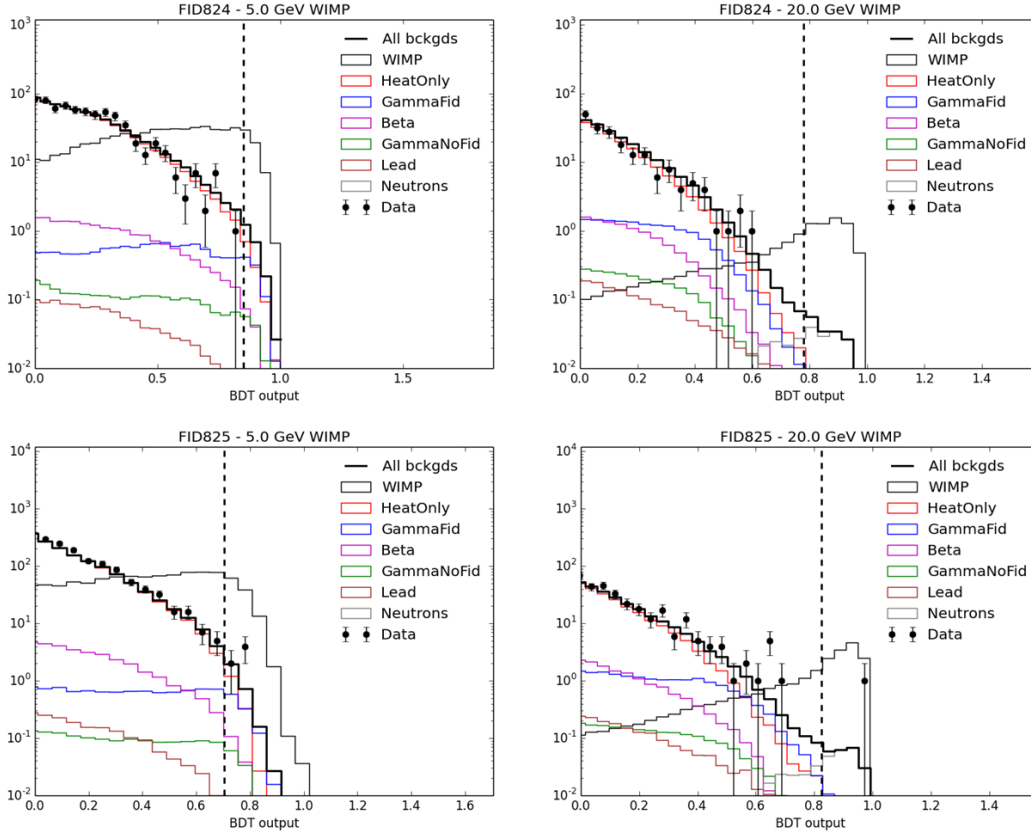
Figure 6.3. – Examples of BDT output distributions for two detectors (FID824 and FID825) and two WIMP masses (5 and 20 GeV). The data is displayed using black markers. The coloured histograms are the expected backgrounds as quoted in the legend whereas the black histogram shows the WIMP signal distribution for a reference cross section. The vertical dashed line shows the BDT cut optimized for each WIMP mass and detector. See text for more details.

no event was observed above the BDT cut. For FID825 however, 9 and 4 events were measured for 5 and 20 GeV respectively, whereas the expected numbers of background events are 6.14 and 1.35 events. However, this excess of observed events is not statistically significant and is compatible with a background fluctuation.

The combined upper limit on the spin-independent WIMP-nucleon scattering cross section was derived using the 8 detectors. For each WIMP mass, the 90% Poisson upper limit on the number of measured events passing the BDT cut was calculated. The upper limit on the cross section was then derived by comparison with the integrated WIMP signal above the BDT cut for a reference cross section. As can be seen in fig. 6.4, the exclusion limit for the spin-independent WIMP-nucleon cross section varies from 4.6×10^{-4} pb at 5 GeV to 6.2×10^{-8} pb at 30 GeV. EDELWEISS-III can therefore exclude the 90% C.L. CDMS-II silicon signal region [157]. Some R&D is ongoing to understand the heat-only background and further improve the energy resolutions and thresholds. It could be achieved by replacing the FET with HEMT (High Electron Mobility Transistors) readout and as well as having a better knowledge of the thermal model of the NTDs [46].
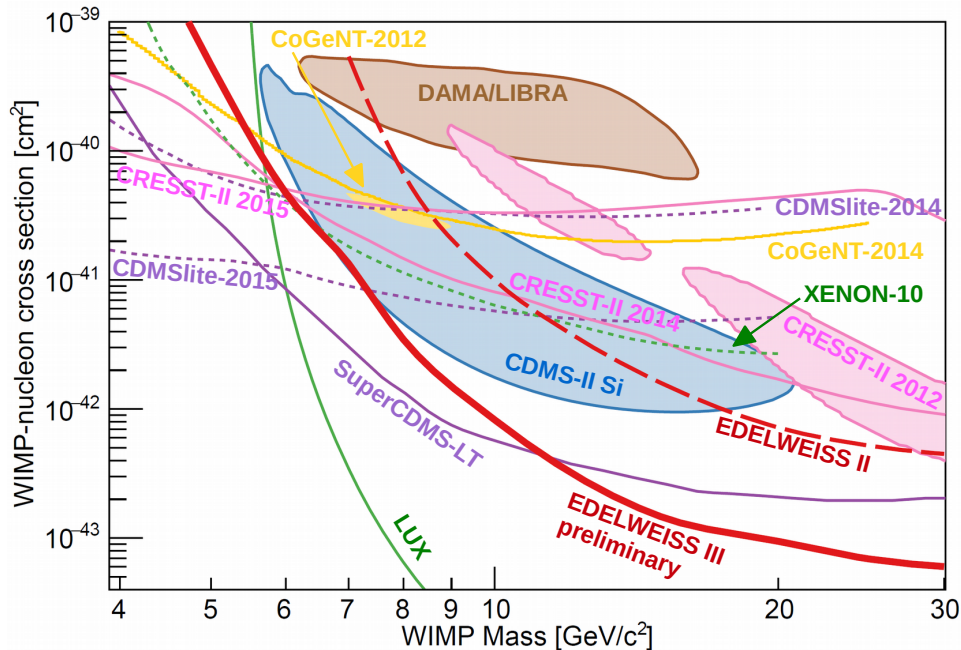
Figure 6.4. – Parameter space of spin-independent WIMP-nucleon scattering cross section versus WIMP mass, showing the exclusion limits and signal claims from various dark matter experiments. The red curves show the EDELWEISS-II (dashed line) and the EDELWEISS-III (solid line) low mass analysis results.

6.3. Expected muon-induced background for the initial goal of EDELWEISS-III

The initial goal of the EDELWEISS experiment for standard WIMP mass was first to obtain a background-free fiducial exposure of $3000 \, \text{kg} \cdot \text{days}$, and then reach a fiducial exposure of $12000 \, \text{kg} \cdot \text{days}$ for which background should start to appear. As shown in section 6.1.1, these goals are compromised due to the presence of an unknown radiogenic neutron source. However, simulations are planned to find out the possible source of background reproducing the high single-to-multiple hit ratio. In case this source would be identified and could be removed, the expected μ-induced background for these initial goals would be of interest. Therefore the rate is extrapolated from the Run308 results.

The 17 detectors selected in the standard WIMP mass analysis are considered with the same average response as in Run308. The estimation was performed for 3 values of the analysis threshold of 10, 15 and $20 \, \text{keV}$. As measured in Run308, the μ-veto is considered to be inefficient for 6% of the accumulated live-time. This accounts for technical problems or interruptions of the data taking. The rest of the time, the conservative lower limit on the μ-veto efficiency to detect μ-induced bolometer events $\varepsilon_{\mu-\text{veto}} = 93\%$ is considered (see section 5.4). The quoted exposures of $3000 \, \text{kg} \cdot \text{days}$ and $12000 \, \text{kg} \cdot \text{days}$ would be reached in 0.9 and 3.7 years of effective data taking, respectively [6]. Reaching an exposure of $12000 \, \text{kg} \cdot \text{days}$ with 17 detectors is therefore not conceivable. However, the extracted number gives an upper limit on the number of expected background. Indeed, the μ-induced background scales linearly with the measurement time and the effective surface covered by the array but not with the detection mass. By increasing the number of bolometers, the measured time decreases and the number of single events is additionally suppressed. Thus, deriving the expected number of μ-induced WIMP-like events for 3.7 years with 17

---

6. Note that these exposures should be achieved after the acceptance of the nuclear recoils, estimated conservatively to be 86% [150], has been taken into account. The live-time necessary to reach these values is then 14% higher

Table 6.4. – Upper limit on the number of expected μ-induced WIMP-like events in 17 detectors before and after vetoing for 3000 and 12000 kg · days exposure, considering a μ-veto efficiency $\varepsilon_{\mu-\text{veto}} > 93\%$ at 90% C.L. during 94% of the live-time and a μ-veto system off for 6% of the live-time to account for technical issues.

	Analysis threshold (keV)	10	15	20
before vetoing	3000 kg · days	$2.07^{+0.71}_{-0.40}$	$1.41^{+0.48}_{-0.27}$	$1.08^{+0.37}_{-0.21}$
	12000 kg · days	$8.29^{+2.82}_{-1.61}$	$5.63^{+1.92}_{-1.09}$	$4.34^{+1.48}_{-0.84}$
after vetoing	3000 kg · days	$0.24^{+0.08}_{-0.05}$	$0.16^{+0.06}_{-0.03}$	$0.13^{+0.04}_{-0.02}$
	12000 kg · days	$0.97^{+0.33}_{-0.19}$	$0.66^{+0.22}_{-0.13}$	$0.51^{+0.17}_{-0.10}$

bolometers gives an upper limit on the expected background for this exposure.

Knowing the rate of μ-induced WIMP-like events $\Gamma_{\text{WIMP-like}}$ given in table 6.1, the upper limit on the number of expected μ-induced neutron background before vetoing and after vetoing (using eq. 6.4) can be derived. The results are listed in table 6.4. Under the assumptions described above, the residual μ-induced neutron background for an accumulated exposure of 3000 kg · days will not limit the sensitivity of EDELWEISS-III for dark matter search. Muon-induced background might start to appear for an exposure of 12000 kg · days, depending on the actual number of bolometers taking data.

For a more precise estimation of the residual background, a better knowledge of the μ-veto efficiency to tag muons inducing bolometer events is needed. This can be achieved with a longer accumulated live-time and thus a larger number of clear μ-induced bolometer events, used to obtain the efficiency following the method described in section 5.4. In addition, the μ-veto efficiency could be derived from simulations knowing the response of the individual modules, which could be extracted using two different methods: for modules with a low trigger threshold, the position dependent response can be extracted with high precision using the method set up in the framework of this thesis (see chapter 4); for modules with a high trigger threshold, the average response over the module length can be extracted with a lower precision using low energy μ-veto data, in a similar way as performed in EDELWEISS-II (see section 3.2.4.1). However, the key task to minimize the μ-induced neutron background remains a daily monitoring of the μ-veto to immediately identify and quickly solve technical issues and thus ensure a full efficiency of the μ-veto system during the whole data taking period.

Conclusions

This thesis was performed in the context of the EDELWEISS-III experiment, whose goal is to probe WIMP-nucleon cross-sections at least one order of magnitude smaller compared to EDELWEISS-II, down to 10^{-9} pb. To reach this objective, many improvements were applied to the experimental setup in order to reduce the residual background level to less than 1 event for one year of data taking. A total of 8 months of data with 24 FID800 detectors have been accumulated for WIMP search during Run308 and has been analysed in terms of μ-induced neutron background.

The work performed in the context of this thesis had two goals: the first was to reduce the dead-time of the μ-veto system to a minimum and ensure its full efficiency during WIMP search. Therefore, daily shifts were performed to guarantee that the system was running continuously and taking data of good quality. The existing monitoring tools were significantly improved to give a complete overview of the proper functioning of the overall μ-veto system and its 46 individual modules. Over the 253 days of Run308, the μ-veto system was taking data for 98.5% of the time. After strict quality cuts requiring a full efficiency of the system, the remaining live-time decreased down to 91.2%.

The second goal of this thesis was to give a precise estimation of the irreducible μ-induced neutron background limiting the sensitivity for dark matter search. This required knowledge of both the rate of μ-induced WIMP-like events, as well as the μ-veto efficiency to tag μ-induced bolometer events. To determine these values, data taken during Run308 was analysed and Geant4-based Monte Carlo simulations of muons in the experimental setup were performed.

The existing EDELWEISS-II simulation software was further developed by the collaboration to include changes to the experimental setup. The newly implemented simulation code is now based on the Geant4 version 4.9.6 together with the `Shielding` physics list. With this simulation software, muons were simulated in the EDELWEISS-III setup to derive the μ-induced neutron background. As expected, the higher density and granularity of the bolometer array suppress single scattering events. In addition, the new PE shields inside and around the cryostat, installed to attenuate radiogenic neutrons, were found to reduce the μ-induced background by a factor of 2.7.

A dedicated analysis was performed with the Run308 data to study coincidences between the μ-veto system and the bolometers. For each selected μ-veto event, the closest bolometer hit in time was associated. With the goal of comparing measurement with simulation, strict cuts were applied to ensure stable data taking conditions which could be reproduced in the simulation. Out of the 24 read-out detectors, 20 were selected for this analysis as well as time periods during which the bolometer array and the μ-veto system were fully efficient. An accumulated live-time of $t^{B+V} = (133.6 \pm 2.7)$ days was derived and used to study the characteristics and extract the rate of coincidence events.

With the aim of analysing the characteristics of these coincidence events, a cut on the μ-veto multiplicity of $M_{\text{veto}} \geq 2$ was first applied in favour of a good signal-to-noise ratio. The time difference $\Delta t = t_{\text{bolo}} - t_{\text{veto}}$ expected from physical coincidences was estimated

to be included in a time window $\Delta t = \pm 12\,\mu$s. A total of 138 coincidences were measured, with an expected number of accidental coincidences of (1.94 ± 0.01) events. Using this sample of pure μ-induced bolometer events, the rate of coincidences was found to be:

$$\Gamma^{\mu}_{\mathrm{M_{veto}\geq 2}} = 1.02 \pm 0.09 \text{ (stat) } {}^{+0.03}_{-0.02} \text{ (sys) events/day}$$

This rate is in good agreement with the rate determined using an independent analysis pipeline [152]. Signatures of μ-induced bolometer events were compared between simulation and data, showing an excess of 15% of single bolometer events in the simulation, which was taken into account as a negative uncertainty on the simulated rate.

The requirement on the μ-veto multiplicity was then discarded to additionally include coincidences for which only one module of the μ-veto was hit. For this scenario, a total of 190 coincidences were measured, with an expected number of accidental coincidences of (32.1 ± 0.4) events. The coincidence rate between the μ-veto and the bolometer array was found to be:

$$\Gamma^{\mu}_{\mathrm{M_{veto}\geq 1}} = 1.18 \pm 0.10 \text{ (stat) } {}^{+0.03}_{-0.02} \text{ (sys) events/day}$$

The rate of μ-induced WIMP-like events (single nuclear recoils) was also extracted by selecting single fiducial events in the 90% C.L. nuclear recoil band with $E_{\mathrm{rec}} = [10,200]$ keV. No events were seen in coincidence with the μ-veto, leading to an upper limit of the measured rate of WIMP-like events of:

$$\Gamma^{\mathrm{WIMP\text{-}like}}_{\mathrm{M_{veto}\geq 1}} < (1.7 \times 10^{-2}) \text{ events/day} \quad (90\% \text{ C.L.})$$

For comparison, these rates were estimated from simulations of muons in the EDELWEISS-III setup by applying the same selection cuts and taking into account the average bolometer response over the Run308. The rate of coincidences before vetoing was estimated to be:

$$\Gamma^{\mu}_{\mathrm{simu}} = 1.09 \pm 0.01 \text{ (stat) } {}^{+0.24}_{-0.00} \text{ (sys) events/day}$$

whereas the rate of WIMP-like events was found to be:

$$\Gamma^{\mathrm{WIMP-like}}_{\mathrm{simu}} = (7.6 \pm 0.1 \text{ (stat) } {}^{+2.6}_{-1.7} \text{ (sys)}) \times 10^{-3} \text{ events/day}$$

Both simulation and measurement were shown to agree within uncertainties.

The coincidence analysis showed that μ-induced bolometer events can be distinguished from other backgrounds on the basis of their bolometer multiplicity and their total energy deposit in the bolometer array. A lower limit on the μ-veto efficiency was derived by identifying a sample of μ-induced bolometer events and verifying that they were seen in coincidence with the μ-veto. A sample of 32 bolometer events was selected from the full data set, all seen by the μ-veto in a time window of $\pm 12\,\mu$s, leading to a lower limit on the tagging efficiency of:

$$\varepsilon_{\mu\text{-veto}} > 93\% \quad (90\% \text{ C.L.})$$

This analysis gave a reliable lower boundary on the efficiency and is only limited by statistical uncertainty. In the future, the uncertainty on this efficiency can be reduced using the data taken during the second half of 2015 in the so-called Run309.

The efficiency can also be derived from simulation, knowing the response of the 46 individual scintillator modules. As the scintillator panels are up to 4 m long, the light attenuation together with the trigger condition lead to a strong position-dependence of the module response, in particular of the trigger threshold. One of the drawbacks of going underground to shield the experiment against cosmic rays is that muons cannot be used for probing this threshold anymore, as their flux is too low to give sufficient statistics. In the previous EDELWEISS-II experiment, the module response was extracted from low energy

μ-veto data by averaging over the module length. Consequently, the determination of this efficiency was limited by the lack of knowledge of the module response at low energies. Therefore, a new method was set up to derive the position-dependent trigger threshold of individual μ-veto modules. The method is based on the comparison of the measured energy spectrum of an AmBe source with the simulated spectrum, which is folded with the parametrized module response function. The module response is characterized using 4 parameters: a smearing of the energy deposit σ_{E}, a threshold efficiency curve described by an error function with parameters E_{thr} and the σ_0, and an energy scaling factor C_{cal}. The set of parameters giving the best match between the two spectra was derived with a likelihood analysis, while the systematic uncertainty on the parameters was estimated using a Monte Carlo Markov Chain. By repeating this procedure for several positions of the source along the module axis, the position-dependent trigger threshold was extracted. To finally derive the muon detection efficiency of a module, its position-dependent response was applied on the simulated energy spectrum of muon interactions.

The method was successfully applied on test module M42 and gave an efficiency of:

$$\varepsilon_{\mathrm{M42}} = (95 \pm 0.5)\%$$

where the error is dominated by the uncertainty on the source activity of $\pm 20\%$. From here on, it is possible to calculate the overall μ-veto efficiency and its uncertainty by applying the method to the remaining modules. However, this method has several limitations. The most significant is that a neutron source cannot be used in the vicinity of the bolometers during dark matter search. With this constraint and considering the low activity of the AmBe source, only a fraction of the modules could be calibrated. In some cases, the trigger threshold of the modules was too high for the source to be detected at all.

With a higher activity calibration source whose activity is more precisely determined, the calibration could be performed for all modules in a reasonable time. For those modules for which the trigger threshold was too high, the average response over the module length, as extracted in EDELWEISS-II could be used in combination with the method shown in this thesis.

An estimation of the expected μ-induced neutron background was performed for the WIMP search analysis of EDELWEISS-III data. An analysis for WIMPs in the standard mass range $[10,1000]$ GeV was completed for an accumulated exposure of $600 \, \mathrm{kg} \cdot \mathrm{days}$ based on a the selection of 17 bolometers. Five single nuclear events have been observed in the region of interest, revealing the presence of an unexpected neutron source. Two dedicated studies performed in the framework of this thesis showed that this background cannot be induced by untagged muons and must thus be of radiogenic origin. First, the expected μ-induced neutron background before vetoing was derived. For the specific bolometer selection and cuts of this analysis it was found to be:

$$N_{\mathrm{simu}}^{\mathrm{WIMP\text{-}like}} = 0.36 \pm 0.02 \text{ (stat) } {}^{+0.12}_{-0.08} \text{ (sys) events}$$

Considering the lower limit on the μ-veto efficiency and the accumulated live-time during which the μ-veto was either off or not fully efficient, the following upper limit on the irreducible μ-induced WIMP-like event was derived:

$$N_{\mathrm{WIMP\text{-}like}}^{\mu} < 0.06 \text{ events} \quad (90\% \text{ C.L.})$$

Even neglecting the μ-veto, the expected μ-induced neutron background is far from explaining the observed single nuclear recoils. Further evidence for the radiogenic origin of the observed neutron background was found by comparing the topology of the untagged events with the expected signatures of μ-induced events, notably the bolometer and μ-veto multiplicities as well as the Δt value for the closest veto event. An estimation was also

performed for the low mass WIMP analysis with 8 selected bolometers and a similar fiducial exposure for the mass range [3,30] GeV. The expected μ-induced neutron background after vetoing, above the analysis threshold and for $E_{\text{heat}} < 15\,\text{keV}$, was calculated to be:

$$N_{\text{simu}}^{\text{WIMP-like, after } \mu\text{-veto}} < 0.04 \quad \text{events} \quad (90\% \text{ C.L.})$$

and thus negligible.

A coincidence analysis performed for both standard and low mass WIMP search data confirmed that there are no events in the signal region in coincidence with the μ-veto as expected from these simulation results.

The initial design goal of EDELWEISS-III was to reach a background free exposure of first $3000\,\text{kg}\cdot\text{days}$ and then $12000\,\text{kg}\cdot\text{days}$, after which background is expected to appear. A projection of the μ-induced neutron background for these two exposures, extrapolated from Run308 results, was performed as well. Whereas no WIMP-like event was measured in Run308, an efficient rejection of the μ-veto is necessary for larger exposure. For $3000\,\text{kg}\cdot\text{days}$ and an analysis threshold of $10\,\text{keV}$, $2.07^{+0.71}_{-0.40}$ WIMP-like events are expected before vetoing. Considering the lower boundary of the μ-veto efficiency of 93% and a dead-time of the μ-veto during 6% of the bolometer data taking, an upper limit on the irreducible μ-induced neutron background is estimated to be $0.24^{+0.08}_{-0.05}$. Even for the extended exposure scenario, the remaining background after vetoing is below 1 event.

While μ-induced neutron background could be an irreducible background limiting the sensitivity for direct dark matter search, it can be efficiently rejected using a μ-veto system. In conclusion, it can be stated that μ-induced neutron background is not a limiting factor for WIMP search with EDELWEISS-III. If well handled, μ-induced neutron background is therefore not a show-stopper for future direct dark matter searches.

Bibliography

[1] Zwicky, F. *Die Rotverschiebung von extragalaktischen Nebeln.* Helv. Phys. Acta, 6:110–127, 1933.

[2] Sanders, R. *À la recherche de la matière noire.* De Boeck, 2012.

[3] Milgrom, M. *A modification of the Newtonian dynamics as a possible alternative to the hidden mass hypothesis.* Astrophys. J., 270:365, jul 1983. doi:10.1086/161130.

[4] Bertone, G.; Hooper, D.; and Silk, J. *Particle dark matter: evidence, candidates and constraints.* Phys. Rep., 405(5-6):279–390, jan 2005. doi:10.1016/j.physrep.2004.08. 031.

[5] Carroll, S.M. *The Cosmological Constant.* Living Rev. Relativ., 4(May 2008):1–56, 2001. doi:10.12942/lrr-2001-1.

[6] Weinberg, S. *The cosmological constant problem.* Rev. Mod. Phys., 61(1):1–23, jan 1989. doi:10.1103/RevModPhys.61.1.

[7] Baer, H.; Choi, K.Y.; Kim, J.E.; et al. *Dark matter production in the early Universe: Beyond the thermal WIMP paradigm.* Phys. Rep., 555:1–60, 2015. doi:10.1016/j. physrep.2014.10.002.

[8] Ade, P.A.R.; Aghanim, N.; Alves, M.I.R.; et al. *Planck 2013 results. I. Overview of products and scientific results.* Astron. Astrophys., 571(May):A1, nov 2014. doi: 10.1051/0004-6361/201321529.

[9] Smoot, G.F.; Bennett, C.L.; Kogut, A.; et al. *Structure in the COBE differential microwave radiometer first-year maps.* Astrophys. J., 396:L1, sep 1992. doi:10.1086/ 186504.

[10] Komatsu, E.; Dunkley, J.; Nolta, M.R.; et al. *Seven-year wilkinson microwave anisotropy probe (WMAP*) observations: cosmological interpretation.* Astrophys. J. Suppl. Ser., 180(2):330–376, feb 2009. doi:10.1088/0067-0049/180/2/330.

[11] Planck Collaboration; Ade, P.A.R.; Aghanim, N.; et al. *Planck 2015 results. XIII. Cosmological parameters.* arXiv:1502.01589, 2015.

[12] Perlmutter, S.; Aldering, G.; Goldhaber, G.; et al. *Measurements of Ω and Λ from 42 High-Redshift Supernovae.* Astrophys. J., 517(2):565–586, jun 1999. doi:10.1086/ 307221.

[13] Riess, A.G.; Filippenko, A.V.; Challis, P.; et al. *Observational Evidence from Supernovae for an Accelerating Universe and a Cosmological Constant.* Astron. J., 116(3):1009–1038, sep 1998. doi:10.1086/300499.

[14] Steigman, G. *Big Bang Nucleosynthesis: Probing the First 20 Minutes.* C02-11-17, 2:169–195, jul 2003.

[15] Particle Data Group. *Big-Bang nucleosynthesis.* Phys. Lett. B, 667(1-5):29–30, sep 2008. doi:10.1016/j.physletb.2008.07.023.

[16] Feng, J.L. *Dark Matter Candidates from Particle Physics and Methods of Detection.* Annu. Rev. Astron. Astrophys., 48(1):495–545, aug 2010. doi:10.1146/annurev-astro-082708-101659.

[17] Olive, K.A, et al., P.D.G. *Review of Particle Physics.* Chinese Phys. C, 38(9):090001, aug 2014. doi:10.1088/1674-1137/38/9/090001.

[18] Mohapatra, R.N. *Supersymmetry and R-parity: an Overview.* Phys. Scr., 90(8):1–21, 2015. doi:10.1088/0031-8949/90/8/088004.

[19] Navarro, J.F.; Frenk, C.S.; and White, S.D.M. *The Structure of Cold Dark Matter Halos.* Astrophys. J., 462:563, may 1996. doi:10.1086/177173.

[20] Catena, R. and Ullio, P. *A novel determination of the local dark matter density.* J. Cosmol. Astropart. Phys., 2010(08):004–004, aug 2010. doi:10.1088/1475-7516/2010/08/004.

[21] Mitsou, V.A. *Overview of searches for dark matter at the LHC.* J. Phys. Conf. Ser., 651(Cdm):012023, nov 2015. doi:10.1088/1742-6596/651/1/012023.

[22] Klasen, M.; Pohl, M.; and Sigl, G. *Indirect and direct search for dark matter.* eprint arXiv:1507.03800, 2015. doi:10.1016/j.ppnp.2015.07.001.

[23] Donato, F. *Indirect searches for dark matter.* Phys. Dark Universe, 4(1):41–43, 2014. doi:10.1016/j.dark.2014.06.001.

[24] Ackermann, M.; Ajello, M.; Albert, a.; et al. *Search for gamma-ray spectral lines with the Fermi Large Area Telescope and dark matter implications.* Phys. Rev. D - Part. Fields, Gravit. Cosmol., 88(8):1–44, 2013. doi:10.1103/PhysRevD.88.082002.

[25] Aguilar, M.; Alberti, G.; Alpat, B.; et al. *First Result from the Alpha Magnetic Spectrometer on the International Space Station: Precision Measurement of the Positron Fraction in Primary Cosmic Rays of 0.5–350 GeV.* Phys. Rev. Lett., 110(14):141102, apr 2013. doi:10.1103/PhysRevLett.110.141102.

[26] Adriani, O.; Barbarino, G.C.; Bazilevskaya, G.A.; et al. *Cosmic-Ray Positron Energy Spectrum Measured by PAMELA.* Phys. Rev. Lett., 111(8):081102, aug 2013. doi:10.1103/PhysRevLett.111.081102.

[27] Donato, F.; Fornengo, N.; and Scopel, S. *Effects of galactic dark halo rotation on WIMP direct detection.* Astropart. Phys., 9(3):247–260, 2003. doi:10.1016/S0927-6505(98)00025-5.

[28] Ellis, J.; Flores, R.; and Lewin, J. *Rates for inelastic nuclear excitation by dark matter particles.* Phys. Lett. B, 212(3):375–380, 1988. doi:10.1016/0370-2693(88)91332-9.

[29] Schumann, M. *Dark Matter 2014.* EPJ Web Conf., 96(1):01027, jan 2015. doi:10.1051/epjconf/20159601027.

[30] Bernabei, R.; Belli, P.; Cappella, F.; et al. *Final model independent result of DAMA/LIBRA-phase1.* Eur. Phys. J. C, 73(12):2648, aug 2013. doi:10.1140/epjc/s10052-013-2648-7.

[31] Roth, S.; Ciemniak, C.; Coppi, C.; et al. *Cryogenic composite detectors for the dark matter experiments CRESST and EURECA.* Opt. Mater. (Amst)., 31(10):1415–1420, aug 2009. doi:10.1016/j.optmat.2008.09.013.

[32] Schmidt, B.; Armengaud, E.; Augier, C.; et al. *Muon-induced background in the EDELWEISS dark matter search.* Astropart. Phys., 44:28–39, apr 2013. doi:10.1016/j.astropartphys.2013.01.014.

[33] Horn, O.M. *Simulations of the Muon-Induced Neutron Background of the EDELWEISS-II Experiment for Dark Matter Search.* Ph.D. thesis, Forschungszentrum Karlsruhe, 2008.

[34] Armengaud, E.; Augier, C.; Benoît, A.; et al. *Background studies for the EDELWEISS dark matter experiment.* Astropart. Phys., 47(May):1–9, jul 2013. doi:10.1016/j.astropartphys.2013.05.004.

[35] Chazal, V.; Brissot, R.; Cavaignac, J.; et al. *Neutron background measurements in the Underground Laboratory of Modane.* Astropart. Phys., 9(2):163–172, 1998. doi:10.1016/S0927-6505(98)00012-7.

[36] Rozov, S.; Armengaud, E.; Augier, C.; et al. *Monitoring of the thermal neutron flux in the LSM underground laboratory.* Bull. Russ. Acad. Sci. Phys., 74(4):464–466, jan 2012.

[37] Lemrani, R.; Gerbier, G.; and EDELWEISS Collaboration. *Update of neutron studies in EDELWEISS.* J. Phys. Conf. Ser., 39:145–147, may 2006. doi:10.1088/1742-6596/39/1/033.

[38] L'Hour, M. *Un site sous-marin sur la côte de l'Armorique. L'épave antique de Ploumanac'h.* Rev. archéologique l'ouest, 4(1):113–131, 1987. doi:10.3406/rao.

[39] Zhang, X. *A Novel Phonon-Scintillation Cryogenic Detector and Cabling Solution for Dark Matter Direct Detection Xiaohe Zhang.* Ph.D. thesis, Oxford University, 2015.

[40] Klein, C. *Bandgap dependence and related features of radiation ionization energies in semiconductors.* J. Appl. Phys., 39(4):2029–2038, 1968. doi:10.1063/1.1656484.

[41] Luke, P.; Beeman, J.; Goulding, F.; et al. *Calorimetric ionization detector.* Nucl. Instruments Methods Phys. Res. Sect. A Accel. Spectrometers, Detect. Assoc. Equip., 289(3):406–409, apr 1990. doi:10.1016/0168-9002(90)91510-I.

[42] Lindhard, J.; Scharff, M.; and Schiøtt, H. *Range concepts and heavy ion ranges.* Det K. Danske Vidensk. Selsk., 33(14):1, 1963.

[43] Lindhard, J.; Nielsen, V.; and Scharff, M. *Approximation method in classical scattering by screened coulomb fields: (notes on atomic collisions ; 1).* Mat. meddelelser, 10(36):32, 1968.

[44] Di Stefano, P.; Bergé, L.; Chambon, B.; et al. *Background discrimination capabilities of a heat and ionization germanium cryogenic detector.* Astropart. Phys., 14(4):329–337, 2001. doi:10.1016/S0927-6505(00)00127-4.

[45] Akerib, D.; Attisha, M.; Bailey, C.; et al. *Surface Event Rejection Using Phonon Information in CDMS.* Nucl. Phys. B - Proc. Suppl., 173:137–140, nov 2007. doi:10.1016/j.nuclphysbps.2007.08.038.

[46] Billard, J.; De Jesus, M.; Juillard, A.; et al. *Characterization and optimization of EDELWEISS-III FID800 heat signals.* In *J. Low Temp. Phys.* Proceedings of LTD-16, 2016.

[47] Haller, E. *Physics and design of advanced IR bolometers and photoconductors.* Infrared Phys., 25(1-2):257–266, feb 1985. doi:10.1016/0020-0891(85)90088-0.

[48] Mathimalar, S.; Singh, V.; Dokania, N.; et al. *Characterization of Neutron Transmutation Doped (NTD) Ge for low temperature sensor development.* Nucl. Instruments Methods Phys. Res. Sect. B Beam Interact. with Mater. Atoms, 345:33–36, feb 2015. doi:10.1016/j.nimb.2014.12.020.

[49] Neganov, B.; Trofimov, V. *Otkrytia i Izobret.* URRS Pat. No 1037771, pages 146–215, 1985.

[50] Luke, P. *Voltage-assisted calorimetric ionization detector.* J. Appl. Phys., 64(12):6858, 1988. doi:10.1063/1.341976.

[51] Censier, B.; Broniatowski, A.; Juillard, A.; et al. *Surface trapping and detector degradation in Ge bolometers for the EDELWEISS Dark Matter search: experiment and simulation.* Nucl. Instruments Methods Phys. Res. Sect. A Accel. Spectrometers, Detect. Assoc. Equip., 520(1-3):156–158, mar 2004. doi:10.1016/j.nima.2003.11.281.

[52] Benoit, a.; Bergé, L.; Broniatowski, A.; et al. *Event categories in the EDELWEISS WIMP search experiment.* Phys. Lett. B, 479(1-3):8–14, apr 2000. doi:10.1016/S0370-2693(00)00264-1.

[53] Mandic, V.; Mirabolfathi, N.; Meunier, P.; et al. *Study of the dead layer in germanium for the CDMS detectors.* Nucl. Instruments Methods Phys. Res. Sect. A Accel. Spectrometers, Detect. Assoc. Equip., 520(1-3):171–174, mar 2004. doi:10.1016/j.nima.2003.11.285.

[54] Shutt, T.; Emes, J.; Haller, E.; et al. *A solution to the dead-layer problem in ionization and phonon-based dark matter detectors.* Nucl. Instruments Methods Phys. Res. Sect. A Accel. Spectrometers, Detect. Assoc. Equip., 444(1-2):340–344, apr 2000. doi:10.1016/S0168-9002(99)01379-0.

[55] Broniatowski, A.; Defay, X.; Armengaud, E.; et al. *A new high-background-rejection dark matter Ge cryogenic detector.* Phys. Lett. B, 681(4):305–309, nov 2009. doi:10.1016/j.physletb.2009.10.036.

[56] Luke, P. *Unipolar charge sensing with coplanar electrodes-application to semiconductor detectors.* IEEE Trans. Nucl. Sci., 42(4):207–213, 1995. doi:10.1109/23.467848.

[57] Amman, M. and Luke, P. *Three-dimensional position sensing and field shaping in orthogonal-strip germanium gamma-ray detectors.* Nucl. Instruments Methods Phys. Res. Sect. A Accel. Spectrometers, Detect. Assoc. Equip., 452(1-2):155–166, sep 2000. doi:10.1016/S0168-9002(00)00351-X.

[58] Poda, D.V.; Armengaud, E.; Arnaud, Q.; et al. *Scintillating bolometers based on $ZnMoO_4$ and $Zn^{100}MoO_4$ crystals to search for $0\nu2\beta$ decay of ^{100}Mo (LUMINEU project): first tests at the Modane Underground Laboratory.* Contrib. to Proc. 37th Int. Conf. High Energy Phys. (ICHEP 2014), pages 1–7, feb 2015.

[59] Censier, B.; Benoit, A.; Bres, G.; et al. *EDELWEISS Read-out Electronics and Future Prospects.* J. Low Temp. Phys., 167(5-6):645–651, jun 2012. doi:10.1007/s10909-012-0568-9.

[60] Kopmann, A.; Bergmann, T.; Gemmeke, H.; et al. *FPGA-based DAQ system for multi-channel detectors.* In *2008 IEEE Nucl. Sci. Symp. Conf. Rec.*, pages 3186–3190. IEEE, oct 2008. ISBN 978-1-4244-2714-7. doi:10.1109/NSSMIC.2008.4775027.

[61] Armengaud, E.; Augier, C.; Benoît, A.; et al. *Final results of the EDELWEISS-II WIMP search using a 4-kg array of cryogenic germanium detectors with interleaved electrodes.* Phys. Lett. B, 702(5):329–335, aug 2011. doi:10.1016/j.physletb.2011.07.034.

[62] Armengaud, E.; Augier, C.; Benoît, A.; et al. *Search for low-mass WIMPs with EDELWEISS-II heat-and-ionization detectors.* Phys. Rev. D, 86(5):051701, sep 2012. doi:10.1103/PhysRevD.86.051701.

[63] Armengaud, E.; Arnaud, Q.; Augier, C.; et al. *Axion searches with the EDELWEISS-II experiment.* J. Cosmol. Astropart. Phys., 2013(11):067–067, nov 2013. doi:10.1088/1475-7516/2013/11/067.

[64] Juillard, A. *Status and Prospects of the EDELWEISS Direct WIMP Search Experiment.* J. Low Temp. Phys., 167(5-6):1056–1062, jun 2012. doi:10.1007/s10909-012-0512-z.

[65] Gascon, J. and Bastidon, N. *The EDELWEISS-III Project and the Rejection Performance of Its Cryogenic Germanium Detectors.* J. Low Temp. Phys., 176(5-6):870–875, sep 2014. doi:10.1007/s10909-014-1096-6.

[66] Agostinelli, S.; Allison, J.; Amako, K.; et al. *Geant4 – a simulation toolkit.* Nucl. Instruments Methods Phys. Res. Sect. A Accel. Spectrometers, Detect. Assoc. Equip., 506(3):250–303, jul 2003. doi:10.1016/S0168-9002(03)01368-8.

[67] Laubenstein, M. *Radiopurity measurements of the NOSV copper (private comunication)*, 2014.

[68] GEANT4 Collaboration. *Shielding physics list description.* `http://www.slac.stanford.edu/comp/physics/geant4/slac_physics_lists/shielding/physlistdoc.html`.

[69] Scorza, S. *Background investigation in EDELWEISS-III*. In *AIP Conf. Proc.*, page 100002. 2015. doi:10.1063/1.4928002.

[70] Wilson, W.; Perry, R.; Charlton, W.; et al. *Sources: A code for calculating (alpha, n), spontaneous fission, and delayed neutron sources and spectra.* Prog. Nucl. Energy, 51(4-5):608–613, may 2009. doi:10.1016/j.pnucene.2008.11.007.

[71] Lemrani, R.; Robinson, M.; Kudryavtsev, V.; et al. *Low-energy neutron propagation in MCNPX and GEANT4.* Nucl. Instruments Methods Phys. Res. Sect. A Accel. Spectrometers, Detect. Assoc. Equip., 560(2):454–459, may 2006. doi:10.1016/j.nima.2005.12.238.

[72] Tomasello, V.; Kudryavtsev, V.A.; and Robinson, M. *Calculation of neutron background for underground experiments.* Nucl. Instruments Methods Phys. Res. Sect. A Accel. Spectrometers, Detect. Assoc. Equip., 595(2):431–438, 2008. doi:10.1016/j.nima.2008.07.071.

[73] Tomasello, V.; Robinson, M.; and Kudryavtsev, V.A. *Radioactive background in a cryogenic dark matter experiment.* Astropart. Phys., 34(2):70–79, 2010. doi:10.1016/j.astropartphys.2010.05.005.

[74] Carson, M.J.; Davies, J.C.; Daw, E.; et al. *Neutron background in large-scale xenon detectors for dark matter searches.* Astropart. Phys., 21(6):667–687, 2004. doi:10.1016/j.astropartphys.2004.05.001.

[75] Chauvie, S.; Guatelli, S.; Ivanchenko, V.; et al. *Geant4 low energy electromagnetic physics.* In *IEEE Symp. Conf. Rec. Nucl. Sci. 2004.*, volume 3, pages 1881–1885. IEEE, 2004. doi:10.1109/NSSMIC.2004.1462612.

[76] De Jesus, M. *EDELWEISS-III Geant4.9.6 simulations.* Internal note for the edelweiss collaboration, 2014.

[77] De Jesus, M. *Estimation of neutrons induced by Beryllium content on the sockets of delrin detectors.* Internal note for the edelweiss collaboration, 2015.

[78] Schmidt, B. *Measurement of the rate of muon-induced events in the EDELWEISS Dark Matter search 2009-2010.* Ph.D. thesis, Karlsruhe Institute of Technology, 2010.

[79] Anderson, C.D. and Neddermeyer, S.H. *Cloud chamber observations of cosmic rays at 4300 meters elevation and near sea-level.* Phys. Rev., 50(4):263–271, 1936. doi:10.1103/PhysRev.50.263.

[80] Apel, W.D.; Arteaga-Velàzquez, J.C.; Bekk, K.; et al. *Ankle-like feature in the energy spectrum of light elements of cosmic rays observed with KASCADE-Grande.* Phys. Rev. D, 87(8):081101, 2013. doi:10.1103/PhysRevD.87.081101.

[81] Gaisser, T.K. *Cosmic Rays and Particle Physics.* Cambridge University Press, cambridge edition, 1990.

[82] Scheck, F. *Muon physics.* Phys. Rep., 44(4):187–248, aug 1978. doi:10.1016/0370-1573(78)90014-5.

[83] Kluck, H.M. *Measurement of the cosmic-induced neutron yield at the Modane underground laboratory.* Ph.D. thesis, Karlsruher Instituts für Technologie, 2013.

[84] Beringer, J.; Arguin, J.F.; Barnett, R.M.; et al. *Review of Particle Physics.* Phys. Rev. D, 86(1):010001, jul 2012. doi:10.1103/PhysRevD.86.010001.

[85] Groom, D.E.; Mokhov, N.V.; and Striganov, S.I. *Muon Stopping Power and Range Tables 10 MeV – 100 TeV*. At. Data Nucl. Data Tables, 78(2):183–356, jul 2001. doi:10.1006/adnd.2001.0861.

[86] Bogdanov, A.; Burkhardt, H.; Ivanchenko, V.; et al. *Geant4 simulation of production and interaction of muons*. IEEE Trans. Nucl. Sci., 53(2):513–519, apr 2006. doi:10.1109/TNS.2006.872633.

[87] Barrett, P.H.; Bollinger, L.M.; Cocconi, G.; et al. *Interpretation of Cosmic-Ray Measurements Far Underground*. Rev. Mod. Phys., 24(3):133–178, jul 1952. doi:10.1103/RevModPhys.24.133.

[88] Beringer, J.; Arguin, J.F.; Barnett, R.M.; et al. *Review of Particle Physics*. Phys. Rev. D, 86(1):010001, jul 2012. doi:10.1103/PhysRevD.86.010001.

[89] Bethe, H. and Heitler, W. *On the Stopping of Fast Particles and on the Creation of Positive Electrons*. Proc. R. Soc. A Math. Phys. Eng. Sci., 146(856):83–112, aug 1934. doi:10.1098/rspa.1934.0140.

[90] Petrukhin, A.A. and Shestakov, V.V. *The influence of the nuclear and atomic form factors on the muon bremsstrahlung cross section*. Can. J. Phys., 46(10):S377–S380, may 1968. doi:10.1139/p68-251.

[91] Kelner, S.; Kokoulin, R.; and Petrukhin, A. *About Cross Section for High Energy Muon Bremsstrahlung*, 1995.

[92] Motz, J.W.; Olsen, H.A.; and Koch, H.W. *Pair Production by Photons*. Rev. Mod. Phys., 41(4):581–639, oct 1969. doi:10.1103/RevModPhys.41.581.

[93] Hubbell, J.H. *Electron-positron pair production by photons: A historical overview*. Radiat. Phys. Chem., 75:614–623, 2006. doi:10.1016/j.radphyschem.2005.10.008.

[94] Butkevich, A.V. and Mikheyev, S.P. *The cross-section of muon-nuclear inelastic interaction*. Submitt. to Eur.Phys.J. hep-ph/0109060, pages 1–35, sep 2001.

[95] Scapparone, E. *Study of photonuclear interaction of muons in rock with the MACRO experiment*. Nucl. Phys. B - Proc. Suppl., 75(1-2):397–399, mar 1999. doi:10.1016/S0920-5632(99)00304-7.

[96] Weizsäcker, C. *Ausstrahlung bei Stößen sehr schneller Elektronen*. Zeitschrift für Phys., 88(9-10):612–625, sep 1934. doi:10.1007/BF01333110.

[97] Malgin, A.S. and Ryazhskaya, O.G. *Neutrons from muons underground*. Phys. At. Nucl., 71(10):1769–1781, 2009. doi:10.1134/S1063778808100116.

[98] Wang, Y.F.; Balic, V.; Gratta, G.; et al. *Predicting neutron production from cosmic-ray muons*. Phys. Rev. D, 64(1):13012, 2001. doi:10.1103/PhysRevD.64.013012.

[99] Borie, E. and Rinker, G.A. *The energy levels of muonic atoms*. Rev. Mod. Phys., 54(1):67, 1982. doi:10.1103/RevModPhys.54.67.

[100] Reichenbacher, J. *Untersuchung der optischen Eigenschaften grossflächiger Plastikszintillatoren für den KARMEN-Upgrade*. Ph.D. thesis, Forschungszentrum Karlsruhe GmbH, Karlsruhe, 1998.

[101] Habermehl, F. *Entwicklung der Datenaufnahme und Tests der Vetomodule für das EDELWEISS II muon-Vetozählersystem*. Diploma thesis, Universität Karlsruhe (TH), 2004.

[102] Chantelauze, A. *Investigation of the muon-induced background of the EDELWEISS-II experiment*. Ph.D. thesis, Université Blaise Pascal, 2009.

[103] Chabert, L. *Étude du bruit de fond neutron induit par les muons dans l´expérience EDELWEISS-II*. Ph.D. thesis, Université Claude Bernard Lyon 1, 2004.

[104] Landau, L. *On the Energy Loss of Fast Particles by Ionization*. J.Phys.(USSR), 8(201), 1944.

[105] Vavilov, P.V. *Ionization losses of high energy heavy particles.* J.Phys.(USSR), 5(4):749–751, 1957.

[106] SAINT-GOBAIN. *Premium Plastic Scintillators.* `http://www.crystals.saint-gobain.com/uploadedFiles/SG-Crystals/Documents/SGC%20BC400-404-408-412-416%20Data%20Sheet.pdf`.

[107] Förster, T. *10th Spiers Memorial Lecture. Transfer mechanisms of electronic excitation.* Discuss. Faraday Soc., 27(10):7, 1959. doi:10.1039/df9592700007.

[108] Avakian, P.; Abramson, E.; Kepler, R.G.; et al. *Indirect Observation of Singlet-Triplet Absorption in Anthracene Crystals.* J. Chem. Phys., 39(4):1127, 1963. doi:10.1063/1.1734366.

[109] Brooks, F. *Development of organic scintillators.* Nucl. Instruments Methods, 162(1-3):477–505, 1979. doi:10.1016/0029-554X(79)90729-8.

[110] Birks, J. *Front Matter.* In *Theory Pract. Scintill. Count.*, page iii. Elsevier, 1964. doi:10.1016/B978-0-08-010472-0.50001-X.

[111] Schipperges, V. *Vermessung der Auslesetotzeit des EDELWEISS-3 Myon-Veto-Systems.* Bachelor thesis, Karlsruher Institut für Technologie (KIT), 2013.

[112] Brun, R. and Rademakers, F. *ROOT — An object oriented data analysis framework.* Nucl. Instruments Methods Phys. Res. Sect. A Accel. Spectrometers, Detect. Assoc. Equip., 389(1-2):81–86, 1997. doi:10.1016/S0168-9002(97)00048-X.

[113] Cox, G.; Armengaud, E.; Augier, C.; et al. *A multi-tiered data structure and process management system based on ROOT and CouchDB.* Nucl. Instruments Methods Phys. Res. Sect. A Accel. Spectrometers, Detect. Assoc. Equip., 684:63–72, aug 2012. doi:10.1016/j.nima.2012.04.049.

[114] Eitel, K.; Gemmeke, H.; Maschuw, R.; et al. *Wavelength Dependent Light Attenuation in Organic Scintillators.* Nucl. Instr. Meth. A, 340:346–352, 1994.

[115] Rozman, I. and Zimmer, K. *The damage to plastic scintillators by ionizing radiations.* Int. J. Appl. Radiat. Isot., 3(1):36–42, jan 1958. doi:10.1016/0020-708X(58)90054-1.

[116] Berger, C.; Fröhlich, M.; and Mönch, H. *Muon bundles observed in the Frejus underground detector and primary cosmic ray composition.* Nucl. Phys. B - Proc. Suppl., 16(7):477–478, aug 1990. doi:10.1016/0920-5632(90)90557-B.

[117] GEANT4 Collaboration. *Geant4 9.6 Release Notes.* `http://geant4.cern.ch/support/ReleaseNotes4.9.6.html`, 2012.

[118] Reichhart, L.; Lindote, A.; Akimov, D.; et al. *Measurement and simulation of the muon-induced neutron yield in lead.* Astropart. Phys., 47:67–76, jul 2013. doi:10.1016/j.astropartphys.2013.06.002.

[119] Japan Atomic Energy Agency. *Japanese Evaluated Nuclear Data Library.* `https://www.jaea.go.jp/english/index.html`.

[120] Araújo, H.M.; Blockley, J.; Bungau, C.; et al. *Measurements of neutrons produced by high-energy muons at the Boulby Underground Laboratory.* Astropart. Phys., 29:471–481, 2008. doi:10.1016/j.astropartphys.2008.05.004.

[121] Wei, Y. *Untersuchung der neutrinoinduzierten Myonen im Fréjus Untergrunddetektor.* Ph.D. thesis, Bergische Universität Gesamthochschule Wuppertal, 1993.

[122] The International Commission On Radiation Units And Measurements. *Fundamental Quantities And Units For Ionizing Radiation (Revised).* J. ICRU Rep. 85, 11(1), 2011.

[123] Berger, C.; Fröhlich, M.; Mönch, H.; et al. *Results from the Fréjus experiment on nucleon decay modes with charged leptons.* Zeitschrift für Phys. C Part. Fields, 50(3):385–394, sep 1991. doi:10.1007/BF01551450.

[124] Girardin, G. *Etude d'une source neutrons par détection du rayonnement gamma émis en coïncidence.* Bachelor thesis, Université Claude Bernard Lyon 1, 2006.

[125] Croft, S. *The use of neutron intensity calibrated $^9BeC(\alpha, n)$ sources as 4438 keV gamma-ray reference standards.* Nucl. Instruments Methods Phys. Res. Sect. A Accel. Spectrometers, Detect. Assoc. Equip., 281(1):103–116, aug 1989. doi:10.1016/0168-9002(89)91221-7.

[126] Lehman, R. *The origin of neutron groups in $Be(\alpha,n)$ sources.* Nucl. Instruments Methods, 60:253–260, 1968. doi:10.1016/0029-554X(68)90128-6.

[127] Ajzenberg-Selove, F. *Energy levels of light nuclei A = 11-12.* Nucl. Phys. A, 433(1):1–157, jan 1985. doi:10.1016/0375-9474(85)90484-1.

[128] Kibédi, T.; Stuchbery, A.; Dracoulis, G.; et al. *Towards the pair spectroscopy of the Hoyle state in 12 C.* EPJ Web Conf., 35:06001, oct 2012. doi:10.1051/epjconf/20123506001.

[129] Chu, S.; Ekström, L.; and Firestone, R. *WWW Table of Radioactive Isotopes.* `http://nucleardata.nuclear.lu.se/toi/`, 1999.

[130] Sogbadji, R.; Abrefah, R.; Nyarko, B.; et al. *The design of a multisource americium-beryllium (Am-Be) neutron irradiation facility using MCNP for the neutronic performance calculation.* Appl. Radiat. Isot., 90:192–196, 2014. doi:10.1016/j.apradiso.2014.03.017.

[131] Geiger, K. and Van der Zwan, L. *Neutrons and γ-rays from radioactive $^{13}C(\alpha, n)$ sources.* Nucl. Instruments Methods, 157(1):199–201, nov 1978. doi:10.1016/0029-554X(78)90607-9.

[132] Vijaya, A. and Kumar, A. *The neutron spectrum of Am–Be neutron sources.* Nucl. Instruments Methods, 111(3):435–440, sep 1973. doi:10.1016/0029-554X(73)90199-7.

[133] Garg, J.; Calvert, J.; and Gale, N. *Angular correlation studies of the $^9Be(\alpha, n\gamma)$ ^{12}C reaction.* Nucl. Phys., 19:264–279, sep 1960. doi:10.1016/0029-5582(60)90237-6.

[134] Geiger, K. and Van Der Zwan, L. *Radioactive neutron source spectra from $^9Be(\alpha, n)$ cross section data.* Nucl. Instruments Methods, 131:315–321, 1975. doi:10.1016/0029-554X(75)90336-5.

[135] Chamberlin, D.; Bodansky, D.; Jacobs, W.W.; et al. *Electromagnetic decay of the 7.65-MeV state of ^{12}C.* Phys. Rev. C, 9(1):69–75, jan 1974. doi:10.1103/PhysRevC.9.69.

[136] Markham, R.G.; Austin, S.M.; and Shahabuddin, M.A.M. *A Measurement of Γ_{rad}/Γ for the 7.654 MeV State of ^{12}C and the rate of the stellar 3 α reaction.* Nucl. Phys. A, 270:489–500, 1976.

[137] Mak, H.B.; Evans, H.C.; Ewan, G.T.; et al. *Radiative decay of the second excited state of ^{12}C.* Phys. Rev. C, 12(4):1158, 1975.

[138] Butler, J. and Gossett, C. *Radiative Proton Capture by Ni^{58}, Ni^{60}, and Co^{59}.* Phys. Rev., 108(6):1473–1495, 1957. doi:10.1103/PhysRev.108.1473.

[139] Hubbell, J.H.; Gimm, H.A.; and Øverbø, I. *Pair, Triplet, and Total Atomic Cross Sections (and Mass Attenuation Coefficients) for 1 MeV-100 GeV Photons in Elements Z=1 to 100.* J. Phys. Chem. Ref. Data, 9(4):1023, 1980. doi:10.1063/1.555629.

[140] O'Rielly, G.V.; Kolb, N.R.; and Pywell, R.E. *The response of plastic scintillator to protons and deuterons.* Nucl. Instruments Methods Phys. Res. Sect. A Accel. Spectrometers, Detect. Assoc. Equip., 368:745–749, 1996. doi:10.1016/0168-9002(95)00671-0.

[141] Chou, C.N. *The Nature of the Saturation Effect of Fluorescent Scintillators.* Phys. Rev., 87(5):904–905, sep 1952. doi:10.1103/PhysRev.87.904.

[142] Wright, G.T. *Scintillation Response of Organic Phosphors.* Phys. Rev., 91(5):1282–1283, sep 1953. doi:10.1103/PhysRev.91.1282.2.

[143] Reichhart, L.; Akimov, D.; Araújo, H.M.; et al. *Quenching factor for low-energy nuclear recoils in a plastic scintillator.* Phys. Rev. C, 85(6):065801, jun 2012. doi:10.1103/PhysRevC.85.065801.

[144] Badhwar, G.; Deney, C.; Dennis, B.; et al. *The non-linear response of the plastic scintillator NE102.* Nucl. Instruments Methods, 57(7):116–120, 1967. doi:10.1016/0029-554X(67)90507-1.

[145] Billard, J. *Détection directionnelle de matière sombre avec MIMAC.* Ph.D. thesis, Université de Grenoble, 2012.

[146] Geyer, C.J. *Markov chain Monte Carlo maximum likelihood.* Comput. Sci. Stat. Proc. 23rd Symp. Interface, (1):156–163, 1991.

[147] George, E. *Lecture I: A Gentle Introduction to Markov Chain Monte Carlo (MCMC).* Spring seminar villard-sur-ollon, 2005.

[148] Ziegel, E.; Press, W.; Flannery, B.; et al. *Numerical Recipes: The Art of Scientific Computing.* Technometrics, 29(4):501, nov 1987. doi:10.2307/1269484.

[149] Putze, a.; Derome, L.; Maurin, D.; et al. *A Markov Chain Monte Carlo technique to sample transport and source parameters of Galactic cosmic rays.* Astron. Astrophys., 497:991–1007, 2009. doi:10.1051/0004-6361/200810824.

[150] Arnaud, Q. *Détection directe de matière noire avec l´experience EDELWEISS-III: Etude des signaux induits par le piegeage de charges, analyse de donnees et caractérisation de la sensibilité des detecteurs cryogeniques aux WIMPs de basse mas.* Ph.D. thesis, Université Claude Bernard Lyon 1, 2015.

[151] Förster, N. *Rise time of ionization pulse in FID800 type detectors (private communication)*, 2015.

[152] Götz, M. *Identifikation von koinzidenten Signalen in mehreren Detektoren des EDELWEISS-III Experiments.* Bachelor thesis, 2015.

[153] Main de Boissière, T. *Recherches de WIMPs de basse masse et d´axions avec l´expérience EDELWEISS.* Ph.D. thesis, Université Paris-Sud, 2015.

[154] Yellin, S. *Finding an upper limit in the presence of an unknown background.* Phys. Rev. D, 66(3):032005, 2002. doi:10.1103/PhysRevD.66.032005.

[155] Kudryavtsev, V.a.; Pandola, L.; and Tomasello, V. *Neutron- and muon-induced background in underground physics experiments.* Eur. Phys. J. A, 36(2):171–180, 2008. doi:10.1140/epja/i2007-10539-6.

[156] Lindote, a.; Araújo, H.; Kudryavtsev, V.; et al. *Simulation of neutrons produced by high-energy muons underground.* Astropart. Phys., 31(5):366–375, jun 2009. doi:10.1016/j.astropartphys.2009.03.008.

[157] Agnese, R.; Ahmed, Z.; Anderson, a.J.; et al. *Silicon Detector Dark Matter Results from the Final Exposure of CDMS II.* Phys. Rev. Lett., 111(25):251301, 2013. doi:10.1103/PhysRevLett.111.251301.

[158] Goodenough, L. and Hooper, D. *Possible Evidence For Dark Matter Annihilation In The Inner Milky Way From The Fermi Gamma Ray Space Telescope.* FERMILAB-PUB-09-494-A, pages 1–5, oct 2009.

[159] Beskidt, C.; de Boer, W.; and Kazakov, D.I. *The impact of a 126 GeV Higgs on the neutralino mass.* Phys. Lett. B, 738:505–511, 2014. doi:10.1016/j.physletb.2014.08.011.

[160] Armengaud, E.; Augier, C.; Benoît, A.; et al. *Constraints on low-mass WIMP from the EDELWEISS-III dark matter search (in preparation).*

[161] Hehn, L. *Search for Dark Matter signals in EDELWEISS-III with a multidimensional maximum likelihood method (in preparation)*. Ph.D. thesis, Karlsruher Institut für Technologie.

Appendix

A. Radioactive decay chains
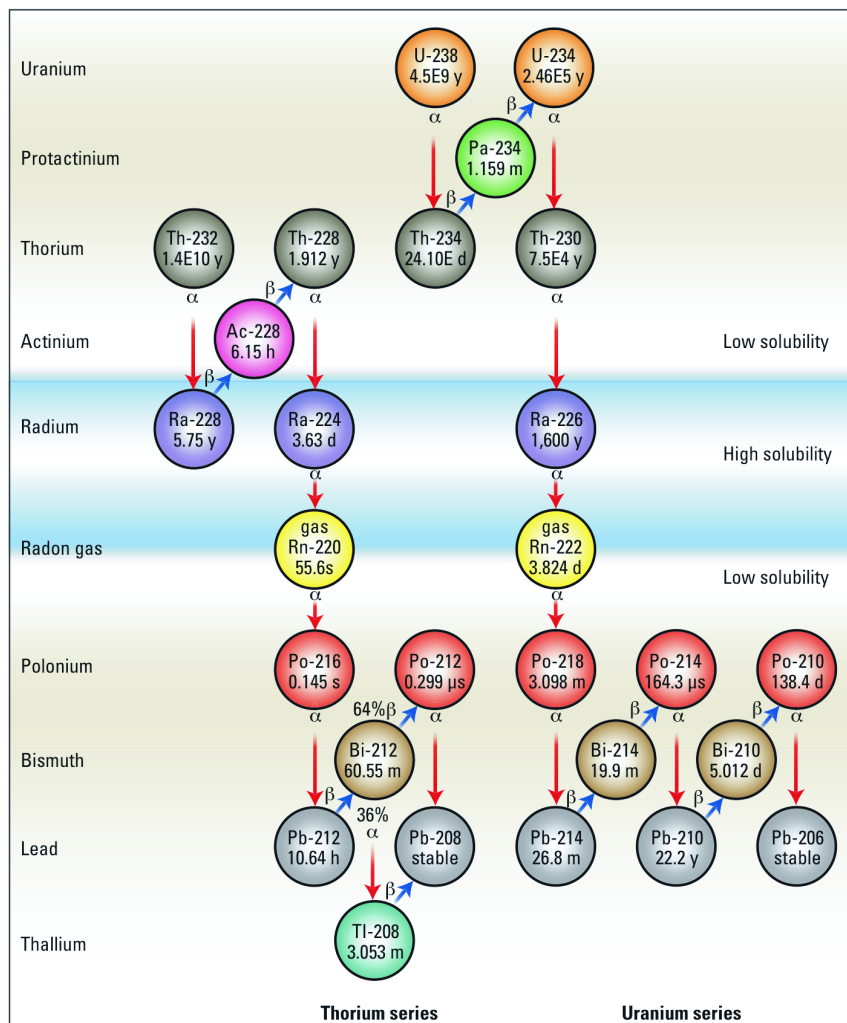
Figure A.1. – Radioactive decay chains of ^{232}Th and ^{238}U.

Acknowledgements